HESAM UNIVERSITÉ

Arts et Métiers Sciences et Technologies

ÉCOLE DOCTORALE SCIENCES DES MÉTIERS DE L'INGÉNIEUR
Laboratoire de PIMM– Campus de Paris

THÈSE

présentée par : **Xixi LI**

soutenue le : **14 Décembre 2021**

pour obtenir le grade de : **Docteur d'HESAM Université**

préparée à : **École Nationale Supérieure d'Arts et Métiers**

Spécialité : **Mécanique et Matériaux**

Wave propagation in composite structures in presence of LASER induced delamination: simulation and experiments

THÈSE dirigée par :
Prof. MECHBAL Nazih

et co-encadrée par :
REBILLAT Marc
GUSKOV Mikhail

Jury

M. BENJEDDOU Ayech, Professeur des universités, ROBERVAL, ISAE-SUPMECA Paris	Président
M. MENCIK Jean-Mathieu, Professeur des universités, INSA Centre Val de Loire	Rapporteur
M. SHOKHIN Alexander, Senior researcher, BIMS, Russian Academy of Sciences, Russia	Rapporteur
M. MECHBAL Nazih, Professeur des universités, PIMM, ENSAM, Paris	Examinateur
M. REBILLAT Marc, Maître de Conférences, PIMM, ENSAM, Paris	Examinateur
M. GUSKOV Mikhail, Maître de Conférences, PIMM, ENSAM, Paris	Examinateur

T H È S E

Abstract

This dissertation addresses structural health monitoring (SHM) problematic, related to the use of a wave-based ultrasonic technique for thin-walled structures, particularly focusing on delamination-type damage in composite structure components. The mechanical behavior of the delamination, as well as the interaction between Lamb waves and delamination are addressed.

An experimental investigation is conducted employing an SHM system, which is composed of a signal generator, an amplifier, a multiplexer, specimens, a data acquisition system and a computer. The specimens are carbon fiber reinforced polymer laminate plates equipped with piezoelectric transducers (PZT). Sample set including intact ones and damaged ones with delaminations of different extent are employed for the experiments. The delaminations are generated using a Laser Shock technique, which can provide specific location and size of the delamination. PZT elements bonded to the structure surface are used as actuator and sensor of the Lamb waves in pitch-and-catch interrogations. Several damage indicators (DI) are implemented and employed to evaluate the severity of the delamination, based on time and frequency domain features. The proposed DIs are employed to evaluate the delamination severity and the nonlinear effects. Results show that the system's sensitivity to various damage sizes induces different responses depending on the DI considered.

Finite element modeling of damaged structures includes a layered construction of the composite plates, split in the delamination area. The use of piezoelectric plate elements for the sensors-actuators enables a direct simulation of an SHM interrogation in terms of electric input and output signals.

At the stage of delamination interface model parameters analysis, preliminary investigations are conducted on 2D models. Thus, relevant parameter ranges were examined, in terms of physical behaviour, but also in terms of DI. Finally, once those observations are transposed to a 3D model, full structure model is built, leading to a comparison to the experimental observation, directly in signals and in terms of various DIs.

Key words: Structural health monitoring, Lamb waves, Nonlinear dynamics, composite structures

Contents

Abstract iii

List of Figures ix

List of Tables xvii

List of Abbreviations xix

1 Introduction 1
- 1.1 Context . . . 1
- 1.2 Research goal and objective of the thesis . . . 2
- 1.3 Structure of the thesis . . . 2

2 State of art on modeling for nonlinearity-based structural health monitoring of composites 5
- 2.1 Introduction . . . 5
- 2.2 Composite materials in aeronautic applications . . . 6
  - 2.2.1 Introduction . . . 6
  - 2.2.2 Basic concepts of classical lamination theory . . . 6
  - 2.2.3 Damage types in composite materials and formation of delamination . . . 11
- 2.3 Nonlinear phenomena in structural health monitoring using Lamb waves 12
  - 2.3.1 Classical nonlinearity . . . 13
  - 2.3.2 Non-classical nonlinearity . . . 14
    - 2.3.2.1 Bilinear stiffness model . . . 14
    - 2.3.2.2 Material hysteresis behavior . . . 14
- 2.4 Numerical models for delamination . . . 15
  - 2.4.1 Stiffness reduction model . . . 15
  - 2.4.2 Surface-to-surface contact interaction model . . . 18
  - 2.4.3 Spring-type contact interface model . . . 19
  - 2.4.4 Nonlinear spring model . . . 20
- 2.5 Finite element techniques for delamination modeling . . . 21
  - 2.5.1 Duplicated node method . . . 21
  - 2.5.2 Unbonded layer . . . 22
  - 2.5.3 Thin elastic layer . . . 22
- 2.6 Damage index . . . 22

2.6.1 Damage index based on time domain features . . . 23
2.6.2 Damage index based on frequency domain features . . . 23
2.6.3 Damage index for evaluating nonlinear effects . . . 24
2.7 Conclusion . . . 24

3 Experiments on Delamination Detection in Composite Plates 25
3.1 Introduction . . . 25
3.2 Specimens and delamination generation by laser shock wave technique 25
3.2.1 Introduction . . . 25
3.2.2 Principles of laser shock wave technique for damage generation 26
3.2.2.1 High power laser . . . 26
3.2.2.2 Generation of laser shock wave . . . 26
3.2.2.3 Damage generated by shock wave . . . 26
3.2.3 Composite specimens . . . 29
3.3 Description of the SHM system . . . 31
3.4 Selection of input signals . . . 32
3.4.1 Type of input signals . . . 32
3.4.2 Excitation frequency . . . 33
3.5 Damage index . . . 33
3.6 Experimental results . . . 35
3.6.1 Sine wave excitation . . . 35
3.6.2 Modulated sine wave excitation . . . 38
3.7 Conclusion . . . 40

4 Numerical Model for Composite Plate 43
4.1 Modeling composite plates . . . 43
4.1.1 Study on element size and time increment . . . 44
4.1.1.1 Time increment study . . . 45
4.1.1.2 Global element size study . . . 47
4.1.1.3 Local element size study . . . 49
4.1.2 Study on damping coefficient . . . 50
4.2 Damage Model for delamination-type damage in composites . . . 52
4.2.1 Beam model employed for damage model investigation . . . 53
4.2.2 Stiffness reduction model . . . 54
4.2.3 Spring models . . . 57
4.2.3.1 Linear spring model . . . 57
4.2.3.2 Nonlinear spring model . . . 58
4.2.3.3 Contact/friction model . . . 71
4.3 Simulation results and discussion . . . 75
4.3.1 Time domain signals . . . 75
4.3.2 Parametric study . . . 76
4.3.2.1 Stiffness reduction model . . . 76
4.3.2.2 Nonlinear spring model . . . 76

4.3.2.3 Contact/friction model . . . 86
4.3.2.4 Comparison between different models and determination of model parameters . . . 93
4.3.3 DI comparison . . . 94
4.4 Verification of finite element model . . . 98
4.4.1 Comparison with experiments . . . 98
4.4.1.1 Intact plate . . . 99
4.4.1.2 Damaged plates . . . 100
4.4.1.3 DI investigation . . . 101
4.4.2 Compare with literature results . . . 106
4.5 Conclusion . . . 109

5 Conclusion and future work **111**
5.1 Conclusion . . . 111
5.2 Future works . . . 112

A Résumé de la thèse **113**
A.1 Introduction . . . 113
A.1.1 Context . . . 113
A.1.2 Objectif de la thèse . . . 114
A.2 Expériences sur la détection des dommages dans les plaques composites 114
A.2.1 Spécimens composites . . . 114
A.2.2 Description du système SHM . . . 116
A.2.3 Sélection des signaux d'entrée . . . 117
A.2.4 Indice de dégâts . . . 118
A.2.5 Résultats expérimentaux . . . 119
A.2.5.1 Excitation sinusoïdale . . . 119
A.2.5.2 Excitation sinusoïdale modulée . . . 121
A.3 Simulations par éléments finis . . . 123
A.3.1 Modèles éléments finis pour plaques composites et délaminage . 123
A.3.2 Modèle de dommages pour les dommages de type délaminage dans les composites . . . 124
A.3.2.1 Modèle de réduction de rigidité . . . 124
A.3.3 Modèles à ressort . . . 125
A.3.3.1 Modèle à ressort linéaire . . . 125
A.3.3.2 Modèle de ressort non linéaire . . . 125
A.3.3.3 Modèle contact/frottement . . . 127
A.4 Résultats et discussion . . . 128
A.4.1 Plaque intacte . . . 129
A.4.2 Plaques endommagées . . . 129
A.4.2.1 Signaux dans le domaine temporel . . . 129
A.4.2.2 Signaux dans le domaine fréquentiel . . . 130
A.4.2.3 Indice de dommage . . . 131

A.5 Conclusion 134

Bibliography **137**

List of Figures

2.1 Schematic of lamina(a) and laminates(b). 7
2.2 Plate deformation in $x-z$ plane [8]. 8
2.3 Positive sign of stress, resultant forces and moments. 10
2.4 Laminate stacking sequence nomenclature [8]. 11
2.5 (a) Side view of delaminations in a four-layer cross-ply CFRP laminate after quasi-static loading. (b) Plan view of delaminations, which are represented by the dark spots in the X-radiograph [11]. 12
2.6 Schematic of the "breathing" type crack in structures having a bi-linear contact behavior [20]. 15
2.7 Example of a bi-linear stiffness model showing force-displacement relationship. For positive displacement (in tension) the stiffness has a different value than for the negative displacements (in compression). . 16
2.8 A typical example of material hysteresis behavior [12]. 16
2.9 The 2D modeling of a beam containing a delamination using stiffness reduction method based on Ref. [23]. 17
2.10 Kinematic assumptions of generalized laminate theory with single delamination [24]. U^m indicates the displacement of mth delamination along x-axis. 18
2.11 Pressure-overclosure relationship of "hard" contact [31]. 19
2.12 Schematic of delamination modeling using duplicated node method. . 21
2.13 Schematic of the unbonded layer technique for modeling delamination. 22
2.14 Schematic of the thin elastic layer technique for modelling delamination. 23

3.1 Principle of Laser-matter interaction and shock wave generation, presented with a confinement Layer (C) and a sacrificial layer (S) [51]. 27
3.2 Schematic of time-position relations for the one side laser case. The pulse duration in (a) is longer than that in (b). The thickness of the sample is h [7]. 27
3.3 Schematic of the symmetrical LASER shock configuration with a sacrificial layer and a confinement medium [51]. 28
3.4 Schematic of time-position relations for the two side laser case. The laser pulse on the right side in (b) is delayed by TD and the D-SHM point is shifted by DO. The thickness of the sample is h [7]. 28
3.5 Side view of the delamination inside the composite specimen [51]. . . . 29

3.6 Schematic of the four specimens and the positions of the delaminations [51]. . . . 30
3.7 A composite specimen equipped with two PZTs. . . . 31
3.8 The experimental system. . . . 32
3.9 Schematic of experimental process. . . . 32
3.10 Simulation results of natural frequency analysis of the fundamental radial mode shape of the PZT disk. . . . 33
3.11 Typical output signals of sinusoidal excitations of undamaged case (left) and damaged case with two impacts (right). . . . 35
3.12 Frequency domain responses of sine wave input obtained from undamaged plate and damaged plate containing two impacts. . . . 36
3.13 Frequency spectrum of residual signal between the two-impact damaged plate and the undamaged plate subject to sinusoidal excitation. . . 37
3.14 Variation of DI based on relative total harmonic distortion (THD) against number of delamination impacts. The solid blue line indicates that the excitation amplitude is 10V and the red dash-dot line 50V. . 37
3.15 Variation of DI based on relative total harmonic distortion (THD) against excitation amplitude on different specimens. . . . 38
3.16 Frequency domain responses of signals obtained from undamaged plate and damaged plate containing two impacts. . . . 39
3.17 Frequency spectrum of residual signal between the two-impact damaged plate and the undamaged plate subject to modulated wave excitation. . . . 39
3.18 Variation of DI based on relative THD against the number of delamination impacts for different excitation amplitudes. . . . 40
3.19 Variation of DI based on relative THD against excitation amplitude on different specimens. . . . 40

4.1 Schematic of finite element model in thee-dimensions. . . . 44
4.2 Time responses from models with different time increments. . . . 45
4.3 Time of flight of the simulated responses with different time increments. 46
4.4 RMSD of first wave packet between simulated and experimental responses with different time increments. . . . 47
4.5 Time responses from models with different global element sizes. . . . 48
4.6 Time of flight of the simulated responses with different global element size. . . . 49
4.7 RMSD of first wave packet between simulated and experimental responses with different global element size. . . . 49
4.8 Time of flight of the simulated responses with different global and local element size. . . . 50
4.9 RMSD between simulated and experimental responses with different global and local element size. . . . 51

4.10 Comparison between raw responses from undamped model and damped model. 53
4.11 Comparison between raw responses from simulation and experiments. 53
4.12 Beam model for the investigation of delamination model parameters. . 54
4.13 Effect of reduction coefficient on indicator CRC based on correlation coefficient of the received electrical signal. 56
4.14 Effect of reduction coefficient on DI based on the normalized residual energy of the received electrical signal with respect to the reference signal. 56
4.15 Schematic of surface interaction modeling at delamination region by applying nonlinear springs. 57
4.16 Effect of spring stiffness on indicator CRC extracted from the received electrical signal. 58
4.17 Effect of spring stiffness on indicator NRE extracted from the received electrical signal. 59
4.18 Effect of spring stiffness on relative THD extracted from the received electrical signal. 59
4.19 Force to relative displacement relationship of the nonlinear springs at the delamination region. 60
4.20 Simulation results for the one-impact beam model: relative displacements between the upper and lower surfaces of the delamination. The measurement point is located at the center of the delamination. Left: temporal signals; right: FFT of the relative displacement normalized to the maximum value of each signal in log scale. 62
4.21 Simulation results for the two-impact beam model: relative displacements between the upper and lower surfaces of the delamination. The measurement point is located at the center of the delamination. Left: temporal signals; right: FFT of the relative displacement normalized to the maximum value of each signal in log scale. 63
4.22 Simulation results for the three-impact beam model: relative displacements between the upper and lower surfaces of the delamination. The measurement point is located at the center of the delamination. Left: temporal signals; right: FFT of the relative displacement normalized to the maximum value of each signal in log scale. 64
4.23 The signal maximum to minimum value ratio of all three impacts with different spring stiffness. 65
4.24 The THD of relative normal displacement of all three impacts with different spring stiffness. 66
4.25 Electrical raw outputs for the beam models with different spring stiffness. Left: time domain signals; right: frequency spectra. 67
4.26 Schematic of nonlinear in-plane interaction model 68

4.27 Relative velocity of the center node of the delamination. The corresponding model is the three-impact beam, and no out-of-plane or in-plane interaction exists in the delamination region. 69
4.28 Time domain responses from the three-impact beam models with fixed v_f (1×10^{-6} m/s). 70
4.29 Time domain responses from in-plane models with fixed F_0 (1×10^{-6} N). 70
4.30 The convergence of the raw responses in time domain from the three-impact beam models with different v_f and F_0 parameters in the in-plane interaction model. 71
4.31 Schematic of the interaction model at delamination area with penetration through nodes 2 and 5. F_T and F_N are the tangential and normal forces, and u_x and v_x are the displacement and velocity in x-direction respectively. 73
4.32 Electrical outputs from the three-impact beam models with different friction coefficients. 73
4.33 Responses of in-plane displacements in time and frequency domain from different beam models. The amplitudes in frequency domain are normalized to the maximum value of each signal. 74
4.34 Responses of out-of-plane displacements in time and frequency domain from different beam models. The amplitudes in frequency domain are normalized to the maximum value of each signal. 75
4.35 Time domain signals of different damage models. 76
4.36 Time domain signals from stiffness reduction model with different reduction coefficients. 77
4.37 Effect of reduction coefficient on indicator CRC based on correlation coefficient of the received electrical signal. 78
4.38 Effect of reduction coefficient on indicator NRE based on normalized residual energy of the received electrical signal. 78
4.39 Effect of different spring stiffness on relative THD of the received electrical signal with respect to the undamaged plate. 79
4.40 Relative displacements between the upper and lower interfaces in out-of-plane direction of the center node at delamination from the one-impact plate model with $k^{spr} = 0$ N/m. 80
4.41 Mechanical behavior of the center point of the delamination from one-impact plate with different spring stiffness values. Left: relative out-of-plane displacement of the center point. Right: relationship between spring force and relative displacement in out-of-plane direction. . . . 81
4.42 Typical raw responses of two extreme cases for the two-impact plate: $k^{spr} = 0$ and $k^{spr} = 8 \times 10^6$ N/m. 82
4.43 Relative displacement in out-of-plane direction of the center node for $k^{spr} = 0$ case of the two-impact plate. 83

4.44 Relative displacement in out-of-plane direction of the center node for $k^{spr} = 8 \times 10^6$ N/m case of two-impact plate. 83
4.45 Spring force-relative displacement relationship for $k^{spr} = 8 \times 10^6$ N/m case of the two-impact plate model. 84
4.46 Two-impact plate: relative displacements (left) and spring force-relative displacement relationships (right) of the center node of the delamination: (a) and (b) are for the $k^{spr} = 4 \times 10^4$ N/m case, (c) and (d) are for the $k^{spr} = 1 \times 10^5$ N/m case, and (e) and (f) are for the $k^{spr} = 1 \times 10^6$ N/m case. 85
4.47 Three-impact plate: relative displacement for the 0 spring stiffness case. 86
4.48 Three-impact plate: relative displacements (left) and spring force-relative displacement relationships (right) of the center node of the delamination for the two-impact plate model: (a) and (b) are for the $k^{spr} = 1 \times 10^5$ N/m case, (c) and (d) are for the $k^{spr} = 1 \times 10^6$ N/m case, and (e) and (f) are for the $k^{spr} = 8 \times 10^6$ N/m case. 87
4.49 The convergence of the one-impact plate model with various (v_f,F_0) pairs. 88
4.50 The convergence of the two-impact plate model with various (v_f,F_0) pairs. 88
4.51 The convergence of three-impact plate model with various (v_f,F_0) pairs. 89
4.52 Example of the numerical resonance: electrical outputs from three-impact plate model with $v_f = 1 \times 10^{-5}$ m/s and $F_0 = 1 \times 10^{-6}$ N. . . . 89
4.53 Electrical output signals in both time and frequency domains from three-impact plate using contact/friction model with different friction coefficients. 90
4.54 Effect of friction coefficient on CRC and NRE of the electrical output signals of the three-impact plate. 90
4.55 Effect of friction coefficient on relative THD of the electrical output signals of the three-impact plate. 91
4.56 Relative displacement in out-of-plane direction between upper and lower surface of the center point at delamination region. Results are from the three-impact plate using contact/friction models with different friction coefficients. The left column illustrates displacements in time domain and the right column shows their frequency spectra. . . 92
4.57 Electrical output signals in both time and frequency domains from three-impact plate using contact/friction model with different spring stiffness values. 93
4.58 Effect of spring stiffness on CRC and NRE of the electrical output signals of the three-impact plate. 93
4.59 Effect of spring stiffness on relative THD of the electrical output signals of the three-impact plate. 94

4.60 Relative displacement in out-of-plane direction between upper and lower surface of the center point at delamination region. Results are from the three-impact plate using the contact/friction model with different spring stiffnesses. The left column illustrates displacements in time domain and the right column shows their frequency spectra. . . 95
4.61 Variation of CRC values against reduction coefficient in stiffness reduction model and the log scale values of spring stiffness in bi-linear spring model. 96
4.62 Variation of CRC values against friction coefficient in contsct/friction model and the log scale values of stiffness in bi-linear spring model. . . 96
4.63 Effect of delamination diameter on relative THD of the received electrical signals. 97
4.64 Effect of delamination diameter on THD value extracted from the difference signals after baseline subtraction. 98
4.65 Effect of delamination diameter on CRC of the received electrical signals. 99
4.66 Effect of delamination diameter on NRE of the received electrical signals. 99
4.67 Comparison of the electrical output in both time and frequency domains between simulation and experiment results for the undamaged plate. The frequency signals are normalized to the maximum value of each spectrum respectively. 100
4.68 Comparison of electrical output signals in time domain between experiment and simulation results. 101
4.69 Normalized FFT of the output signals of both the healthy plate and the three-impact plate from experiment and simulations respectively. 102
4.70 Comparison of CRC between simulations and experiment. 103
4.71 Comparison of NRE between simulations and experiment. 103
4.72 Comparison of NRE2 between simulations and experiment. 104
4.73 Comparison of CCMPD between simulations and experiment. 105
4.74 Comparison of relative THD between simulations and experiment. . . 105
4.75 Comparison of THD from the residual signals after baseline subtraction between simulations and experiment. 106
4.76 Schematic diagram of a composite beam specimen with delamination and its cross-section. 107
4.77 A typical contour snapshot of FE-simulated out-of-plane displacement of the guided wave in the composite beam with a delamination (time = 128.9 ms and scale factor = 250) [26]. 108
4.78 Normalized FFT of the signal obtained from the experiment and FE simulation: (a) intact beam and (b) beam with the delamination located between third and fourth ply. The response measured at 70 mm from excitation and 35 mm from center of the delamination [26]. . . . 108

4.79 Comparison between ABAQUS results and SDT results using the same plate model stated in Ref.[26]. 109

A.1 Schéma des quatre éprouvettes et des positions des délaminations [51]. 115
A.2 Vue latérale du délaminage à l'intérieur de l'éprouvette composite [51]. 115
A.3 Une éprouvette composite équipée de deux PZTs. 116
A.4 Système expérimental. 117
A.5 Résultats de simulation de l'analyse de fréquence naturelle du disque PZT. 118
A.6 Signaux de sortie typiques des excitations sinusoïdales du boîtier non endommagé (à gauche) et du boîtier endommagé avec deux impacts (à droite). 120
A.7 Spectre de fréquence des signaux de sortie à partir de signaux d'entrée sinusoïdaux continus. Chaque courbe est dérivée du signal correspondant dans le domaine temporel à l'aide d'une transformée de Fourier rapide et est normalisée à son amplitude maximale. 121
A.8 Etude du THD relatif sur les amplitudes d'excitation et différents spécimens. 121
A.9 Spectre de fréquence des signaux de sortie à partir des signaux d'entrée modulés. Chaque courbe est normalisée à son amplitude maximale. . . 122
A.10 Etude du THD relatif sur différentes amplitudes d'excitation et différents spécimens. 123
A.11 Schéma du modèle éléments finis en trois dimensions. 124
A.12 Schéma du modèle de réduction de rigidité. 125
A.13 Schéma de la modélisation de l'interaction de surface dans la région de délaminage en appliquant des ressorts non linéaires. 126
A.14 Relation entre la force et le déplacement relatif des ressorts non linéaires dans la région de délaminage. 126
A.15 Schéma du modèle d'interaction non linéaire dans le plan. 127
A.16 Comparaison de la sortie électrique dans les domaines temporel et fréquentiel entre les résultats de la simulation et de l'expérience pour la plaque non endommagée. Les signaux de fréquence sont normalisés à la valeur maximale de chaque spectre respectivement. 129
A.17 Comparaison des signaux de sortie électriques dans le domaine temporel entre les résultats de l'expérience et de la simulation. 130
A.18 FFT normalisée des signaux de sortie de la plaque saine et de la plaque à trois impacts provenant respectivement de l'expérience et des simulations. 131
A.20 Comparaison de NRE2 entre simulations et expérience. 133
A.21 Comparaison du CCMPD entre simulations et expérience. 133
A.22 Comparaison du THD relatif entre les simulations et l'expérience. . . . 134

List of Tables

3.1 Composite specimen material properties [60]. 29
3.2 Properties of NCE51 from Noliac [51]. 30
3.3 Mass and size of NCE51 from Noliac. 31

4.1 Initial and final values of specimen material properties. 44
4.2 Investigation on global and local element size. 50
4.3 Computational time for all cases with different global and local element sizes. 51
4.4 Simulation parameters. 51
4.5 Bending stiffness at the delamination region for the undamaged and damaged plates 55
4.6 Four different spring stiffness k^{spr} cases. 61
4.7 Three different damaged beam models. 61
4.8 Characteristics in delamination region of damaged plate models with different damage severity. 79
4.9 Signal peak to trough ratios from cases with different friction coefficients 90
4.10 Elastic properties of the composite lamina. 106

A.1 Propriétés du matériau de l'éprouvette composite [60]. 114
A.2 Mass and size of NCE51 from Noliac. 116
A.3 Propriétés matérielles des plaques composites. 124

List of Abbreviations

SHM	**S**tructural **H**ealth **M**onitoring
FE	**F**inite **E**lement
DI	**D**amage **I**ndex
THD	**T**otal **H**armonic **D**istorsion
SDT	**S**tructural **D**ynamics **T**oolbox
LSWT	**L**aser **S**hock **W**ave **T**echnique
CRC	**C**oRrelation **C**oefficient
NRE	**N**ormal **R**esidual **E**nergy
RMSD	**R**oot **M**ean **S**quare **D**ifference
FFT	**F**ast **F**ourier **T**ransform
CLT	**C**lassical **L**amination **T**heory

To my parents...

Chapter 1

Introduction

1.1 Context

One of the most important issues in engineering is the monitoring and the early detection of structural damages to prevent catastrophic failures[1, 2, 3]. This process is referred to as Structural Health Monitoring (SHM) and its implementation is expected to provide considerable improvements with respect to safety and maintenance costs [1]. SHM is a revolutionary and innovative technology to determine the structural integrity of structures and is mainly used in aeronautical engineering, civil engineering, etc. It is developed from traditional non-destructive testing. This technology uses a transducer network integrated into the structure to perform real-time online detection, and obtain real-time information about the structure status, operational condition, and service environment. Based on the sensor data, real-time diagnosis results are obtained, the health status of the structure is predicted, and the corresponding control decision is assisted. In the aeronautical industry, the implementation of aircraft SHM technology can effectively improve the safety of aircraft structure, greatly increase flight safety, reduce aircraft maintenance costs and extend service cycles.

In the past few decades, SHM technology based on sensor networks has been extensively studied. According to its development stage, SHM has the following four levels [4]:

1. Damage detection. This is to determine whether the damage exists.
2. Damage localization. This is to localize the damage, i.e. to determine where the damage locates.
3. Damage classification. This is to clarify the characteristics and types of damage.
4. Damage quantification. This is to evaluate the severity of the damage.

In different SHM studies, researchers may focus on one or several of the above four aspects. Among them, damage detection is relatively basic, and researchers cannot bypass it.

In recent years, composite materials have been increasingly used in various industrial fields and especially in aeronautics due to their low density, high specific strength and stiffness. For commercial aircrafts, the percentage of fiber-reinforced composite

materials can reach 50% of mass. Despite having great advantages, composite materials are not exempt from drawbacks. Particularly, composites can be subject to various types of damage. Since the degradation of the composites occurs usually inside the composites, the damage is generally invisible and hard to be observed. Therefore, the application of SHM to composites for damage detection is crucial.

Delamination is one of the most common types of damage in composite materials. It can be defined as the separation of adjacent composite plies. Delamination-type damage can severely degrade the performance of composites and should be identified in time. In this thesis, we focus on the detection and quantification of delamination-type damage in composite laminates.

1.2 Research goal and objective of the thesis

The objective of this thesis is to better understand physically the Lamb waves interaction with a realistic delamination, which, as a contact interface, can feature nonlinear behavior. More precisely, its goal is to investigate the physical mechanism of the generation of the nonlinear phenomena, i.e. the super-harmonics due to the presence of the delamination damage in a composite plate, and to evaluate quantitively the influences of delamination existence on acoustic nonlinear properties of the composite plates. To achieve this, experiments and finite element simulations are conducted. Several models representing the mechanical behavior of the delamination damage are presented to investigate the interaction between Lamb wave and a well-controlled real delamination damage. Four composite plates containing different sizes of delamination are used to investigate the influence of damage size on the acoustic nonlinearity, including one composite plate containing no damage as reference. Several damage indexes (DIs) are analyzed, in particular those sensitive to nonlinear responses, such as THD, in order to evaluate the sensitivity of the DIs to the nonlinearities induced by damage.

1.3 Structure of the thesis

This thesis is composed of 5 chapters:

- Chapter 1 briefly introduces the context and background of this study. The research objective and the structure of this thesis are also depicted in this chapter.
- Chapter 2 briefly introduces the basic concepts of composite materials and the classical lamination theory. Then the acoustic non-linear effects in structural health monitoring based on Lamb waves are introduced. Next, we introduce several commonly used physical models for delamination damage, as well as modeling techniques of damage in composite materials. Finally, we review some damage indicators commonly used in other literature.

- Chapter 3 illustrates the SHM experiments. The experimental system, the composite samples, the selection of input signals, and the choice of experimental parameters are all described in this chapter. There are four samples in the experiment, three of which contain damage of different severities. An intact plate is employed as a baseline in the experiments. In this chapter, we also proposed a damage indicator based on total harmonic distortion (THD). Finally, we describe the results of the experiments in detail.
- Chapter 4 illustrates the finite element simulation. We first establish a finite element model of composite plates. Then we propose several physical models of delamination-type damage and apply these models to the composite plate model. In this chapter, we adopted a beam model having the same length, thickness and material properties as the original plate model, but only one element in the width direction. We investigate the corresponding parameters of each physical model of the delamination damage in detail and locate the sensitivity zone of each parameter. Then the sensitive parameters are applied to the original model to obtain the simulation results. Finally, we compare the simulation results with the experimental results.
- Chapter 5 depicts the conclusion and future work of this thesis.

Chapter 2

State of art on modeling for nonlinearity-based structural health monitoring of composites

2.1 Introduction

Composite materials have been increasingly used in various fields, especially in the aerospace industry. Composites have the advantages of low density, light weight, high stiffness and resistance to high temperature and corrosion. In the case of commercial aircrafts, the percentage of fiber-reinforced composite materials used in the latest Boeing B787 and newly designed Airbus A350-XWB reaches 50% and 52% respectively [5]. Despite these advantages of composites in manufacturing aerospace structure components, they still suffer from many modes of damage. Due to the inherent properties of composites, most degradation modes occur internally and cannot be detected by visual inspection of the surface. However, they can severely reduce structure performance. In this case, the application of SHM in aerospace composite structures has become crucial.

In this chapter, we start with a brief introduction to some basic concepts of composite materials. We will introduce the classical lamination theory and different types of damage that may occur in composite structures. We then turn our attention to the nonlinear phenomena in SHM using Lamb waves. We briefly introduce the basic principles of classical nonlinearity and several mechanisms that produce non-classical nonlinear phenomena. Next, finite element simulations of structural health monitoring on composite structures are presented. For this purpose, we review several physical models commonly used to simulate the mechanical behavior of damage in composites and finite element techniques for the damage modeling. Finally, we review some commonly used damage indexes for evaluating the severity of defects, including indicators based on time-domain signals and frequency-domain signals, as well as those that can be used to evaluate nonlinear phenomena.

2.2 Composite materials in aeronautic applications

2.2.1 Introduction

From a macro perspective, a composite material can be regarded as a combination of two or more constituents with a significantly different macroscopic behavior and a clearly recognizable interface between each constituent. One of the materials acts as a support matrix, while the other enhances the whole material. In the field of aerospace, the dominant material is the fiber-reinforced composite materials. These materials contain thin and long fibers having high strength and stiffness. The length of the fibers can be comparable to the length of the structure components, and much larger than the other two dimensions [1]. The matrix material can be polymer, ceramic or metal [6], and fibers can be glass fibers, carbon fibers or aramid fibers. Among those fiber-reinforced composites, carbon fiber reinforced polymer is the most commonly used in the aeronautic industry.

Compared with other materials, carbon fiber reinforced polymer composites offer the following advantages:

- Lower density and higher stiffness, which can significantly reduce the weight of the structure, thereby reducing fuel consumption and pollutant emissions in the case of air transportation [7]
- High temperature and corrosion resistance. In the high temperature aging test, the strength loss of carbon fiber reinforced polymer is less than that of glass fiber reinforced polymer. Compared with glass fiber, it also provides better resistance to corrosion, fatigue and instantaneous high temperature.
- Well suited for anisotropic loading situations. The orientation of the fibers can be adjusted according to load direction, wasting less materials on unnecessary reinforcement [1].

2.2.2 Basic concepts of classical lamination theory

Since the detection and evaluation of delamination-type damage is the main topic of this thesis, the stiffness of composite laminates needs to be depicted since the damage can be regarded as degradation in structural stiffness.

Classical lamination theory is a theoretical tool used to describe the mechanical properties of laminates, including deformation, stress, strain, stiffness matrix, and compliance matrix. In this section, we will briefly introduce some basic concepts of the classic laminate theory and derive the expression of the stiffness matrix of laminates $[A]$, $[B]$ and $[D]$.

Since composite materials have high strength in the fiber direction and low strength in other directions, composite materials are often fabricated in the form of laminates. A laminate is a stacking of multiple unidirectional composite plies in an organized way. Adjacent plies can have different fiber orientations, but one individual ply only has one fiber orientation. A schematic of the model of one ply and the fiber orientation is shown in Figure 2.1.

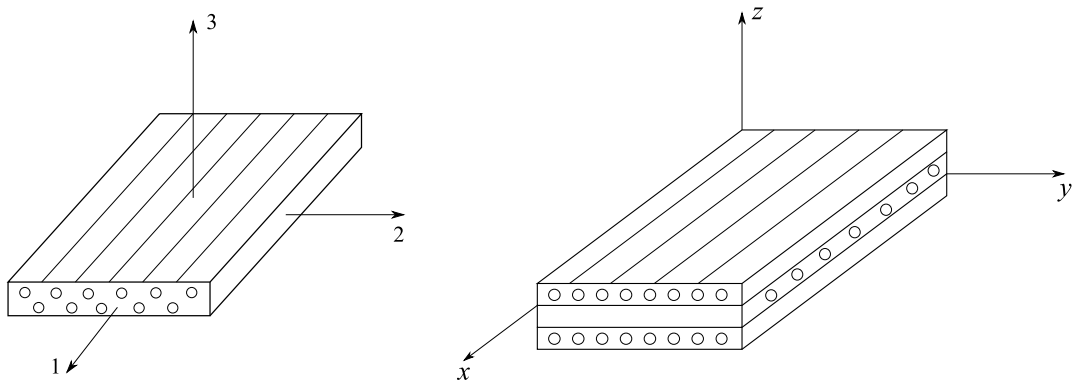

(A) Lamina. (B) Laminates.

FIGURE 2.1: Schematic of lamina(a) and laminates(b).

The left figure shows the schematic of one lamina (ply). The 1, 2 and 3 axes are the principal directions of the local (material) coordinate system and defined as [8]:

1: direction along the fiber length;

2: in-plane direction perpendicular to the fibers;

3: out-of-plane direction perpendicular to the fibers.

The right figure shows a schematic of a composite laminate. The x- and y- axes are the two in-plane axes and z-axis is the out-of-plane axis. The x-axis is not necessarily the fiber orientation.

In order to analyze the mechanical behavior of the laminate, several assumptions are made as follows [8, 9]:

1. The thickness of the laminate is constant, thus the strain of the laminate in the normal direction (out-of-plane direction) is negligible, i.e. $\varepsilon_z = 0$.
2. The deflections and in-plane displacements of the midplane of the laminate are less than the thickness of the plate.
3. The plane perpendicular to the midplane of the laminate in the initial state is still perpendicular to the mid-plane after pure bending. Therefore, the transverse shear strains γ_{yz} and γ_{xz} are negligible.
4. The shear stresses τ_{xz} and τ_{yz} are negligible on the laminate top and bottom surfaces.

Assume that the elastic constants of the material properties for one ply are as follows:

– $[E_1, E_2, E_3]$ are the Young's moduli
– $[\nu_{12}, \nu_{13}, \nu_{23}]$ are the Poisson's ratios
– $[G_{12}, G_{13}, G_{23}]$ are the shear moduli

Supposing that the laminate is displaced from point A to point A'(A is the reference point) after being subjected to a transverse load (see Figure 2.2 [8]), any point in this section has displacements as U, V, and W in the x, y, and z directions respectively. For composite laminates, the thickness is much smaller than the other

two dimensions. Based on the assumptions mentioned above, the displacement can be expressed as follows:

$$\begin{aligned} U &= U_0(x,y) - z\frac{\partial W_0(x,y)}{\partial x} \\ V &= V_0(x,y) - z\frac{\partial W_0(x,y)}{\partial y} \\ W &= W_0(x,y) \end{aligned} \tag{2.1}$$

where the terms U_0, V_0 and W_0 are the displacements of the midplane of the laminates in x, y and z directions.

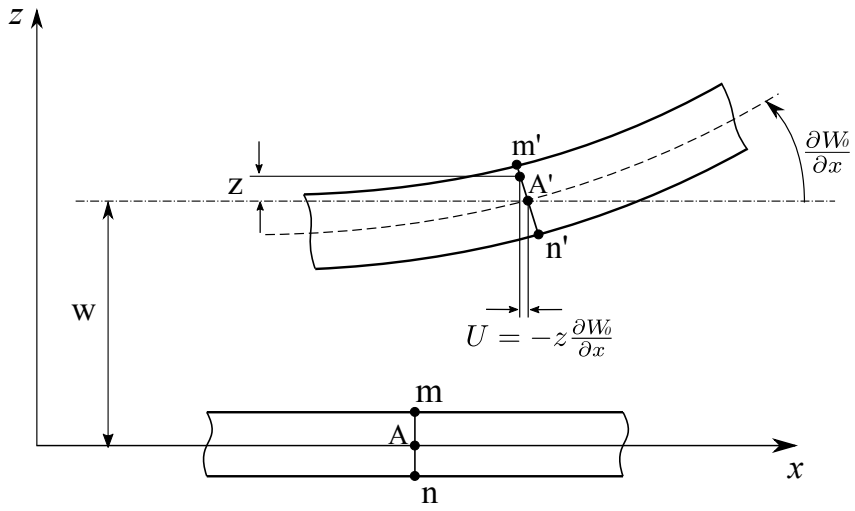

FIGURE 2.2: Plate deformation in $x - z$ plane [8].

From the assumptions mentioned above, we can know that the normal out-of-plane strain $\varepsilon_z = 0$ and that the transverse shear strains γ_{xz} and γ_{yz} are also zero. According to the 3D relationships between displacements and strains, we can get

$$\begin{aligned} \varepsilon_x &= \frac{\partial U}{\partial x} = \frac{\partial U_0}{\partial x} - z\frac{\partial^2 W_0}{\partial x^2} \\ \varepsilon_y &= \frac{\partial V}{\partial y} = \frac{\partial V_0}{\partial y} - z\frac{\partial^2 W_0}{\partial y^2} \\ \varepsilon_z &= \frac{\partial W}{\partial z} = \frac{\partial W_0}{\partial z} = 0 \\ \gamma_{xy} &= \frac{\partial V}{\partial x} + \frac{\partial U}{\partial y} = \frac{\partial V_0}{\partial x} + \frac{\partial U_0}{\partial y} - 2z\frac{\partial^2 W_0}{\partial x \partial y} \\ \gamma_{xz} &= \frac{\partial U}{\partial z} + \frac{\partial W}{\partial x} = \frac{\partial}{\partial z}\left(U_0 - z\frac{\partial W_0}{\partial x}\right) + \frac{\partial W_0}{\partial x} = 0 \\ \gamma_{yz} &= \frac{\partial V}{\partial z} + \frac{\partial W}{\partial y} = \frac{\partial}{\partial z}\left(V_0 - z\frac{\partial W_0}{\partial y}\right) + \frac{\partial W_0}{\partial y} = 0 \end{aligned} \tag{2.2}$$

The curvatures of the laminates are related to the normal displacement of the mid-plane:

$$\begin{aligned}\kappa_x &= -\frac{\partial^2 W_0}{\partial x^2} \\ \kappa_y &= -\frac{\partial^2 W_0}{\partial y^2} \\ \kappa_{xy} &= -2\frac{\partial^2 W_0}{\partial x \partial y}\end{aligned} \tag{2.3}$$

Combining Equation 2.2 and Equation 2.3, we can get

$$\begin{Bmatrix}\varepsilon_x \\ \varepsilon_y \\ \varepsilon_{xy}\end{Bmatrix} = \begin{Bmatrix}\varepsilon_x^0 \\ \varepsilon_y^0 \\ \varepsilon_{xy}^0\end{Bmatrix} + z\begin{Bmatrix}\kappa_x \\ \kappa_y \\ \kappa_{xy}\end{Bmatrix} \tag{2.4}$$

where ε_x^0, ε_y^0 and γ_{xy}^0 are the strains of the midplane of the laminates.

When a laminate is subjected to a load, stresses and strains are generated inside the laminate. The strains in a laminate are continuous through the thickness direction, while the stresses are not necessarily continuous. Since the fiber orientation might be different for each ply, the stiffness along a certain direction might be different throughout the plate thickness. For example, in the laminates shown in Figure 2.1b, the Young's modulus along the x-axis of the 1st ply (the ply on the bottom) is E_1, while the Young's modulus in x-axis of the 2nd ply (the ply in the middle) is E_2. Generally, the transverse stiffness is much smaller than the stiffness along the fiber direction. For the kth ply, the stress-strain relationship can be expressed as follows:

$$\begin{Bmatrix}\sigma_x \\ \sigma_y \\ \sigma_{xy}\end{Bmatrix}_k = [\bar{Q}]_k \begin{Bmatrix}\varepsilon_x \\ \varepsilon_y \\ \varepsilon_{xy}\end{Bmatrix} = [\bar{Q}]_k \left(\begin{Bmatrix}\varepsilon_x^0 \\ \varepsilon_y^0 \\ \varepsilon_{xy}^0\end{Bmatrix} + z_k \begin{Bmatrix}\kappa_x \\ \kappa_y \\ \kappa_{xy}\end{Bmatrix} \right) \tag{2.5}$$

where $[\bar{Q}]_k$ is the matrix of elastic constants of the kth ply and z is the coordinate in the out-of-plane direction.

For thin plates, considering the most general case, the external loads exerted on the plate can be the resultant forces and resultant moments with respect to the mid-plane. In order to facilitate the analysis, we take a section from the kth ply with the thickness of h from the laminate. The resultant force and moment on this section, as well as the resulting stresses and their directions, are shown in Figure 2.3. In this figure, F represents the resultant force and M represents the resultant moment with respect to the $z = 0$ plane, which is set to be the mid-plane of this section. To satisfy the conditions of equilibrium, the balance should be reached between the resultant forces and the integral of stresses over the section thickness. Assuming $\sigma_z = 0$, the

resultant forces can be expressed as

$$\begin{Bmatrix} F_x \\ F_y \\ F_{xy} \\ F_{xz} \\ F_{yz} \end{Bmatrix}_k = \int_{-h/2}^{h/2} \begin{Bmatrix} \sigma_x \\ \sigma_y \\ \tau_{xy} \\ \tau_{xz} \\ \tau_{yz} \end{Bmatrix}_k dz \tag{2.6}$$

The results moments are

$$\begin{Bmatrix} M_x \\ M_y \\ M_{xy} \end{Bmatrix}_k = \int_{-h/2}^{h/2} z \begin{Bmatrix} \sigma_x \\ \sigma_y \\ \tau_{xy} \end{Bmatrix}_k dz \tag{2.7}$$

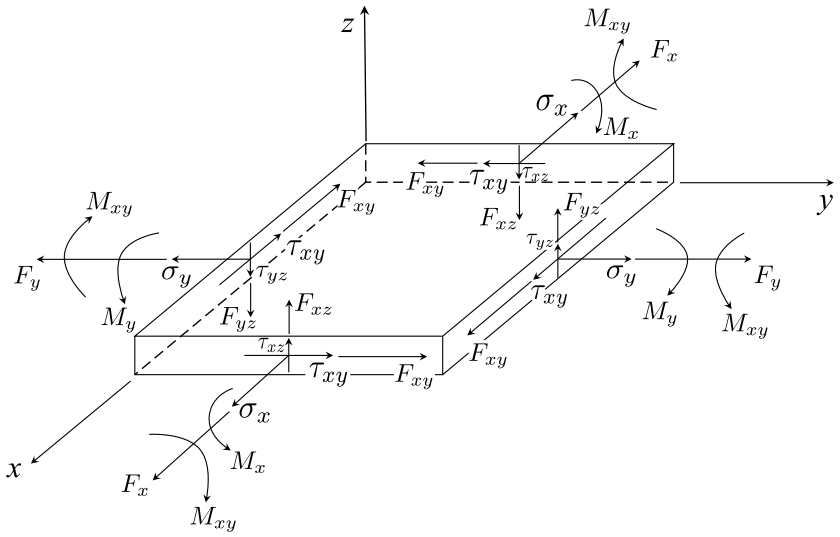

FIGURE 2.3: Positive sign of stress, resultant forces and moments.

After obtaining the stress-strain relationship of a layer, the stiffness matrix of the entire laminate can be calculated. Since the fiber orientation of each ply in the laminate is not the same, the stress variation is discontinuous. When calculating the overall stiffness matrix and the stress-strain relationship of the laminate, the stiffness of each ply in the x, y and z directions need to be considered. For a laminate containing n plies, as shown in Figure 2.4, assuming that the midplane is the $z = 0$ plane, the coordinate in out-of-plane direction (z-axis) of the lower surface of the kth ply is z_{k-1}, and the coordinate of the upper surface is z_k. Substituting Equation 2.5 into Equations 2.6 and 2.7, the generalized stress-strain relationship of the entire

laminate can be expressed as

$$\begin{Bmatrix} F_x \\ F_y \\ F_{xy} \\ M_x \\ M_y \\ M_{xy} \end{Bmatrix} = \sum_{k=1}^{n} [\bar{Q}]_k \left(\int_{z_{k-1}}^{z_k} \begin{Bmatrix} \varepsilon_x^0 \\ \varepsilon_y^0 \\ \varepsilon_{xy}^0 \\ z\varepsilon_x^0 \\ z\varepsilon_y^0 \\ z\varepsilon_{xy}^0 \end{Bmatrix} dz + \int_{z_{k-1}}^{z_k} \begin{Bmatrix} z\kappa_x \\ z\kappa_y \\ z\kappa_{xy} \\ z^2\kappa_x \\ z^2\kappa_y \\ z^2\kappa_{xy} \end{Bmatrix} dz \right) \tag{2.8}$$

The above equation can be written in the following form

$$\begin{Bmatrix} F \\ M \end{Bmatrix} = \begin{bmatrix} A & B \\ B & D \end{bmatrix} \begin{Bmatrix} \varepsilon^0 \\ \kappa \end{Bmatrix} \tag{2.9}$$

where A, B and D are the extensional stiffness matrix, extension-bending coupling matrix and the bending stiffness matrix respectively. They can be calculated using the following equations:

$$\begin{aligned} [A_{ij}] &= \int_{z_{k-1}}^{z_k} [\bar{Q}_{ij}]_k \, dz = \sum_{k=1}^{n} [\bar{Q}_{ij}]_k (z_k - z_{k-1}) \\ [B_{ij}] &= \int_{z_{k-1}}^{z_k} z[\bar{Q}_{ij}]_k \, dz = \frac{1}{2} \sum_{k=1}^{n} [\bar{Q}_{ij}]_k (z_k^2 - z_{k-1}^2) \\ [D_{ij}] &= \int_{z_{k-1}}^{z_k} z^2[\bar{Q}_{ij}]_k \, dz = \frac{1}{3} \sum_{k=1}^{n} [\bar{Q}_{ij}]_k (z_k^3 - z_{k-1}^3) \end{aligned} \tag{2.10}$$

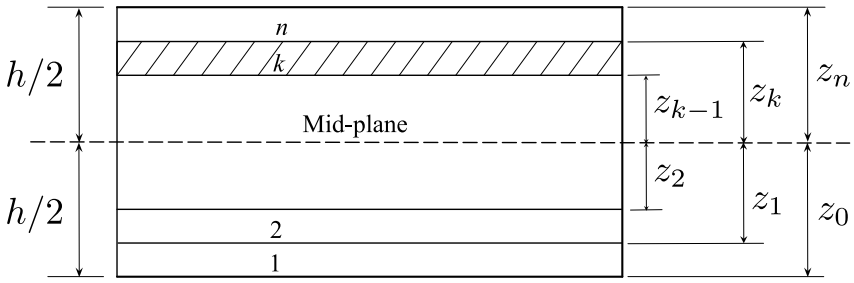

FIGURE 2.4: Laminate stacking sequence nomenclature [8].

2.2.3 Damage types in composite materials and formation of delamination

In the manufacturing process of composite materials, various internal defects, such as porosity, etc. are generated. These defects usually do not affect the performance of the component. However, these defects can be the starting point for more severe defects. The damage in composite materials due to loading can occur on various scales, from microscopic damage including almost imperceptible fiber-matrix debonding to macroscopic damage such as matrix cracking and delamination [10].

Fiber-matrix debonding is usually caused by thermomechanical loads. Matrix cracking is a relatively serious type of damage in composite materials. The crack may extend through the thickness of the laminate, which may cause other types of damage, such as fiber fracture and delamination. Fiber fractures are due to the local stress concentration caused by the isolated fiber break. Since fiber-reinforced composites are manufactured from fiber bundles, due to the unequal length of each fiber and the defects generated during the manufacturing process, certain fibers generate higher stress and strain than other fibers when subjected to load, which may cause isolated fiber break. Delamination damage is a phenomenon of debonding between adjacent plies in composites, which is the result of the unmatched elastic properties of adjacent plies (see Figure 2.5 [11]). Fatigue, impact load, and matrix fracture may all cause delamination. In this study, we mainly focus on the detection and evaluation of delamination damage of carbon fiber reinforced polymers.

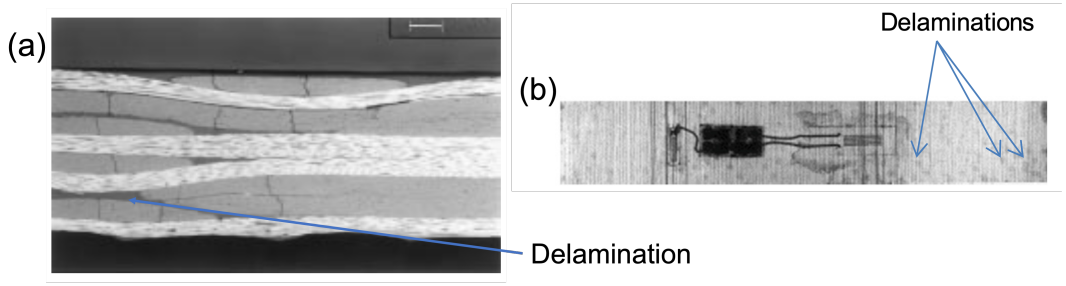

FIGURE 2.5: (a) Side view of delaminations in a four-layer cross-ply CFRP laminate after quasi-static loading. (b) Plan view of delaminations, which are represented by the dark spots in the X-radiograph [11].

2.3 Nonlinear phenomena in structural health monitoring using Lamb waves

Nonlinear properties of elastic waves have been investigated for many years in acoustics, seismology, and ultrasonic testing. Generally, the nonlinear phenomena are generated mainly due to two types of physical mechanisms: the classical nonlinear elasticity and the non-classical nonlinearity. As proposed by [12], two types of classical nonlinearities are commonly investigated in general, one is the geometrical nonlinearity and the other is the material (physical) nonlinearity. The geometric nonlinearity is referred to the nonlinear relationship between strain and the gradient of deformation. It often exists in large deformation problems or stability problems [12, 13]. The material nonlinearity is referred to the nonlinear relationship between strain and stress in certain kinds of materials. In elastic theories, this can be represented by higher-order elastic terms in Hooke's law [12, 13]. The non-classical nonlinear phenomenon is due to other aspects, such as the material hysteresis behavior and the contact acoustic nonlinearity (CAN) [12]. In the following sections, we will briefly introduce the two mechanisms of the nonlinearity generation. In this study, we only focus on

the delamination-type damage, which is induced mainly by the contact interaction mechanism.

2.3.1 Classical nonlinearity

A classical nonlinear acoustic theory, with observations of higher harmonics, has been formulated in the 18th and 19th centuries [12, 14]. However, a lot of harmonic generation methods used in ultrasonic wave propagation and damage detection are those so-called 'non-classical' nonlinearities, which are different and should be distinguished from the classical nonlinearities [12]. In this section, the nonlinear relationship between stress and strain in elastic components is briefly described. The equation of motion in one-dimension in a homogeneous medium writes as follows:

$$\rho \frac{\partial^2 u}{\partial t^2} = \frac{\partial \sigma}{\partial x} + f \tag{2.11}$$

where u is the displacement, σ is the stress and ε is strain. f represents the external force and is often neglected in calculations.

The nonlinear relation between stress and strain is [15]

$$\sigma = E_0 \varepsilon \left(1 + \frac{1}{2}\beta\varepsilon\right) \tag{2.12}$$

where β is the coefficient of the second order nonlinear term. Substitute this relation into the equation of motion, and assuming $f = 0$, the wave equation can be derived as follows:

$$\frac{\partial^2 u}{\partial t^2} - c_0^2 \left(1 + \beta \frac{\partial u}{\partial x}\right) \frac{\partial^2 u}{\partial x^2} = 0, \quad c_0^2 = \frac{E_0}{\rho} \tag{2.13}$$

Assuming the nonlinearity is weak and employing a perturbation theory, the displacement term u can be replaced by the sum of a linear term and a small nonlinear term, which can be written as [16]

$$u = u_l + u_{nl} \tag{2.14}$$

where u_l and u_{nl} represent the initial wave and the first-order perturbation solution, respectively, which also represent the linear and nonlinear parts of displacement. Substituting u into Equation (2.13), the following equation can be derived:

$$\frac{\partial^2 u_l}{\partial t^2} + \frac{\partial^2 u_{nl}}{\partial t^2} - c_0^2 \left[\frac{\partial^2 u_l}{\partial x^2} + \frac{\partial^2 u_{nl}}{\partial x^2} + \beta \left(\frac{\partial u_l}{\partial x} + \frac{\partial u_{nl}}{\partial x}\right)\left(\frac{\partial^2 u_l}{\partial x^2} + \frac{\partial^2 u_{nl}}{\partial x^2}\right)\right] = 0 \tag{2.15}$$

Neglecting the higher order infinitesimals (i.e., u_{nl} and β), and the solution can be derived as

$$u(x,t) = A_1 \cos(\omega t - kx) + A_2 \cos[2(\omega t - kx)] \tag{2.16}$$

where $A_2 = \frac{x\beta A_1^2 k^2}{8}$. The first term of this solution is the fundamental wave component, and the last term is the second harmonic frequency component. In this

equation, it is shown that the amplitude of the second term A_2 is proportional to the square of the amplitude of the fundamental term and is dependent on β, the nonlinear parameter of the material. In many articles, a simplified parameter β' is often used and defined as follows:

$$\beta' = \frac{\beta k^2 x}{8} = \frac{A_2}{A_1^2} \tag{2.17}$$

This indicator illustrates the effect of the second harmonic in material nonlinearity. Although we do not use this β' indicator to describe the nonlinearities due to damage, we can follow this idea to evaluate the effect of the total higher harmonics.

2.3.2 Non-classical nonlinearity

2.3.2.1 Bilinear stiffness model

The bi-linear stiffness model is a typical non-classical nonlinear model and it's one of the contact nonlinearity cases. This model is initially established to describe the opening and closing effects of cracks in materials – the crack opens under tension and closes under compression. Cracks with this effect are also called "breathing" cracks [17, 18, 12]. Figure 2.6 illustrates the "breathing" type crack having a bi-linear contact behavior in structures [18]. When the crack region is subject to tension, the crack opens, leading to a reduction in the global stiffness of the structure compared with the intact state; when the crack area is compressed, the crack closes, and the stiffness remains unchanged with the original stiffness [19]. For simplification, the stiffness of the model can be expressed as [18]:

$$k(x) = \begin{cases} k_t, & x > 0 \\ k_c, & x < 0 \end{cases} \tag{2.18}$$

where $k(x)$ represents the stiffness, and x represents the relative displacement between interfaces of a "breathing" crack. k_t and k_c stand for the stiffness in tension and compression, respectively (generally $k_c > k_t$). The force-displacement relationship is shown in Figure 2.7. When the displacement is above 0 (in tension), the stiffness is lower than the stiffness in compression.

2.3.2.2 Material hysteresis behavior

Another indicator for material nonlinear behavior is stress-strain hysteresis [21]. If a material's behavior follows different stress-strain curves in loading and unloading [22], this material is hysteretic. That is to say, the state of a material with hysteretic characteristics depends not only on the instantaneous conditions, but also on the loading history [12].

A typical example of hysteresis is shown in Figure 2.8 [12]. During initial loading, the material behavior is described by the curve ABC. When unloading the material, the behavior path goes back through path CDE, and to point E under compression,

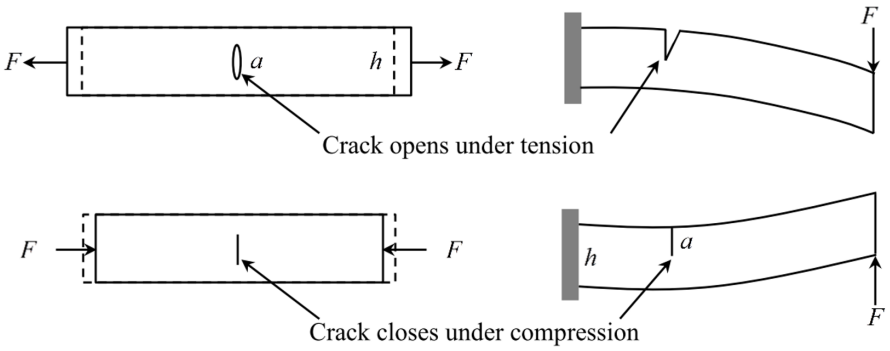

FIGURE 2.6: Schematic of the "breathing" type crack in structures having a bi-linear contact behavior [20].

instead of going back along the original path, where a classical nonlinear material would behave. When the material is loaded again, it will move to point C along the path EFC. If the material is unloaded at point G during the second loading process, another small loop GHG would be created, and the internal loop will start and end at the same point [12].

Although the hysteretic phenomenon has been observed in a lot of experiments, its theoretical explanation is still not clear. Several mechanisms might be the cause of this phenomenon, such as plasticity, viscosity, and the presence of damage [19].

2.4 Numerical models for delamination

In order to deeply understand the physical mechanism of the delamination behavior, numerical methods are usually employed for the analysis of wave propagation in the presence of delamination in composite structures. Several models can be used for characterizing the mechanical behavior of delamination interfaces, such as the contact model, the local stiffness reduction model, the linear and nonlinear spring models and so on. These models will be illustrated in this section.

2.4.1 Stiffness reduction model

The existence of defects in materials can cause a reduction of stiffness in structures. Therefore, it is possible to model the defects in structures by assigning a reduced local stiffness in the defect region. The schematic is shown in Figure 2.9, where Figure 2.9a describes a two-dimensional beam model containing a through-width delamination and Figure 2.9b shows the equivalent model using stiffness reduction method containing a material degradation zone [23].

To simulate the Lamb wave propagation in composite laminates, the stiffness of the laminate can be calculated using classical lamination theory:

$$\langle [A], [B], [D] \rangle = \sum_{k=1}^{n} \int_{z_{k-1}}^{z_k} [\bar{Q}_{ij}]_k \langle 1, z, z^2 \rangle \, dz, \tag{2.19}$$

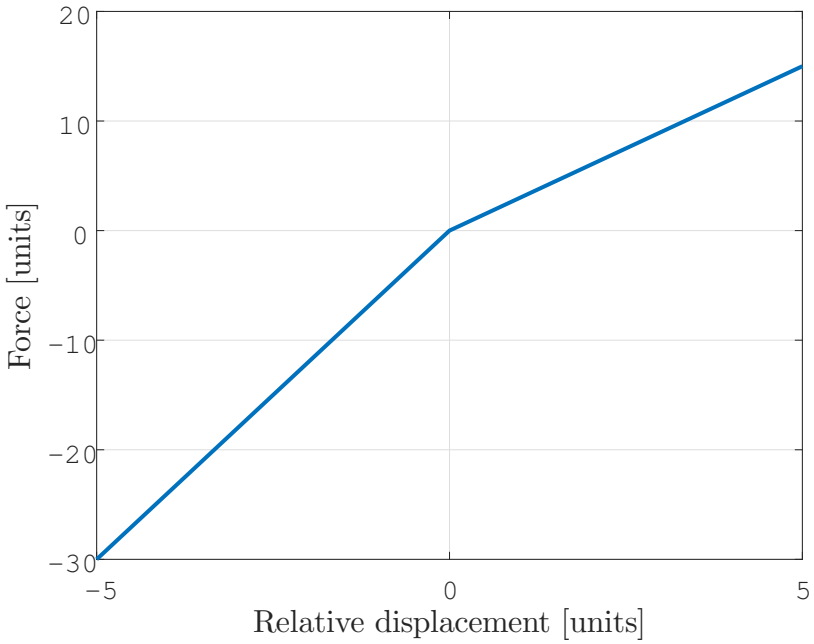

FIGURE 2.7: Example of a bi-linear stiffness model showing force-displacement relationship. For positive displacement (in tension) the stiffness has a different value than for the negative displacements (in compression).

where $[A]$, $[B]$ and $[D]$ are the extensional stiffness matrix, extension-bending coupling matrix and bending stiffness matrix respectively. N is the number of plies of the laminate, h_k is the thickness of ply k, $[\bar{Q}_{ij}]_k$ is the stiffness matrix of ply k corresponding to the fiber direction and z is the coordinate of the ply in through-thickness direction. When a delamination is introduced to the laminates, kinematic assumptions are made to represent discontinuities in both in-plane and out-of-plane displacement fields [24], as shown in Figure 2.10:

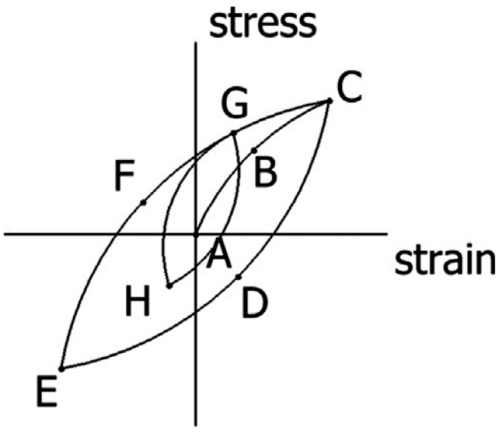

FIGURE 2.8: A typical example of material hysteresis behavior [12].

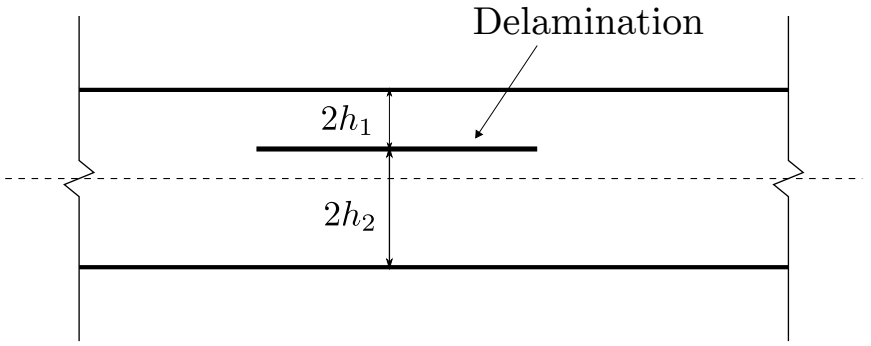

(A) Beam containing a delamination.

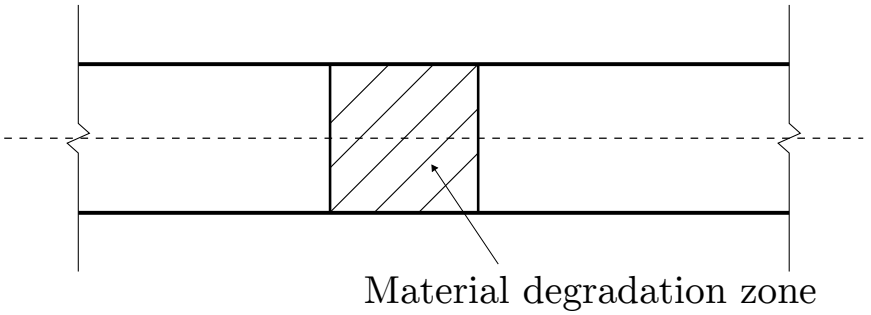

(B) Equivalent stiffness-reduced beam.

FIGURE 2.9: The 2D modeling of a beam containing a delamination using stiffness reduction method based on Ref. [23].

$$
\begin{aligned}
u_x(x,y,z) &= u_x^0(x,y) + \alpha_x^0(x,y)z + \sum_{m=1}^{N_d} [u_x^m(x,y)\mathrm{H}(z-z_m) + \alpha_x^m z\mathrm{H}(z-z_m)],\\
u_y(x,y,z) &= u_y^0(x,y) + \alpha_y^0(x,y)z + \sum_{m=1}^{N_d} [u_y^m(x,y)\mathrm{H}(z-z_m) + \alpha_y^m z\mathrm{H}(z-z_m)],\\
u_z(x,y,z) &= u_z^0(x,y) + \sum_{m=1}^{N_d} u_z^m(x,y)\mathrm{H}(z-z_m),
\end{aligned}
\tag{2.20}
$$

where u_x, u_y and u_z are the in-plane and out-of-plane displacements respectively; α_x and α_y are the slopes of the in-plane displacements along the x- and y-axes; H is the Heaviside step function; N_d is the number of delaminations. The superscript 0 indicates the mid-plane variables, superscript m indicates quantities at mth delamination, and z_m indicates the distance of the mth delamination from mid-plane.

In Ref. [25], the stiffness at delamination is defined as

$$
\langle [B^m], [D^m] \rangle = \begin{cases} \sum_{k=1}^{n} \int_{z_{k-1}}^{z_k} [\bar{Q}_{ij}]_k \mathrm{H}(z_m - z) \langle z, z^2 \rangle \, dz, & z_m \geqslant z_l \\ \sum_{k=1}^{n} \int_{z_{k-1}}^{z_k} [\bar{Q}_{ij}]_k \mathrm{H}(z - z_m) \langle z, z^2 \rangle \, dz, & z_m < z_l \end{cases}
\tag{2.21}
$$

where $[B^m]$ and $[D^m]$ are the membrane-bending coupling stiffness and bending stiffness at the delamination region respectively. z_m and z_l are the coordinates of the

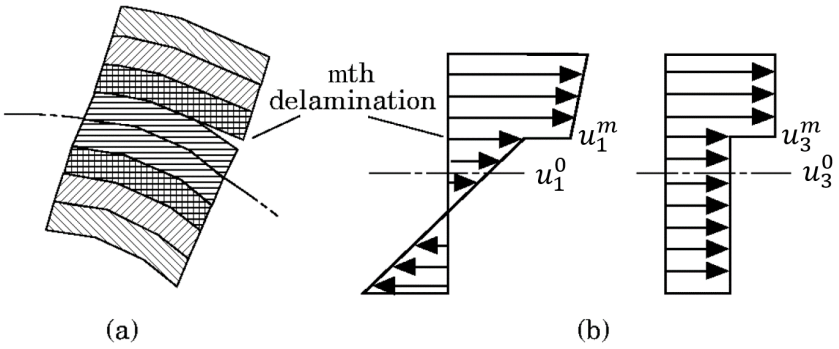

FIGURE 2.10: Kinematic assumptions of generalized laminate theory with single delamination [24]. U^m indicates the displacement of mth delamination along x-axis.

delamination and the mid-plane of the plate in the out-of-plane direction, respectively. The loss of the extensional stiffness of the delamination is negligible. The effects of the smaller sub-laminate of the delamination on coupling matrix and bending stiffness matrix are ignored. That is, only the thicker sub-laminate is considered when calculating the coupling and bending stiffness at the delamination region.

2.4.2 Surface-to-surface contact interaction model

The most commonly used method for modeling delamination behavior is to apply a surface-to-surface contact pair to the interfaces to model the mechanical behavior of the delamination [26, 27, 28, 29, 30]. Yang *et al.* [28] carried out a three-dimensional (3D) simulation and also experiments on an aluminum plate to investigate the second harmonic generation due to a fatigue crack. An embedded seam crack was used for modeling the fatigue crack. Hong *et al.* [30] developed a solid model for simulating the generation of the nonlinearities when ultrasonic waves traverse a fatigued medium. A seam crack definition was imposed on each surface of the crack for modeling the fatigue crack. Soleimanpour *et al.* [26] studied the potential of a baseline-free SHM technique based on higher harmonics resulting from the interaction of guided waves with delamination. A contact-pair interaction was employed in a 3D FE model to simulate the delamination damage behavior in a composite beam. Shen *et al.* [19] presented modeling of the propagation of nonlinear guided waves generated by interaction with a nonlinear breathing crack. Two methods were proposed for simulating the breathing crack: element activation/deactivation method and contact analysis.

The surfaces exhibit an interaction behavior that can be characterized by the contact pressure and the penetration (overclosure). When no penetration is allowed between surfaces, the contact virtual work contribution is obtained as

$$\delta\Pi = \delta p h + p \delta h \tag{2.22}$$

where p is the contact pressure and h is the interpenetration between contact surfaces. The relationship between contact pressure and interpenetration can be expressed as [31]

$$\begin{cases} p = 0, & \text{for } h < 0 \quad \text{(surfaces are separated)} \\ h = 0, & \text{for } p > 0 \quad \text{(surfaces are in contact)} \end{cases} \tag{2.23}$$

This indicates that when the surfaces are in contact, no penetration is allowed, and any contact pressure can be transmitted between them. If contact pressure reduces to zero, the surfaces separate, and separated surfaces come into contact if the gap between them reduces to zero.

If the surfaces in contact keep strictly no interpenetration, the computation cost might be extremely large and numerical convergence problems can be caused. Therefore, the "softened" pressure-overclosure relationship can be applied to make it easier to resolve the contact condition. The pressure-penetration relationship for both contact models is shown in Figure 2.11. However, if the contact model is too "soft", indicating that large interpenetration might be caused when surfaces are in contact, which is not the realistic case. Thus, a trade-off between the computation cost and the accuracy of the simulation should be achieved.

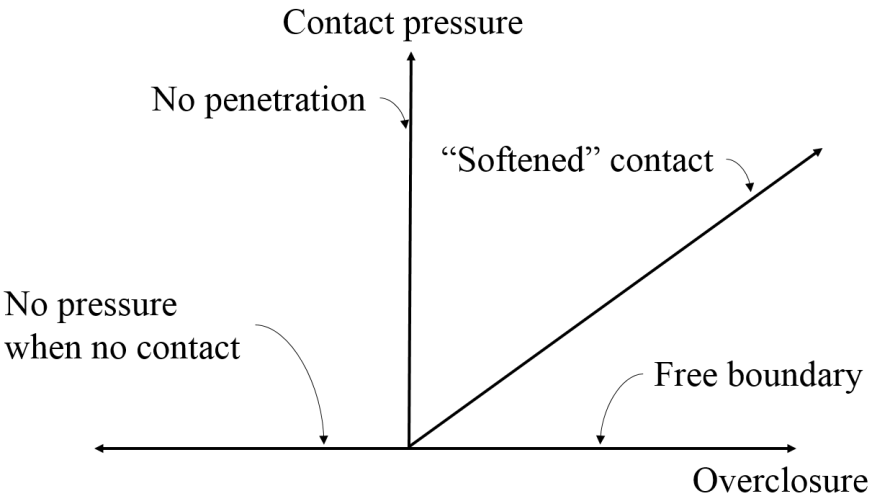

FIGURE 2.11: Pressure-overclosure relationship of "hard" contact [31].

2.4.3 Spring-type contact interface model

The nonlinear ultrasonic responses from contact interaction between rough surfaces can be expressed as a relation between the surface traction and the relative displacement of the two surfaces, i.e., change of gap distance h in the out-of-plane direction and sliding displacement s in the in-plane direction [32, 33, 34]. The contacting rough surfaces can be modeled as a spring-type interface characterized by interfacial normal and tangential stiffnesses [35, 36, 37]:

$$\begin{aligned} \sigma &= -p_0 + K_{\mathrm{N}}(h-h_0) - K_{\mathrm{NN}}(h-h_0)^2 - K_{\mathrm{TT}}s^2, \\ \tau &= K_{\mathrm{T}}s - K_{\mathrm{NT}}(h-h_0)s \end{aligned} \tag{2.24}$$

where K_{N} and K_{T} are the interfacial normal and tangential stiffnesses respectively. K_{NN}, K_{TT} and K_{NT} characterize the quadratic nonlinear response of the contacting interface. h_0 is the gap distance of the interface at equilibrium. The stiffness parameters are usually derived from experimental measurements.

This spring-type interface model can also be replaced by a very thin elastic layer with a thickness δ having zero mass density. The elastic constants of this thin layer λ_{c} and μ_{c} are determined by the following equations [37]:

$$K_{\mathrm{N}} = \frac{\lambda_{\mathrm{c}} + 2\mu_{\mathrm{c}}}{\delta}, \quad K_{\mathrm{T}} = \frac{\mu_{\mathrm{c}}}{\delta} \tag{2.25}$$

2.4.4 Nonlinear spring model

Nonlinear springs can also be used to describe the interaction between delamination interfaces. Delrue [38] proposed a three-dimensional finite element model which makes use of node-splitting and spring-damper elements. The nonlinear behavior of the closed delamination was implemented by introducing a set of spring-damper elements, which connect every two corresponding points at the top and bottom interface of the delamination. The mechanical behavior was realized by defining two spring forces $F_{\mathrm{s_t}}$ and $F_{\mathrm{s_b}}$ and two damping forces $F_{\mathrm{d_t}}$ and $F_{\mathrm{d_b}}$ on the top and bottom interfaces respectively. The spring force on the top interface $F_{\mathrm{s_t}}$ is defined as

$$F_{\mathrm{s_t}} = \begin{cases} k_1(Z_0 - \Delta z) & \text{if} \quad \Delta z < Z_0 \\ k_2(Z_0 - \Delta z) & \text{if} \quad Z_0 \leqslant \Delta z < aZ_0 \\ k_3(bZ_0 - \Delta z) & \text{if} \quad aZ_0 \leqslant \Delta z < bZ_0 \\ 0 & \text{if} \quad \Delta z \geqslant bZ_0 \end{cases} \tag{2.26}$$

where Δz is the gap distance between the two corresponding points at the delamination interfaces, Z_0 is a small characteristic distance between the interfaces at equilibrium, a and b are parameters with $a > 1$ and $b \geqslant a$, and k_1, k_2 and k_3 are constants of the virtual springs. The spring force on the bottom interface $F_{\mathrm{s_b}}$ is equal in value but opposite in direction to the spring force $F_{\mathrm{s_t}}$.

The damping forces are defined as

$$F_{\mathrm{d_t}} = \begin{cases} -\gamma(v_{z_{\mathrm{t}}} - v_{z_{\mathrm{b}}}) & \text{if} \quad \Delta z < bZ_0 \\ 0 & \text{if} \quad \Delta z \geqslant bZ_0 \end{cases} \tag{2.27}$$

where $v_{z_{\mathrm{t}}}$ and $v_{z_{\mathrm{b}}}$ are the velocities of the corresponding points on the top and bottom interfaces of the delamination respectively, and γ is the damping coefficient. The absolute value of the damping force on the bottom interface $F_{\mathrm{d_b}}$ is equal to $F_{\mathrm{d_t}}$ but in the opposite direction.

2.5 Finite element techniques for delamination modeling

In finite element simulations, a lot of techniques can be used for delamination modeling, such as the extended finite element method, the cohesive zone method, the duplicate node method and so on. Among them, the extended finite element method and the cohesive zone method are mainly used for the prediction of delamination growth when specimens are subject to cyclic loadings, and thus not considered here for delamination modeling in SHM context. Other techniques that are more widely used will be depicted in this section.

2.5.1 Duplicated node method

A common way for modeling the damage in structures is called duplicated node method [23]. It is implemented by duplicating the nodes along the delamination area and attaching the upper nodes to elements in the upper layer of the delamination and the lower nodes to elements in the lower layer. Thus the nodes at the delamination area have the same nodal coordinates but different node numbers. The schematic of this method is shown in Figure 2.12. In this figure, nodes 24-27 have the same coordinates as nodes 31-34, but they belong to the elements on the upper layer of the delamination while nodes 31-34 belong to the lower layer. This procedure ensures the separation of delamination interfaces and discontinuity in the medium arising due to the presence of the delamination.

Shoja *et al.* [25] modeled the delamination by duplicating the nodes between the adjacent two plies, where the upper and lower nodes are attached to the upper and lower elements, respectively, thus creating two free surfaces in that region. Murat *et al.* [39] modeled the delamination by creating an additional layer of nodes along the delamination with same coordinates, but not connected to the coinciding original nodes. In this way, two separated layers were defined, connected to the respective nodes along the delaminated area.

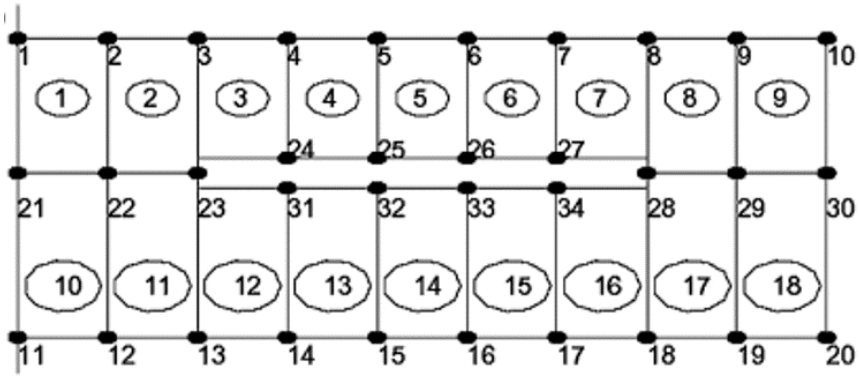

FIGURE 2.12: Schematic of delamination modeling using duplicated node method.

2.5.2 Unbonded layer

A similar way to model delamination is to unbond the layers at the delaminated region. In finite element analysis, one way for modeling the composites is to model each ply individually and connect the plies together rigidly at the interface to build the laminates. Then at the delaminated region, the rigid tie connection is replaced by the free boundary condition or other physical models for the interaction of the delamination interfaces. Leckey *et al.* [40] employed rigid tie to connect the composite plies to the neighbors except at the delaminated region, which was modeled as a stress-free (i.e., non-bonded) contact surface between the interfaces. Chiu *et al.* [41] modelled the delamination as a volume split while other parts were tied rigidly to each ply for the composite modeling. Figure 2.13 shows a schematic of the unbonded layer technique for delamination modeling. Except for the delamination area, elements in other parts are bonded to the neighboring layer by rigid connections.

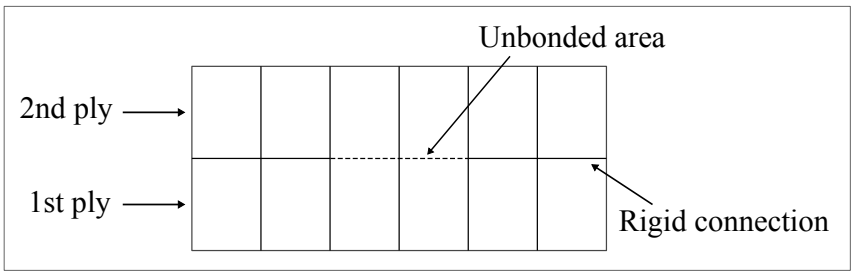

FIGURE 2.13: Schematic of the unbonded layer technique for modeling delamination.

2.5.3 Thin elastic layer

A thin elastic layer with zero mass density can be also used to model the delamination in finite element modeling. A schematic is shown in Figure 2.14. In this model, the delamination can be modeled by a very thin elastic layer between neighboring plies with certain adjustable parameters, to simulate the mechanical behavior of a delamination. Segers *et al.* [27] employed a very thin elastic layer with the thickness $\delta = 10^{-6}$ of the plate thickness, replacing a spring-type interface, to model the delamination interaction. Leckey *et al.* [40] employed a thin elastic layer with two adjustable parameters (spring and damping constants) in COMSOL for the modeling of delamination damage.

2.6 Damage index

Damage index (DI) approach is widely used in structural health monitoring to determine whether there are defects in the structure. The main idea is to extract certain dynamic features from the response of the structures, and compare the difference in the dynamic properties between the pristine structure and damaged structure. The

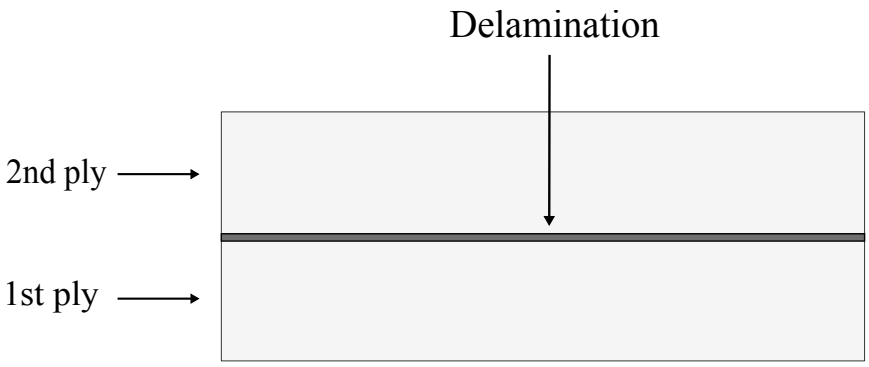

FIGURE 2.14: Schematic of the thin elastic layer technique for modelling delamination.

index provides a scalar output for the determination of the existence of damage, and furthermore, to quantify the severity of the damage.

A lot of dynamic features have been used for evaluating structure damage, among which two main types of features are of major interest: time domain features and frequency domain features. Therefore, DIs based on time domain data and based on frequency domain features are mainly used for damage detection. In addition, the nonlinear properties are also of large interest and are widely used in damage identification. The nonlinear DIs will be depicted in the next section.

2.6.1 Damage index based on time domain features

In time domain analysis, features such as time delay, response energy, signal amplitude, can all be employed to determine the structure state.

Fenza *et al.* [42] proposed a DI based on the amplitude of the response signals in "undamaged state" and in "damaged state" by calculating the root mean square of the relative difference of the amplitudes between two response signals with respect to the "undamaged" one. Hong *et al.* [43] proposed a time of flight (ToF) based detection philosophy to extend the application of time-domain signal processing to the field of nonlinear Lamb waves, which are highly sensitive to small-scale damage. Sohn and Kim [44] proposed a DI based on two arbitrary temporal signals and their amplitudes to measure their closeness. Chen *et al.* [45] proposed a DI based on the cross-correlation of the baseline signal and the damage signal, and also the autocorrelation of the baseline signal to quantify the changes in structure state.

2.6.2 Damage index based on frequency domain features

Besides DIs based on temporal features of response signals, DIs based on frequency domain features are also of interest. Ihn and Chang [46] proposed a DI for the detection of fatigue crack growth based on the scattered energy of the Lamb wave calculated from the short-time Fourier transform (STFT). Prawin and Rao [47] proposed a DI based on spectral correlation to exploit the non-linear intermodulation in the response signals.

2.6.3 Damage index for evaluating nonlinear effects

In damage detection using nonlinear Lamb wave techniques, the classical nonlinear coefficient, defined as in Equation (2.17) are often employed to evaluate the nonlinearity of the system [19, 28, 48], thus representing the severity of the damage.

Besides, other nonlinear DIs are also employed. Mandal and Banerjee [49] proposed a DI based on the wavelet coefficient of the extracted second harmonic signal and also the time of arrival of the second harmonic pulse corresponding to a certain actuator-sensor path. Yelve *et al.* [50] proposed a spectral damage index based on the spectral envelope, which is defined as a set of lines joining the normalized amplitude peak points versus the mapped frequencies (fundamental frequency and harmonics).

2.7 Conclusion

In this chapter, we first briefly introduced some basic concepts of composite materials in aeronautic applications, as well as the damage types in aerospace composites. Then we introduced the nonlinear phenomenon in Lamb waves propagation, including classical nonlinearity, which is represented by the material nonlinear stress-strain relationship, and non-classical nonlinearity. Next, the finite element models and modeling techniques for the delamination-type damage are reviewed. At last, we reviewed some damage indexes using characteristics extracted from both time domain signals and frequency spectra.

Chapter 3

Experiments on Delamination Detection in Composite Plates

3.1 Introduction

As mentioned previously, the objective of this thesis is to deeply understand the mechanisms of the interaction between Lamb waves and delamination damage. In other words, the goal is to investigate whether the nonlinear phenomena can be observed in experiments.

In this chapter, the experiment will be depicted in detail. First, we introduce the principles of laser shock wave technique (LSWT), which is employed to generate the delamination damage in the composite specimens. Following this, the results regarding delamination detection and nonlinear effects are presented. Specimens with different damage sizes are studied, and different types of signals are employed as the excitations. Sensitivity analysis is conducted for various parameters in experiments.

3.2 Specimens and delamination generation by laser shock wave technique

3.2.1 Introduction

This work continues from previous work in our group conducted by Ghrib [7, 51]. The same structure is also used by her. However, she employed a broad-band sine sweep signal as the excitation and studied the characteristics of the output signals, while in my work, the tone burst signals are used as input signals to investigate the nonlinear effects induced by the delamination damage.

The generation of delamination damage is a very important aspect. In particular, it is difficult to produce realistic delamination damage in a calibrated manner. In previous studies, scholars usually use a Teflon insert to generate delamination in composites, but this method cannot represent a realistic delamination damage. The impact load method can be used to generate realistic damage, but it also generates other types of damage, such as fiber breakage. Moreover, the impact cannot generate

a calibrated delamination and the location and size of the delamination cannot be controlled.

Laser Shock Wave Technique (LSWT) is a promising alternative method to generate calibrated damages in composite materials. LSWT is capable of generating local and intense tensile stresses within the target, which may damage the material if the local damage threshold is exceeded. The level of tensile stress, and therefore the degree of damage, is directly related to the laser beam energy, and its localization in the material thickness depends mainly on the pulse duration [52]. Therefore, the damage can be calibrated by appropriate adjustment of the laser source parameters.

3.2.2 Principles of laser shock wave technique for damage generation

3.2.2.1 High power laser

The laser used for LSWT is a high-power nanosecond prototype laser with a beam intensity of several GW/cm^2. The high-power laser beam is focused on the target surface through a convex lens, which greatly increases the beam intensity. The beam intensity I can be defined as

$$I = \frac{E}{S\Delta t} \tag{3.1}$$

where E is the beam energy, Δt is the pulse time and S is the focal surface.

3.2.2.2 Generation of laser shock wave

Laser-matter interaction is responsible for generating shock waves and the consequent high pressure load on the surface of the object. When a high power laser pulse wave reaches the target surface, a strong plasma is generated on the surface of the object where the laser is applied and expands rapidly on the target surface. The release of the plasma produces a strong shock wave on the surface of the test material, and the resulting pressure can range from MPa to GPa [53] [54].

When there is water covering the surface of the target object, the plasma is confined and the expansion is delayed. As a result, the induced pressure is an order of magnitude greater and the shock wave duration is 2 to 3 times longer than direct action when the laser pulse has the same power density [55, 56, 57]. Thus, water confinement is used to drive significant shock pressure. Besides, an aluminum painting is used as a sacrificial layer since laser-aluminum interaction is well documented [58].

3.2.2.3 Damage generated by shock wave

According to the number and distribution of laser beams, laser shock wave technology can be divided into single-sided laser shock and symmetrical laser shock.

Single-sided laser shock is to emit the laser beam on only one side of the sample, as shown in Figure 3.2. When the laser pulse is irradiated vertically on the surface of the sample, the generated incident shock S1 propagates inside the specimen in

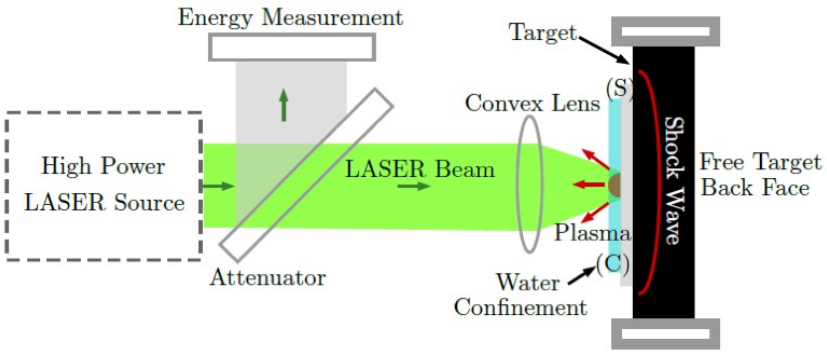

FIGURE 3.1: Principle of Laser-matter interaction and shock wave generation, presented with a confinement Layer (C) and a sacrificial layer (S) [51].

the thickness direction and is reflected at the back surface of the sample, forming a backward propagating reflected wave R1. At the same time, the incident unloading wave S2 initiated by the end of the pulse propagates from the front surface to the back end of the sample and forms a reflected wave R2 on the back surface. In this way, the incident wave S2 and the reflected wave R1 intersect inside the sample. Depending on the length of the pulse time, as well as the thickness and impedance of the sample, the intersection can be located inside the sample or outside the sample. If the intersection is inside the sample, the crossed waves can generate high tensile stress, leading to local stress concentration. If the induced tensile stress is higher than the damage threshold of the material, damage can be generated at the internal intersection point (D) of the sample.

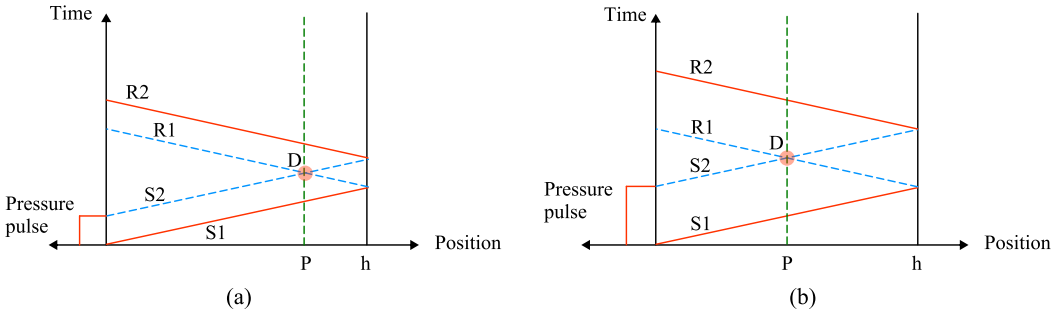

FIGURE 3.2: Schematic of time-position relations for the one side laser case. The pulse duration in (a) is longer than that in (b). The thickness of the sample is h [7].

It is worth noting that the duration of the laser pulse and the energy of the laser beam are two important parameters. The pulse duration controls the position of the intersection D in the depth direction. Therefore, if the location of damage needs to be controlled, the pulse duration is a parameter that needs to be adjusted. The severity of damage, on the other hand, is controlled by the energy of the laser beam since the magnitude of the tensile stress in the material is directly related to the laser energy. Therefore, if the damage severity needs to be adjusted, it can be achieved by tuning

the energy of the laser beam.

The symmetrical Laser shock approach (see Figure 3.3) was proposed by Boustie et al. as an optimization of the Laser Shock Adhesion Test (LASAT) [58].

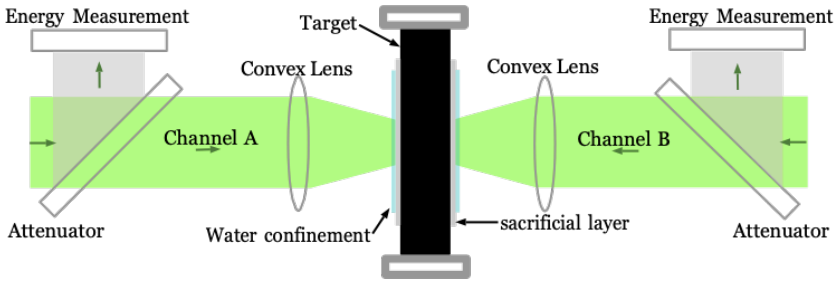

FIGURE 3.3: Schematic of the symmetrical LASER shock configuration with a sacrificial layer and a confinement medium [51].

This method uses two laser pulse beams to irradiate the target object on the left and right surfaces, as shown in Figure 3.4. The laser pulse on the left side irradiates the left surface of the target object. The generated plasma excites the incident wave SL1 inside the target and propagates in the thickness direction. When the incident wave reaches the right edge of the target object, a reflected wave RL1 is generated. Similarly, the laser pulse on the right irradiates the right surface of the object, generating incident waves SR1 and reflected waves RR1 inside the target object. The intersection of these two reflected waves RL1 and RR1 generates high tensile stress locally. When the tensile stress exceeds the material damage threshold, it will cause local damage (D-SHM). The incident unloading wave SL2 and the reflected wave RL1 intersect at a position close to the right surface of the sample, which can generate strong tensile stress. If the tensile stress is large enough to exceed the threshold, the intersection of the two waves may cause damage inside the sample. The incident unloading wave SR2 intersects with the reflected wave RR1 near the left surface of the specimen and may cause damage.

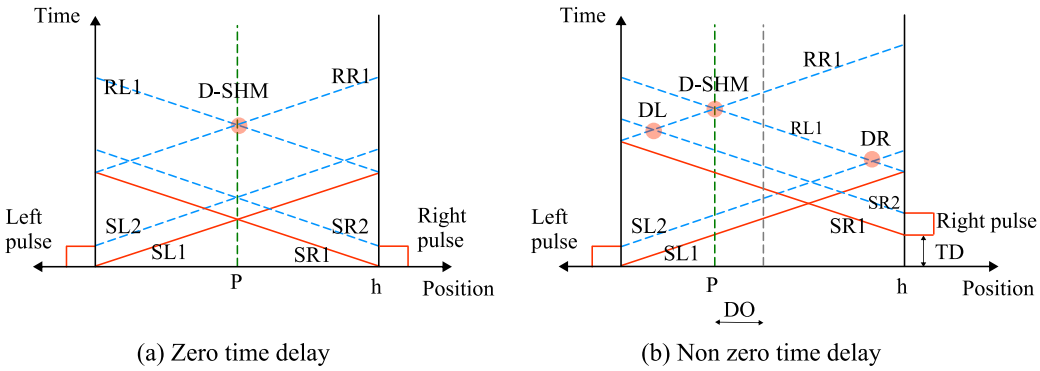

FIGURE 3.4: Schematic of time-position relations for the two side laser case. The laser pulse on the right side in (b) is delayed by TD and the D-SHM point is shifted by DO. The thickness of the sample is h [7].

If the lasers on both sides are perfectly symmetrical, the position of the defect D-SHM is in the middle of the thickness direction of the sample, as shown in Figure a. However, if we introduce a time delay TD to the laser on one side, the position of the defect D-SHM shifts by a distance denoted by DO (damage offset), as shown in Figure 3.4. Assuming that the wave velocity in the material is c, the damage offset distance DO can be expressed as

$$DO = TD \times c \tag{3.2}$$

Similar to the single-sided laser, the symmetrical laser shock wave can also be used to control the magnitude of the induced tensile stress by adjusting the laser pulse energy, thereby controlling the severity of the induced defect. In the case of a single-sided laser pulse, since the pulse duration is very short, usually only a few nanoseconds, damage often occurs near the back surface. The short laser may even cause ablation of the back surface of the sample. Therefore, the defects in the specimens used in this study were excited by a symmetrical laser.

Figure A.2 shows an example of the C-scan image of delamination damage calibrated by laser shock. In this example, the size and the in-depth position of this delamination is precisely determined by controlling the energy and time delay of the laser beams [51, 59].

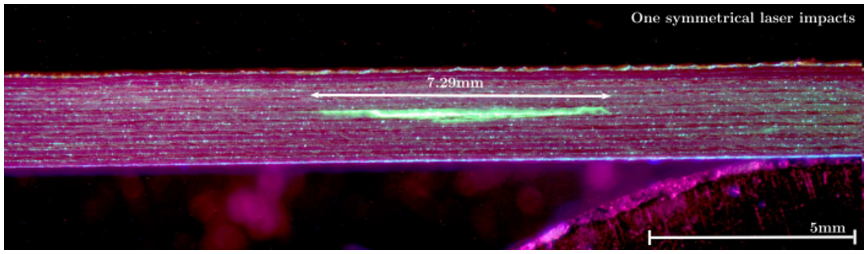

FIGURE 3.5: Side view of the delamination inside the composite specimen [51].

3.2.3 Composite specimens

The samples used in experiments are fabricated of carbon fiber reinforced polymer (CFRP) composites. The thickness of each ply is 0.14 mm. Each plate contains 16 plies at the stacking sequence of $[0°/90°]_8$ with the dimensions of $315 \times 100 \times 2.24$ mm^3. The material properties of the specimens are listed in Table A.1

TABLE 3.1: Composite specimen material properties [60].

Poisson's ratio ν	E_{11}(per ply)	E_{22}(per ply)	G_{12}(per ply)	Mass density ρ
0.3	140 GPa	9 GPa	4.5 GPa	1594 kg/m^3

In our experiments, four composite plates are considered here:

– One intact plate containing no damage. This plate is for reference.

– The plate contains one laser impact that introduces the delamination-type damage at the diameter of 7mm in the midplane of the plate. The damage is located at the center of the plate.
– The plate containing two laser impacts representing a delamination-type damage of approximately 14mm created at the midplane.
– The plate containing three laser impacts representing a delamination-type damage of approximately 21mm at the midplane.

The schematic is as shown in Figure A.1. The delamination damage was introduced into samples in a calibrated way using laser shock wave technique. The specimen was subjected to a symmetrical laser impact of two laser beams. This resulted in a nearly circular delamination of 7 mm diameter at midplane of the composite plate [7].

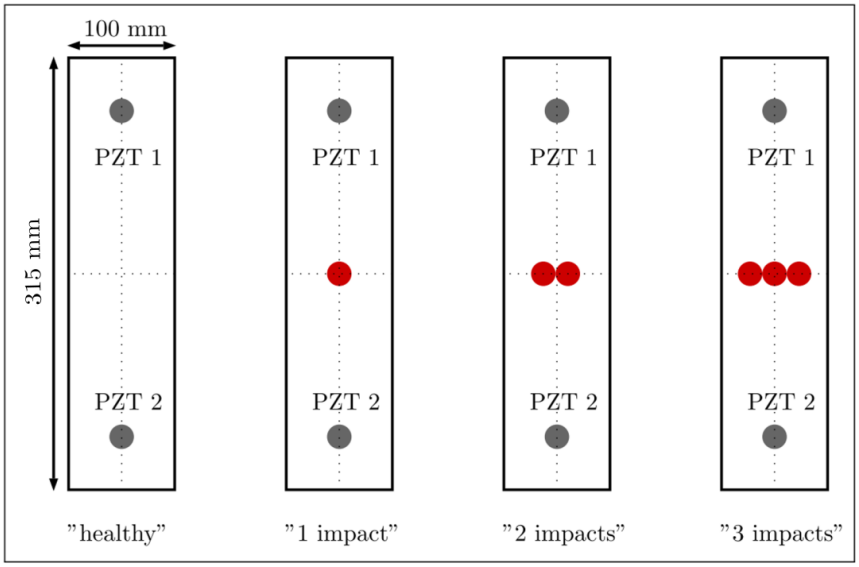

FIGURE 3.6: Schematic of the four specimens and the positions of the delaminations [51].

Each composite plate is equipped with two piezoelectric elements (PZT NCE51, manufactured by Noliac), as shown in Figure A.3. These piezoelectric elements, which can operate in both actuating and sensing modes, are permanently bonded to the surface of the composite plate to ensure they have the same coupling effects. When carrying out SHM experiments, one PZT is used as a transmitter (PZT1) and the other is used as a signal receiver (PZT2). The properties of the piezoelectric elements are listed in Tables 3.2 and A.2

TABLE 3.2: Properties of NCE51 from Noliac [51].

Nominal voltage	−120 V to 120 V
Curie temperature	360 °C
Maximum current	60 mA

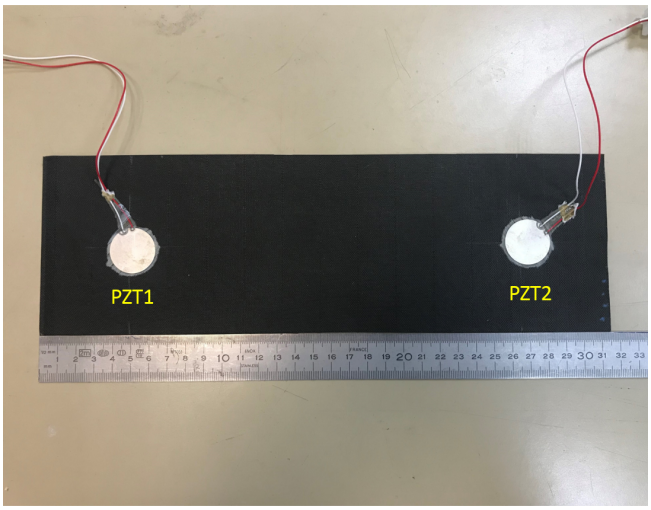

FIGURE 3.7: A composite specimen equipped with two PZTs.

TABLE 3.3: Mass and size of NCE51 from Noliac.

Diameter	Thickness	Weight	Mass density
25 mm	0.5 mm	1.86 g	7600 kg/m^3

3.3 Description of the SHM system

The experiments are conducted using an SHM system developed by the author's laboratory. This system is composed of the specimen, the piezoelectric transducers, the signal generator, amplifier and data acquisition system. A picture of the SHM experimental system is shown in Figure A.4a. The specimen is suspended from a beam so that the edges of the structure are free from all external constraints to prevent the specimen from interacting with other supports (e.g. test bench).

The pitch-catch method is used for the delamination damage detection. Figure A.4b shows a schematic illustrating the procedure for the SHM experiments. When carrying out experiments, an electrical excitation signal is generated by the signal generator and amplified by the amplifier. Then, this signal is transmitted to PZT1 (used as an actuator), which transforms the electrical signal to a mechanical vibration (inverse piezoelectric effect), thus generating elastic waves inside the test structure. The elastic waves propagate through the damage region inside the sample and arrive at PZT2. Then PZT2 (used as a sensor) measures the mechanical deformation of the structure, which is then converted to electrical signals. A Nicolet Genesis LDS acquisition system records the measured signals. A multiplexer is also used to automate the excitation-acquisition procedure, thus avoiding connecting and disconnecting the cables of the PZTs when they act in "actuator" mode or in "sensor" mode. In fact, this automation is essential when a large number of data acquisitions need to be carried out on several test structures. Finally, all the collected data are post-processed using MATLAB software.

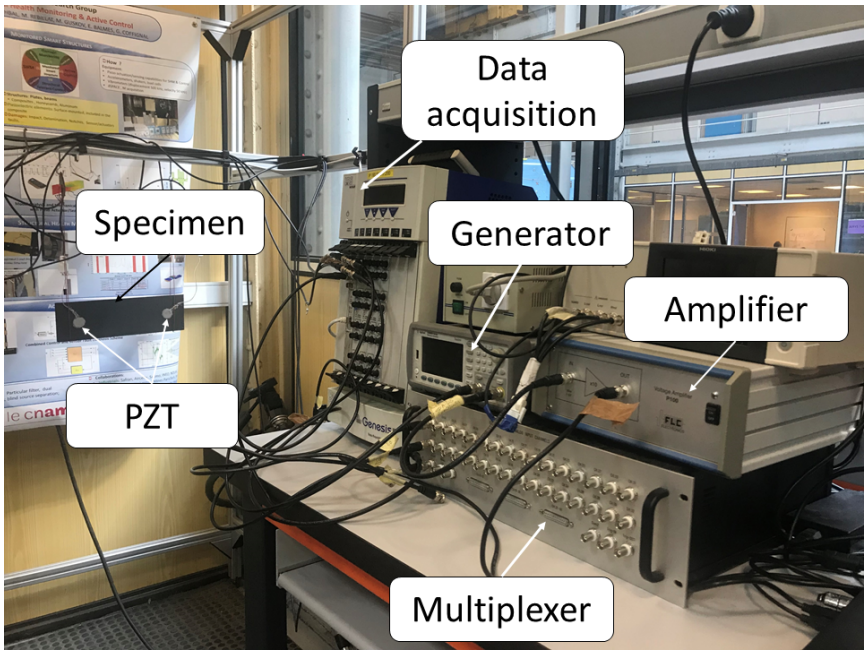

FIGURE 3.8: The experimental system.

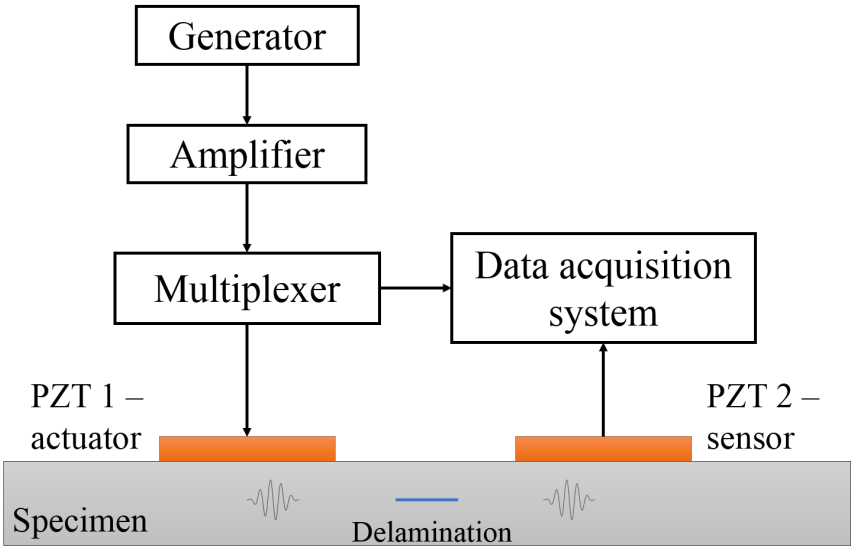

FIGURE 3.9: Schematic of experimental process.

3.4 Selection of input signals

Before tackling the damage induced nonlinearity investigation, it is of interest to determine the input signals. A proper Lamb wave mode should be selected considering its dispersive properties, sensitive frequency range and excitation amplitudes, which could all influence the detection of damage [61].

3.4.1 Type of input signals

For the waveform selection, pure sinusoidal shapes and a windowed sinusoidal signal are often used as input signals in SHM. In particular, the latter is widely used for its

narrow bandwidth, centralized energy and non-dispersion characteristic [62]. In this study, both continuous sine wave excitations and modulated sinusoidal excitations at various frequencies are excited, and the responses are measured and compared to select a proper Lamb wave excitation mode.

3.4.2 Excitation frequency

Except for the waveform of the excitation signals, it is also important to determine the input frequency since the fundamental waves and higher harmonics are all dependent on the input frequency. In this section, the PZT resonance frequencies are calculated analytically and numerically for the analysis of the excitation frequency.

The PZT resonance frequency in the radial direction can be calculated as follows [1]:

$$f_r = \frac{N_p}{2r} \tag{3.3}$$

where f_r indicates the resonance frequency of the PZT, N_p represents the radial mode resonance frequency constant of the PZT disk, and r is the radius. In this study, the N_p of the PZT disks is 1300 m/s provided by the PZT manufacturer. Therefore, the resonance frequency of the PZT disk in the radial direction is 52 kHz. Besides, a finite element simulation is conducted in ABAQUS to identify the in-plane mode of a PZT disk as a supplement to the analytical calculation. The resonance frequency of the first mode in radial direction happens at 51.6 kHz, approximately 52 kHz. The distribution of the magnitude of PZT displacement is shown in Figure A.5. Therefore, from the above investigations, the input frequency can be 52kHz.

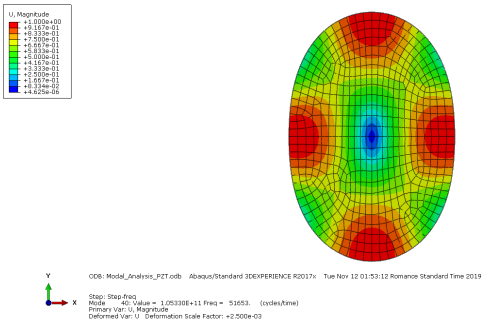

FIGURE 3.10: Simulation results of natural frequency analysis of the fundamental radial mode shape of the PZT disk.

3.5 Damage index

In order to evaluate the severity of the delamination, damage indexes (DI) are employed in this study. Particularly in this study, the nonlinear acoustic effects in the propagation of Lamb waves in the composite plates are focused and used for delamination detection. For those waves that are induced by contact of damage interfaces,

not only the second harmonic but also other higher order harmonics exist. However, in most of the literature, only the effect of the second harmonic is evaluated. Therefore, a damage index that can be used to evaluate the energy of multiple higher harmonics is necessary.

Total harmonic distortion (THD) is a common value used to measure the harmonic distortion present in a signal in an audio system. It is defined as the ratio of the sum of the powers of all harmonic components to the power of the fundamental frequency:

$$THD_n = \frac{\sqrt{\sum_{j=2}^{n} A_j^2}}{A_1} \tag{3.4}$$

where n is the calculated maximum order of higher harmonics, A_1 indicates the amplitude of the fundamental frequency, and A_j represents the amplitude of the jth order super-harmonic.

Here in our study, due to the limitation of test equipment (frequency spectra beyond third harmonics are all background noise), we set n as $n = 3$, implying that only the second and third harmonics are concerned, and this THD becomes

$$THD_3 = \frac{\sqrt{A_2^2 + A_3^2}}{A_1} \tag{3.5}$$

where A_2 and A_3 are the amplitudes of the second and third harmonics respectively. Thus, the THD value in this study can be used to evaluate the total energy of the second and third harmonics with respect to the energy of the fundamental frequency of the output signals.

To evaluate quantitatively how the delamination damage in the specimens affects the acoustic nonlinear effects, a damage index (DI) is proposed based on the relative THD value of the output signals from damaged case with respect to output signals from healthy case, which is defined as

$$\widehat{THD} = \frac{THD_3^{damage} - THD_3^{healthy}}{THD_3^{healthy}} \tag{3.6}$$

where THD_3^{damage} and $THD_3^{healthy}$ are the THD ($n = 3$) value of damaged case and undamaged case respectively. This DI evaluates the difference between the energy of second and third order harmonics of the damaged case and that of the healthy case.

In addition, some other DIs are employed [63], which are defined based on the linear characteristics extracted from the time domain output signals. One DI based on the Pearson correlation coefficient between signals from damaged case and intact case is defined as [63]:

$$CRC = 1 - r[x(t), y(t)] \tag{3.7}$$

where $r(x, y)$ is the Pearson's correlation coefficient between signals x and y, $x(t)$ is the reference signal (undamaged case) and $y(t)$ is the signal to be compared (damaged case). The Pearson correlation coefficient $r(x, y)$ is a measure of the linear correlation

of the two signals x and y. The coefficient has a value between 1 and -1, since it is essentially a normalized measurement of the covariance of the two signals [64]. If each signal has N scalar observations, then the correlation coefficient between reference signal x and the current signal y is defined as [63]:

$$r(x,y) = \frac{1}{N-1}\sum_{i=1}^{N}\left(\frac{x_i-\mu_x}{\sigma_x}\right)\left(\frac{y_i-\mu_y}{\sigma_y}\right) \tag{3.8}$$

where μ_x and σ_x are the mean and standard deviation of signal x, and μ_y and σ_y are the mean and standard deviation of signal y, respectively.

Another DI is defined based on the normalized residual energy between the current signal and the reference signal [63]:

$$NRE = \frac{\int_0^T [x(t)-y(t)]^2\,dt}{2\times\left(\int_0^T x(t)^2\,dt + \int_0^T y(t)^2\,dt\right)} \tag{3.9}$$

3.6 Experimental results

In this section, the pure sine wave input, as well as the modulated sine wave input signals, are both used for the nonlinearity investigation. The two-impact plate is used as an example for the investigation in the following study.

3.6.1 Sine wave excitation

The results from sine wave input are illustrated in this section. The excitation frequency is chosen to be 52kHz, and the amplitude is 10V from peak to zero.

Figure A.6 shows the typical response of the undamaged and damaged structure subject to sinusoidal excitation respectively. In both diagrams, it can be observed that the time response signals tend to stabilize after a short period of transient zone.

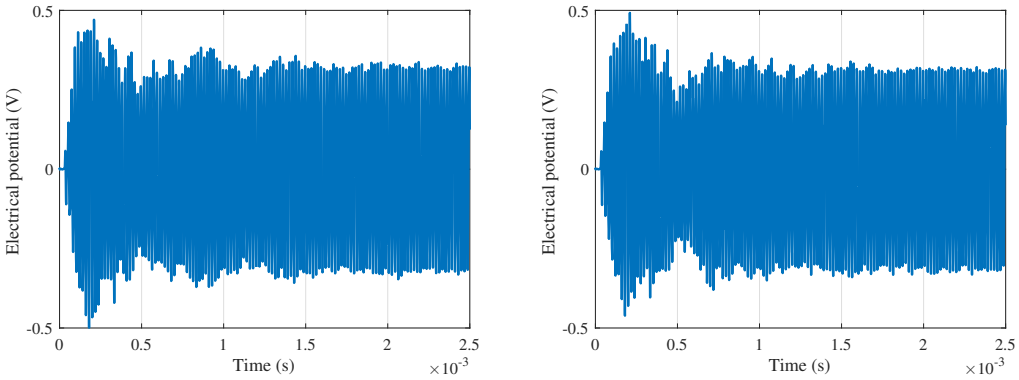

FIGURE 3.11: Typical output signals of sinusoidal excitations of undamaged case (left) and damaged case with two impacts (right).

Figure A.7a shows a comparison of the responses in the frequency domain for the intact plate and the damaged plate containing two impacts. The frequency spectra curves are obtained by applying fast Fourier transform (FFT) to the raw signals

received by the PZT and are normalized with respect to their maximum values respectively. The magnitudes are shown in dB scale. From this figure, except for the main peak at the fundamental frequency, several other peaks at multiples of the fundamental frequency can be observed clearly. In the inset of Figure A.7a, two super-harmonics are given for comparison: the second and third order harmonics; the amplitudes of both the second and the third harmonics from the spectrum of the two-impact plate are larger than those from the undamaged plate. It can be concluded that the presence of the delamination impact amplifies the nonlinear effects.

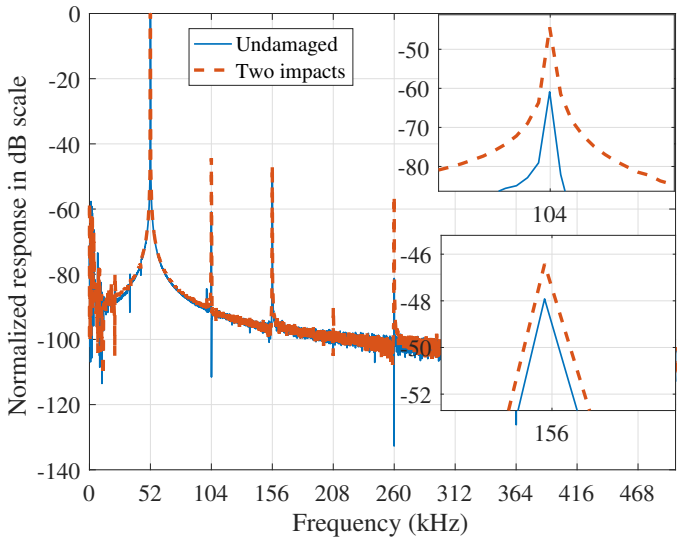

FIGURE 3.12: Frequency domain responses of sine wave input obtained from undamaged plate and damaged plate containing two impacts.

Figure A.7b shows the frequency spectrum of the residual signal between the two-impact plate and the intact plate, which is obtained by subtracting the response signal of the intact plate from the response of the two-impact plate and transforming to the frequency domain. Note that the spectrum is normalized to the maximum value. In this figure, the higher harmonics can be obviously observed. This indicates that strong nonlinearities exist in the difference signal of the damaged plate with respect to the reference case.

In order to investigate the effects of the delamination size on the nonlinearity, same input signals are tested on all four specimens. Figure A.8a shows the variation of DI based on relative THD against number of impacts contained in the composite specimens with the excitation amplitudes of 10V and 50V respectively. For both excitation amplitudes, this DI increases monotonically with the increase of the number of impacts.

Next, the effects of the excitation amplitude on the nonlinearity are investigated. To implement this, five different excitation amplitudes, 10V, 20V, 30V, 40V and 50V are excited on all four specimens. The DIs based on relative THD are plotted for each specimen against the excitation amplitudes, and the results are shown in Figure A.8b.

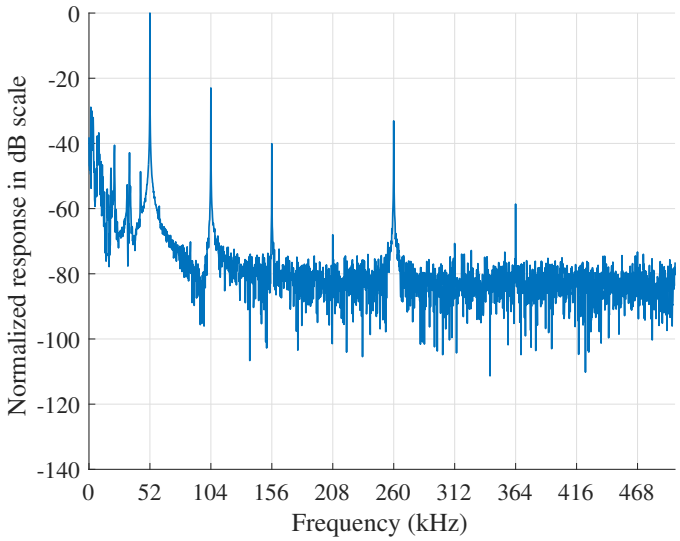

FIGURE 3.13: Frequency spectrum of residual signal between the two-impact damaged plate and the undamaged plate subject to sinusoidal excitation.

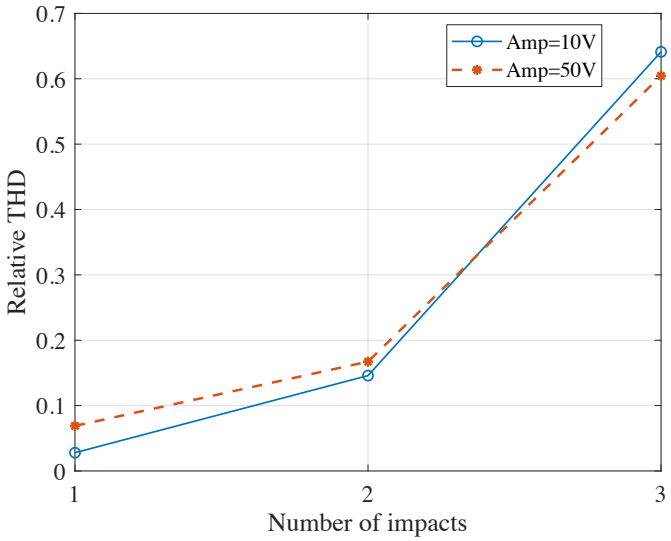

FIGURE 3.14: Variation of DI based on relative total harmonic distortion (THD) against number of delamination impacts. The solid blue line indicates that the excitation amplitude is 10V and the red dash-dot line 50V.

From this figure, it can be observed that with the increase of the excitation amplitude, the variations from the one-impact and two-impact specimens increase first and then decrease slightly, while the variation from the three-impact plate shows a slightly decrease trend with small fluctuations. For all excitation amplitudes, the relative THD values increase with the increasing number of impacts of damage, indicating that the relative THD is sensitive to the severity of the delamination damage.

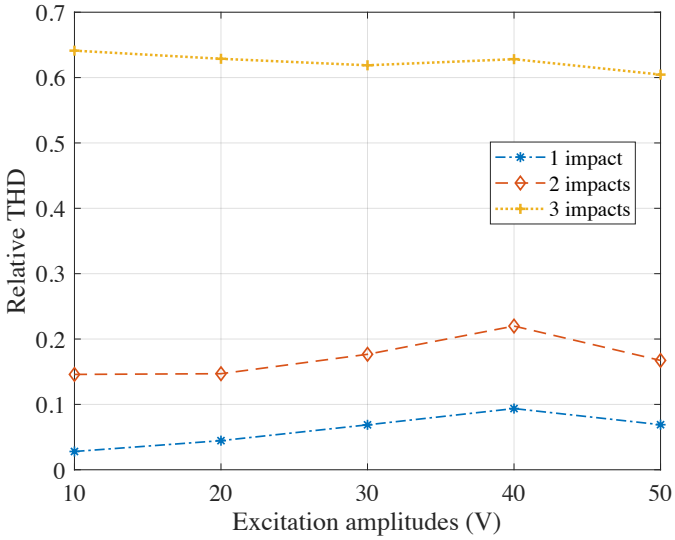

FIGURE 3.15: Variation of DI based on relative total harmonic distortion (THD) against excitation amplitude on different specimens.

3.6.2 Modulated sine wave excitation

In this section, a five-cycle sine wave modulated by a sine window was used as the excitation signal. The results were illustrated in both time domain and frequency domain signals.

Figure A.9a shows the comparison of the responses in frequency domain for the undamaged plate and the damaged plate containing two impacts subject to the modulated wave excitation. From this figure, except for the peak at the fundamental frequency, there are two perceptible peaks corresponding to the second and third harmonics (104kHz and 156kHz) respectively. In the inset of Figure A.9a, the harmonics are given for comparison; the amplitudes of the second and third harmonics from the spectrum of the two-impact plate are larger than those from the undamaged plate. It can be concluded that the nonlinearities are amplified by the presence of the delamination impacts. This can also be proved by the frequency spectrum of the residual signal between the two-impact damaged plate and undamaged plate shown in Figure A.9b. Note that the frequency response is normalized to the maximum value. Therefore, the super-harmonics, especially the second and third harmonics, provide a sensitive tool for the detection of laser impact delamination in composite plates.

Then the effects of delamination size and excitation amplitude on the nonlinearity are studied and presented in the following.

Figure A.10a displays the variation of the proposed DI against the number of delamination impacts with the excitation amplitude of 10V and 50V. From this figure, it can be observed that the DI increases monotonically with the number of delamination impacts regardless of the excitation amplitude. This indicated that the proposed DI is remarkably sensitive to the size of the delamination.

Figure A.10b presents the variation of DI against the excitation amplitude on

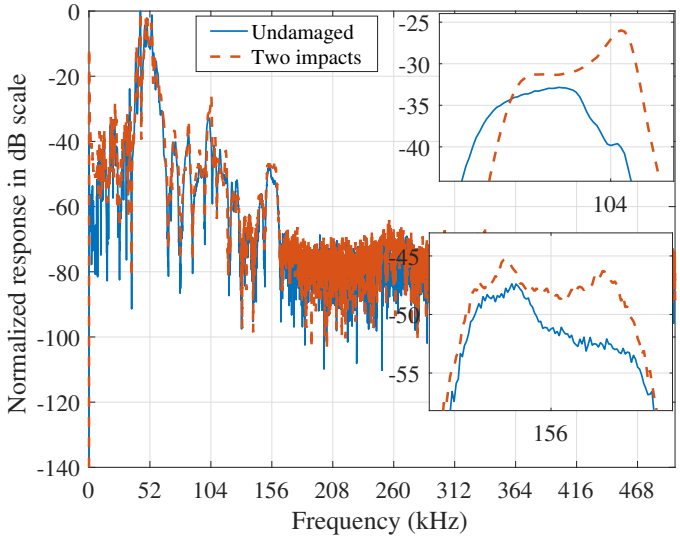

FIGURE 3.16: Frequency domain responses of signals obtained from undamaged plate and damaged plate containing two impacts.

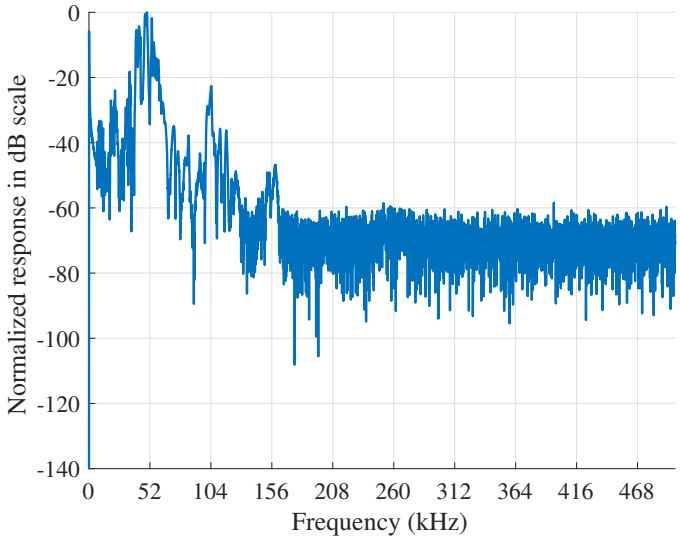

FIGURE 3.17: Frequency spectrum of residual signal between the two-impact damaged plate and the undamaged plate subject to modulated wave excitation.

different specimens. The excitation amplitude varies from 10V to 50V at the step of 10V. From this figure, it can be observed that the DI displays rather flat trends with some small variations. For the one-impact specimen, the curve of DI shows a slightly increasing trend with the increase of excitation amplitude. For the two-impact and three-impact specimens, the DI curves are almost flat. This variation trend might be due to the nonlinearities of the system. In conclusion, compared to the influence of the damage size, the excitation amplitude has minor effects on the proposed DI.

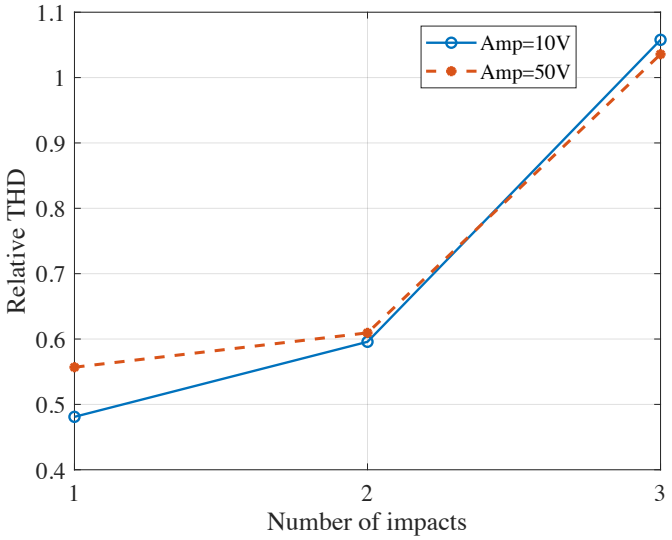

FIGURE 3.18: Variation of DI based on relative THD against the number of delamination impacts for different excitation amplitudes.

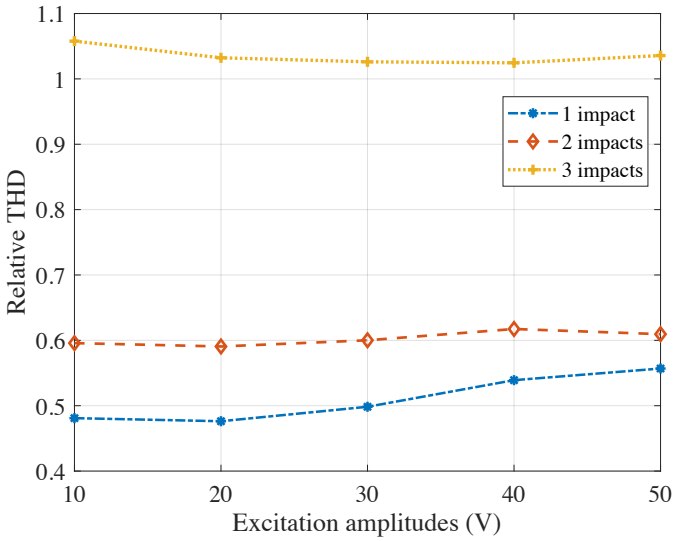

FIGURE 3.19: Variation of DI based on relative THD against excitation amplitude on different specimens.

3.7 Conclusion

In this chapter, the experimental system and the composite specimens are depicted. The delamination in the composite specimens are generated using the laser shock wave technique, and the size and locations are specified. Then the excitation signals are studied and compared. Then, we obtain the experimental output signals and transform the raw signals into the frequency domain using the fast Fourier transform. Results show that the delamination damage adds to the nonlinearity of the system and that severer delamination induces larger nonlinear effects. At last, the DI based on the relative THD is employed to evaluate the delamination severity and the nonlinear

effects. Results show that the relative THD reveals high sensitivity to the nonlinearity induced by the delamination damage.

Chapter 4

Numerical Model for Composite Plate

In this chapter, the simulation models of composite plate specimens and delamination are introduced. The simulation model for the healthy plate is first illustrated to identify the model parameters such as element size, time increment and damping coefficient. Then, the physical model for delamination is depicted, as well as the implementation of the physical model for finite element simulation. All the simulations are completed using the Matlab toolbox Structural Dynamics Toolbox (SDTools).

4.1 Modeling composite plates

In this section, the finite element (FE) method is employed to simulate the propagation of Lamb waves in the cross-ply laminated composite plate which is available experimentally. Figure A.11 shows the FE model of the composite plate built in MATLAB. The composite plate containing 16 plies is modeled by bonding two shell layers together using rigid connections except for the delamination region. Each shell layer contains 8 plies, assuring that the delamination locates at the midplane of the composite plate. The delaminaiton is located at the center in the in-plane direction. Since the model is symmetric with respect to the x-axis, only half of the plate is modeled and a symmetric boundary condition is applied to the longitudinal axis. Quadratic shell elements are used to ensure the accuracy of the results. Two piezoelectric patches (PZT) are bonded to the surface of the plate for the generation and detection of Lamb waves. An intact plate is modeled as a reference with all the regions of the plate bonding together using rigid connections. The global mesh size is set to be 1 mm and finer mesh (0.5 mm) is used locally at the delamination region. The time step is 2×10^{-7} s. The study of mesh size and time increment will be illustrated in detail in the next section.

The initial material properties for simulation are taken from the previous work in our group [60]. However, there are inevitable errors during manufacturing processes. Therefore, it is necessary to investigate the material properties of simulation models to keep the simulation results consistent with experimental results. In the current study, Newton's method is employed to update the material properties.

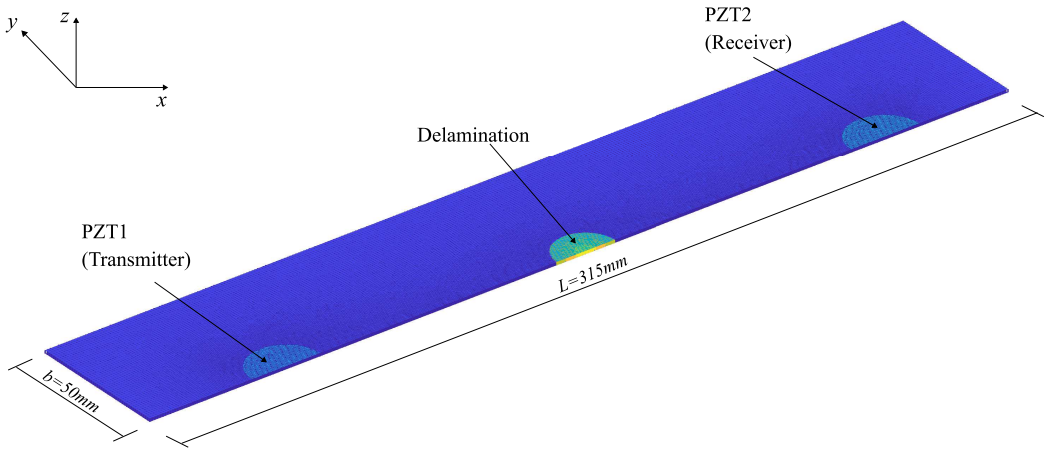

FIGURE 4.1: Schematic of finite element model in thee-dimensions.

To perform this method, the time of flight and response amplitude are regarded as target functions. Two material properties, E_{11} and G_{12}, are regarded as independent variables to be updated. We first took several values around the initial values of E_{11} and G_{12} for study. Using these values as material parameters, we calculated the corresponding time of flight and response amplitude, which are then plotted against the material properties. The approximate tangent lines are then obtained to form the Jacobian matrix, which is used in the multidimensional Newton's method. After several iterations, the final values of E_{11} and G_{12} are obtained. The initial values and final values after updating are listed in Table A.3.

TABLE 4.1: Initial and final values of specimen material properties.

Material property	**Initial value**	**Final value**
Poisson's ratio ν	0.3	0.3
E_{11}(per ply)	140 GPa	149 GPa
E_{22}(per ply)	9 GPa	9 GPa
E_{12}(per ply)	4.5 GPa	4.9 GPa

4.1.1 Study on element size and time increment

In finite element simulations, the temporal and spatial resolution should be high enough to meet the requirements of calculation precision. However, high resolutions are usually achieved through a very small time increment and element size, which will lead to huge computation costs (e.g., computation time, CPUs, and disk space, etc.). In this context, to obtain a trade-off between calculation precision and cost, a healthy plate model has been investigated with respect to time increment and element size.

4.1.1.1 Time increment study

It was shown previously [65] that, in simulation of wave propagation, time increment and mesh size should be small enough to satisfy the numerical convergence requirements. Generally speaking, the time increment required for a dynamic analysis is

$$\Delta t < \frac{1}{20 f_{max}} \tag{4.1}$$

where Δt is the time increment in the analysis procedure, and f_{max} is the highest frequency of interest. By determining the highest frequency for waves propagating through the specimen, and using Eq. 4.1, a time step Δt can be obtained which is small enough to model the temporal behavior of the propagation with sufficient temporal resolution. In this study, higher harmonics, in particular the second and third harmonics in the received signals, are of interest. Therefore, the highest frequency of interest should be the frequency of the third harmonic, i.e. $3 \times 52\,\text{kHz} = 156$ kHz. Then, the time increment should satisfy

$$\Delta t < \frac{1}{20 \times 156\,\text{kHz}} = 3.2 \times 10^{-7} s = 0.32\,\mu\text{s} \tag{4.2}$$

However, very small time steps usually lead to long simulation time and large computational cost. A trade-off between accuracy requirement and computation cost must be considered. In order to achieve this, several studies are conducted using different time increments: 1 µs, 0.5 µs, 0.2 µs, 0.1 µs, 0.05 µs, 0.02 µs and 0.01 µs.

Figure 4.2 shows the electrical responses in time domain from models with different time increments. From this figure, it can be observed that the difference between time responses is not so obvious. Therefore, indicators that characterize the time domain responses, such as time of flight and root mean square difference (RMSD), are extracted.

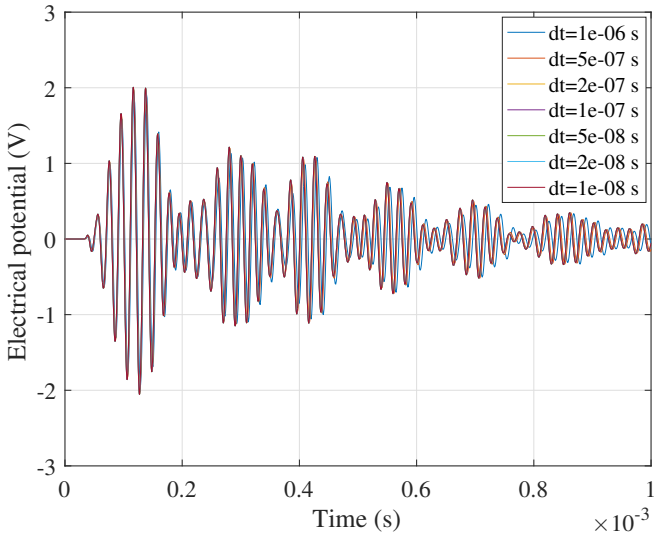

FIGURE 4.2: Time responses from models with different time increments.

The time of flight (ToF) is calculated from each response and compared with experimental results. The root mean square difference (RMSD) of the first wave packet between simulated and experimental responses is calculated to evaluate the difference between simulation and experimental results.

Figure 4.3 shows the time of flight of the output responses from each simulation with different time increments. From this figure, it can be observed that when time increment is less than 0.1 µs, the time of flight keeps constant at 4.5×10^{-5} s , which is equal to the results from experiments. When time increment is less than 0.1 µs, the time of flight varies between 4.5×10^{-5} s and 4.495×10^{-5} s. Since smaller time increment leads to higher time resolution, the calculated time of flight with smaller time increment should be more precise than larger time increment. The discrepancy between simulations with a smaller time increment and experiments might originate from the low sampling frequency in experiments. The sampling frequency in experiments is 2 MHz, and the corresponding time increment is 0.5 µs. However, the largest discrepancy is 0.005×10^{-5} s, only 0.1% of the experimentally measured time of flight (4.5×10^{-5} s). This error is too small to be considered. It can be concluded that for all the simulations with different time increments, the time of flight is equal or approximately equal to that from experiments.

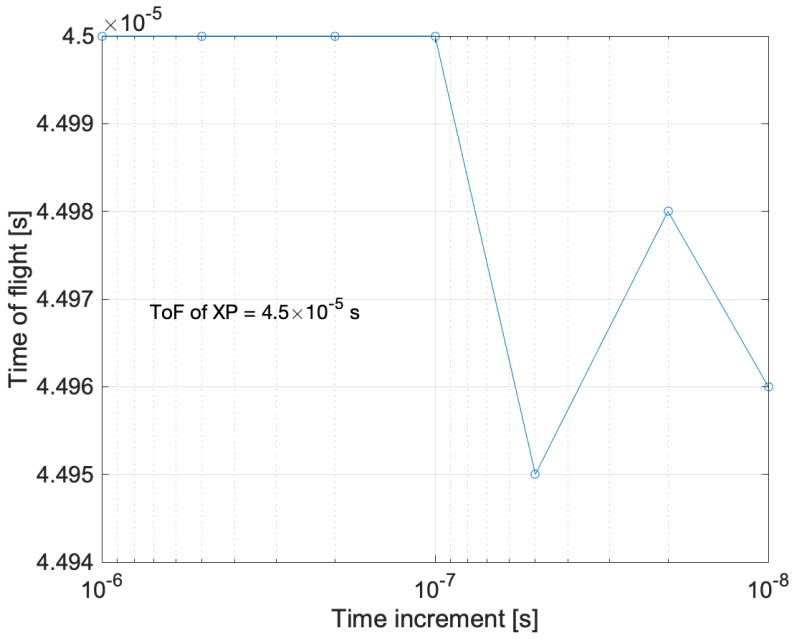

FIGURE 4.3: Time of flight of the simulated responses with different time increments.

Figure 4.4 shows the variation of RMSD between simulation and experiments with decreasing time increment. From this figure, it can be observed that the RMSD first decreases from 0.371 to 0.351, and then increases to 0.355. The smallest value occurs at 2×10^{-7} s, and the RMSD at $\Delta t = 1 \times 10^{-8}$ s is only 0.97% larger than RMSD at $\Delta t = 2 \times 10^{-7}$ s. Since the RMSD evaluates the energy of difference signals between simulations and experiments, it can be concluded that this difference is the smallest

when time increment is set as $\Delta t = 2 \times 10^{-7}$ s. Thus, the time increment can be set as

$$\Delta t = 2 \times 10^{-7} s \tag{4.3}$$

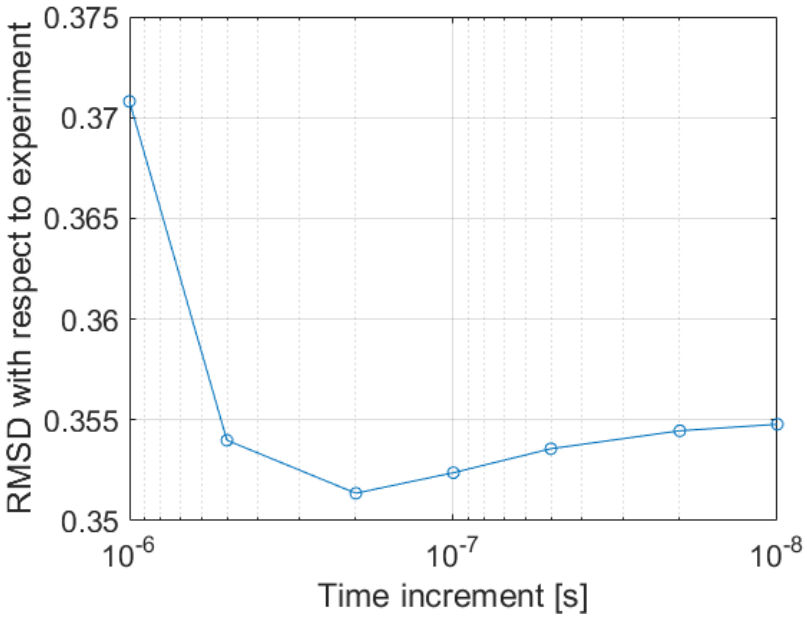

FIGURE 4.4: RMSD of first wave packet between simulated and experimental responses with different time increments.

4.1.1.2 Global element size study

In a wave propagation study, the element size is usually associated with the minimum wavelength λ_{min}. It is generally recommended to use more than 20 nodes per wavelength. This criterion can be expressed as [65].

$$le < \frac{1}{20}\lambda_{min} \tag{4.4}$$

where le is the element size. Thus, the element size can be determined by finding the minimum wavelength that is used in the investigation. Since the Lamb wave is dispersive, the velocity changes with the frequency. As mentioned in the previous section, the highest frequency to be studied is the frequency at third harmonic, i.e. 156 kHz. Then the corresponding phase velocity of S0 mode is 7049 m/s, and the wavelength is

$$\lambda = \frac{c_p}{f} = 45.2\,\text{mm} \tag{4.5}$$

where f is the frequency and c_p is the corresponding phase velocity. Therefore, the element size should satisfy

$$le < \frac{1}{20} \times 45.2 = 2.26\,\text{mm} \tag{4.6}$$

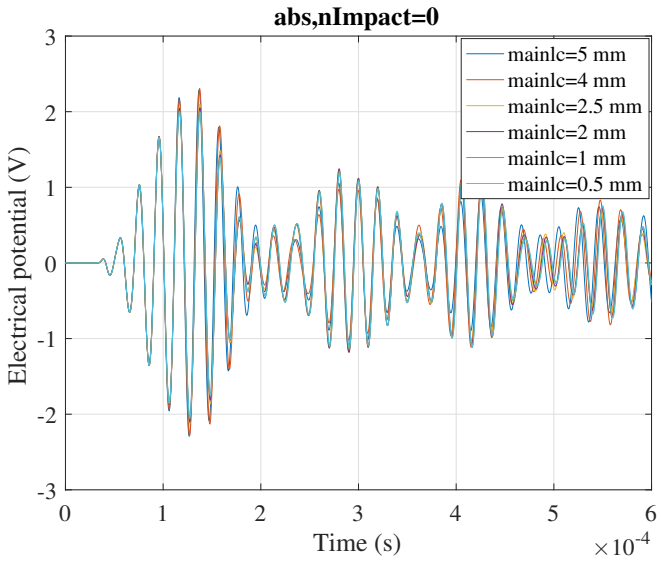

FIGURE 4.5: Time responses from models with different global element sizes.

Several cases are investigated with different element sizes: 5 mm, 4 mm, 2.5 mm, 2 mm, 1 mm, 0.5 mm, 0.4 mm and 0.25 mm. Figure 4.5 presents the electrical responses in the time domain from models with different global element sizes. From this figure, it is obvious that there is a large difference among each response. Similar to the time increment study, some indexes, such as the time of flight and RMSD between simulated and experimental results are calculated.

To identify whether the time of flight converges with decreasing element size, the time of flight of each response signal is calculated. The RMSD of the first wave packet between each simulated response and experimental response is derived to evaluate the difference between simulation and experiments, serving as an indicator for identifying the proper element size.

Figure 4.6 illustrates the variation of time of flight with the refining element size. It can be observed from this figure that for element size from 5 mm to 2 mm, the time of flight is 4.48×10^{-5} s, while for element size from 1 mm to 0.25 mm, the time of flight is 4.5×10^{-5} s. Although the time of flight measured in experiments is equal to the latter, the difference between the two values is 2×10^{-7} s, which is exactly the time increment used in the simulations. This indicates that varying element size has little influence on time of fight. Therefore, it can be concluded that in terms of the time of flight, it is proper to use the element size smaller than 5 mm.

Figure 4.7 shows the variation of RMSD of the first wave packet between each simulated response and experiment with respect to refined element size. It can be observed that the RMSD initially increases from 0.389 to 0.417 when element size changes from 5 mm to 4 mm. Then the RMSD decreases monotonically from 0.417 to 0.349 along with reducing element size from 4 mm to 0.25 mm. This indicates that from 4 mm, the finer element size, the smaller the discrepancy between simulation and experiments. Thus, the global element size is set as 2×10^{-7} s.

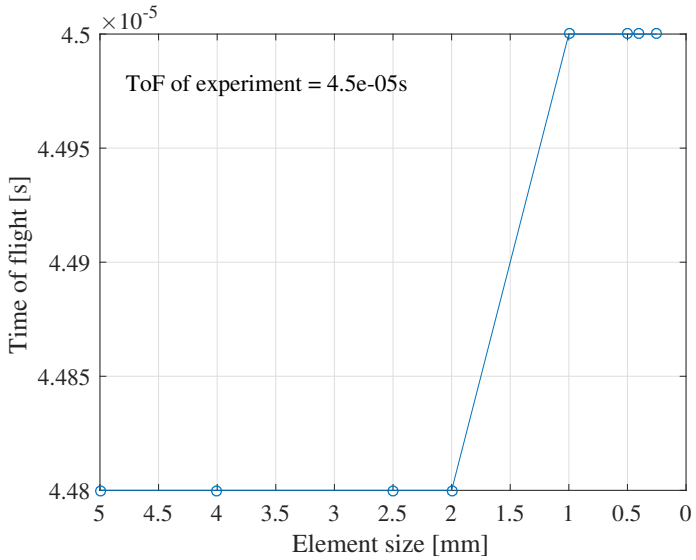

FIGURE 4.6: Time of flight of the simulated responses with different global element size.

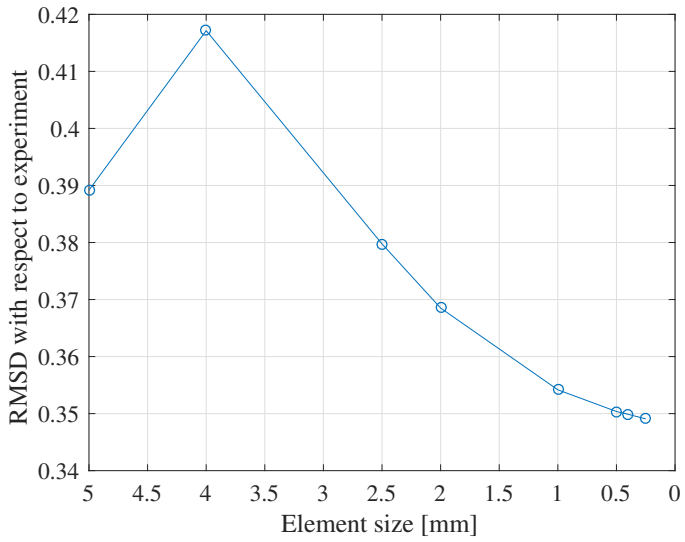

FIGURE 4.7: RMSD of first wave packet between simulated and experimental responses with different global element size.

4.1.1.3 Local element size study

In order to obtain more accurate simulation results with less computation time, mesh size is refined in local regions around delamination and PZT using GMSH [66]. Five cases are investigated as listed in Table 4.2. The time increment is set as 1×10^{-7} s, and the time span in simulation is 6×10^{-4} s. The time of flight is calculated and RMSD of the first wave packet between simulated and experimental responses is derived.

Figure 4.8 gives the time of flight from all simulated responses in the five cases. They are all equal to the time of flight measured from experiments, i.e. 4.5×10^{-5} s. Therefore, from the aspect of time of flight, there is no preference among all five

TABLE 4.2: Investigation on global and local element size.

Case	Global element size (mm)	Local element size (mm)
1	2	1
2	2	0.5
3	1	0.5
4	1	0.25
5	0.5	0.25

cases.

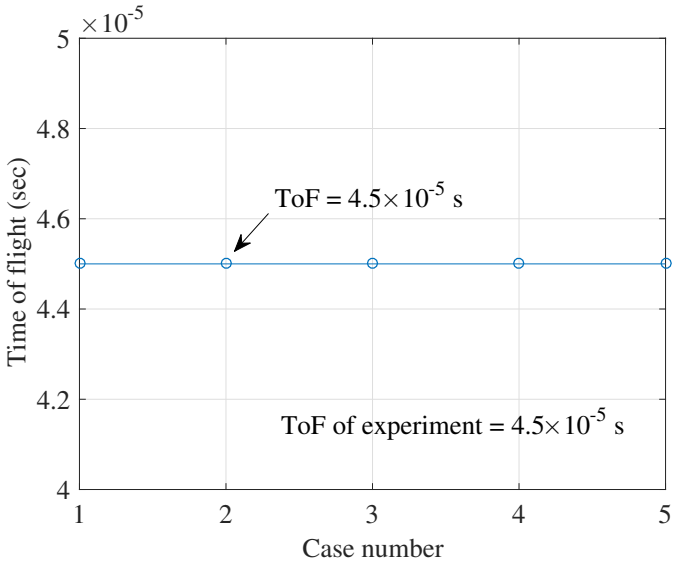

FIGURE 4.8: Time of flight of the simulated responses with different global and local element size.

In Figure 4.9, the values of RMSD of the first wave packet between each simulated and experimental response are presented. It can be observed from this figure that the smallest RMSD is from Case 5 (global element size equals 0.5 mm, local element size is 0.25 mm) with the value of 0.3507, and the second smallest is from Case 3 (global element size equals to 1 mm, local element size is 0.5 mm) with the value of 0.3524.

From the perspective of RMSD separately, Case 5 is obviously the case with the smallest difference from the experiment. However, the calculation time is much longer (more than 4 hours) compared with Case 3 (less than 40 minutes) as shown in Table 4.3, and the RMSD is not far away (only 0.48% difference). Therefore, Case 3 is the most appropriate among all five cases.

The parameters used in the following simulations are listed in Table 4.4.

4.1.2 Study on damping coefficient

In this subsection, the damping coefficient will be discussed. Classical Rayleigh damping is viscous damping which is proportional to a linear combination of mass and

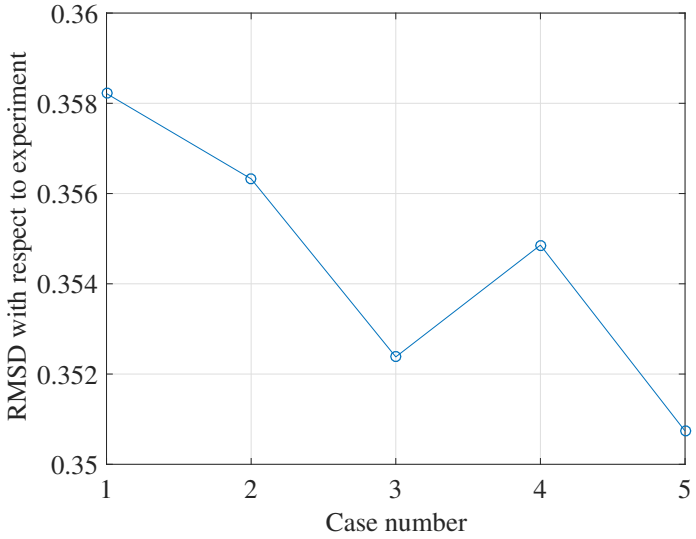

FIGURE 4.9: RMSD between simulated and experimental responses with different global and local element size.

TABLE 4.3: Computational time for all cases with different global and local element sizes.

Case	Computational time (min)
1	4.9
2	11.7
3	38.5
4	150.0
5	258.5

TABLE 4.4: Simulation parameters.

Time increment	Global element size	Local element size
2×10^{-4} s	1 mm	0.5 mm

stiffness. The damping matrix gives

$$\boldsymbol{C} = \alpha \boldsymbol{M} + \beta \boldsymbol{K} \tag{4.7}$$

where $\boldsymbol{M}$ and $\boldsymbol{K}$ are the mass and stiffness matrices respectively, and α and β are the mass and stiffness proportional factors with units of the inverse of second s^{-1} and second s respectively.

In general, damping is a material property specified as part of the material definition. Classical Rayleigh damping results in different damping ratios for different response frequencies, which can be referred to the equation

$$\zeta = \frac{\alpha}{2\omega} + \frac{\beta}{2}\omega \tag{4.8}$$

where ζ is the damping ratio and ω is the angular frequency. The stiffness proportional

term contributes damping by a linearly proportional relation to response frequency. For the mass proportional term, it is inversely proportional to response frequency. This equation implies that the mass proportional Rayleigh damping, α, damps the lower frequencies and the stiffness proportional Rayleigh damping, β, damps the higher frequencies.

In this study, the frequency of interest is under 200kHz so that the mass proportional Rayleigh damping factor α can be ignored. Based on the spectrum of the response signals of the real structure, the damping coefficient was identified with the SDT routines corresponding to modal damping of the order of 0.7%, in the whole range of frequencies considered[7]. This led to the representation of the modal damping coefficient

$$\zeta(\omega) = \frac{\beta}{2}\omega \approx 0.007 \tag{4.9}$$

As the excitation frequency in this study is 52kHz, the stiffness proportional damping factor β can be derived as

$$\beta \approx 4.3 \times 10^{-8} \tag{4.10}$$

Studies were conducted on a healthy plate model using the above estimated damping factor.In addition, a study without applying any damping to the model was also conducted for reference. The derived raw responses in the time domain are compared with the experimental results.

Figure 4.10 shows the comparison between time-domain raw responses from the undamped model and the damped model respectively. The amplitude of the time domain signal from the model without damping is much higher than the amplitude from the damped model. In addition, the amplitudes of each wave-packet from the model without damping are almost constant, while the amplitudes from the damped model decay.

Figure 4.11 shows the comparison between raw responses in time domain from simulation and experiments respectively. From both curves, the amplitude of each wave-packet decreases.

4.2 Damage Model for delamination-type damage in composites

In this section, we will study several physical models for the delamination and identify the model parameter. In order to reduce the calculation time and computation costs, a beam model is employed for instead of the full plate model. The proposed delamination models and the model parameters are all tested on the beam model. The delamination models and the corresponding parameters after beam model test will be applied to the full plate model. Several delamination models are proposed and analyzed, including a linear model using the local stiffness reduction method and several nonlinear models using the spring element technique. Model parameters are

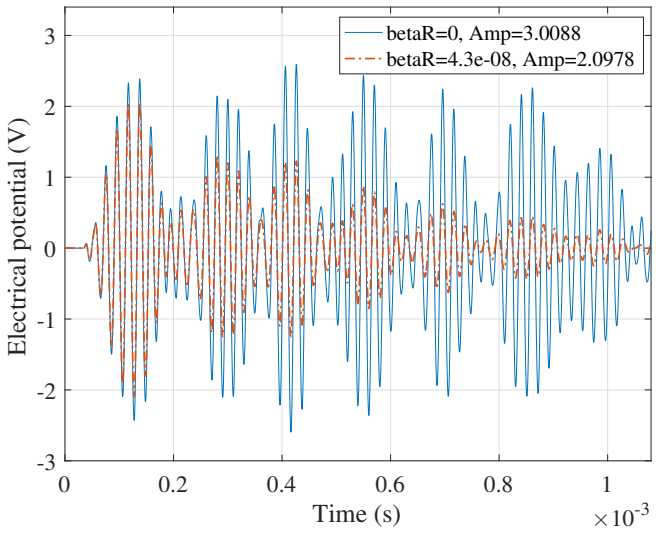

FIGURE 4.10: Comparison between raw responses from undamped model and damped model.

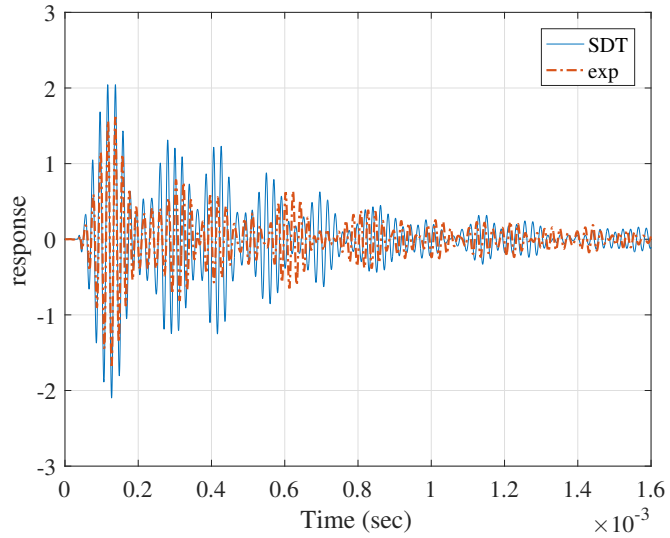

FIGURE 4.11: Comparison between raw responses from simulation and experiments.

investigated by comparing the corresponding results and evaluating them through a set of damage indicators.

4.2.1 Beam model employed for damage model investigation

The beam model employed in this section has the same length and material properties as the full plate specimen, but only 2 mm in the width direction. The model is shown in Figure 4.12. The beam is also equipped with two piezoelectric ceramics that serve as actuator and sensor. The material properties of the PZTs are the same as those used in the plate model. The length of the PZT is equal to the diameter of the PZT quipped in the full plate. Similar to the plate model, in the beam model, the

delamination is also located at the center and in the midplane, with its length equal to the diameter of the delamination in the original full plate model. The widths of the delamination and the two piezoelectric ceramics are equal to the width of the beam.

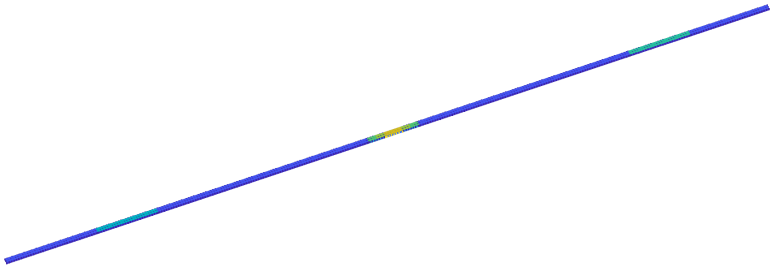

FIGURE 4.12: Beam model for the investigation of delamination model parameters.

4.2.2 Stiffness reduction model

According to the classical lamination theory (CLT) [8], the stiffness of composite laminates containing n plies is defined as

$$\langle [A], [B], [D] \rangle = \sum_{k=1}^{n} \int_{z_{k-1}}^{z_k} [\bar{Q}_{ij}]_k \langle 1, z, z^2 \rangle \, dz, \tag{4.11}$$

where $[A]$ is the extensional stiffness matrix, $[B]$ is the extension-bending coupling matrix and $[D]$ is the bending stiffness matrix. z_j is the coordinate of the upper surface of the kth ply (as illustrated in Figure 2.4), $[\bar{Q}_{ij}]_k$ is the stiffness matrix of ply k along the fiber direction and z is the coordinate in the thickness direction.

As illustrated in Section 2.4.1, the stiffness at mth delamination can then be calculated based on classical lamination theory according to Ref. [25]:

$$\langle [B^m], [D^m] \rangle = \begin{cases} \sum_{k=1}^{n} \int_{z_{k-1}}^{z_k} [\bar{Q}_{ij}]_k \mathrm{H}(z_m - z) \langle z, z^2 \rangle \, dz, & z_m \geqslant z_l \\ \sum_{k=1}^{n} \int_{z_{k-1}}^{z_k} [\bar{Q}_{ij}]_k \mathrm{H}(z - z_m) \langle z, z^2 \rangle \, dz, & z_m < z_l \end{cases} \tag{4.12}$$

where $[B^m]$ and $[D^m]$ are the coupling stiffness and bending stiffness at the delamination region respectively. z_m and z_l are the coordinate of the delamination and coordinate of the mid-plane of the plate in out-of-plane direction respectively. H is the Heaviside step function. The loss of the extensional stiffness of the delamination is negligible.

In the calculations of the stiffness at the delamination region, the effects of the smaller sub-laminate of the delamination in coupling and bending stiffness are ignored.

That is, only the thicker sub-laminate is considered when calculating the coupling and bending stiffness at the delamination region. Since in this study, the delamination is located at the midplane of the composite beam, there is no need to consider which sub-laminate to be calculated, and the loss of bending stiffness reaches the maximum. The calculated bending stiffness at the delamination region for the undamaged and delaminated region are listed in Table 4.5. It can be observed from this table that the bending stiffness at the delaminated region is almost half of the stiffness at the healthy region.

In the following study, this model is implemented by reducing the local material properties at the delamination region to reduce the local stiffness. To simplify the process, all the components of Young's modulus and shear modulus at the delamination region are multiplied by a reduction coefficient $Ecoef$ ($0 < Ecoef < 1$). Several values of $Ecoef$ are tested on models with three different damage sizes (one impact, two impacts and three impacts), in order to evaluate the effects of the reduction coefficient on the results. It should be noted that in this model, the two layers at the delamination region are bonded rigidly, as in the other parts of the plate model.

We also calculate the bending stiffness after applying a set of $Ecoef$ values to Young's modulus and shear modulus. The calculated bending stiffness using reduction coefficient method is then compared with the calculated bending stiffness using Equation 4.12, thus finding the closest bending stiffness and the corresponding $Ecoef$ value. Tests show that $Ecoef$ around 0.6 lead to the closest bending stiffness. The calculated bending stiffness with $Ecoef = 0.6$ is also shown in Table 4.5.

TABLE 4.5: Bending stiffness at the delamination region for the undamaged and damaged plates

Specimen	**Bending stiffness** ($\mathrm{GPa \cdot m^3}$)			
	D_{11}	D_{12}	D_{22}	D_{66}
Undamaged region	72.4	3.51	72.4	4.40
Delamination region	42.1	1.76	30.2	2.20
Reduced modulus method ($Ecoef = 0.6$)	43.4	2.11	43.4	2.63

Two damage indicators are employed to evaluate the reduction coefficient: CRC, which is based on correlation coefficient, and NRE, which is based on the normalized residual energy. The results are shown in Figures 4.13 and 4.14. The case where the reduction coefficient is equal to 1 indicates the undamaged model. From Figure 4.13 it can be observed that the three curves representing respectively the one-impact, two-impact and three-impact beams all have a monotonic decreasing trend when the reduction coefficient increases. The CRC values first drop rapidly as the reduction coefficient increases from 0.1 to 0.5, and then show a slowly declining trend as the $Ecoef$ increases from 0.5 to 1. Besides, if the reduction coefficient is fixed, the CRC values show a general growing trend with the increased number of impacts, i.e., the larger the delamination, the larger the CRC value.

For the indicator NRE, Figure 4.14 shows the same trend: the NRE values decrease monotonically with increasing reduction coefficient, and rise with the increased number of impacts.

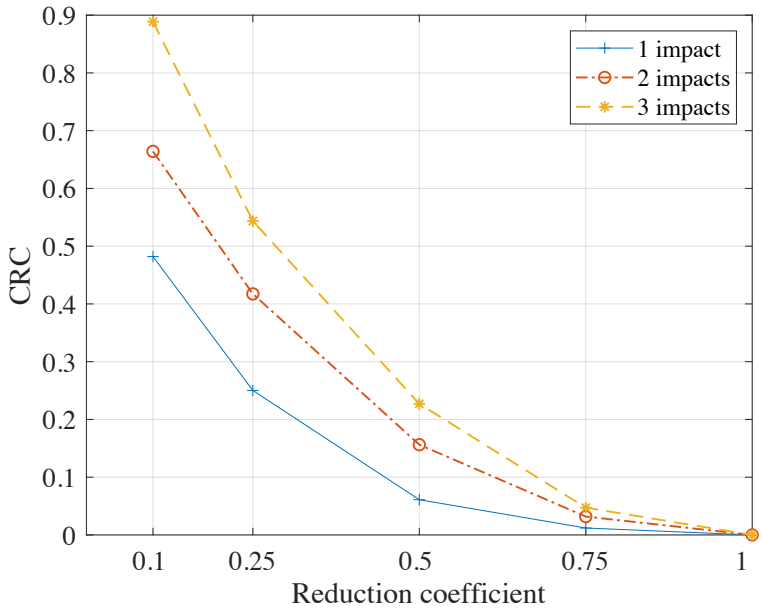

FIGURE 4.13: Effect of reduction coefficient on indicator CRC based on correlation coefficient of the received electrical signal.

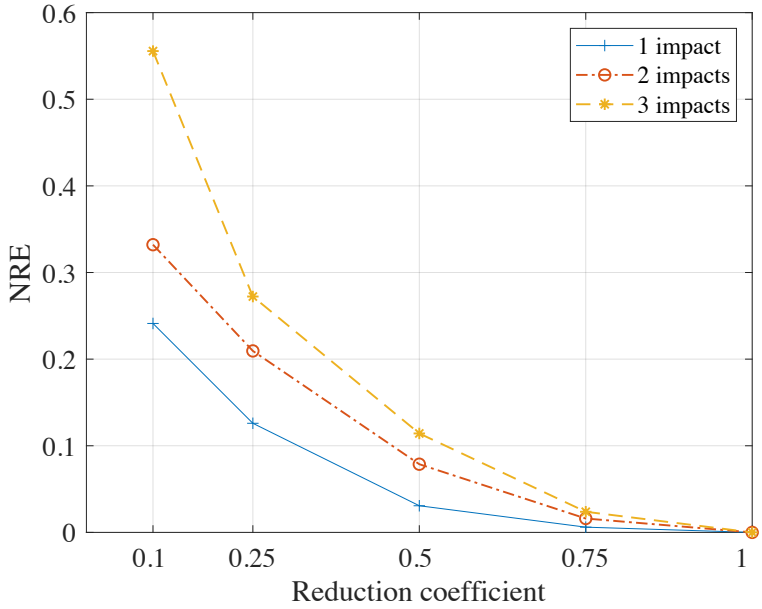

FIGURE 4.14: Effect of reduction coefficient on DI based on the normalized residual energy of the received electrical signal with respect to the reference signal.

4.2.3 Spring models

This damage model is implemented by applying a set of spring elements connecting the nodes of the upper and lower layers distributed at the delamination region, to model the mechanical interactions between delamination interfaces.

Figure A.13 shows the schematic of the nonlinear spring model. In this figure, the dashed lines indicate the midplane of the upper and lower layers of the plate model respectively. The red dots indicate the nodes on the upper and lower layers. The nodes on the upper layer are connected to the corresponding nodes on the lower layer at the same in-plane position. Outside the delamination region, the upper and lower layers are bonded by rigid connection, while within the delamination region, the layers are connected by spring elements. k^{spr} indicates the spring stiffness.

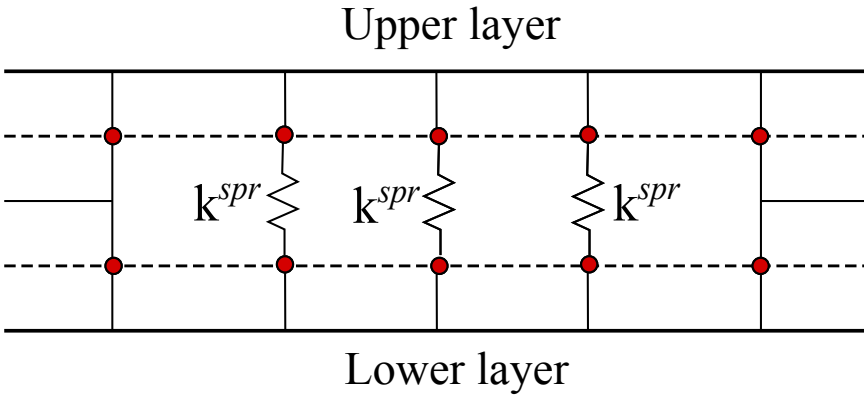

FIGURE 4.15: Schematic of surface interaction modeling at delamination region by applying nonlinear springs.

4.2.3.1 Linear spring model

In this model, a linear relationship between the spring force and the relative displacement between the upper and lower layer in the out-of-plane direction is defined. The ratio between the force and the relative displacement is defined as the spring stiffness.

Several values of the spring stiffness ranging from 0 to 1×10^6 N/m are tested. Damage indexes CRC, NRE and relative THD are employed to evaluate the effects of spring stiffness to the results, as shown in Figures 4.16 to 4.18. Results show that the values of CRC and NRE from all the three beam models with different delamination sizes do not change much with the change of spring stiffness. For example, as the spring stiffness increases from 0 to 1×10^6 N/m, the value of CRC from the one-impact beam decreases slightly from 0.0087 to 0.0082, with CRC from two-impact beam increasing from 0.0193 to 0.0206 and CRC of three-impact beam from 0.0235 to 0.0226. All the changes do not exceed 7% with respect to the minimum value from each beam model. From the perspective of the number of impacts, the CRC values show a monotonic increasing trend with the increase of the number of impacts on all the tested values of spring stiffness. The NRE values present the same trend as CRC. In addition, for the relative THD, the one-impact beam shows a rather stable

trend as the spring stiffness increases from 0 to 1×10^6 N/m. However, relative THD of the two-impact beam declines from 0.265 to 0.221, showing a nearly 20% change, while relative THD from the three-impact plate increases from 0.381 to 0.505 and then decreases to 0.50 presenting a change of about 33%. Similar to the other two linear DIs, the relative THD also shows an increasing trend with the growth of the number of impacts.

The above analyses show that the two DIs extracted from the linear characteristics are not as sensitive as the relative THD extracted from the nonlinear characteristics to the change of spring stiffness. The response from the one-impact plate is not sensitive to the change of spring stiffness. This may be because the size of one delamination is not large enough, so that the change of the interaction properties of delamination has little effect on the output.

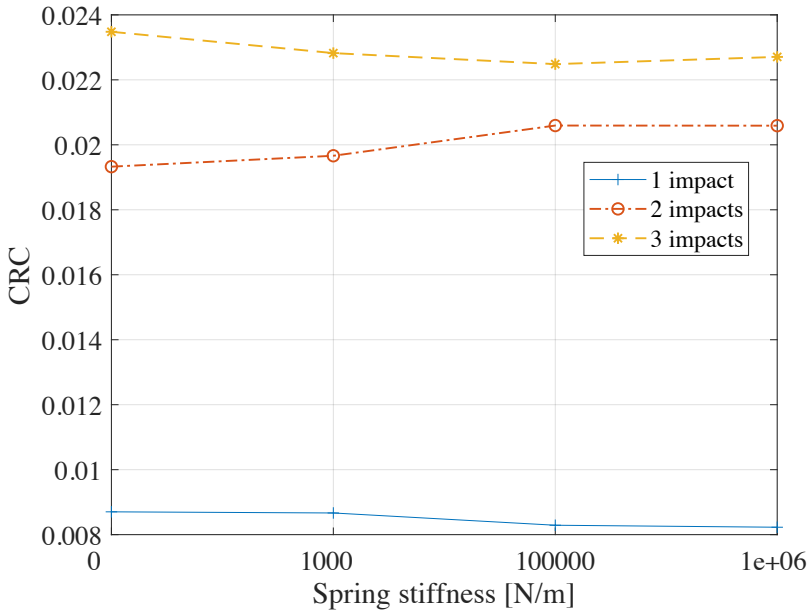

FIGURE 4.16: Effect of spring stiffness on indicator CRC extracted from the received electrical signal.

4.2.3.2 Nonlinear spring model

(a) Out-of-plane interaction

In out-of-plane direction, the interaction between two delamination surfaces are often modeled as "hard" contact, i.e., when two surfaces are in contact, the normal force tends to separate them to avoid penetration between two surfaces, and when the two surfaces are separated, no force is exerted on them. Thus, nonlinear springs are employed in this model, and a simplified bi-linear relationship between deformation and force is assigned to the springs.

Figure A.14 shows the relationship between spring force and the relative displacements between the upper and lower surfaces of the delamination in the out-of-plane direction. F_z is the spring force in the normal direction, u_z is relative displacements

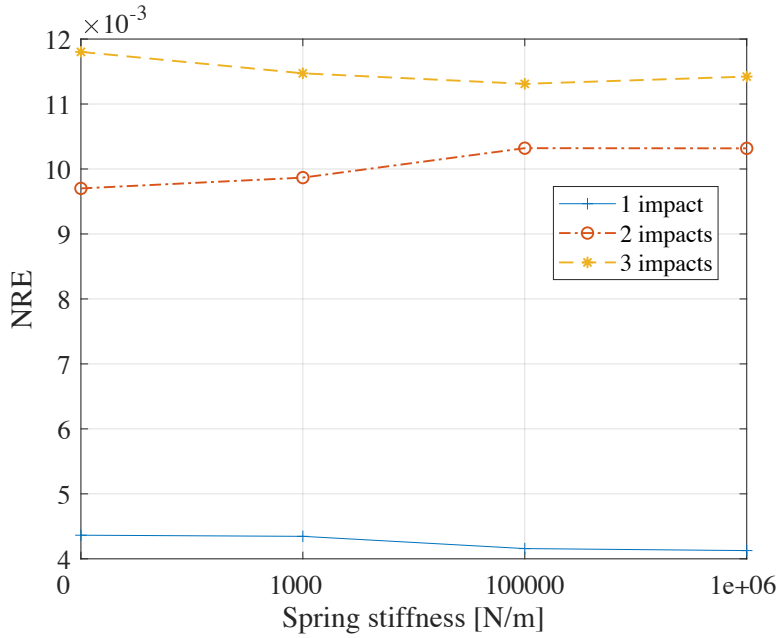

FIGURE 4.17: Effect of spring stiffness on indicator NRE extracted from the received electrical signal.

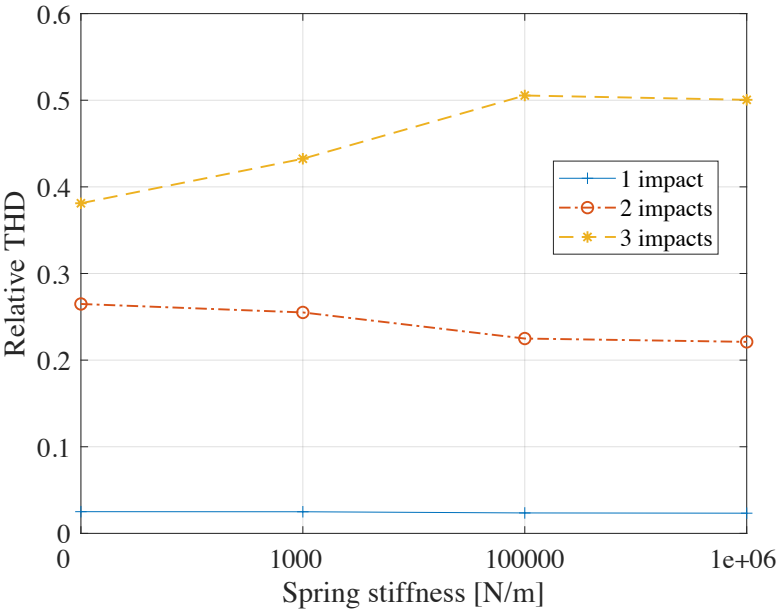

FIGURE 4.18: Effect of spring stiffness on relative THD extracted from the received electrical signal.

in out-of-plane direction between the two delamination interfaces, and k^{spr} indicates the spring stiffness in the linear zone. When u_z is positive, indicating that the contact surfaces are separated and no penetration happens, the spring stiffness is 0, forming a free boundary condition. When u_z is negative, meaning that penetration occurs, a high stiffness is assigned to the springs to keep the penetration as small as possible.

In actual situations, penetration usually does not occur, or only in a very small

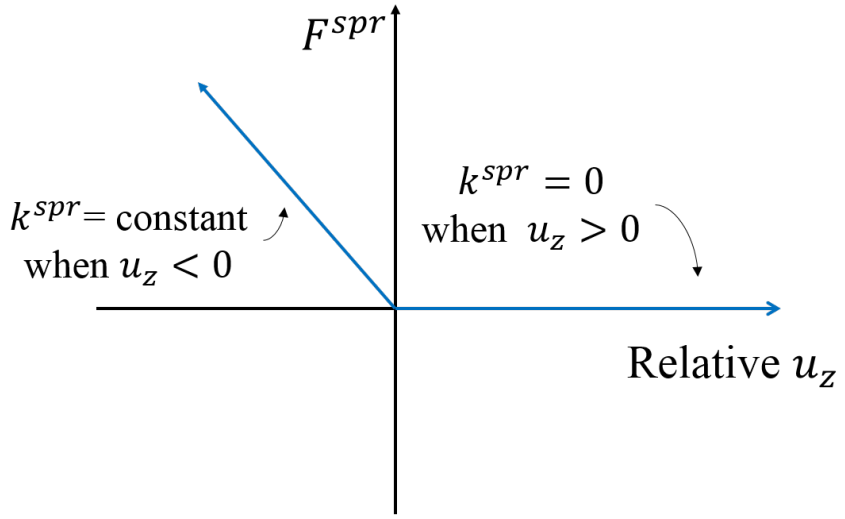

FIGURE 4.19: Force to relative displacement relationship of the non-linear springs at the delamination region.

amount (microscopic). Therefore, the stiffness should be large enough to resist relative movement in the normal direction between the delamination interfaces. However, an excessively large stiffness would cause numerical convergence problems and brings a large computation cost. Therefore, a trade-off must be reached in terms of calculation accuracy and numerical convergence.

To achieve this trade-off, several values of stiffness ranging from 0 to 1×10^7 N/m are tested and the beam model is employed for the test. The values of spring stiffness is chosen based on the following criteria:

- The stiffness value should satisfy the requirements of numerical convergence and stability.
- The stiffness value should be able to induce the "clapping" or contact effect.
- The penetration between delamination interfaces should be at least one order of magnitude less than the maximum value of the normal displacements.
- The overall stiffness for the delamination area should not exceed the stiffness of the specimen. The equivalent contact stiffness at the delamination region can be estimated by

$$K_{contact} = \frac{k^{spr} N}{A_{delam}} \tag{4.13}$$

where $K_{contact}$ is the estimated equivalent contact stiffness, N is the number of nodes at the delamination region, and A_{delam} is the area of the delamination region.

Four different spring stiffness cases (Table 4.6) and three models (Table 4.7) with different sizes of delamination are studied. The length of the delamination and number of nodes in the delamination region are listed Table **??**. The delamination width is the same as the beam width.

The one-impact beam model is first studied. Different spring stiffness values are applied to the delamination region, and the relative displacements between the

TABLE 4.6: Four different spring stiffness k^{spr} cases.

Case 1	Case 2	Case 3	Case 4
$0\,\mathrm{N/m}$	$1\,\mathrm{N/m}$	$1\times10^{5}\,\mathrm{N/m}$	$1\times10^{7}\,\mathrm{N/m}$

TABLE 4.7: Three different damaged beam models.

Beam model	One-impact model	Two-impact model	Three-impact model
Delamination length	7 mm	14 mm	21 mm
Number of nodes	24	48	72

upper and lower surfaces of the delamination are measured at the center point of the delamination.

The output time-domain signals are plotted on the left side of Figure 4.20, and the normalized frequency spectra are plotted on the right side. From the time-domain signals, it can be observed that for the $k^{spr} = 0\,\mathrm{N/m}$ and $k^{spr} = 1\,\mathrm{N/m}$ cases, the positive amplitude and negative amplitude of the signals are almost the same, which is, or is close to, a free boundary condition at the delamination interfaces. For the $k^{spr} = 1\times10^{5}\,\mathrm{N/m}$ case, the negative part of the relative displacements is smaller than the positive part. From this value of stiffness, the nonlinear springs tend to resist the penetration of the contact surfaces. For the $k^{spr} = 1\times10^{7}\,\mathrm{N/m}$ case, the negative amplitude of the relative displacements is much smaller than the positive amplitude, indicating that the delamination interfaces are in contact with very small penetration.

From the frequency spectra, it can be observed that no harmonics are present in the first two rows in Figure 4.20 ($k^{spr} = 0\,\mathrm{N/m}$, $k^{spr} = 1\,\mathrm{N/m}$ and $k^{spr} = 1\times10^{5}\,\mathrm{N/m}$). For the $k^{spr} = 1\times10^{5}\,\mathrm{N/m}$ case, a small peak can be observed at twice of the fundamental frequency (104 kHz), while for the $k^{spr} = 1\times10^{7}\,\mathrm{N/m}$ case, the second and third harmonics can be clearly observed, even the fourth and fifth harmonics can be seen with a small peak. Therefore, it can be concluded that with a spring stiffness around $k^{spr} = 1\times10^{7}\,\mathrm{N/m}$, the delamination has contact interaction with very small penetration.

The displacement results for the two-impact and three-impact beam models are shown in Figures 4.21 and 4.22. Similar to the one-impact beam model, in the other two models, the displacement results also have little difference between the $k^{spr} = 0\,\mathrm{N/m}$ and $k^{spr} = 1\,\mathrm{N/m}$ cases, while for the cases of $k^{spr} = 1\times10^{5}\,\mathrm{N/m}$ and $k^{spr} = 1\times10^{7}\,\mathrm{N/m}$, the relative displacements are almost in the positive zone, and are equal to, or slightly below zero at some points, meaning that the contact surfaces hit each other for a short period of time. This "clapping" effect results in the presence of super-harmonics, which can be clearly observed in the frequency spectra. Therefore, it can be concluded that for the two-impact and three-impact beam models, when $k^{spr} \geqslant 1\times10^{5}\,\mathrm{N/m}$, the delamination surfaces would induce contact interaction effects.

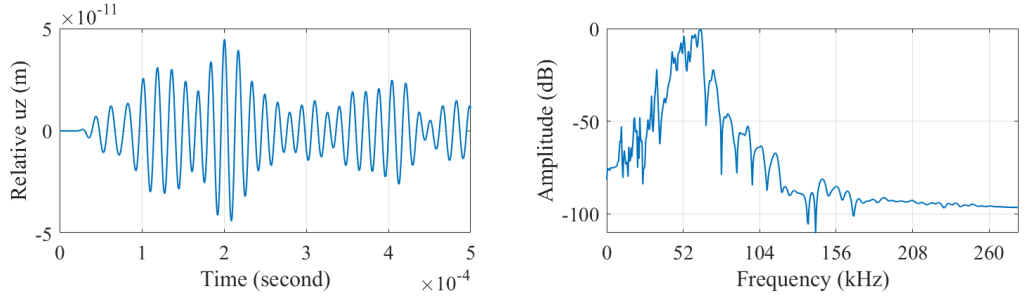

(A) $k^{spr} = 0\,\mathrm{N/m}$

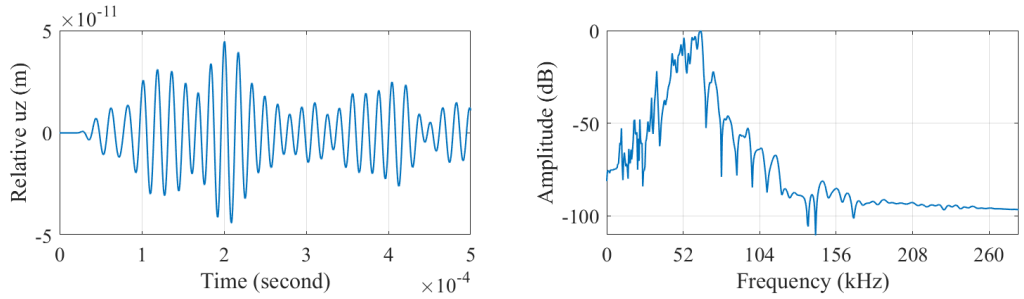

(B) $k^{spr} = 1\,\mathrm{N/m}$

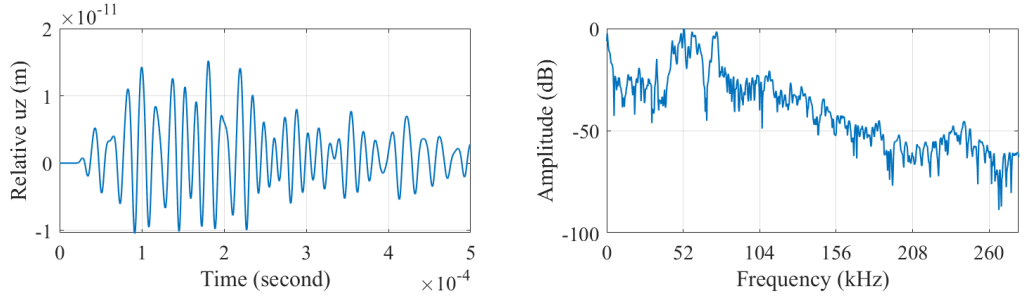

(C) $k^{spr} = 1 \times 10^5\,\mathrm{N/m}$

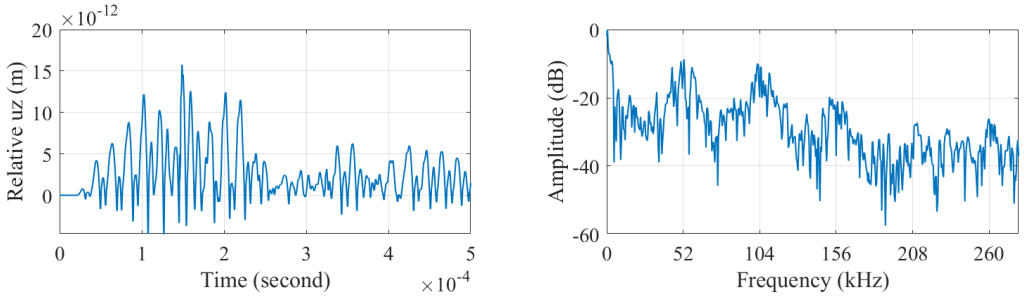

(D) $k^{spr} = 1 \times 10^7\,\mathrm{N/m}$

FIGURE 4.20: Simulation results for the one-impact beam model: relative displacements between the upper and lower surfaces of the delamination. The measurement point is located at the center of the delamination. Left: temporal signals; right: FFT of the relative displacement normalized to the maximum value of each signal in log scale.

Two indicators are extracted from the relative normal displacements to evaluate the contact phenomenon and the nonlinear effects at the delamination region. First, a time-domain indicator is defined as the ratio between the signal peak (highest amplitude value) and the trough (lowest amplitude value, which can be negative):

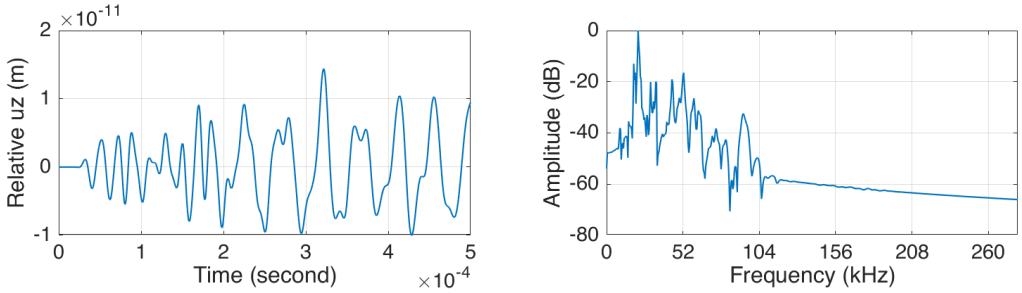

(A) $k^{spr} = 0\,\mathrm{N/m}$

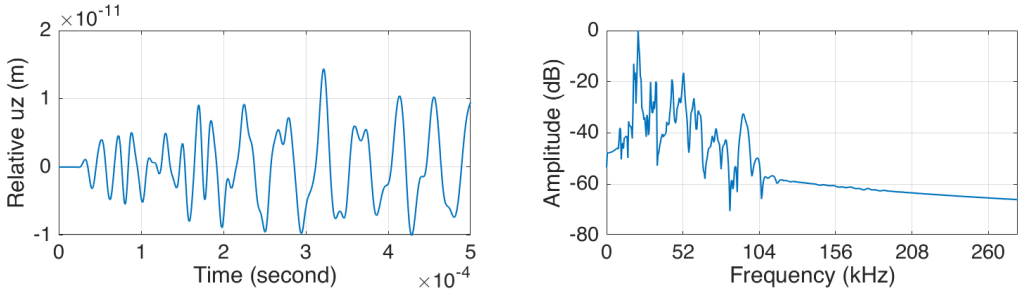

(B) $k^{spr} = 1\,\mathrm{N/m}$

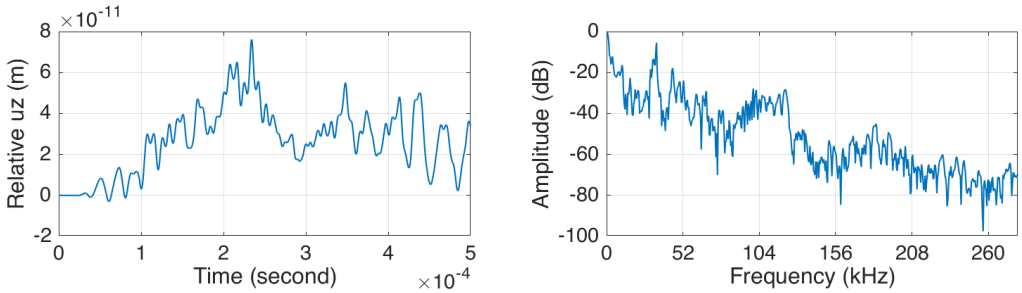

(C) $k^{spr} = 1 \times 10^5\,\mathrm{N/m}$

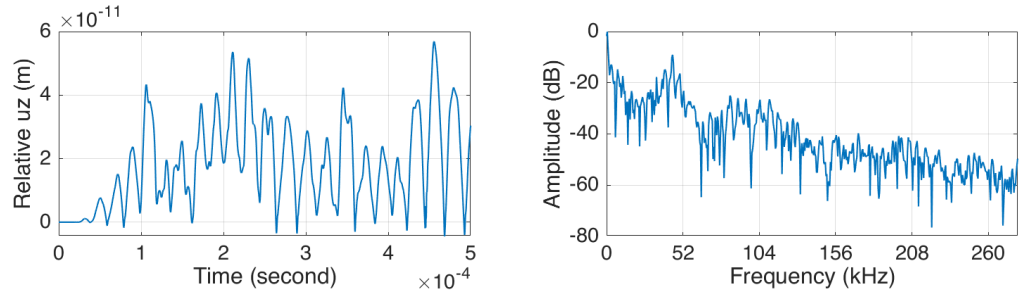

(D) $k^{spr} = 1 \times 10^7\,\mathrm{N/m}$

FIGURE 4.21: Simulation results for the two-impact beam model: relative displacements between the upper and lower surfaces of the delamination. The measurement point is located at the center of the delamination. Left: temporal signals; right: FFT of the relative displacement normalized to the maximum value of each signal in log scale.

$$SPTR = \left| \frac{max(x)}{min(x)} \right| \tag{4.14}$$

where $SPTR$ is the signal peak to trough ratio and x is the displacement time signal. This indicator evaluates the contact effects at delamination by comparing the

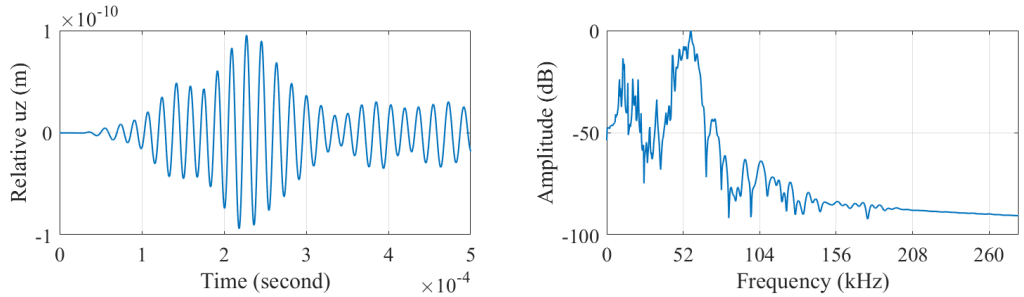

(A) $k^{spr} = 0\,\mathrm{N/m}$

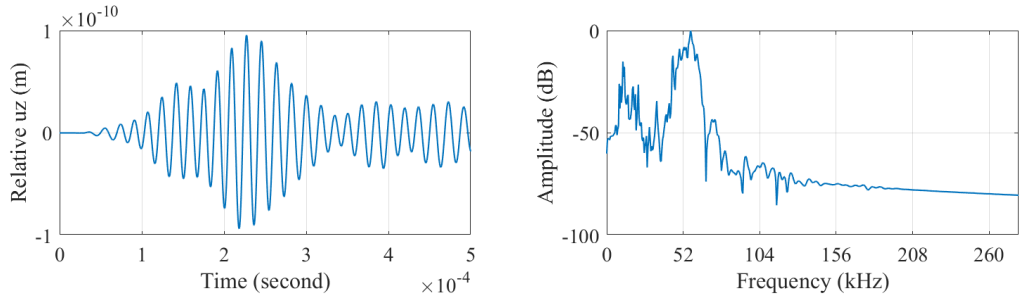

(B) $k^{spr} = 1\,\mathrm{N/m}$

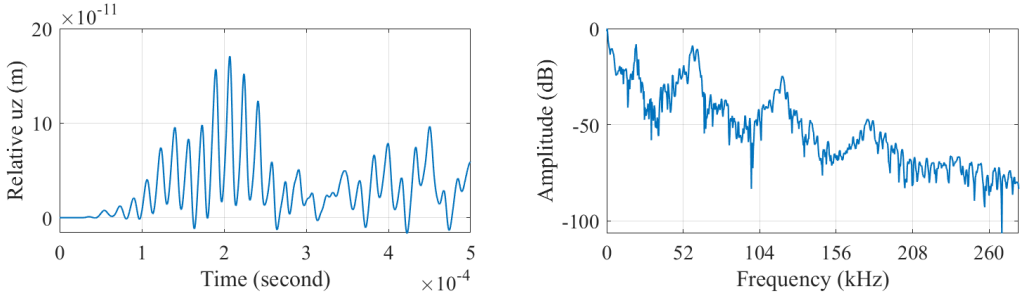

(C) $k^{spr} = 1 \times 10^5\,\mathrm{N/m}$

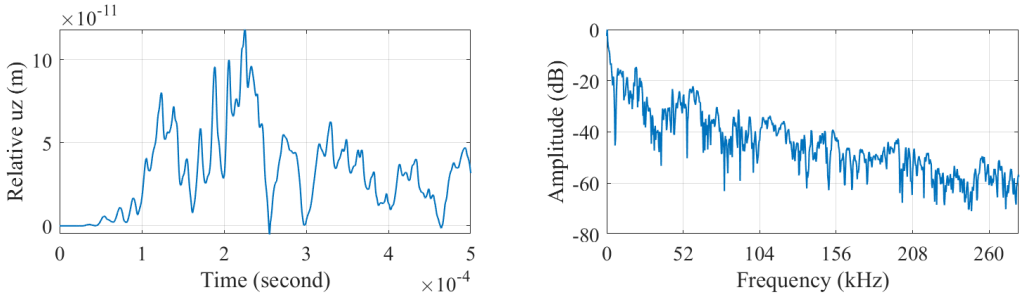

(D) $k^{spr} = 1 \times 10^7\,\mathrm{N/m}$

FIGURE 4.22: Simulation results for the three-impact beam model: relative displacements between the upper and lower surfaces of the delamination. The measurement point is located at the center of the delamination. Left: temporal signals; right: FFT of the relative displacement normalized to the maximum value of each signal in log scale.

maximum value of the signal (signal peak, positive) with the minimum value (signal trough, usually negative in this situation). When this ratio gets larger, the positive components of the relative displacement are larger than the negative components. If the ratio is large enough and the negative trough is close to 0, the delamination interfaces can be seen as in "contact".

Figure 4.23 shows the signal peak to trough ratios for all different spring stiffness values against the number of impacts of the beam model. It can be seen that for the low spring stiffness (0 N/m and 1 N/m), the signal peak to trough ratio is around 1, showing that the amplitudes of the displacement signal above and below 0 are close. This indicates that the delamination interfaces can move towards and opposite to each other freely, forming a nearly free boundary condition. However, when the spring stiffness increased to 1×10^5 N/m, the signal peak to trough ratio also increases sharply, especially for the two-impact and three-impact beam cases. For the one-impact beam model, the signal peak to trough ratios are all under 5 for all four spring stiffness cases. This might be due to the fact that the delamination size of one impact is not large enough to induce more obvious contact phenomenon.

Figure 4.24 shows the total harmonic distortion (THD) of the relative normal displacements. Similar to the signal peak to trough ratio, the THD values of relative normal displacements of low spring stiffness cases are much smaller than the values of high spring stiffness cases. Generally, the structure will induce more obvious nonlinear effects when the spring stiffness is relatively high enough. For the one-impact and three-impact beam model, the THD values also show monotonous growth with the increase of the spring stiffness, and for the two-impact beam model, the THD value from $k^{spr} = 1 \times 10^5$ N/m case is larger than the value from 1×10^7 N/m case.

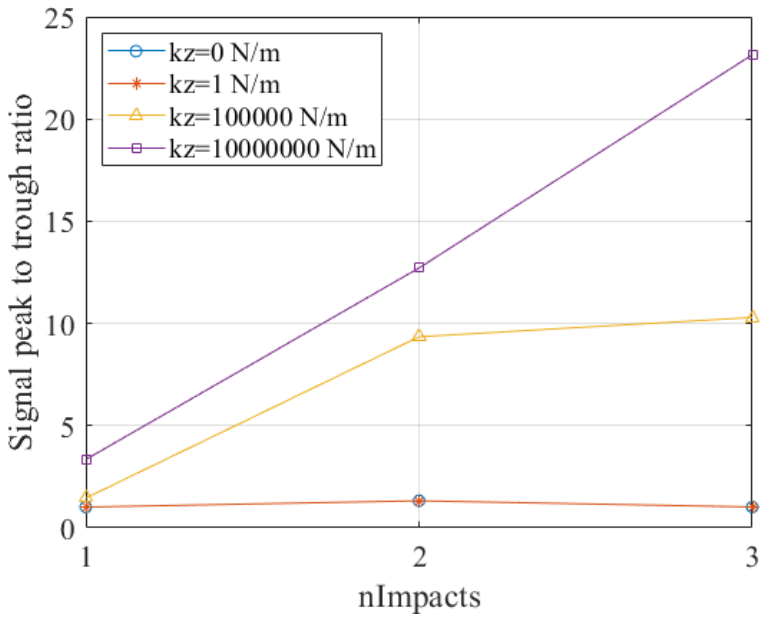

FIGURE 4.23: The signal maximum to minimum value ratio of all three impacts with different spring stiffness.

The electrical raw outputs for all three beam models are shown in Figure 4.25, where the time-domain signals are shown on the left side, and the frequency spectra are shown on the right side. It can be seen that for the same model, the difference between the time domain signals is very small, almost invisible. All the time-domain signals from the three models are convergent. From the frequency spectra of the

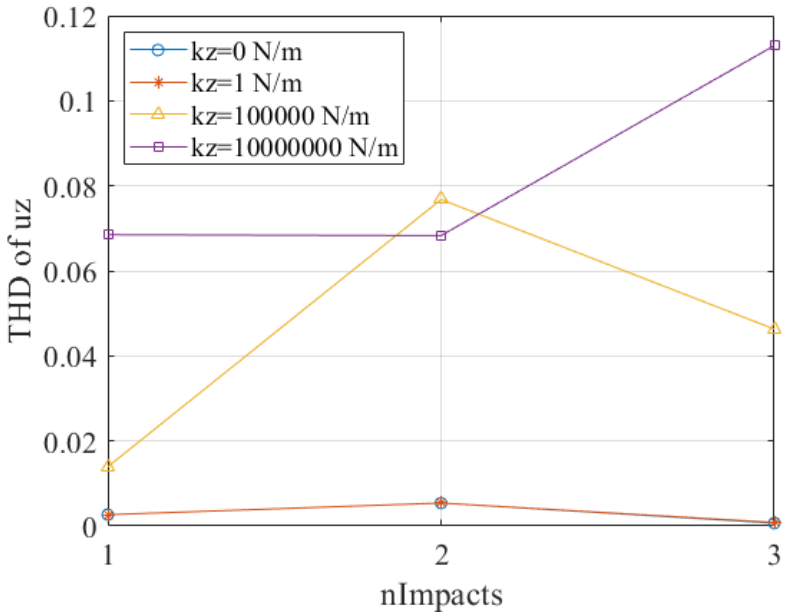

FIGURE 4.24: The THD of relative normal displacement of all three impacts with different spring stiffness.

one-impact beam model, it can be seen that the curves are very close to each other, and the difference is not as great as in the displacement graphs. Although in the local area, the displacement varies greatly under different spring stiffness conditions, the influence on the output signal is limited. This might be due to the fact that the delamination size of one impact is not large enough to excite the nonlinear effect in the whole structure. However, in the graphs of the two-impact and three-impact beam models, the frequency spectra are obviously different from other curves.

The amplitudes of super-harmonics from the $k^{spr} = 1 \times 10^7\,\mathrm{N/m}$ case is obviously higher than other cases, indicating that the value $k^{spr} = 1 \times 10^7\,\mathrm{N/m}$ might be an appropriate value for the contact interaction simulation between delamination interfaces. Thus, the equivalent contact stiffness for the three-impact beam model can be estimated by Equation 4.13 using data from Table 4.7 as:

$$K_{contact} = \frac{k^{spr} N}{A_{delam}} = \frac{1 \times 10^7\,\mathrm{N/m} \times 72}{21\,\mathrm{mm} \times 2\,\mathrm{mm}} = 1.714 \times 10^{13}\,\mathrm{N/m^3} \tag{4.15}$$

Physically, the contact stiffness should be close to the Young's modulus in thickness direction divided by half of the beam thickness. In this case, this value can be calculated by $\frac{E_{33}}{h/2} = \frac{9\,\mathrm{GPa}}{1.12\,\mathrm{mm}} = 8.0357 \times 10^{12}\,\mathrm{N/m^3}$. Although the contact stiffness is not in the same order of magnitude with this value, but it's close to it. Thus, this contact stiffness is reasonable for the calculations.

(b) In-plane interaction

In the in-plane direction, friction is the dominating interaction of the delamination interfaces. Thus, friction is defined on the interfaces of the delamination. In order to achieve this, a modified viscous friction model is implemented to simulate the in-plane

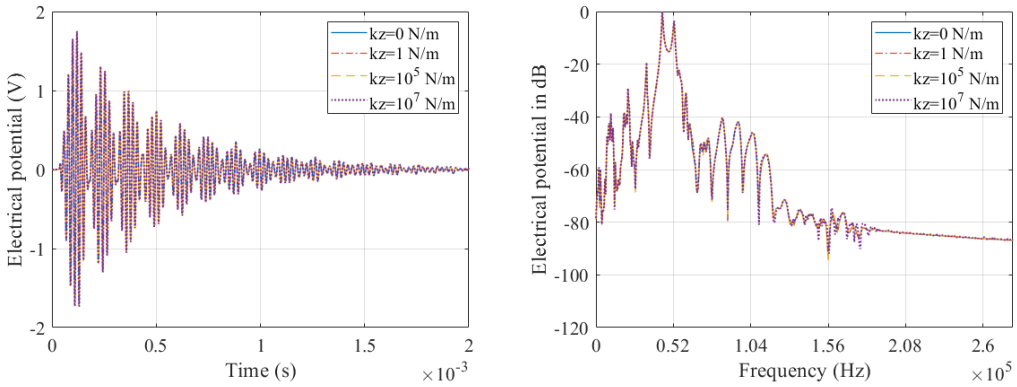

(A) One-impact beam model.

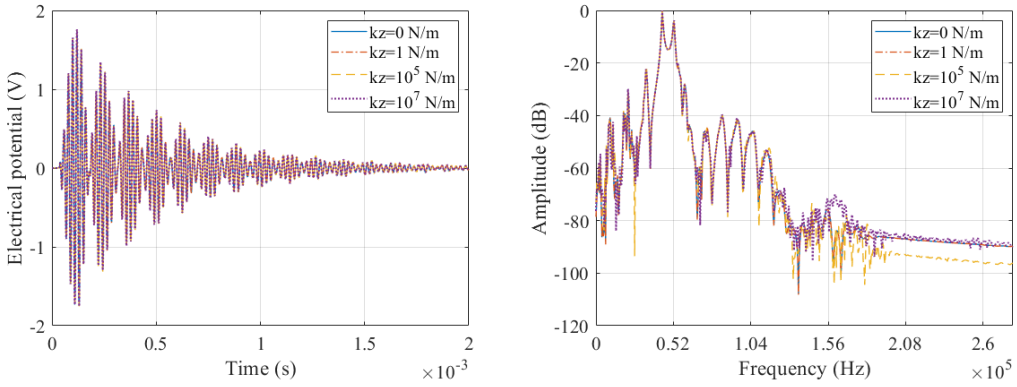

(B) Two-impact beam model.

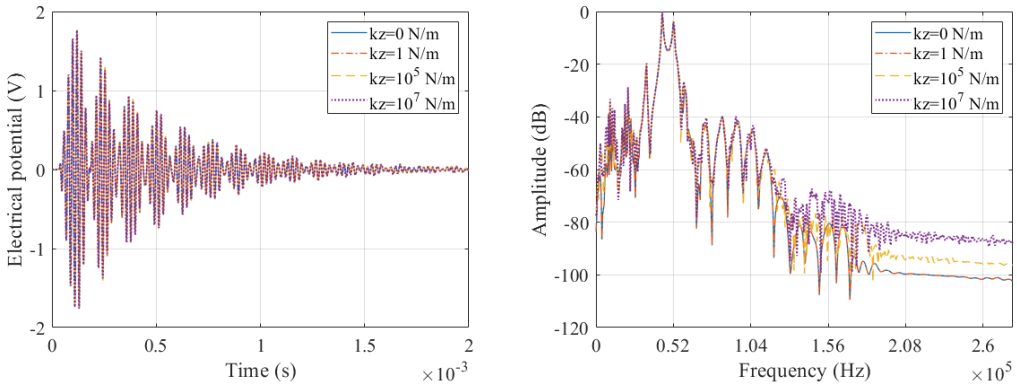

(C) Three-impact beam model.

FIGURE 4.25: Electrical raw outputs for the beam models with different spring stiffness. Left: time domain signals; right: frequency spectra.

mechanical behavior of the delamination.

Figure A.15 shows a schematic of the in-plane model illustrating the nonlinear relationship between interaction force and relative velocity. The force-velocity relationship within $(-v_f, v_f)$ range is linear, while the force keeps constant in other parts. In this model defined by four points, v_f and F_0 are parameters defining this nonlinear

model. They are derived in this way: first, a plate model without any in-plane or out-of-plane interaction in the delamination region is employed and the response of this model is calculated. Then the velocity of the center node of the delamination along the wave propagation direction is derived, and the maximum value of the velocity response is extracted. This maximum value is a reference for setting the v_f value. Since we hope that the velocity response of the nodes at the delamination region covers both the linear and nonlinear zone in the in-plane mechanical model, the applied v_f can not be either too large or too small. If this v_f parameter is too large, the (v_x, F_x) pairs might be all in the plateau zone and only few points locate in the linear zone. If this v_f parameter is too small, the (v_x, F_x) pairs will be all within the linear zone, and we cannot get a nonlinear force-to-velocity relationship. Therefore, this v_f parameter should be a bit smaller than the maximum in-plane velocity extracted in the previous step.

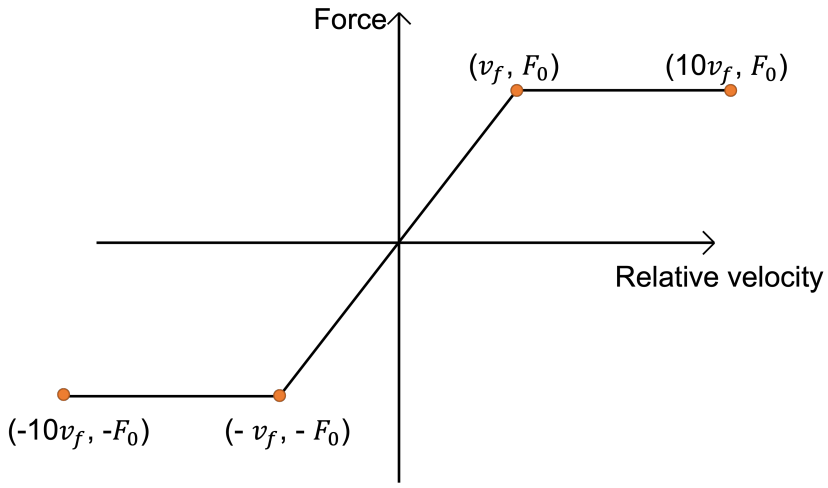

FIGURE 4.26: Schematic of nonlinear in-plane interaction model

Similar to the out-of-plane study, the beam model is employed for the investigation of in-plane model parameters v_f and F_0. All the investigations below are conducted on the three-impact beam model with the delamination length of 21 mm.

Figure 4.27 shows the velocity in all three directions of the center node of the delamination from the beam model without any in-plane or out-of-plane interaction in the delamination region. It can be observed from the figure that the maximum velocity in the x-direction is about 1.8×10^{-6} m/s and in the y-direction, the value is 0. Therefore, the initial trial value of the v_f parameter is set to be 1×10^{-6} m/s.

In order to find the best model parameters, several trial values of F_0 and v_f are explored. First, we fix the v_f value at 1×10^{-6} m/s and change the F_0 value from 1×10^{-7} N to 1×10^{-4} N to investigate the sensitivity of the F_0 value to the structure response. The raw electrical responses in time domain received by PZT sensor are compared, as shown in Figure 4.28. In this figure, it can be observed that for different F_0 values, there is a dramatic difference between the corresponding time-domain responses. When the F_0 is equal to 1×10^{-6} N and 1×10^{-7} N, the

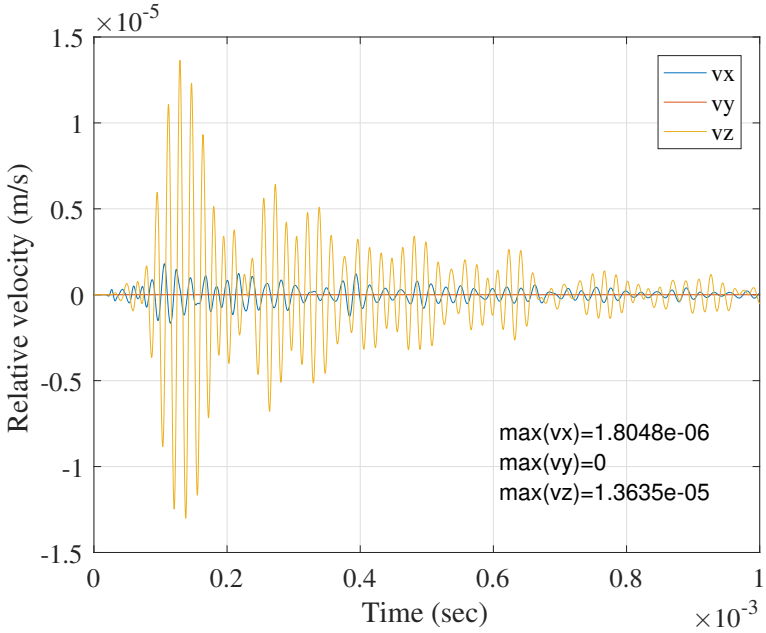

FIGURE 4.27: Relative velocity of the center node of the delamination. The corresponding model is the three-impact beam, and no out-of-plane or in-plane interaction exists in the delamination region.

time responses are close to each other. However, when F_0 is equal to 1×10^{-5} N, the response signal is much different. The magnitude of this signal after 1.5 ms is larger than that of the above-mentioned two signals. When F_0 is increased to 1×10^{-4} N, the time response signal even does not decay as the other three signals and the result is considered to be divergent.

Next, the parameter F_0 is fixed and the sensitivity of the v_f value is studied. Results are shown in Figure 4.29. The F_0 value is fixed at $F_0 = 1 \times 10^{-6}$ N and the v_f varies from 1×10^{-13} m/s to 1×10^{-4} m/s. In this figure, it can be observed that the difference among all the raw responses is visually rather small.

In order to investigate the sensitivity of both F_0 and v_f values to the time domain response, similar analyses are performed with different F_0 and v_f values ranging from 1×10^{-10} m/s to 1×10^{-2} m/s, and the time responses are derived. For ease of explanation, all responses in the time domain are divided into three groups. The time response with the similar shape of the $F_0 = 1 \times 10^{-4}$ case from Figure 4.28 is noted as "divergent", the shape similar to the time response of the $F_0 = 1 \times 10^{-5}$ N case is noted as "to be determined" (TBD), and the signal shape similar to the other two responses from the same figure is noted as "convergent". Thus, the sensitivity of the v_f and F_0 parameters to the convergence of the raw responses in the time domain can be summarized and plotted in Figure 4.30. In this figure, the x-axis indicates the inverse of v_f values, and the y-axis indicates the F_0 values. Note that both axes are in log scale. Each point in this figure indicates one specific case with a certain v_f and F_0 pair. The blue circle indicates that the raw response in the time domain from the corresponding case is convergent, while the red asterisk (*) indicates that

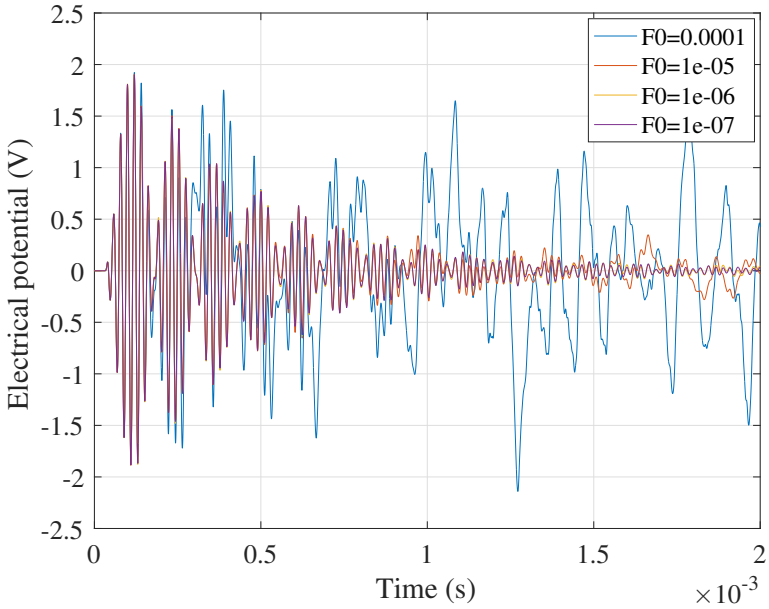

FIGURE 4.28: Time domain responses from the three-impact beam models with fixed v_f (1×10^{-6} m/s).

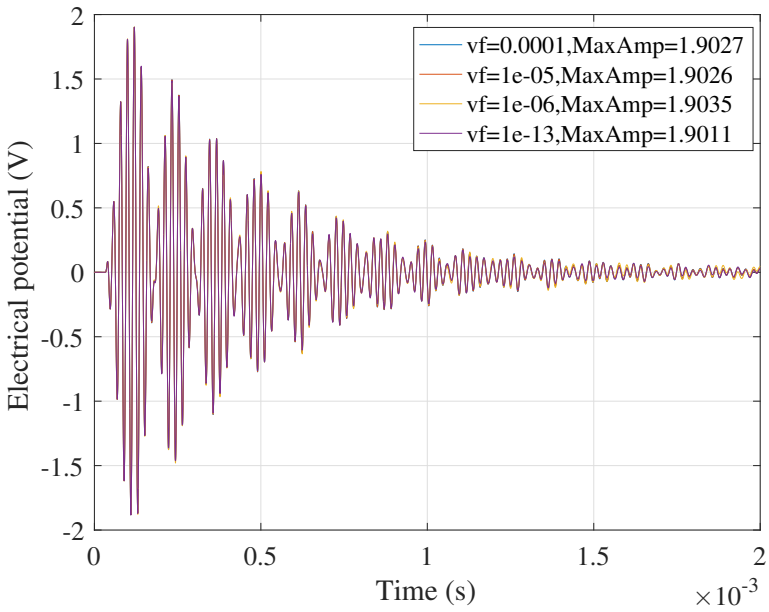

FIGURE 4.29: Time domain responses from in-plane models with fixed F_0 (1×10^{-6} N).

the raw response from the corresponding case is divergent, and the yellow (+) sign indicates the "TBD" case. For example, when v_f is equal to 1×10^{-6} m/s and F_0 is equal to 1×10^{-7} N, the corresponding sign is a blue circle, meaning that the raw response in time domain is convergent, which is proved in Figure 4.28. To sum up, when F_0 is no larger than 1×10^{-6} N, all the raw responses in the time domain are convergent regardless of the v_f value. However, when F_0 is larger than 1×10^{-6} N, the

convergence of the raw responses in the time domain depends on the v_f parameter.

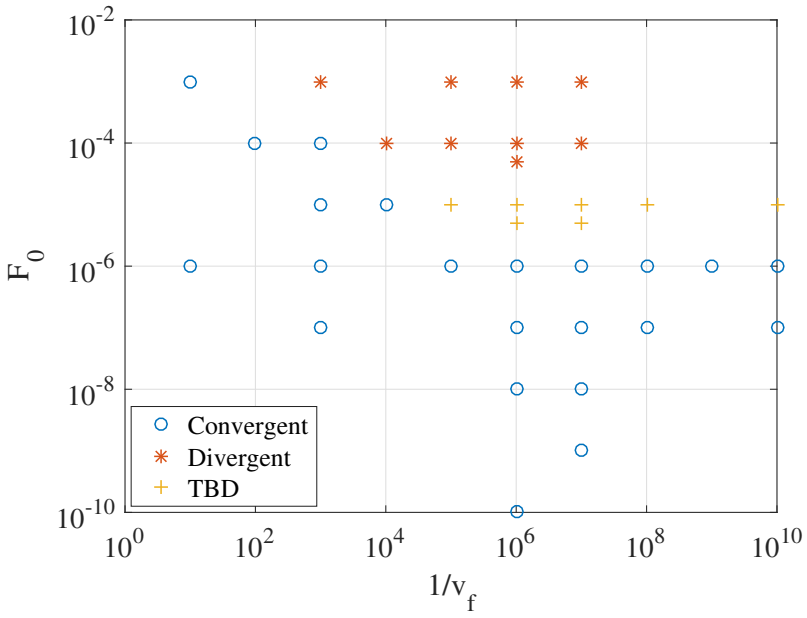

FIGURE 4.30: The convergence of the raw responses in time domain from the three-impact beam models with different v_f and F_0 parameters in the in-plane interaction model.

4.2.3.3 Contact/friction model

In most studies on contact acoustic nonlinearity (CAN), friction is neglected, especially in finite element simulations. However, in reality, the contact surfaces of the delamination region are usually rough surfaces. When the delamination is interacting with Lamb waves, the S_0 mode waves can cause relative in-plane motion of delamination interfaces, thus the friction should be considered in simulations. In the previously stated model, the normal and tangential interactions are calculated separately and do not affect each other. However, in the process of wave/damage interaction, the distribution of stress on the contact surfaces is not uniform, so that the normal contact pressure in some parts is larger, and in some parts very small [**Li**]. As we know, the normal pressure will affect the friction force, thus leading to a particular situation where weakly compressed areas in the contact region and areas not in contact slip, while strongly compressed areas might stick. Therefore, a contact/friction combined model is proposed in this section to better simulate the mechanical behavior of the delamination interfaces.

In this model, the nonlinear springs are still used in out-of-plane direction to formulate the normal contact interaction between delamination interfaces: when the interfaces are separated in the normal direction, the spring force is zero, and when the interfaces are penetrated, the spring will present a high stiffness to resist this penetration. This can be expressed as

$$F_N = \begin{cases} k_z u_z, & u_z < 0 \\ 0, & u_z > 0 \end{cases} \tag{4.16}$$

where k_z is the spring stiffness in the normal direction.

In the tangential (in-plane) direction, the Coulomb friction model is employed. According to the friction law, when the relative sliding happens between the two contact surfaces, the friction force is proportional to the normal force exerted by each surface on the other. When there is no relative displacement between two contacting surfaces, the friction force is actually uncertain [67]. For the simplification of the calculation, the following model is employed representing the in-plane interaction:

$$F_T = \begin{cases} -\mu F_N, & F_N > 0 \ \& \ b \neq 0 \\ 0, & \text{others} \end{cases} \tag{4.17}$$

where F_T is the tangential force, F_N is the normal force exerted by each surface on the other directing perpendicular (normal) to the surface, μ is the coefficient of friction, and b is the relative sliding. When there is relative sliding ($b \neq 0$) and compression ($F_N > 0$) between the contact surfaces, friction force exists and is equal to the product of the coefficient of friction and the normal force, in a direction opposite to the relative sliding.

Figure 4.31 shows a schematic of the in-plane interaction model of the delamination area. In this figure, line 123 represents the midplane of the bottom layer, and line 456 represents the midplane of the top layer. Node pairs (1,6), (2,5) and (3,4) are connected to each other through spring elements. It can be observed in this figure that nodes 2 and 5 are penetrated through each other, and node pairs (1,6) and (3,4) are separated. The springs connecting node pairs (1,6) and (3,4) show zero stiffness, indicating that there is no interaction force between the corresponding nodes, while the spring connecting the node pair (2,5) generates a large force F^{spr} to resist this penetration trend. In the tangential direction, friction is the dominating interaction, and the friction force is opposite to v_x, which is the moving direction of the node.

The sensitivity of the friction coefficient μ is investigated in this section. The three-impact beam is taken as an example. The simulated time length is 0.003 s, the spring stiffness is fixed at $k^{spr} = 1 \times 10^6$ N/m, and the coefficient of friction ranges from 0.1 to 0.5. Figure 4.32 shows the electrical raw outputs from three cases with different coefficients of friction. It can be observed from this figure that the electrical output from the $\mu = 0.5$ case doesn't converge after 0.002 s, and the other two cases have good numerical convergence. Therefore the friction coefficient must be kept below 0.5 to ensure the numerical stability of the simulation results.

To further understand the mechanical behavior of the delamination, displacements of the center point of the delamination in both in-plane and out-of-plane directions are extracted from the three-impact model with different friction coefficients. Figure 4.33 presents the in-plane displacements from cases with different friction coefficients in both time and frequency domains. Each frequency spectrum is normalized to the

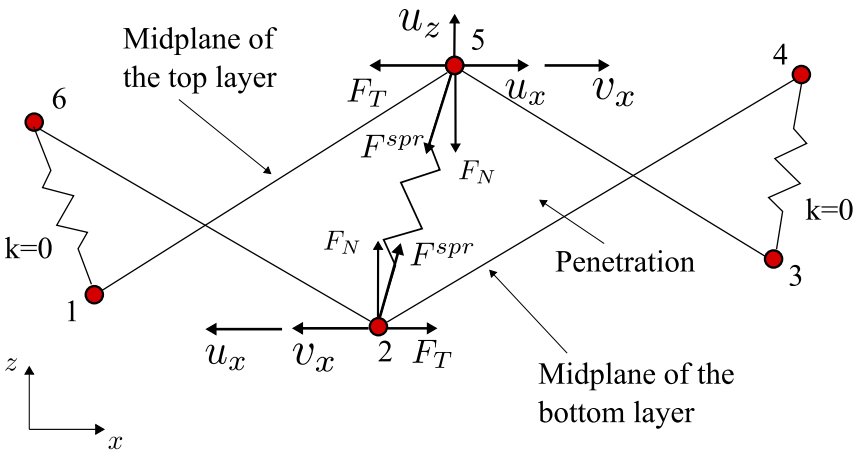

FIGURE 4.31: Schematic of the interaction model at delamination area with penetration through nodes 2 and 5. F_T and F_N are the tangential and normal forces, and u_x and v_x are the displacement and velocity in x-direction respectively.

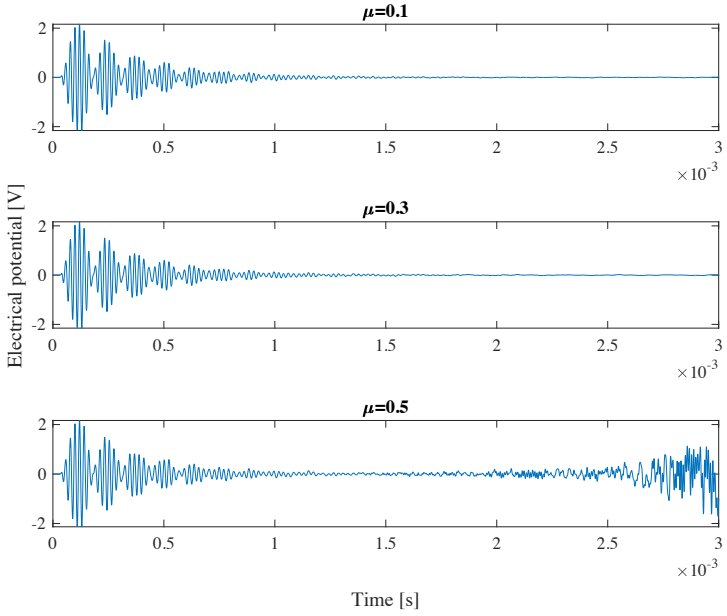

FIGURE 4.32: Electrical outputs from the three-impact beam models with different friction coefficients.

maximum value of each signal. It can be observed that the displacement curve from all three cases show zigzags in both time and frequency domains. As the friction coefficient increases, the amplitude of the relative u_x and the oscillation also increase in time domain signals, along with growing zigzags and noise in the frequency spectra.

Figure 4.34 shows the out-of-plane displacements from the three cases. Similar to the in-plane displacement response, the out-of-plane displacement from the $\mu = 0.1$ case shows smooth response and frequency spectrum, while responses from the other two cases are not so smooth. For all three cases, the positive amplitude is much higher than the negative amplitude. This indicates that the delamination surfaces

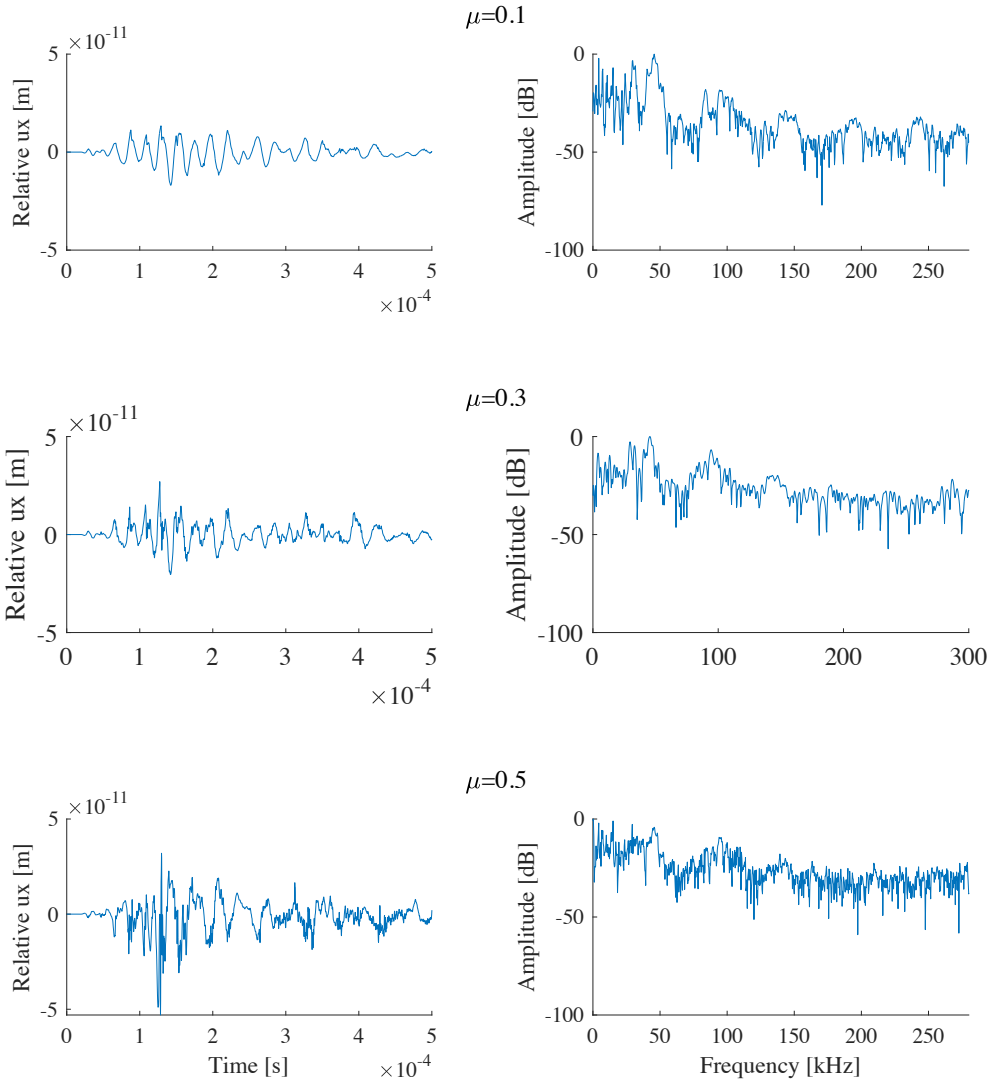

FIGURE 4.33: Responses of in-plane displacements in time and frequency domain from different beam models. The amplitudes in frequency domain are normalized to the maximum value of each signal.

are in contact with each other. When the friction coefficient is increased to 0.5, a large amplitude that is almost one order of magnitude higher than amplitude in the other two cases is observed in the time domain, which might be the cause of the numerical convergence problem in the electrical output. The frequency spectrum presents obvious higher order harmonics in the $\mu = 0.1$ and $\mu = 0.3$ cases, which can also indicate that contact interaction exists.

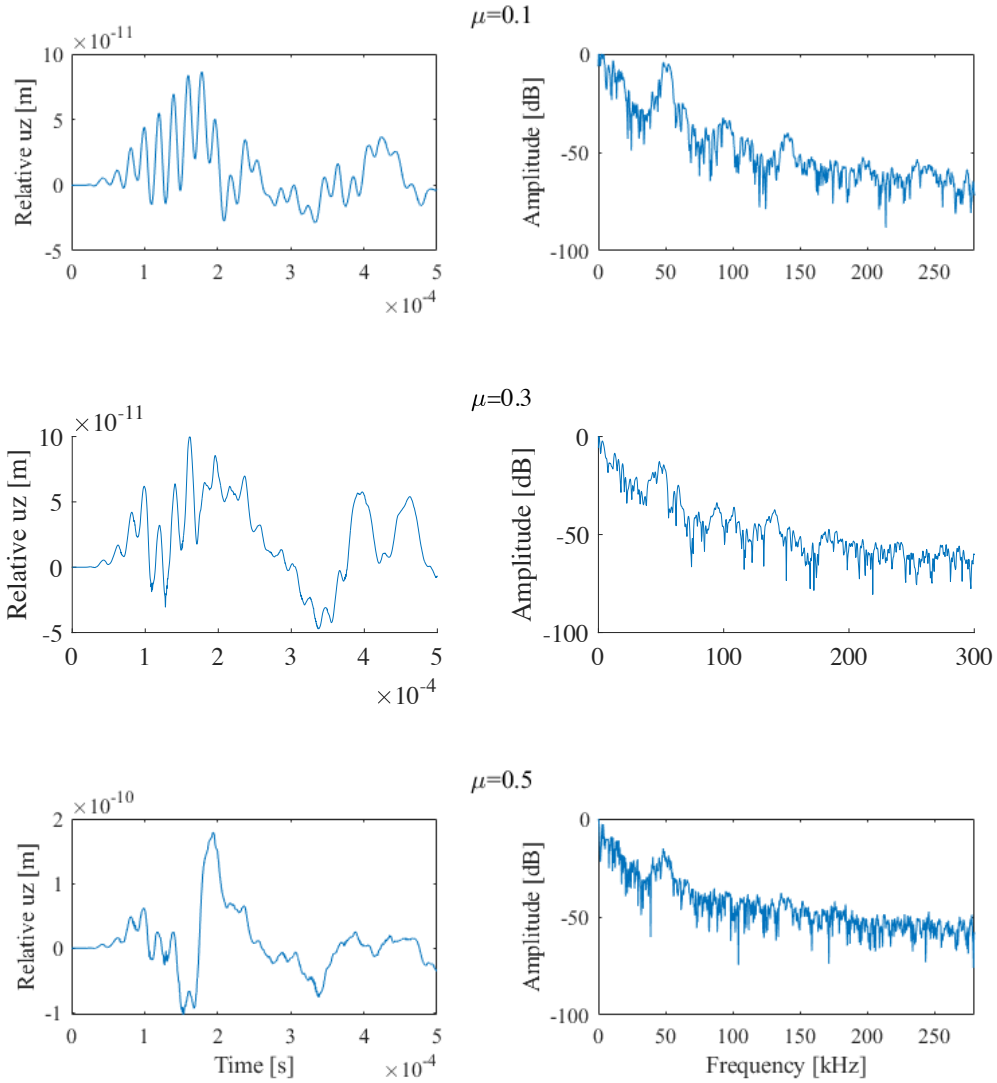

FIGURE 4.34: Responses of out-of-plane displacements in time and frequency domain from different beam models. The amplitudes in frequency domain are normalized to the maximum value of each signal.

4.3 Simulation results and discussion

4.3.1 Time domain signals

A comparison of the time-domain signals from the simulations with different damage models is presented in Figure 4.35 . These signals are received by the PZT sensor using the pitch-catch method. It can be noted that the peaks located around 0.3 µs in signals from spring models are not presented in the signal from the stiffness reduction model. This indicates that the wave packet located at 0.3 µs might be due to the separation of delamination interfaces in the simulation model.

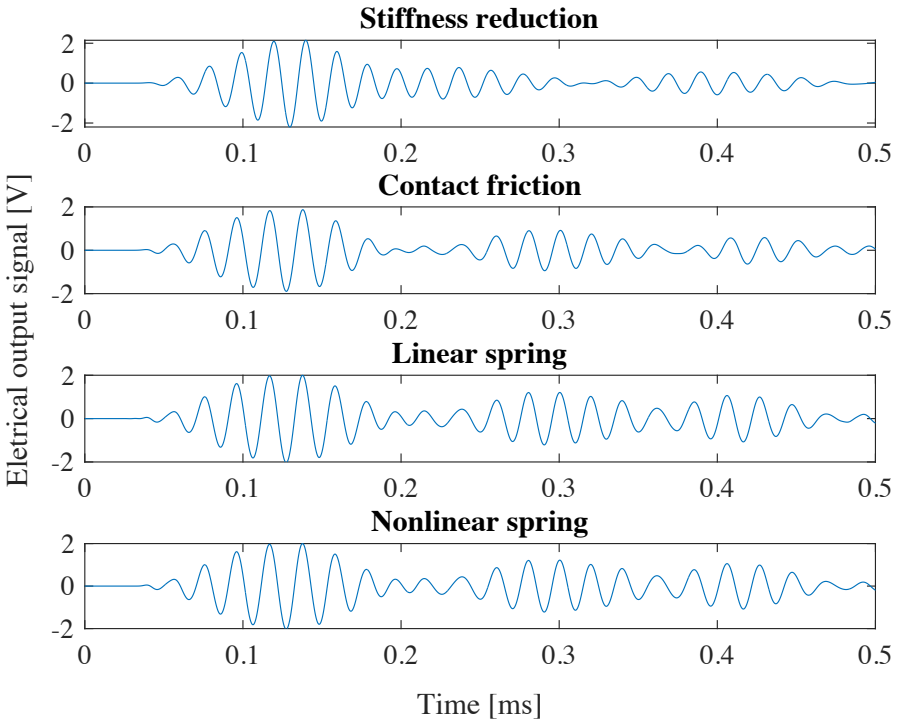

FIGURE 4.35: Time domain signals of different damage models.

4.3.2 Parametric study

This section describes the influence of model parameters on the simulation results.

4.3.2.1 Stiffness reduction model

Various reduction coefficients are tested in this section. The simulation is carried out on the three-impact full plate model, as shown in Section 4.1. The time domain responses are shown in Figure 4.36.

Figures 4.37 and 4.38 show the CRC and NRE values extracted from the electrical outputs of the three-impact plate with different reduction coefficients. The last case, where the reduction coefficient is equal to 1, indicates the undamaged plate. The first case, where the reduction coefficient is equal to 0.1, simulates the 0 stiffness condition. The CRC plot shows a monotonic decrease with the increase of the reduction coefficient. The curve drops sharply from about 0.37 to about 0.036 with the reduction coefficient increasing from 0.1 to 0.5, showing a reduction of about 90%. Then the curve falls slowly to 0 with the reduction coefficient increasing to 1. The NRE plot presents a similar trend to the CRC plot. This indicates that a small stiffness reduction coefficient leads to a larger linear damage indicator value.

4.3.2.2 Nonlinear spring model

In this subsection, the normal spring stiffness and the in-plane parameters are tested on the three-impact full plate model respectively.

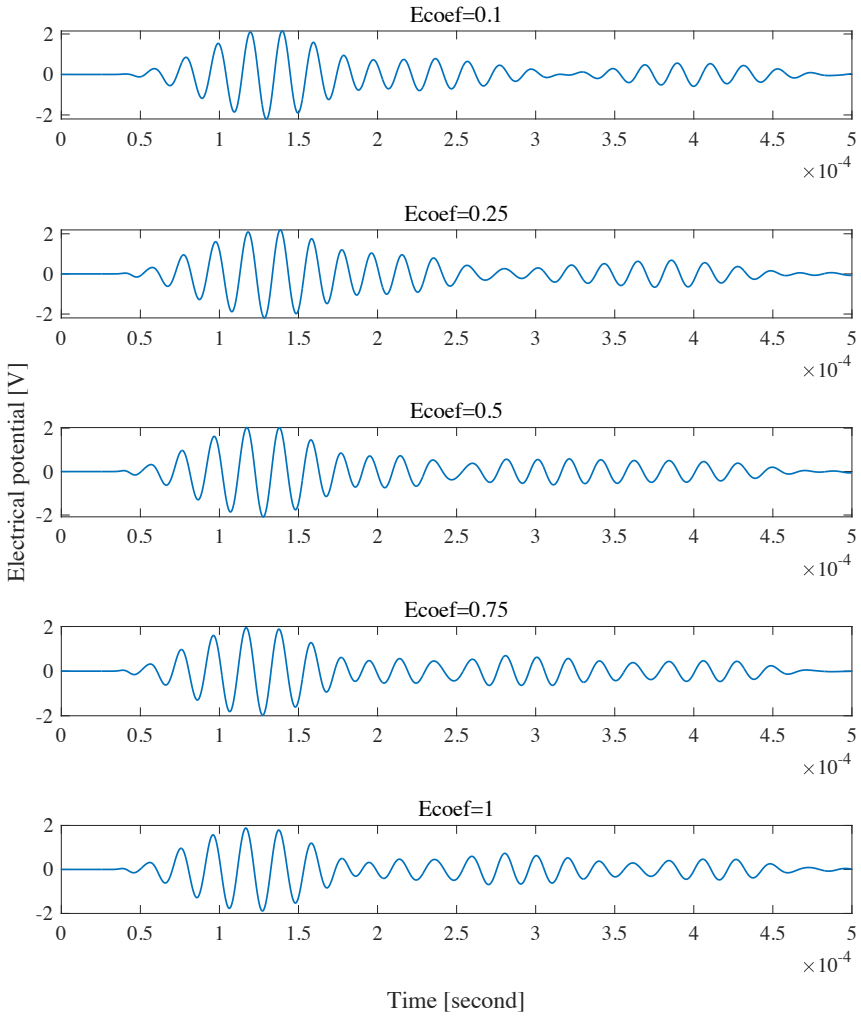

FIGURE 4.36: Time domain signals from stiffness reduction model with different reduction coefficients.

(A) Out-of-plane investigation

The spring stiffness of the linear zone should be large enough to avoid penetration between the delamination interfaces, but can not be too large to cause numerical problems, such as convergence problem. Therefore, the values of the spring stiffness in the linear zone are tested in this part.

Figure 4.39 shows the relative THD of electrical outputs from plate models with various spring stiffness with respect to the undamaged plate. It can be observed that for the one-impact plate, the relative THD values keep steady at about 0.04, while for the two-impact plate models, the relative THD values have slight changes, and the relative THD changes drastically for the three-impact plate. For the two-impact plate, the relative THD first increases slightly and peaks around $k^{spr} = 1 \times 10^5\,\mathrm{N/m}$, and then decreases as the k^{spr} increases to $1 \times 10^6\,\mathrm{N/m}$. For the three-impact plate, the relative THD value first increases sharply and reaches a peak at about 0.156 with $k^{spr} = 1 \times 10^5\,\mathrm{N/m}$, followed by a steep fall to below 0.08 with $k^{spr} = 1 \times 10^6\,\mathrm{N/m}$.

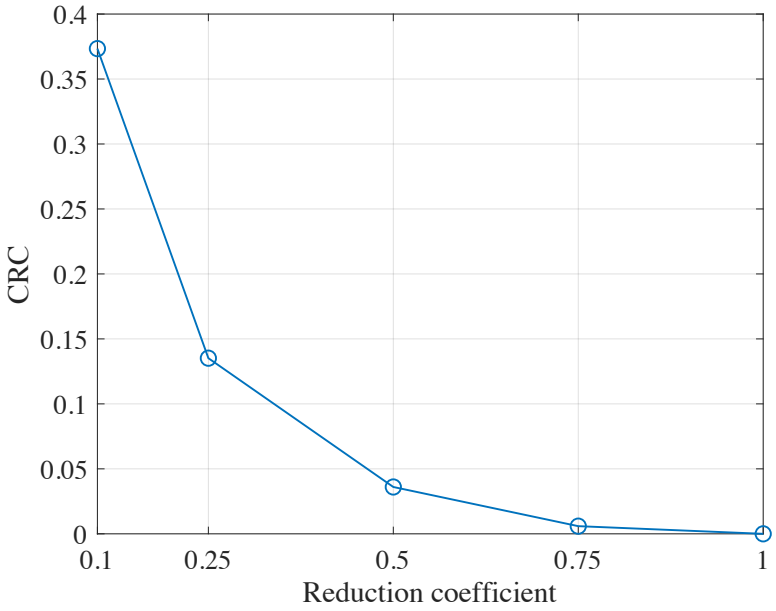

FIGURE 4.37: Effect of reduction coefficient on indicator CRC based on correlation coefficient of the received electrical signal.

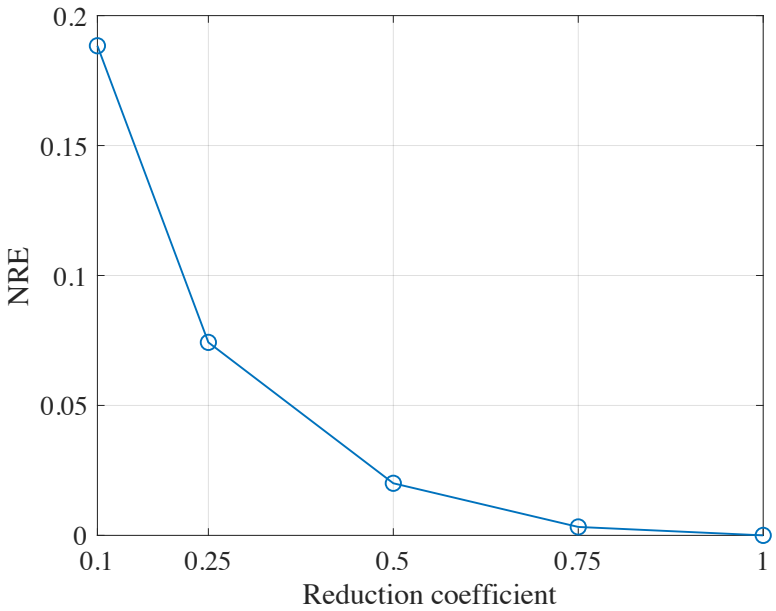

FIGURE 4.38: Effect of reduction coefficient on indicator NRE based on normalized residual energy of the received electrical signal.

Results indicate that for a low spring stiffness, the relative THD does not change much. It can also be concluded that for the one-impact plate, the spring stiffness has limited influence on the relative THD value, i.e., the nonlinear effects are relatively insensitive to the spring stiffness. Then for the other two plates, the relative THD value located around $k^{spr} = 1 \times 10^5\,\mathrm{N/m}$ is larger than other zone, indicating that the nonlinear effects might be larger with spring stiffness in this range.

TABLE 4.8: Characteristics in delamination region of damaged plate models with different damage severity.

Model	One-impact model	Two-impact model	Three-impact model
Delamination diameter	7 mm	14 mm	21 mm
Number of nodes	100	367	800
Spring stiffness	8.9×10^4 N/m	9.7×10^4 N/m	1.0×10^5 N/m

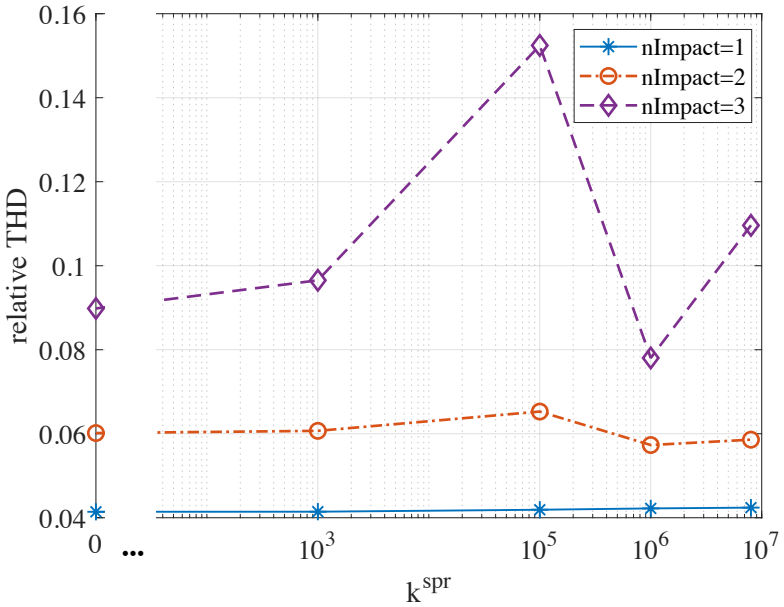

FIGURE 4.39: Effect of different spring stiffness on relative THD of the received electrical signal with respect to the undamaged plate.

(a) One-impact plate investigation

Then, the mechanical behavior of the delamination is investigated. The investigation is first conducted on the one-impact plate. The out-of-plane displacements of the center point of the delamination are extracted and the frequency spectra are calculated.

Several values ranging from 0 to 5×10^6 N/m, which is considered to be a sufficiently large value, are assigned to the nonlinear springs to test if the springs are stiff enough to restrict penetration between delamination interfaces. The relative displacement of the center node of the delamination is extracted, and the relationship between the displacement and the corresponding force is also calculated.

Since for the $k^{spr} = 0$ case, the spring force is zero, the spring-force relationship for this case is omitted. Figure 4.40 shows the relative displacement between the upper and lower interfaces of the center node of the delamination extracted from this case. In this figure, it can be observed that the relative displacement fluctuates up and down near the zero axis, indicating that penetration happens when no constraint is applied to the contact interfaces.

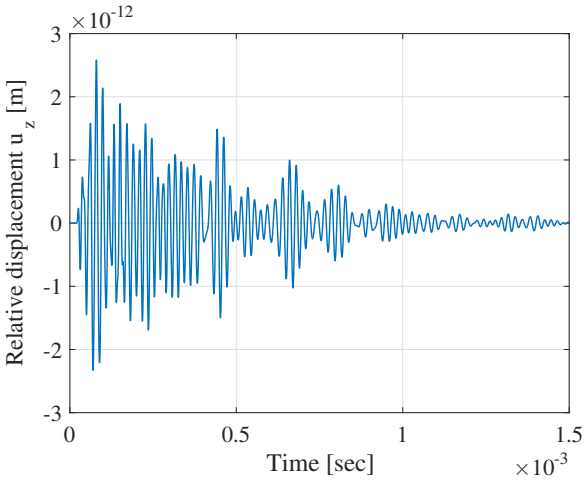

FIGURE 4.40: Relative displacements between the upper and lower interfaces in out-of-plane direction of the center node at delamination from the one-impact plate model with $k^{spr} = 0\,\mathrm{N/m}$.

Figure 4.41 illustrates the mechanical behavior of the center point of the delamination region in the one-impact plate. Different spring stiffness are assigned: the $k^{spr} = 1 \times 10^3\,\mathrm{N/m}$, $k^{spr} = 1 \times 10^5\,\mathrm{N/m}$ and $k^{spr} = 5 \times 10^6\,\mathrm{N/m}$. Figures on the left show the relative displacements in out-of-plane direction, and figures on the right show the relationships between the spring force and relative displacements at the center point. It can be observed that with the increase of the spring stiffness, the difference between the positive components and the negative components in displacement graphs enlarges, i.e., the penetration between delamination interfaces is getting smaller. In Figure 4.41a showing the $k^{spr} = 1 \times 10^3\,\mathrm{N/m}$ case, the amplitude in the positive direction is close to amplitude towards the negative direction. This indicates that the penetration between contact surfaces is still large since the negative displacement shows the penetration. When the spring stiffness increases to $1 \times 10^5\,\mathrm{N/m}$, the negative part of the relative displacement is quite smaller than the positive part, showing a small penetration. This indicates that with these values, the nonlinear springs are stiff enough to resist the penetration and induce contact interaction between the upper and lower surfaces of the delamination.

As for the relationships between spring force and relative displacements in the out-of-plane direction, graphs in the first two rows present similar patterns as defined before: when relative displacement is negative (surfaces are in contact), the force-displacement shows a linear relationship, and when relative displacement is positive (delamination interfaces are separated), no force is applied. However, the force-displacement relationship of the $k^{spr} = 5 \times 10^6\,\mathrm{N/m}$ case shown in the graph on the right in Figure 4.41c is not perfectly matched with the nonlinear model defined in the previous section. This might be due to numerical problems since we have set up a very large stiffness value. Therefore, it can be concluded that the values around 1×10^5 are appropriate for modeling the out-of-plane interaction of the delamination interfaces, thus achieving a trade-off between numerical convergence and mechanical

requirements.

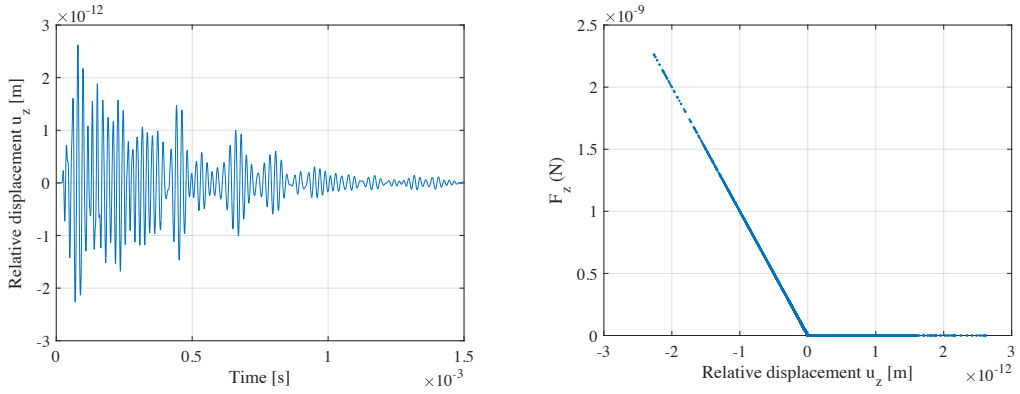

(A) $k^{spr} = 1 \times 10^3\,\mathrm{N/m}$

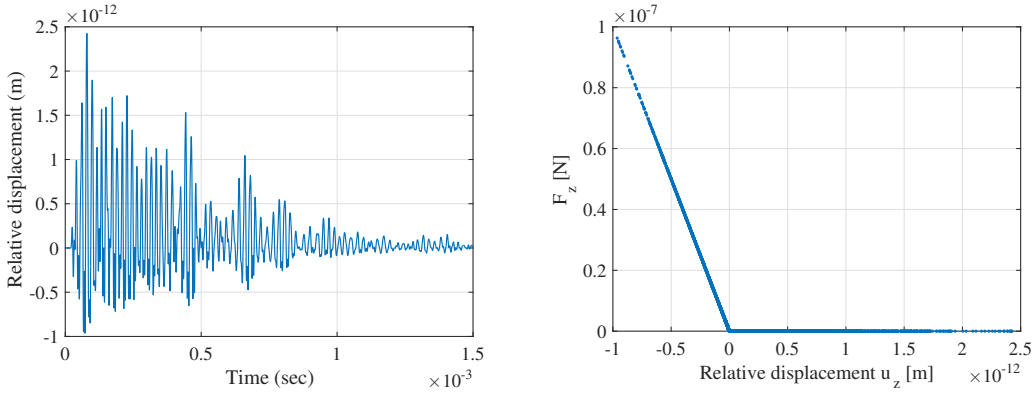

(B) $k^{spr} = 1 \times 10^5\,\mathrm{N/m}$

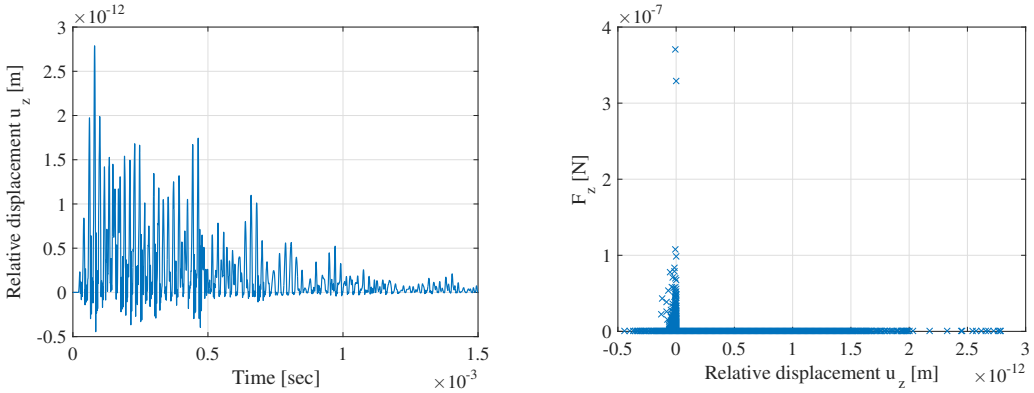

(C) $k^{spr} = 5 \times 10^6\,\mathrm{N/m}$

FIGURE 4.41: Mechanical behavior of the center point of the delamination from one-impact plate with different spring stiffness values. Left: relative out-of-plane displacement of the center point. Right: relationship between spring force and relative displacement in out-of-plane direction.

Similar investigations are also conducted on the two-impact and three-impact plates.

(b) Two-impact plate investigation

For the two-impact case, the following stiffness values are tested: $0\,\mathrm{N/m}$, $4 \times 10^4\,\mathrm{N/m}$, $1 \times 10^5\,\mathrm{N/m}$, $1 \times 10^6\,\mathrm{N/m}$ and $8 \times 10^6\,\mathrm{N/m}$. Typical electrical output signals are shown in Figure 4.42, where two extreme cases: $k^{spr} = 0\,\mathrm{N/m}$ and $k^{spr} = 8 \times 10^6\,\mathrm{N/m}$ are taken as examples. Figure 4.43 and Figure 4.44 show the relative displacements between the upper and lower surfaces of the center point of the delamination region in out-of-plane direction for the $k^{spr} = 0$ and $k^{spr} = 8 \times 10^6\,\mathrm{N/m}$ cases respectively. From Figure 4.43 it can be observed that there is no contact interaction happens between delamination interfaces when $k^{spr} = 0$. On the contrary, when the spring stiffness increases to $8 \times 10^6\,\mathrm{N/m}$, the positive part of the relative displacement is much larger than the negative part, and contact happens between delamination interfaces. However, the relative out-of-plane displacement begins to show a strange pattern after about 2.5 ms, which might be due to the numerical convergence problems. Figure 4.45 also shows the spring force-relative displacement relationship in the out-of-plane direction of the delamination center node for the $k^{spr} = 8 \times 10^6\,\mathrm{N/m}$ case. In this figure, most (force, displacement) pairs locate on the x-axis meaning that the spring force is 0, and points at the negative displacement zone are not linear to the spring force, which does not coincide with the pre-defined model. Thus, $8 \times 10^6\,\mathrm{N/m}$ can be an upper limit of k^{spr}, i.e., the highest stiffness for the nonlinear springs in the two-impact plate should be lower than this value.

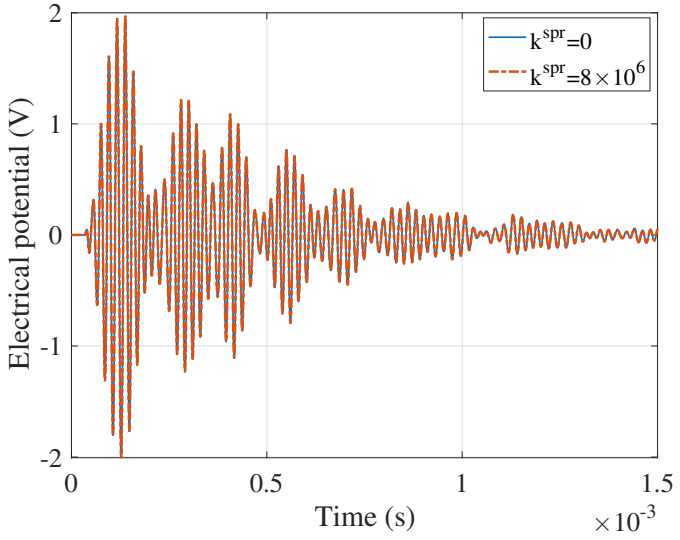

FIGURE 4.42: Typical raw responses of two extreme cases for the two-impact plate: $k^{spr} = 0$ and $k^{spr} = 8 \times 10^6\,\mathrm{N/m}$.

Displacement results of other spring stiffness values for the two-impact plate model are shown in Figure 4.46. The figures on the left column show the out-of-plane relative displacements between the upper and lower surfaces of the center point of the delamination region. It can be seen that with the increasing k_{spr}, the negative part of the displacement becomes smaller compared with the positive part and the contact effects become more obvious. The figures on the right column show the force-relative displacement relationships of the nonlinear springs. They all show linear relationships

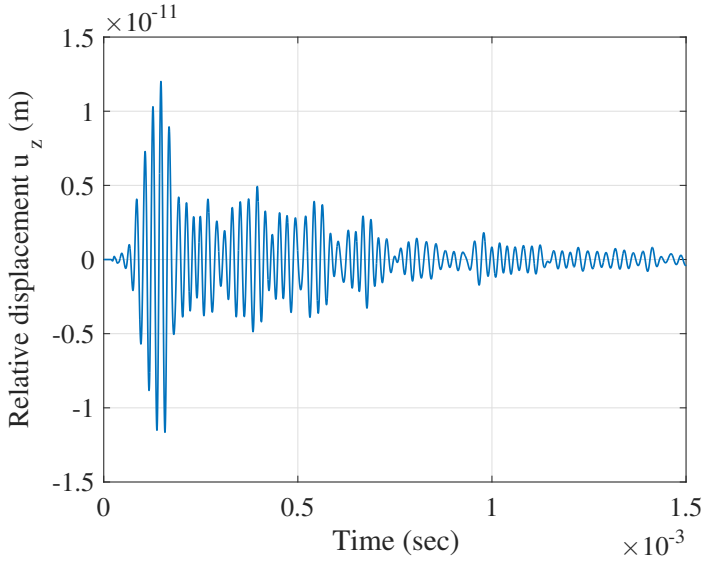

FIGURE 4.43: Relative displacement in out-of-plane direction of the center node for $k^{spr} = 0$ case of the two-impact plate.

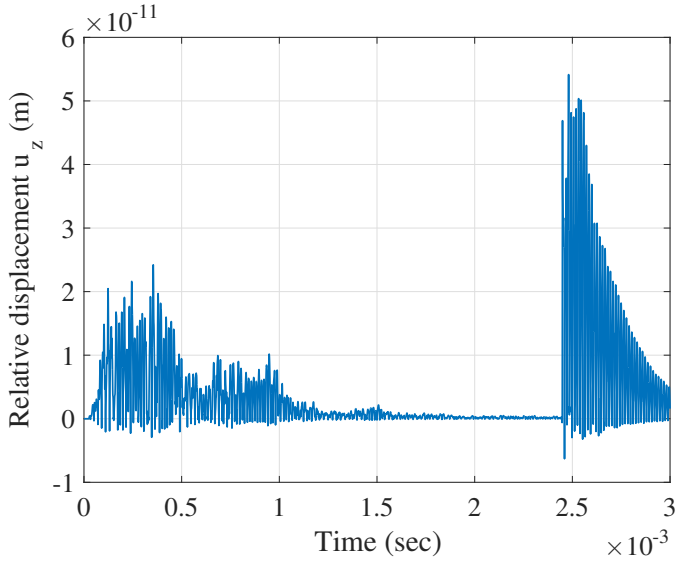

FIGURE 4.44: Relative displacement in out-of-plane direction of the center node for $k^{spr} = 8 \times 10^6$ N/m case of two-impact plate.

when relative negative displacements are negative, as defined in the mechanical model of the nonlinear spring.

(c) Three-impact plate investigation

For the three-impact plate, the following spring stiffness values are tested: 0 N/m, 1×10^5 N/m, 1×10^6 N/m and 8×10^6 N/m. Figure 4.47 shows the relative displacement between delamination interfaces of the delamination center node for the $k^{spr} = 0$ case. Figure 4.48 shows the relative displacements (left column) and spring force-displacement relationships (right column) of other cases with non-zero stiffness values. It can be observed that except for the zero-stiffness case, the displacements in other cases all show contact behavior between delamination interfaces. In the right

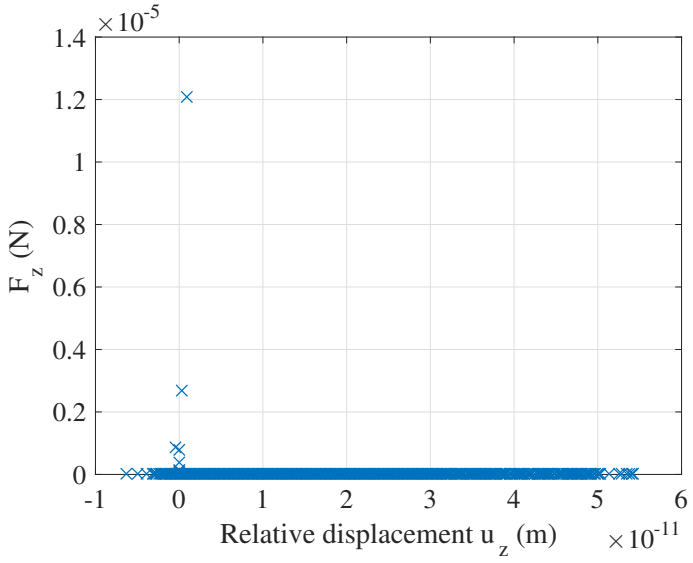

FIGURE 4.45: Spring force-relative displacement relationship for $k^{spr} = 8 \times 10^6$ N/m case of the two-impact plate model.

column of Figure 4.48, the force-displacement relationships in (b) and (d) exhibit bi-linear stiffness behavior, which is consistent with the pre-defined mechanical model of the nonlinear springs. On the contrary, in Figure 4.48(f) where $k^{spr} = 8 \times 10^6$ N/m, most (force, displacement) pairs locate on the x-axis, and even some points locate on the negative half axis, while only several outliers locate close to the y-axis. This does not coincide with the pre-defined mechanical nonlinear spring model. Therefore, the spring stiffness in the negative displacement part is better to be under 8×10^6 N/m.

(B) In-plane investigation

The effect of the two parameters v_f and F_0 in the in-plane interaction model on the simulation convergence are investigated on damaged plate models with no out-of-plane interaction ($k^{spr} = 0$) at the delamination region.

First, the convergence of the response signals with different (v_f,F_0) pairs are tested on all three damaged plates, as shown in Figures 4.49 to 4.51. In these figures, the blue circles indicate the convergent responses, the red asterisks indicate the divergent responses and the violet crosses indicate the responses that have strange resonance at certain frequencies (see Figure 4.52). Note that the x-axis is the reciprocal of v_f. For the one-impact plate, the response signal starts to diverge when $v_f \geqslant 1 \times 10^{-3}$ m/s and $F_0 \geqslant 1 \times 10^{-3}$ N. For the two-impact and three-impact plates, except for the divergent responses, the signals with resonance should also be avoided. It seems that the response tends to resonate when F_0 is close to the value of v_f. Since v_f is infinitely close to zero in the viscous friction model, then in this model, v_f should be as small as possible or at least much less than F_0. Therefore, the following (v_f,F_0) pairs can be considered: (1×10^{-7},1×10^{-4}), (1×10^{-6},1×10^{-5}), (1×10^{-6},1×10^{-4}), etc.

Figure 4.52 shows an example of the previously stated "weird" resonance response. This simulation is conducted on the three-impact plate model with $v_f = 1 \times 10^{-5}$ m/s and $F_0 = 1 \times 10^{-6}$ N. The figure on the left shows the time-domain signal of the

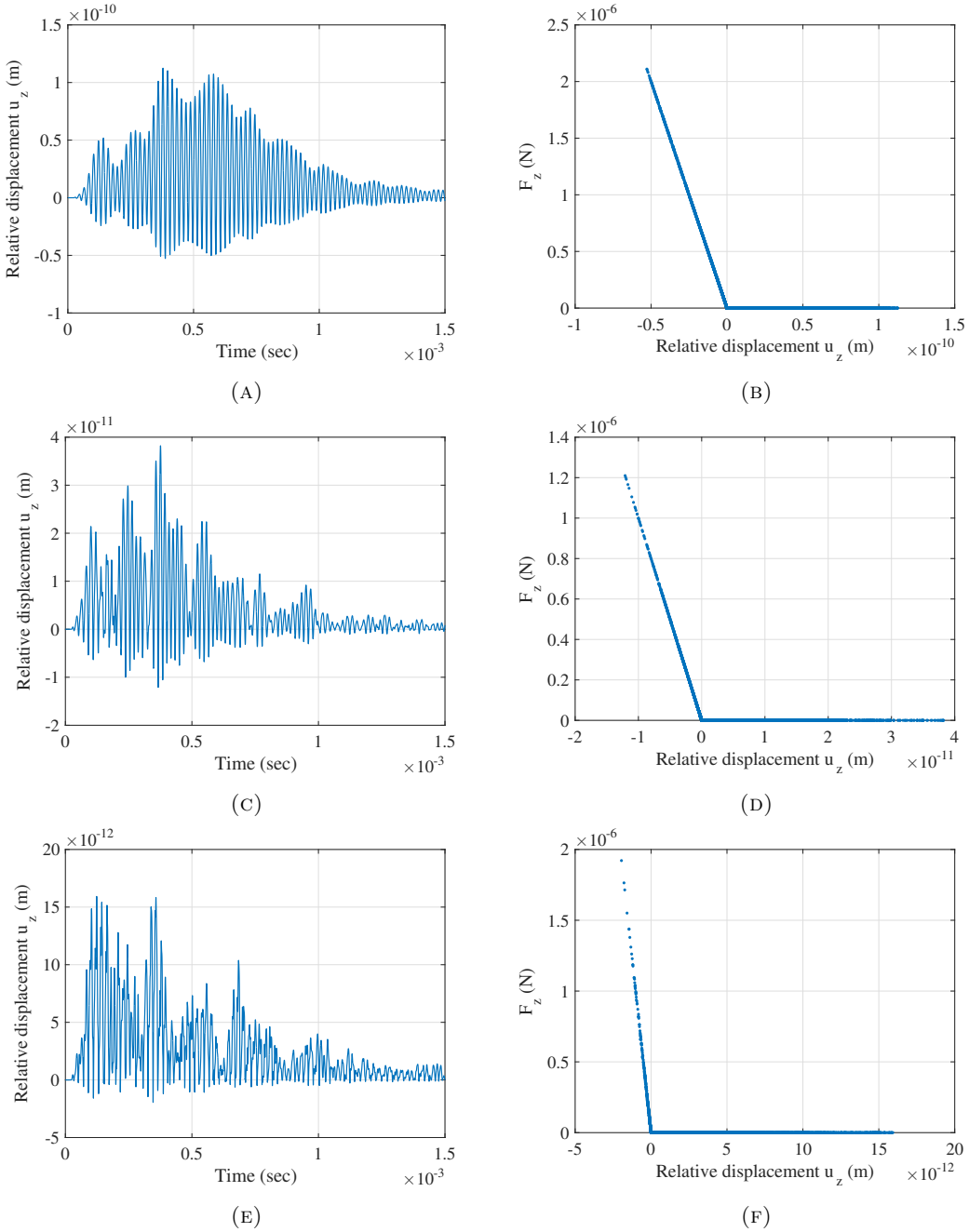

FIGURE 4.46: Two-impact plate: relative displacements (left) and spring force-relative displacement relationships (right) of the center node of the delamination: (a) and (b) are for the $k^{spr} = 4 \times 10^4$ N/m case, (c) and (d) are for the $k^{spr} = 1 \times 10^5$ N/m case, and (e) and (f) are for the $k^{spr} = 1 \times 10^6$ N/m case.

electrical output and the figure on the right shows its frequency spectrum. In the time-domain response, the signal is rather "normal" in the first several wave packets, where no outliers or weird waveforms are observed. However, after 1.2 ms, the response does not attenuate to zero or close to 0. Instead, the responses start to oscillate in a small amplitude. This can be proved in the frequency spectrum, where two unexpected peaks are observed at 140 kHz and 193 kHz besides the peaks at the fundamental

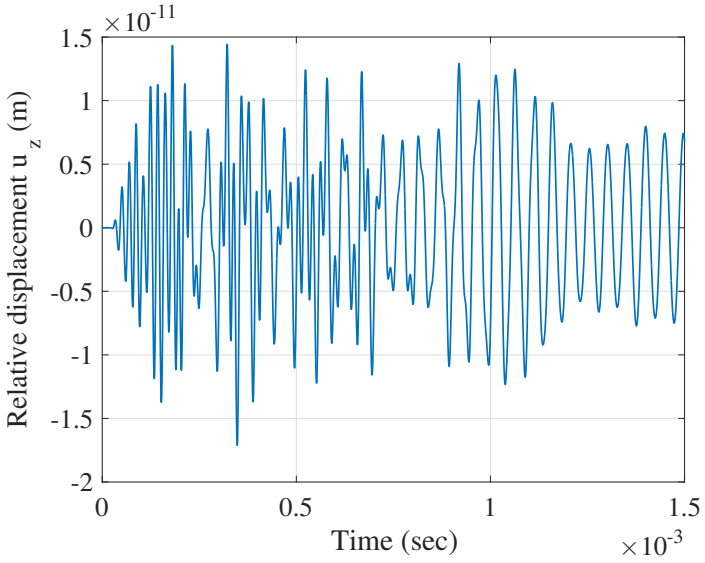

FIGURE 4.47: Three-impact plate: relative displacement for the 0 spring stiffness case.

frequency and second harmonic. This weird resonance might be due to numerical problems in the process of calculation, which should be avoided in the following study.

4.3.2.3 Contact/friction model

In this section, the sensitivity of the friction coefficient μ and spring stiffness are investigated for the three-impact plate.

First, the sensitivity of the friction coefficient is tested with the spring stiffness fixed at 1×10^6 N/m. The friction coefficient ranges from 0.1 to 0.9. The electrical outputs in both time and frequency domains are shown in Figure 4.53. Results show that with a spring stiffness of 1×10^{-6} N/m and time duration of 1.5 ms, the time responses are still converged with $\mu = 0.9$. In frequency domain, the response from $\mu = 0.9$ case is much more noisy than response from the $\mu = 0.1$ case, yet the amplitude of the second harmonic from $\mu = 0.9$ cases is much larger than that from $\mu = 0.1$ case.

Three damage indicators are calculated and plotted with respect to the friction coefficients ranging from 0.1 to 1 to evaluate the effect of the friction coefficients.

Figure 4.54 shows the CRC and NRE values extracted from the electrical output signals from the three-impact plate. It can be seen that both values have an increasing trend as the friction coefficient increases from 0.1 to 0.9, then drop largely when friction coefficient increases to 1.

Figure 4.55 shows the relative THD values variation with the increase of the friction coefficient. Same as CRC and NRE, the relative THD increases monotonically first as the friction coefficient increases from 0.1 to 0.9 and then falls to a smaller

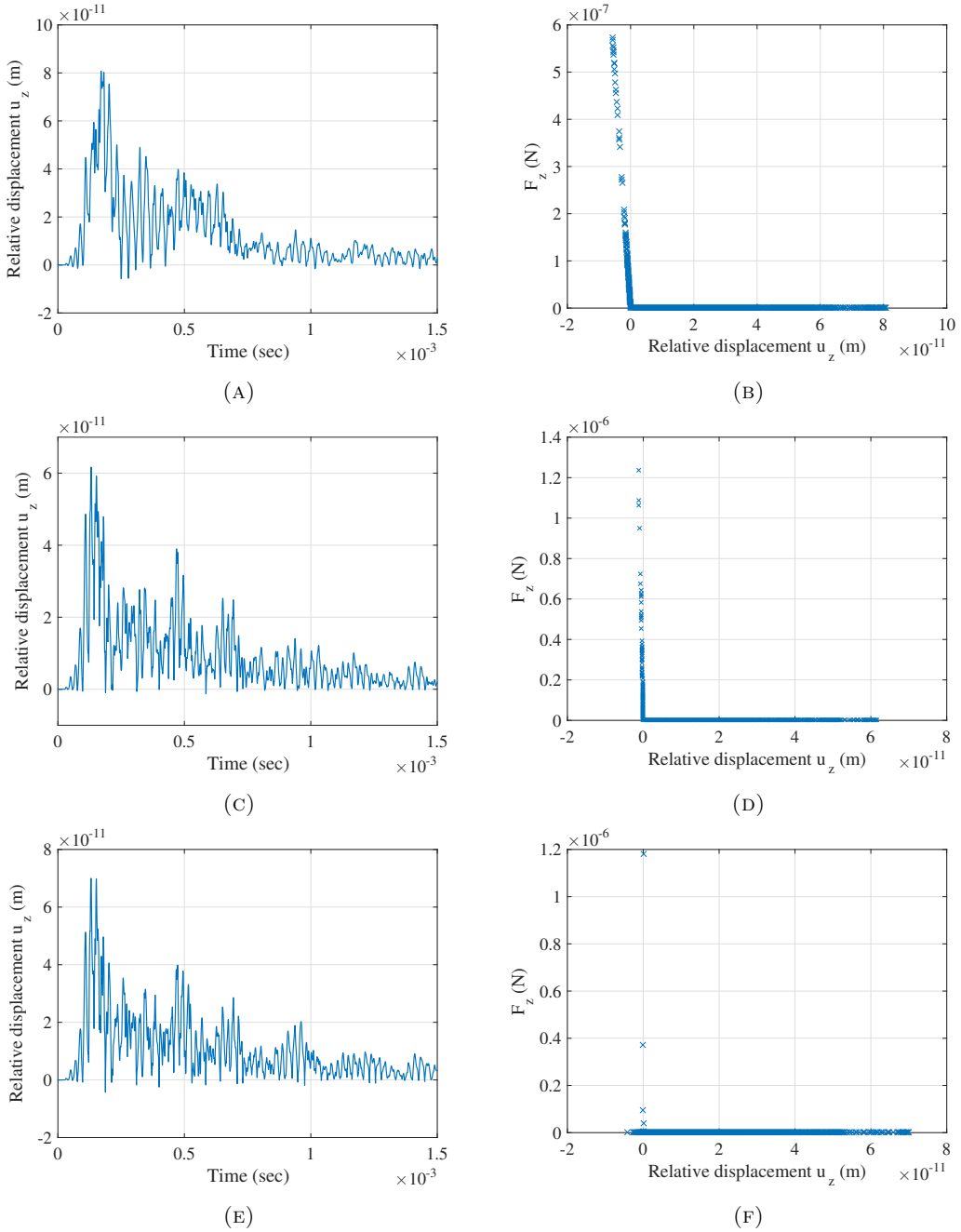

FIGURE 4.48: Three-impact plate: relative displacements (left) and spring force-relative displacement relationships (right) of the center node of the delamination for the two-impact plate model: (a) and (b) are for the $k^{spr} = 1 \times 10^5$ N/m case, (c) and (d) are for the $k^{spr} = 1 \times 10^6$ N/m case, and (e) and (f) are for the $k^{spr} = 8 \times 10^6$ N/m case.

value with the friction coefficient increasing to 1. Results show that all three damage indicators have the same evolution trend and all three curves peak at $\mu = 0.9$.

Then, the relative displacements in out-of-plane direction between upper and lower

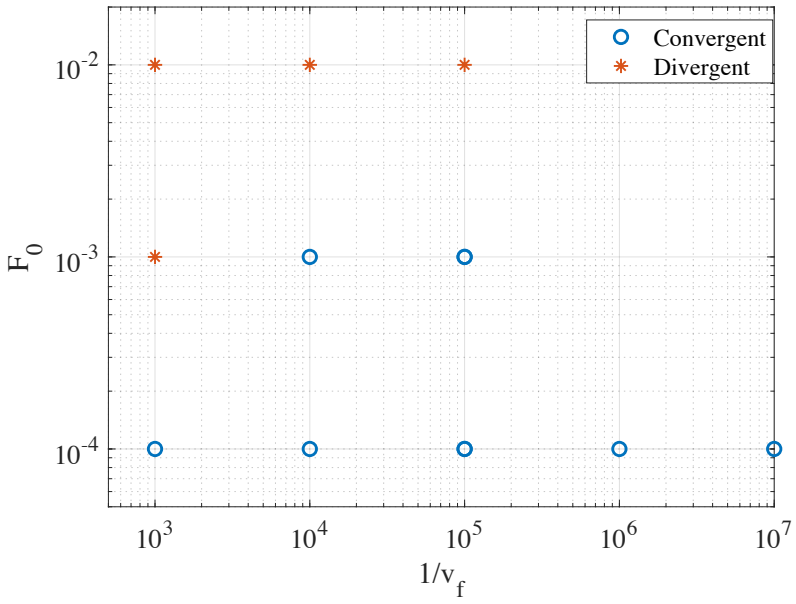

FIGURE 4.49: The convergence of the one-impact plate model with various (v_f,F_0) pairs.

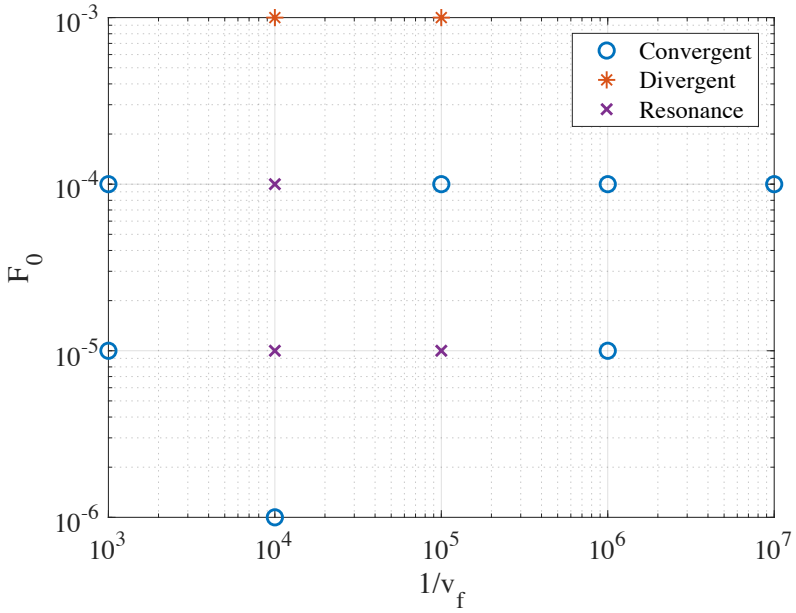

FIGURE 4.50: The convergence of the two-impact plate model with various (v_f,F_0) pairs.

surfaces of the center point at delamination region are calculated and shown in Figure 4.56. The calculations are conducted on the three-impact plate using contact/friction models with different friction coefficients. The figures on the left illustrate displacement curves in the time domain and the figures on the right show their frequency spectra. Results show that the amplitude of the out-of-plane relative displacement increases with the increasing friction coefficients in the model. Relative displacements

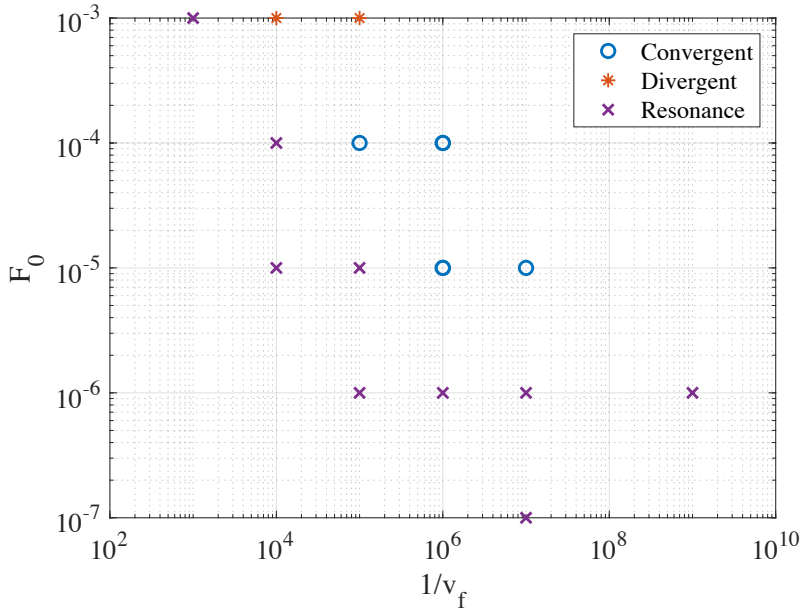

FIGURE 4.51: The convergence of three-impact plate model with various (v_f,F_0) pairs.

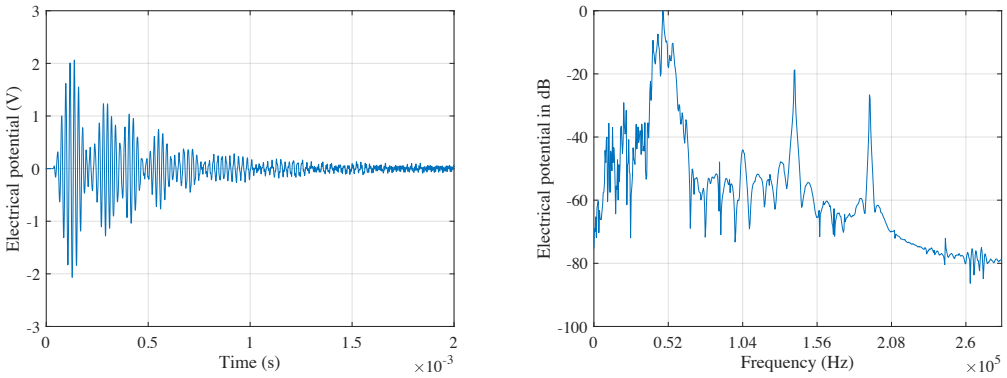

(A) Time domain signal. (B) Frequency spectra.

FIGURE 4.52: Example of the numerical resonance: electrical outputs from three-impact plate model with $v_f = 1 \times 10^{-5}$ m/s and $F_0 = 1 \times 10^{-6}$ N.

from $\mu = 0.1$ and $\mu = 0.3$ cases are close to the contact interaction, while the relative displacement from $\mu = 0.7$ shows a non-smooth trend in time domain.

The signal peak to trough ratios of the three cases with different friction coefficients are listed in Table 4.9. We can see in this table that with the increase of the friction coefficients, the signal peak to trough ratios decreases. It seems that friction reduces the surface contact interaction.

Then the sensitivity of the spring stiffness is investigated. A fixed friction coefficient of 0.7 is assigned to the contact/friction model and calculations are conducted on the three-impact plate.

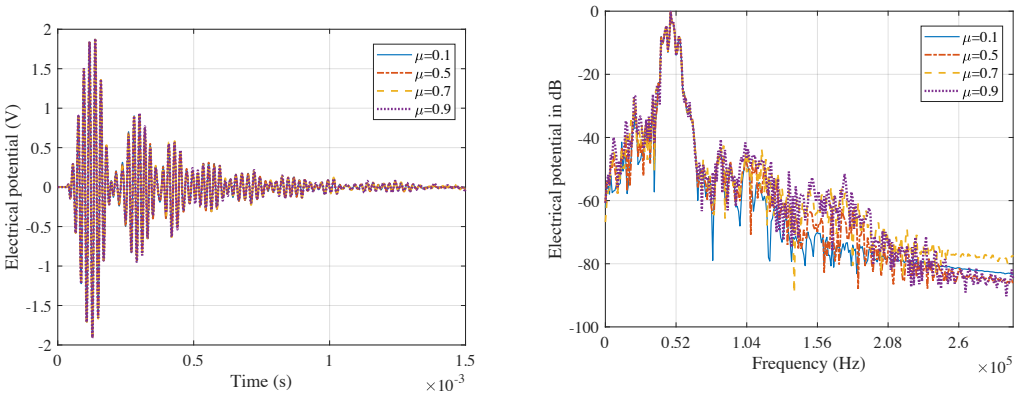

(A) Time domain signal.

(B) Frequency spectrum.

FIGURE 4.53: Electrical output signals in both time and frequency domains from three-impact plate using contact/friction model with different friction coefficients.

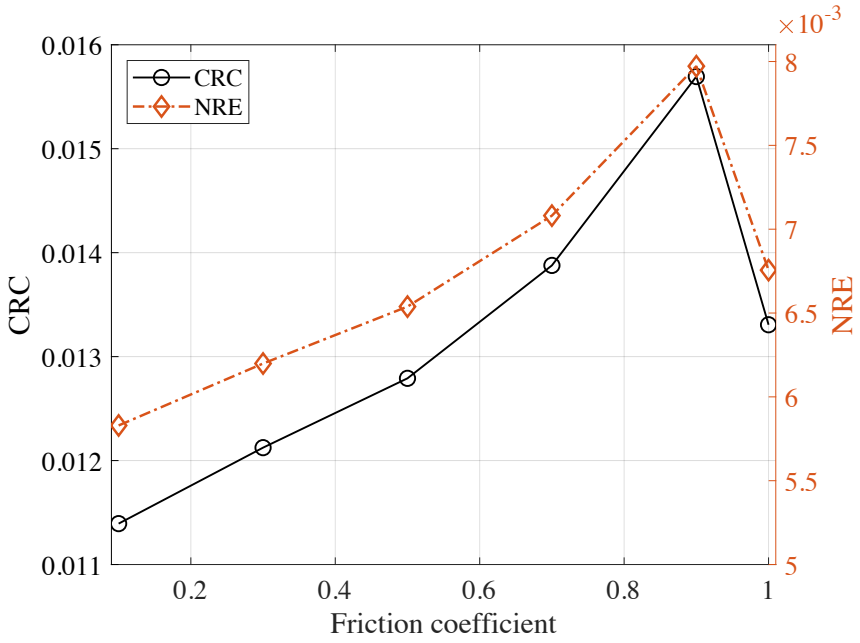

FIGURE 4.54: Effect of friction coefficient on CRC and NRE of the electrical output signals of the three-impact plate.

TABLE 4.9: Signal peak to trough ratios from cases with different friction coefficients

Case number	1	2	3
Friction coefficient	0.1	0.3	0.7
Signal peak to trough ratio	2.42	2.31	1.32

Figure 4.57 shows the electrical output signals in both time and frequency domains. Results show that the frequency spectra from the cases with 0 N/m, 1 N/m and 1000 N/m spring stiffness are close to each other, while the frequency response from $k^{spr} = 1 \times 10^6$ N/m case is much different, having the highest level of noise and

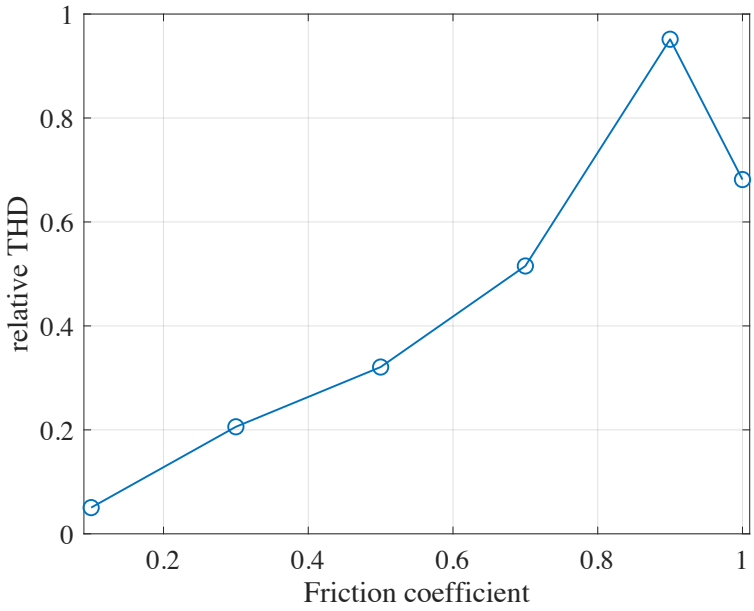

FIGURE 4.55: Effect of friction coefficient on relative THD of the electrical output signals of the three-impact plate.

largest amplitude of the second harmonic. This indicates that the spring stiffness starts to have an impact on the outputs when it reaches a sufficiently large value (1×10^6 N/m in this example). It can also be observed from the above two figures that the electrical output signals seem to be more sensitive to friction coefficient than to spring stiffness.

Figure 4.58 shows the CRC and NRE values from of the electrical output signals of the three-impact plate. It can be seen that both values remain almost unchanged when the spring stiffness increases from 0 to 1×10^3 N/m. Then they decrease slightly as the spring stiffness increases to 1×10^5 N/m, and then grow sharply when k^{spr} increases to 1×10^6 N/m.

Figure 4.59 shows the relative THD values variation with the increase of spring stiffness. Similar to CRC and NRE, the relative THD remains almost unchanged as the spring stiffness increases from 0 to 1×10^3 N/m, but then decreases slightly unlike the other two indicators. Finally the value increases largely when the spring stiffness increases to 1×10^6 N/m.

Then, the displacements at the center point of the delamination are extracted, and the relative out-of-plane displacements between the upper and lower surfaces are derived. Figure 4.60 illustrates the relative displacement in out-of-plane direction between the upper and lower surfaces of the center point at the delamination region. The results are derived from the three-impact plate with different spring stiffness values: 1 N/m, 1×10^3 N/m and 1×10^6 N/m. The figures on the left column illustrate displacements in the time domain and the figures on the right show the corresponding frequency spectra. It can be observed that the displacement curves in time domain from $k^{spr} = 1$ N/m and $k^{spr} = 1 \times 10^3$ N/m are almost symmetric with the x-axis,

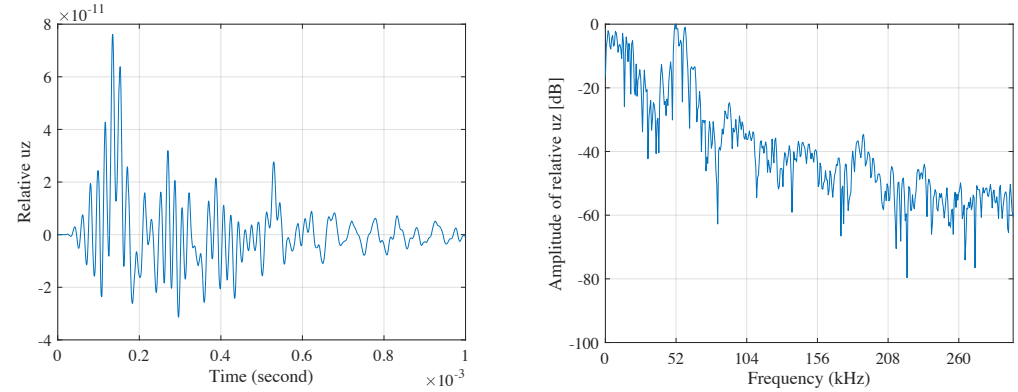

(A) Friction coefficient $\mu = 0.1$.

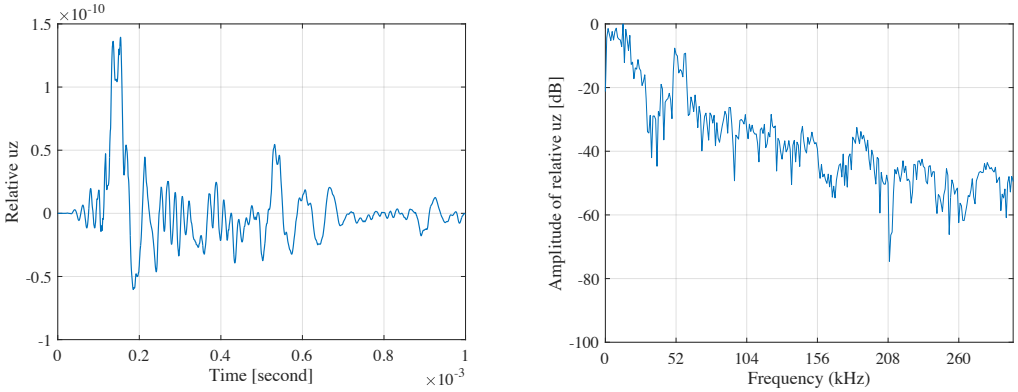

(B) Friction coefficient $\mu = 0.3$.

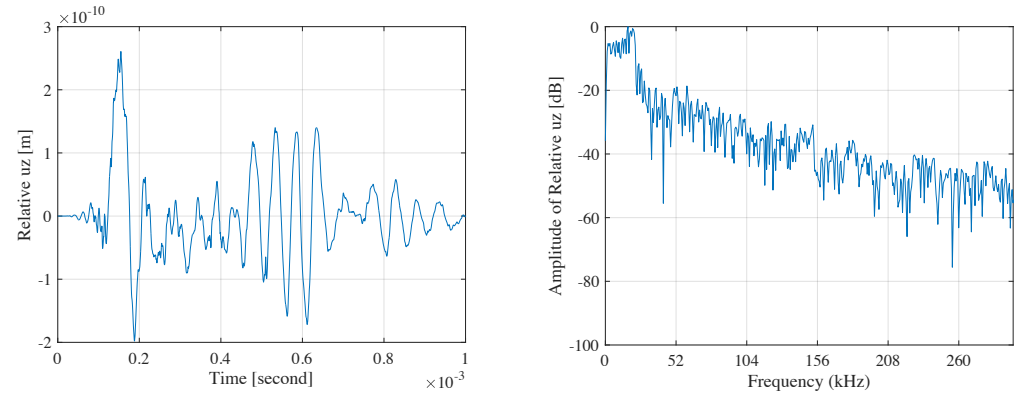

(C) Friction coefficient $\mu = 0.7$.

FIGURE 4.56: Relative displacement in out-of-plane direction between upper and lower surface of the center point at delamination region. Results are from the three-impact plate using contact/friction models with different friction coefficients. The left column illustrates displacements in time domain and the right column shows their frequency spectra.

indicating that there is no contact interaction between delamination interfaces. The displacement from $k^{spr} = 1 \times 10^6$ N/m is less smooth than the other two displacement curves.

From the above analyses, it can be observed that the structure response is insensitive to a low spring stiffness, and k^{spr} should be large enough to induce interactions

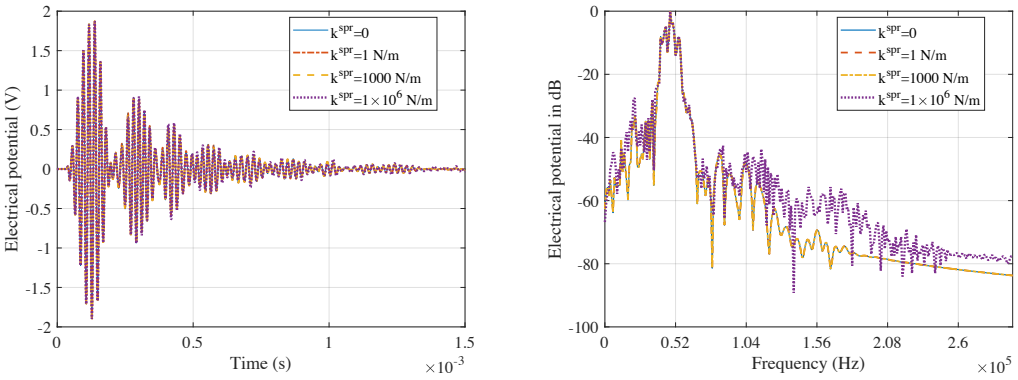

(A) Time domain signal. (B) Frequency spectrum.

FIGURE 4.57: Electrical output signals in both time and frequency domains from three-impact plate using contact/friction model with different spring stiffness values.

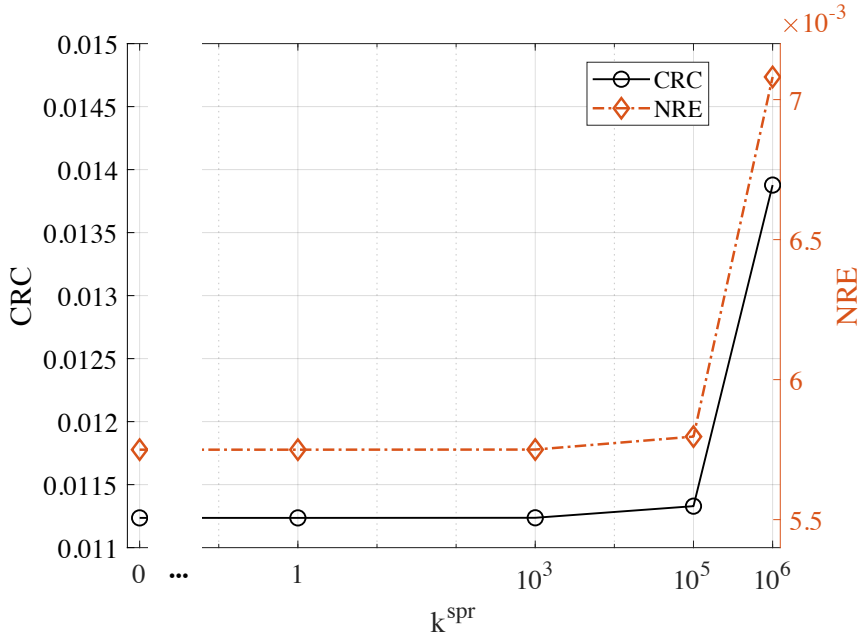

FIGURE 4.58: Effect of spring stiffness on CRC and NRE of the electrical output signals of the three-impact plate.

between delamination interfaces. Therefore, in the following study, the spring stiffness is set as $k^{spr} = 1 \times 10^6\,\mathrm{N/m}$.

4.3.2.4 Comparison between different models and determination of model parameters

In this section, we compare simulation results from different damage models in terms of DI. The main idea is that with different damage models, simulation results (time-domain signals) should be consistent, i.e. the calculated DI from each model should be the same as or close to DI from other models.

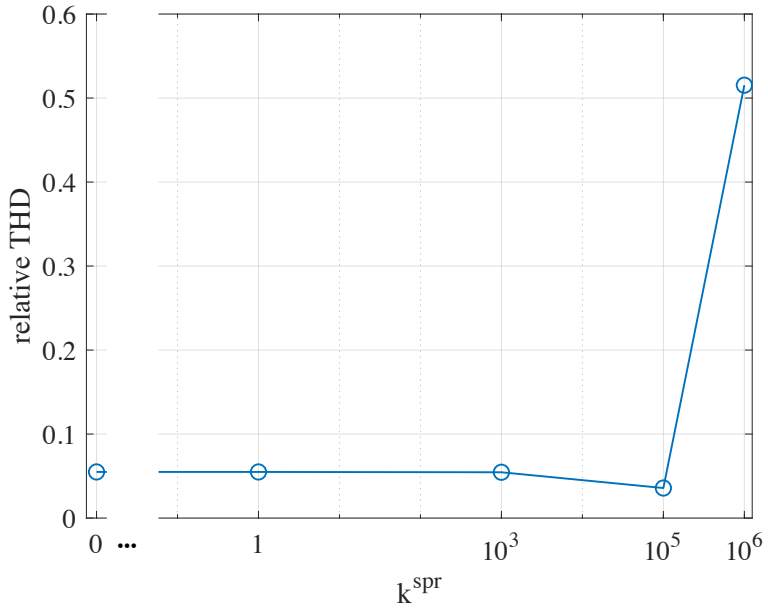

FIGURE 4.59: Effect of spring stiffness on relative THD of the electrical output signals of the three-impact plate.

We consider CRC as the DI to compare. Figure 4.61 shows the sensitivity of reduction coefficient and spring stiffness on CRC values from the stiffness reduction model and bilinear spring model, respectively. In this figure, the CRC values barely change with the spring stiffness, but it increases rapidly as the reduction coefficient decreases. The two curves have common CRC values at around 0.011 85, where the corresponding reduction coefficient is between 0.6 and 0.7. An interpolation is applied and the result value is about 0.64, which is close to the reduction coefficient calculated in **??** A.3.2.1. Therefore, 0.66 is a reasonable value for the stiffness reduction model and is set as the reduction coefficient in the following studies.

Figure 4.62 compares the CRC values between contact/friction model and the bilinear stiffness model. Note that the CRC values do not change much with both parameters. From this figure, we can observe that the two curves intersect at around 0.01185, the same as the previous figure. Therefore, the CRC value of 0.01185 can be used to determine the friction coefficient, which is approximately 0.3. Thus, 0.3 is set as the friction coefficient in the following study.

4.3.3 DI comparison

In this section, we conduct a comparison of the effect of delamination severity on the relative THD values obtained from received signals of the simulations with different damage models. Simulations are conducted with the parameters illustrated in the previous section.

Figure 4.63 illustrates this comparison. Results show a monotonic increase in the relative THD by increasing the diameter of the delamination in signals from all four models. Among them, the relative THD values from the contact/friction model is

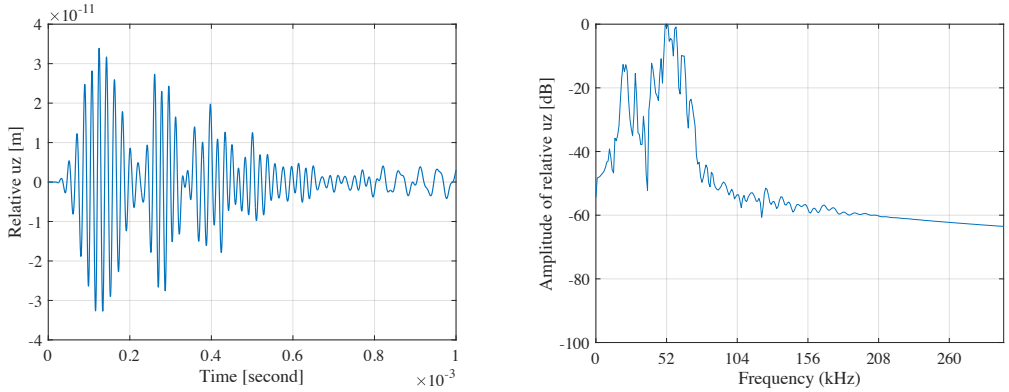

(A) $k^{spr} = 1\,\mathrm{N/m}$.

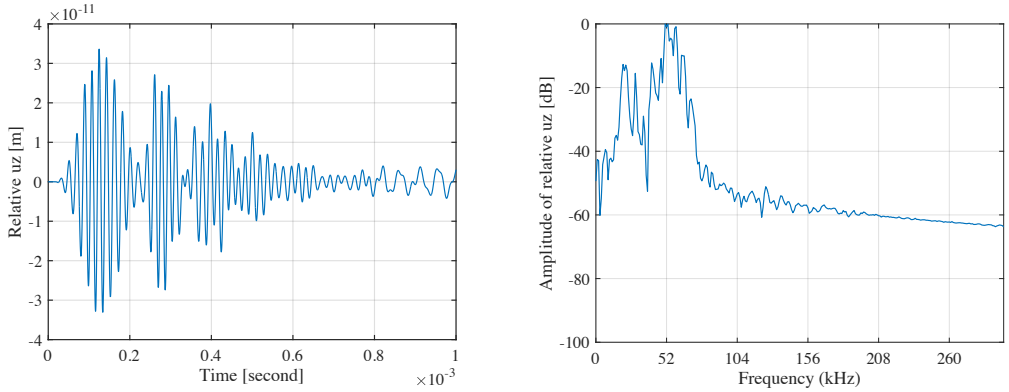

(B) $k^{spr} = 1 \times 10^3\,\mathrm{N/m}$.

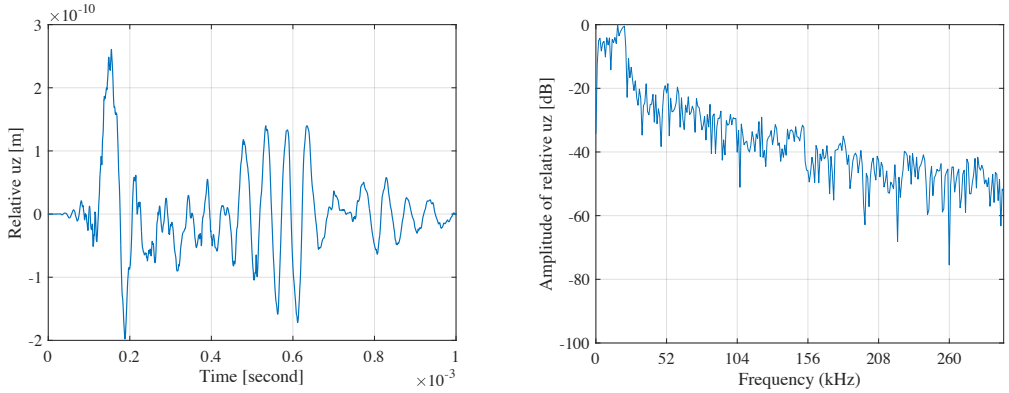

(C) $k^{spr} = 1 \times 10^6\,\mathrm{N/m}$.

FIGURE 4.60: Relative displacement in out-of-plane direction between upper and lower surface of the center point at delamination region. Results are from the three-impact plate using the contact/friction model with different spring stiffnesses. The left column illustrates displacements in time domain and the right column shows their frequency spectra.

the largest in all three damaged cases with different delamination diameters. In this model, the relative THD increases from 0 to above 0.25 when the delamination diameter increasing from 0 to 21 mm. Besides this, the relative THD from the bilinear spring model is the second largest, with a stable increase from 0 to about 0.07 with delamination diameter increase from 0 to 14 mm, followed by a sharp rise to nearly

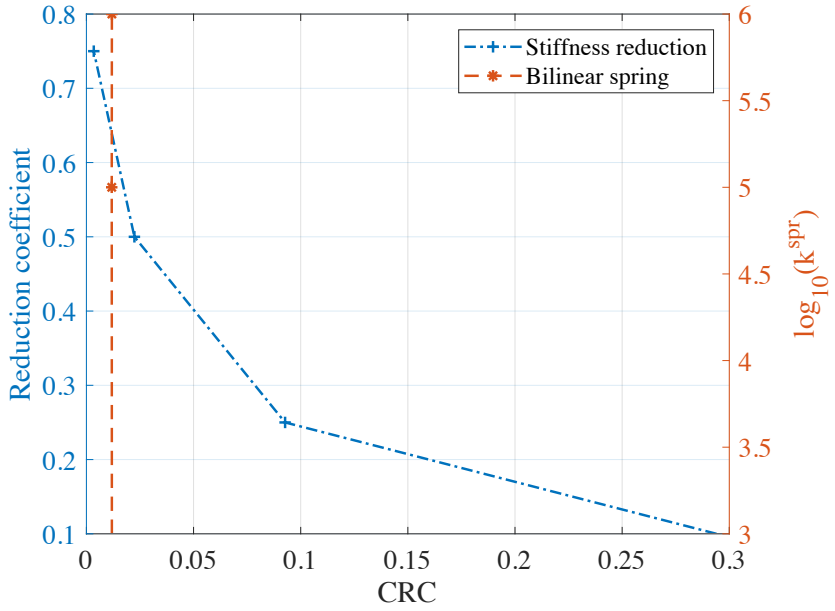

FIGURE 4.61: Variation of CRC values against reduction coefficient in stiffness reduction model and the log scale values of spring stiffness in bi-linear spring model.

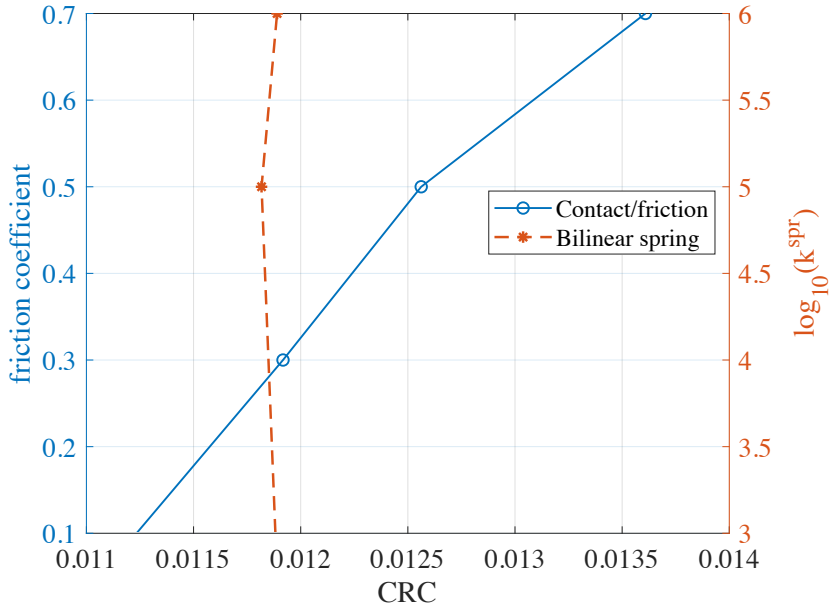

FIGURE 4.62: Variation of CRC values against friction coefficient in contsct/friction model and the log scale values of stiffness in bi-linear spring model.

0.25 as the damage diameter increases to 21 mm. For the linear spring model, the initial growth curve is close to that of the bilinear spring model, but when the delamination diameter increases to 21 mm, the relative THD is much smaller than the value from the bilinear spring model and is close to the value from stiffness reduction model. The first stage of the relative THD curve from the stiffness reduction model

is almost equal to a linear growth as the delamination diameter increases from 0 to 14 mm, but then the curve shows a larger increase. It can be concluded that the nonlinear effects in this system are due to the contact interaction between delamination interfaces, and larger nonlinear effects are related to nonlinear interaction models and delamination severity.

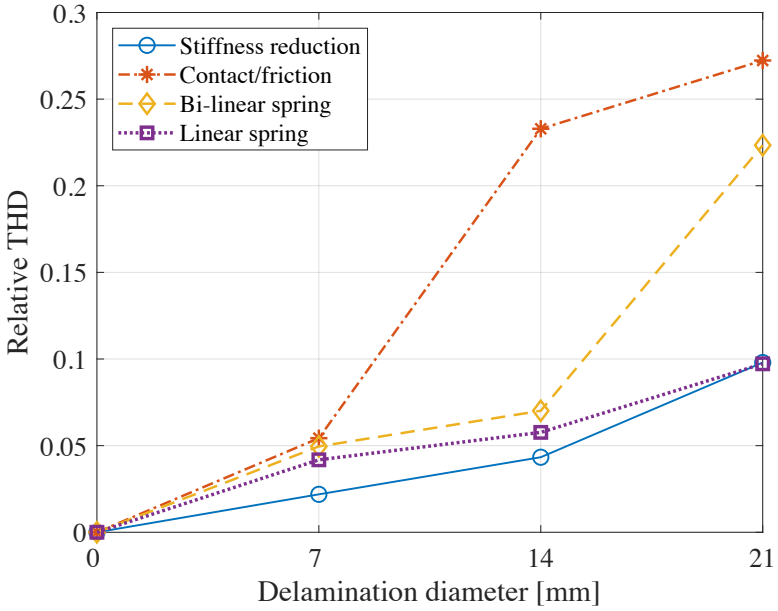

FIGURE 4.63: Effect of delamination diameter on relative THD of the received electrical signals.

The difference signals are obtained by subtracting the baseline signal (intact plate) from the output raw signals, and the THD values of the difference signals are calculated, as shown in Figure 4.64. In this figure, THD values of difference signals from all three spring models show a monotonic increasing trend, while the THD curve from the stiffness reduction model shows a decreasing trend. Among the three spring models, the contact/friction model and the linear spring model both present a stable growing trend in the THD values with the increase of the delamination diameter. The curve representing the bi-linear spring model demonstrates a steady increase first, similar to the other two spring models, but then shows a sharp rise as the delamination diameter increases to 21 mm.

In addition to the relative THD, which evaluates the nonlinear effects in the system, the other two DIs are also investigated to evaluate the damage severity. Figure 4.65 shows a comparison of the effect of delamination diameter on CRC obtained from the received electrical signal of simulations with different damage models. In this figure, the CRC values from all simulation results show a monotonic increasing trend with the increase of delamination diameter. Among these models, the CRC values from the bi-linear spring model and linear spring model both follow stable and similar increasing trends that the two curves are very close to each other. For the contact/friction model, the CRC curve first increases slightly as the delamination

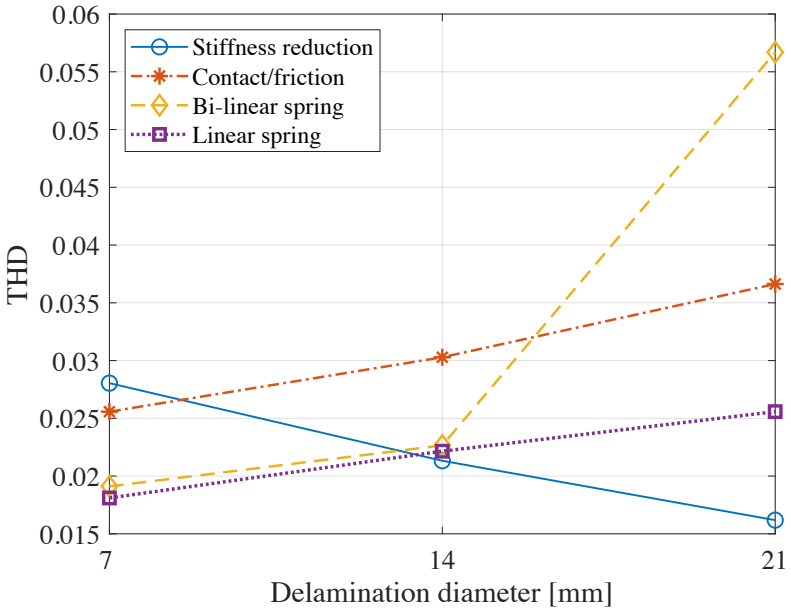

FIGURE 4.64: Effect of delamination diameter on THD value extracted from the difference signals after baseline subtraction.

diameter increases from 0 to 7 mm, but then it shows a sharp increase from near 0 to more than 0.01 as the delamination diameter increases from 7 mm to 14 mm, followed by an increase to 0.014 with delamination diameter increases to 21 mm. For the stiffness reduction model, the CRC curve first increases steadily from 0 to near 0.0034 when the delamination diameter increases from 0 to 14 mm, then it rises drastically to 0.012 35 when the delamination diameter increases to 21 mm. Figure 4.66 shows a comparison of the effect of delamination diameter on the linear DI based on the residual energy of the received signals with different damage models. Similar to the CRC results, all NRE curves in this figure show a monotonic increasing trend, and the trend shown in this figure is the same as in the CRC chart.

It can be seen from the above three figures that all three DIs can be used to evaluate the delamination severity. Among the three indicators, the relative THD suits best for the evaluation of the nonlinear effects induced by delamination damage in the system.

4.4 Verification of finite element model

4.4.1 Comparison with experiments

In this section, the simulation results are compared with the experimental results, in order to verify the simulation model.

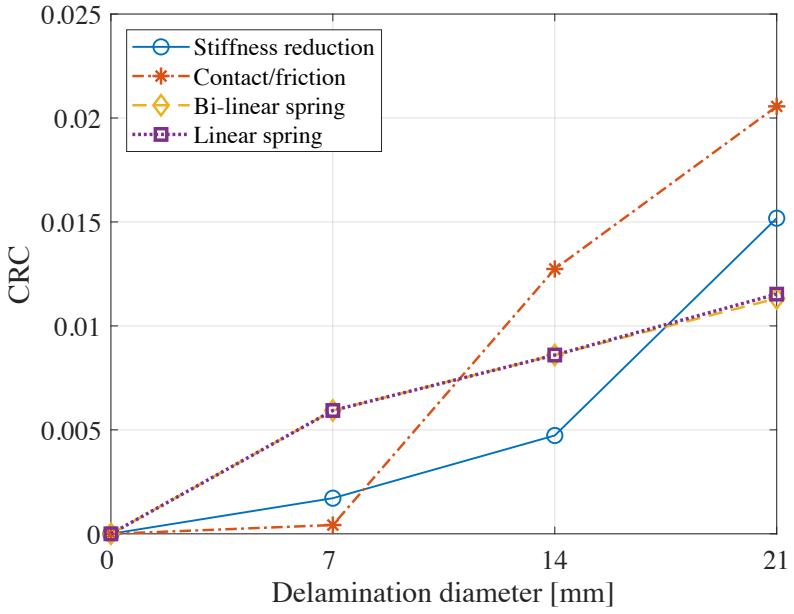

FIGURE 4.65: Effect of delamination diameter on CRC of the received electrical signals.

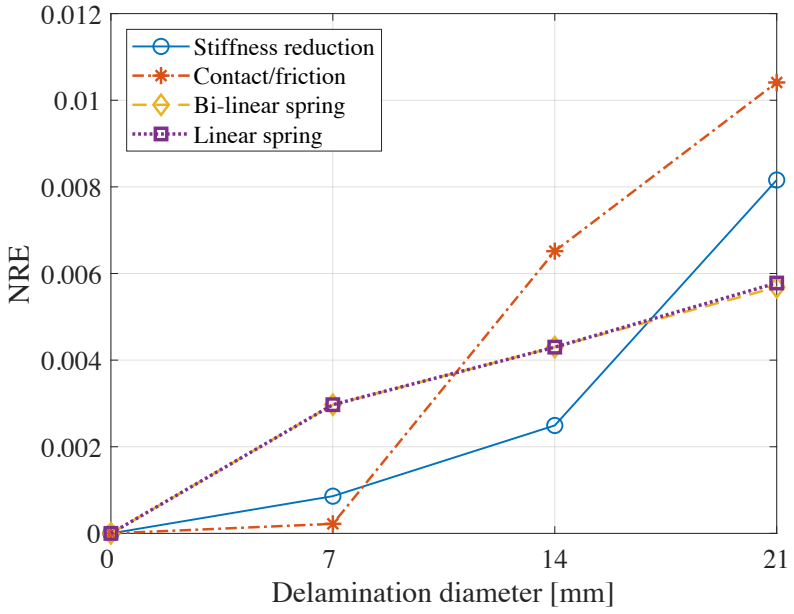

FIGURE 4.66: Effect of delamination diameter on NRE of the received electrical signals.

4.4.1.1 Intact plate

The undamaged plate is used for model verification by comparing the electrical output and its frequency spectrum with experimental results, as shown in Figure A.16. The left figure shows the time-domain signals and the figure on the right shows the frequency-domain features of the two signals. In the left figure, it can be observed that the first wave packets of the time domain raw signals from both simulation and

experiments are in good agreement. In the right figure, it can be seen that except for the fundamental frequency, the second and third harmonics from both simulation and experiment results can be clearly observed. The amplitudes of second and third harmonics from experiments are higher than those from simulation. This discrepancy might be due to the different sampling frequency of simulation and experiments. Moreover, due to the influence of environmental noise and the experimental system, the noise level of the experiment is higher than that of the simulation.

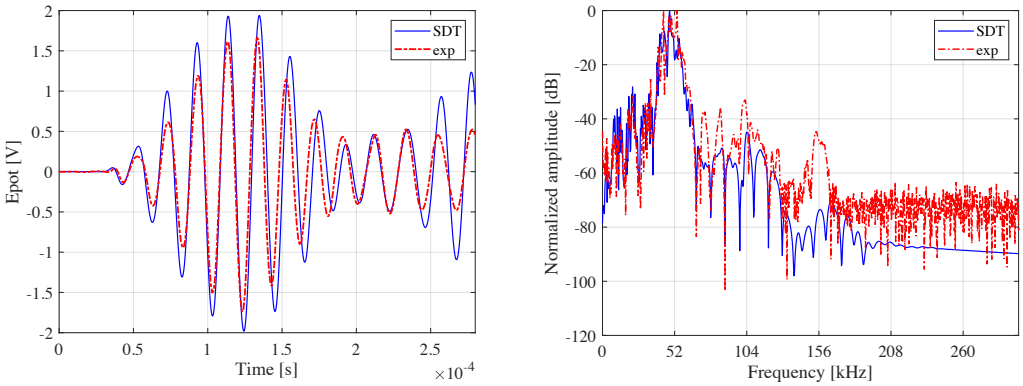

(A) Time domain signal. (B) Frequency spectra.

FIGURE 4.67: Comparison of the electrical output in both time and frequency domains between simulation and experiment results for the undamaged plate. The frequency signals are normalized to the maximum value of each spectrum respectively.

4.4.1.2 Damaged plates

(a) Time-domain signals

Figure A.17 shows the comparison of the electrical output signals in time domain between the experiment and simulation results. These plots represent the amplitudes of waves over the delamination region predicted by different simulation models and experimental results. It can be found that the spring models predict quite similar waves as the experiment.

(b) Frequency-domain signals

In Figure A.18, a series of comparisons between damaged (three-impact) and healthy (intact) plates have been performed through experiments and simulation models. In all plots of Figure A.18, the fundamental frequency component can be clearly observed at 52 kHz where the maximum amplitude appears. The experiment results in Figure A.18a imply that the amplitudes of the second and third harmonics for the damaged plates are much higher than those for the healthy plate. In simulations, the amplitude of the second harmonic for the damaged plates is higher than that of the healthy plate for all simulation models. For the third harmonic, the amplitudes from the contact/friction model and bi-linear stiffness model are more obvious than the

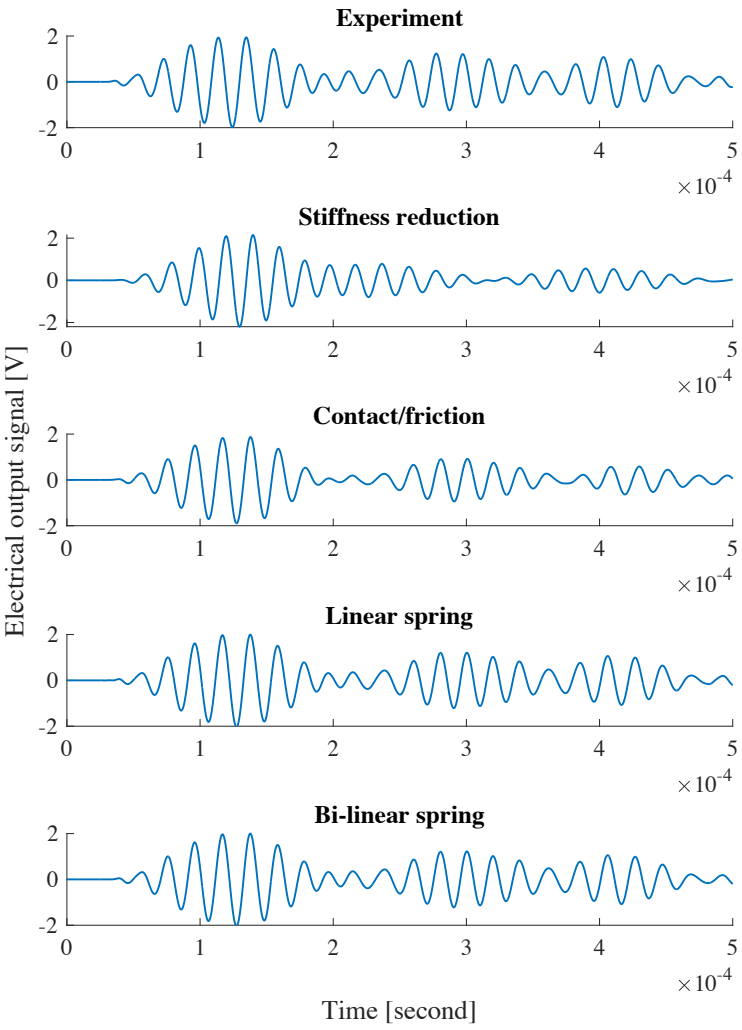

FIGURE 4.68: Comparison of electrical output signals in time domain between experiment and simulation results.

other two models. This indicates that the frequency responses from the bilinear stiffness model and contact/friction model show better agreement with the experimental results.

4.4.1.3 DI investigation

Several DIs are used to evaluate the damage severity.

Figure A.19a presents the comparison of CRC between experimental results and several numerical predictions (stiffness reduction model, contact/friction model, bilinear model and spring model). The experimental response manifests an oscillation behavior with the increase of delamination diameter. Results predicted by these numerical models present a continuous increase tendency with delamination diameter enlarges.

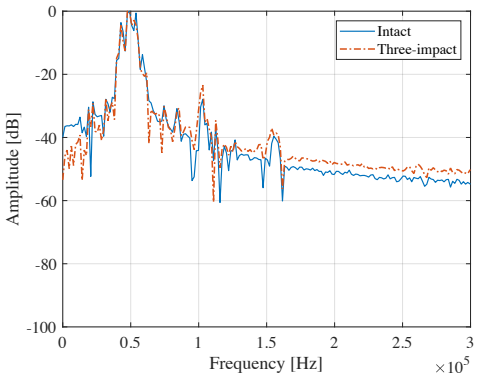

(A) Experiment.

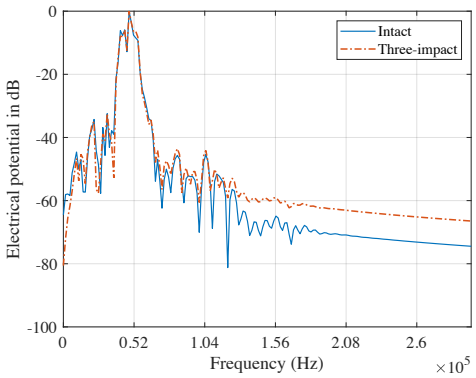

(B) Stiffness reduction model.

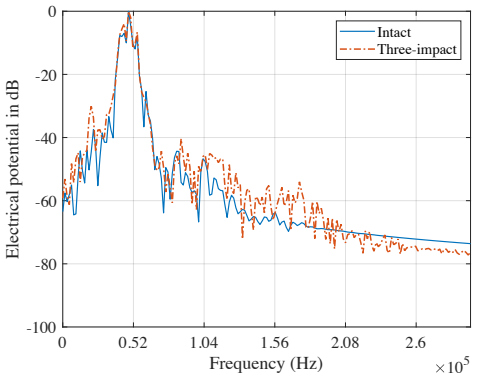

(C) Contact/friction model.

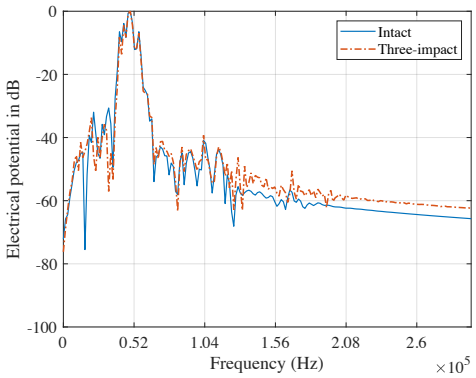

(D) Bi-linear spring model.

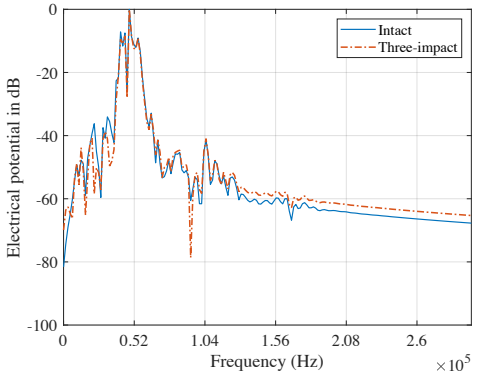

(E) Linear spring model.

FIGURE 4.69: Normalized FFT of the output signals of both the healthy plate and the three-impact plate from experiment and simulations respectively.

The variation of NRE with the increases of delamination diameter for both experimental results and numerical predictions (as shown in Figure A.19b) are similar in tendency to those for CRC in Figure A.19a. In the case of the same delamination diameters, NRE indicates smaller values of damage compared with CRC measurement in terms of both experimental results and numerical simulations.

In order to enrich the considerations and evaluate the results more precisely, some other DIs are employed. One indicator for measuring damage severity based on the normalized residual energy (denoted as NRE2 to distinguish from NRE) is defined as

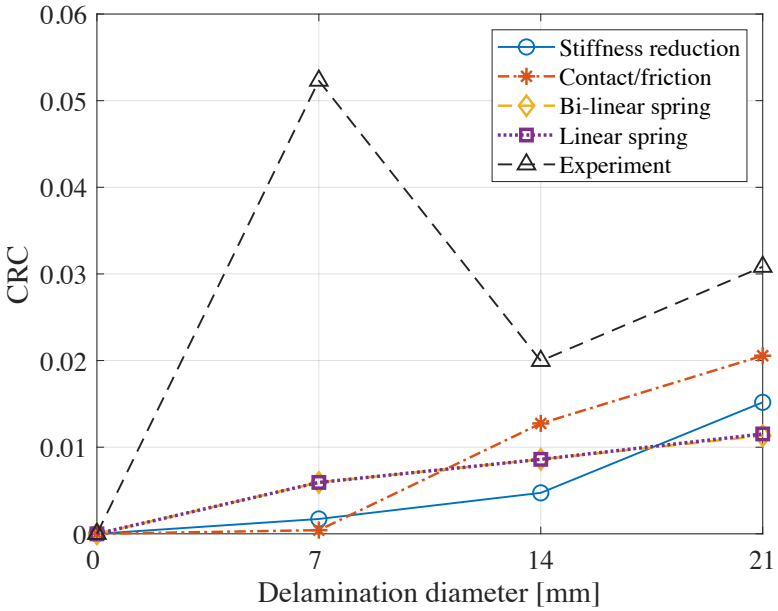

FIGURE 4.70: Comparison of CRC between simulations and experiment.

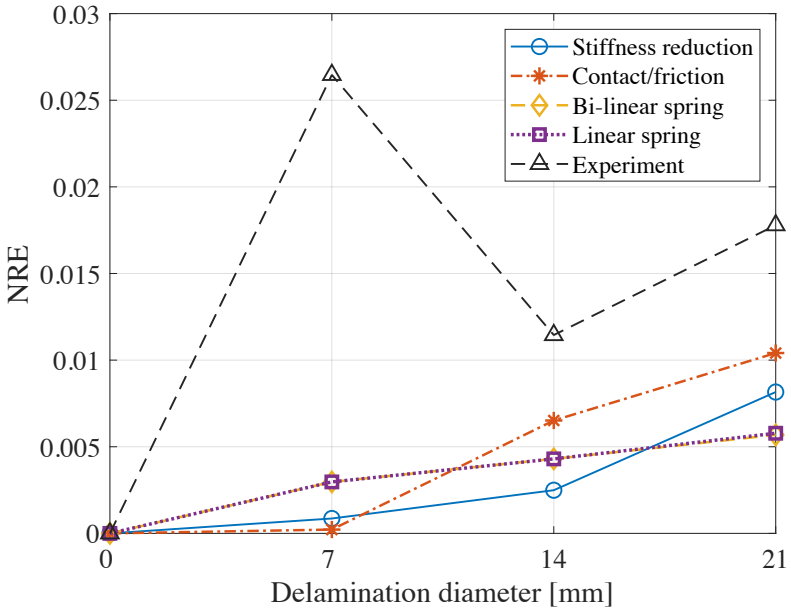

FIGURE 4.71: Comparison of NRE between simulations and experiment.

[63]:

$$NRE2 = \frac{\int_0^T x(t)^2\,dt - \int_0^T y(t)^2\,dt}{max\left(\int_0^T x(t)^2\,dt, \int_0^T y(t)^2\right)} \tag{4.18}$$

where $x(t)$ is the healthy plate response, and $y(t)$ is the damaged plate response.

By employing this indicator, comparisons between experimental results and simulations are illustrated in Figure A.20. Unlike experimental results adopting CRC

and NRE manners, the NRE2 indicator gives a more smooth curve. With respect to numerical predictions, smaller values have been generated compared to experimental results.

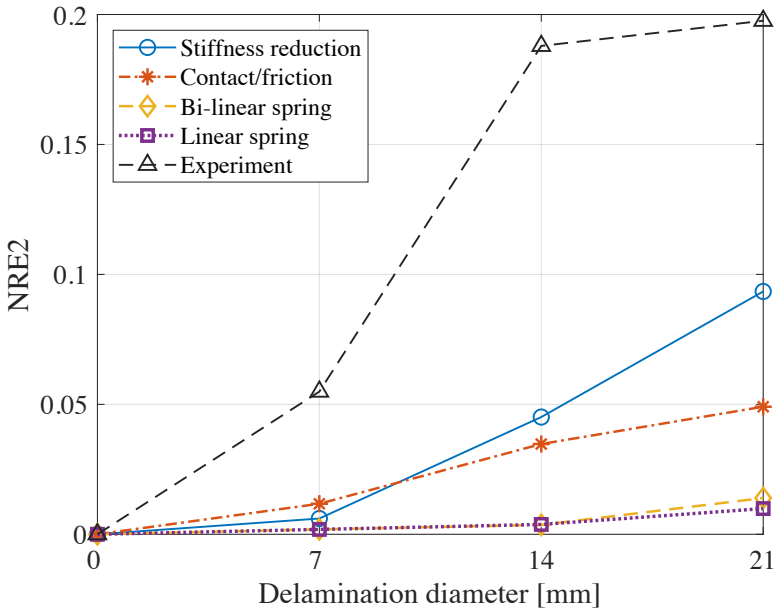

FIGURE 4.72: Comparison of NRE2 between simulations and experiment.

Another DI based Cross-Correlation Maximum Percentage Difference (CCMPD) is defined as [63]:

$$CCMPD = 1 - \frac{\left|\max\left(\hat{R}\{x(t), y(t)\}\right) - \max\left(\hat{R}\{x(t), x(t)\}\right)\right|}{\max\left(\hat{R}\{x(t), x(t)\}\right)} \tag{4.19}$$

where $\hat{R}\{x(t), y(t)\}$ indicates the cross-correlation of signals $x(t)$ and $y(t)$. Figure A.21 presents comparison of CCMPD between experimental results and numerical predictions. It can be found that for small delamination diameter (e.g., 7 mm), experimental results are quite similar to simulation results predicted by these numerical models. It should be noted that contact/friction model predicted a decrease trend at larger delamination diameter.

In Figure A.22, experimental and numerical simulation results are compared by the measurement of relative THD. Focusing on experimental curve in Figure A.22, it shows a much larger magnitude in contrast with several comparisons mentioned above (CRC, NRE, NRE2 and CCMPD). Regarding numerical predictions, the contact/friction model predicts more severe damage (for delamination diameter larger than 7 mm) compared with the other three models which present almost similar predictions.

Figure 4.75 presents the comparison of THD from the residual signals after baseline subtraction between numerical simulations and experimental results. A decrease

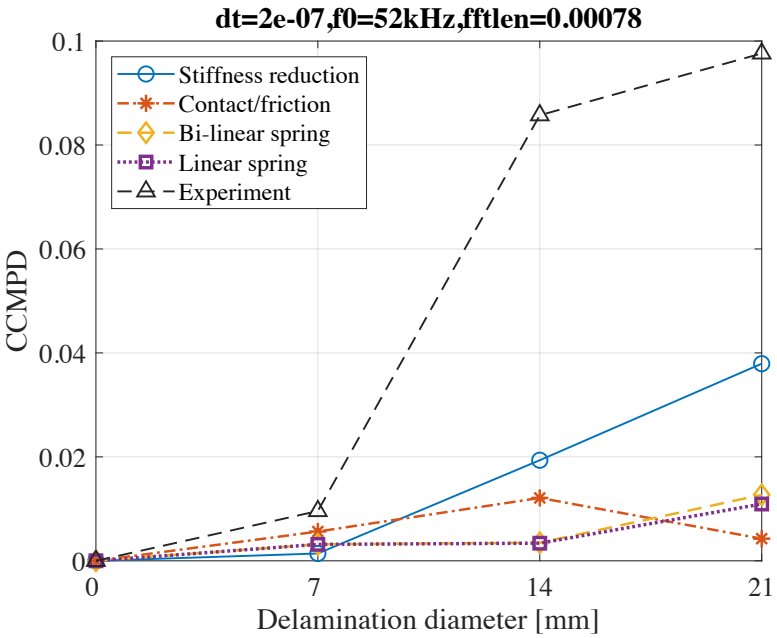

FIGURE 4.73: Comparison of CCMPD between simulations and experiment.

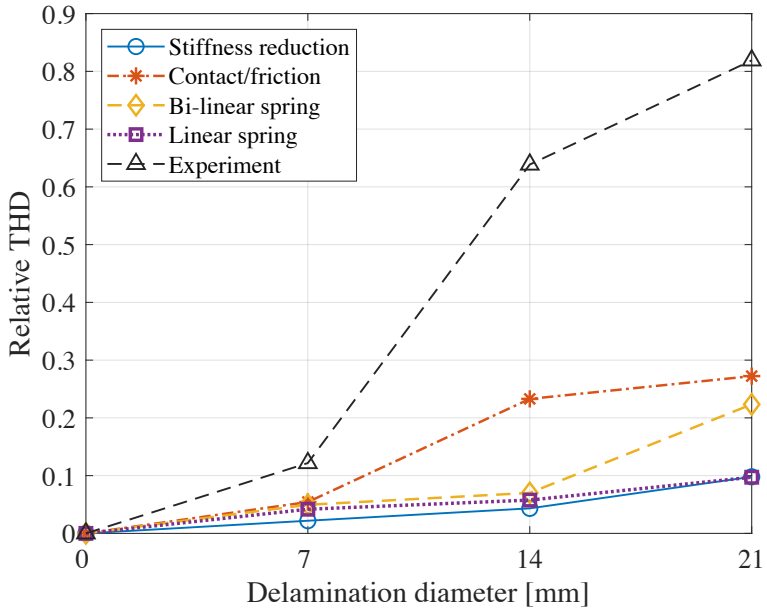

FIGURE 4.74: Comparison of relative THD between simulations and experiment.

trend can be found for experimental results and the same trend occurs in the prediction by stiffness reduction model. The other numerical models in Figure 4.75 predict an increase trend.

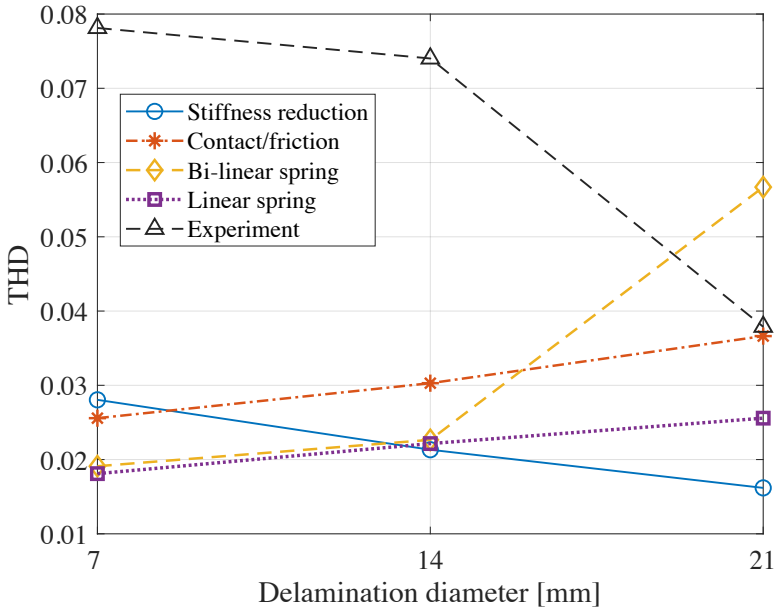

FIGURE 4.75: Comparison of THD from the residual signals after baseline subtraction between simulations and experiment.

4.4.2 Compare with literature results

In this section, the paper from Soleimanpour *et al* [26] is employed as a reference to verify the finite element model for the composite plate described in this chapter.

The structure is a composite beam manufactured from eight plies of VTM264 unidirectional carbon/epoxy prepreg at the stacking sequence of $[0/90/0/90]_s$. The lamina has a fiber volume fraction of 0.55, with density being $1538\,\mathrm{kg/m^3}$ and thickness 0.2 mm. The elastic properties of the composite lamina are listed in Table 4.10.

TABLE 4.10: Elastic properties of the composite lamina.

E1 (GPa)	E2 (GPa)	G12 (GPa)	G23 (GPa)	$\nu 12$	$\nu 13$	$\nu 23$
120.2	7.47	3.94	2.31	0.32	0.32	0.33

The dimensions of the composite beams are $285\,\mathrm{mm} \times 12\,\mathrm{mm} \times 1.6\,\mathrm{mm}$. The beam model has a 15-mm-long delamination located between the third and fourth plies, as schematically shown in Figure 4.76. In literature, the simulation was conducted in ABAQUS, and the delamination was simulated by applying a frictionless surface-to-surface contact interaction using hard contact to the delamination interfaces. A snapshot of the FE results is shown in Figure 4.77. In SDT, the beam model is established by bonding two layers composed of shell elements rigidly, but leaving the delamination region unbonded. One layer contains three plies and the other contains five plies, corresponding to the delamination in-depth position. The delamination is implemented by inserting a set of nonlinear springs with certain elastic properties that connect adjacent plies at the delamination area, as described in the previous

section. In the following study, k^{spr} is set to be 1×10^7 N/m. The time step is set to be 2×10^{-7} s and the mesh size is 0.5 mm.

The excitation is a five-cycle tone burst signal at the central frequency of 140 kHz. In literature, an out-of-plane displacement excitation was employed to excite the Lamb waves and the out-of-plane displacement was recorded in FE simulation to represent the excitation induced by a piezoceramic actuator and the acquired data by a piezoelectric sensor, respectively. However, since we have modeled the PZT actuator and sensor in SDT, the excitation is induced by PZT directly and electrical output data are obtained in our simulation tests. Two 12 mm × 6 mm × 2 mm rectangular piezo-electric solids are connected rigidly to the surface of the beam model to simulate the bonding of the piezoceramic transducers in the experiments presented in [26]. The piezoelectric elements have identical mesh at the contact surfaces with the main body of the beam to ensure the coupling between the transducer and the beam. Thus the piezo-electric solids can be used to excite elastic waves inside the specimen. The two transducers are located at 107.5 mm from the beam ends respectively.

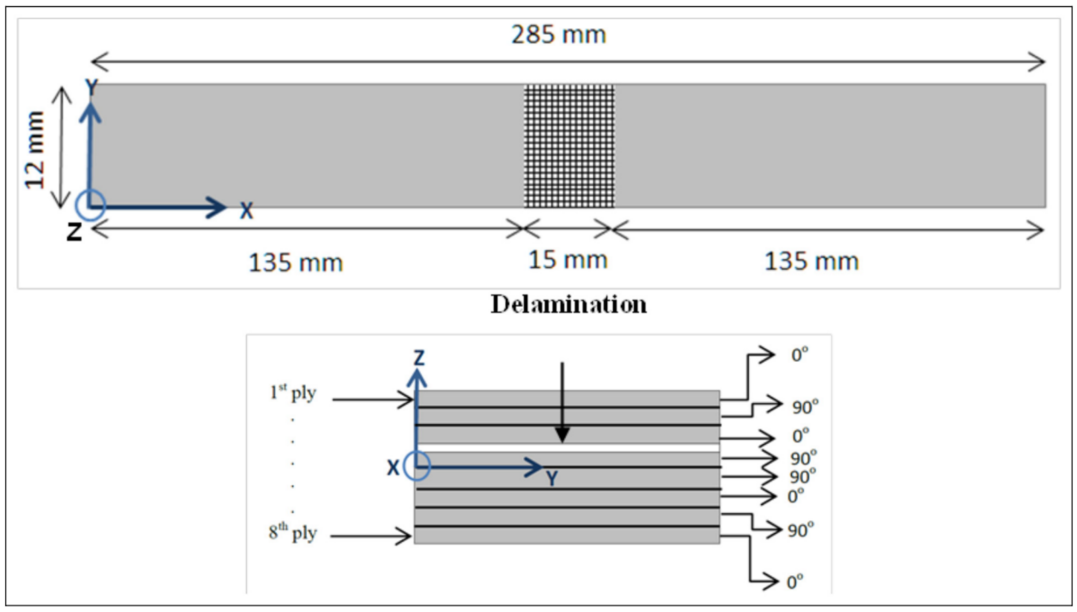

FIGURE 4.76: Schematic diagram of a composite beam specimen with delamination and its cross-section.

Result in literature is shown in Figure 4.78. From the results, it can be observed that the higher harmonics in the picture on the right, which shows the frequency amplitudes from the damaged plate, are much higher and more obvious than those shown in the results from the intact plate. A comparison between the ABAQUS results and the SDT results is shown in Figure 4.79, where the two pictures are super-imposed to have a clear vision for the comparison. In this figure, the red dash-dot line indicates the SDT results, and the blue solid line indicates the ABAQUS results conducted by us using the same configuration as in the reference paper. From the above pictures, it can be observed that in both literature and SDT results, the second harmonic is present and obvious at 280 kHz. Yet the second harmonic from

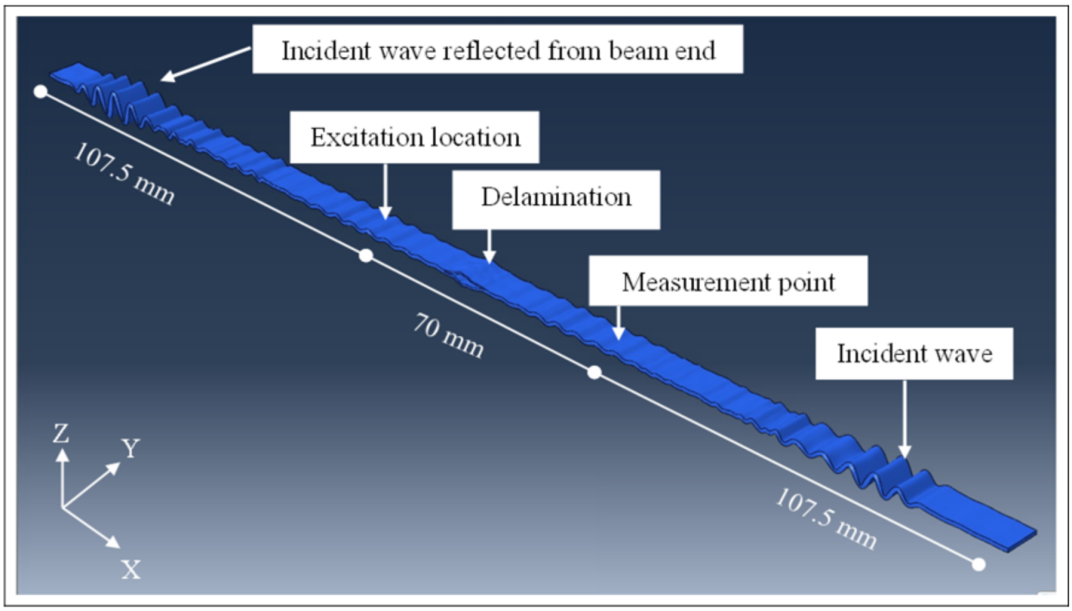

FIGURE 4.77: A typical contour snapshot of FE-simulated out-of-plane displacement of the guided wave in the composite beam with a delamination (time = 128.9 ms and scale factor = 250) [26].

SDT results is smaller than in literature. This might be due to the fact that the spring stiffness in SDT is not large enough for the contact interaction simulation. However, a large value for stiffness might cause convergence problems in the simulation process. Therefore, 1×10^7 N/m is a trade-off between numerical stability and simulation precision. Another reason might be that the dielectric and piezoelectric properties of the piezoelectric ceramics are absent in the literature, which can lead to different sensitive ranges of the piezoelectric transducers. In summary, the comparison to literature results proves that the proposed delamination model implemented in SDT is able to simulate the mechanical behavior of composite delamination.

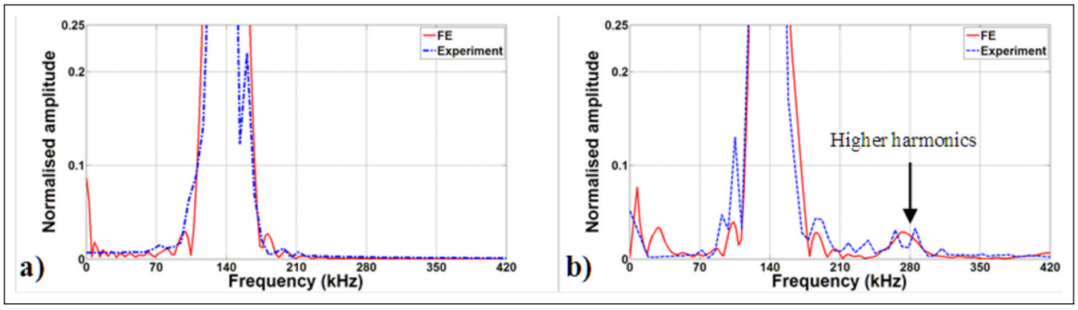

FIGURE 4.78: Normalized FFT of the signal obtained from the experiment and FE simulation: (a) intact beam and (b) beam with the delamination located between third and fourth ply. The response measured at 70 mm from excitation and 35 mm from center of the delamination [26].

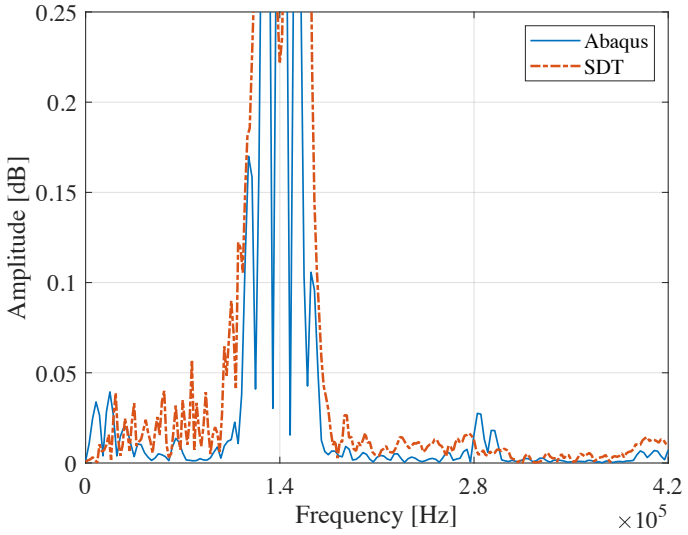

FIGURE 4.79: Comparison between ABAQUS results and SDT results using the same plate model stated in Ref.[26].

4.5 Conclusion

In this chapter, the finite element model for the composite plate specimens employed in the experiments is established. Several physical models are proposed and implemented in the finite element analysis for describing the mechanical behavior of the delamination damage. A beam model is employed with the same length, thickness and material properties, but only one element in the width direction. Model parameters are investigated for each proposed delamination model in the beam model and the sensitivity zone is obtained. Then, the sensitive parameters are applied to the original plate model and output signals are obtained. Several DIs are employed for evaluating the severity of the delamination and the nonlinear effects. Results show that the proposed models are partly able to reproduce the mechanical behavior of the delamination damage in terms of DI. Particularly, the contact/friction model induces the largest nonlinear effects rendered by DI. All the proposed models have similar behavior on the DIs employed in this study. Among all the indicators, the relative THD values show the highest sensitivity to the delamination damage.

Chapter 5

Conclusion and future work

5.1 Conclusion

In this thesis, the acoustic nonlinearities due to the presence of damage were investigated, and damage indexes are used for the evaluation of the delamination damage. In particular, a DI based on the relative total harmonic distortion was calculated and validated experimentally and numerically.

The experiments and simulations were conducted under the excitations of a variety of frequencies. In particular, a five-cycle sine wave excitation modulated by a sine window at 52kHz is employed for nonlinearity investigations. The laser shock wave technique was used to generate realistic delamination-type damages in the composite specimens and control their severities and positions. From the experimental results, it can be concluded that the presence of delamination damage adds to the nonlinearities presented in the output signals. The DI based on the relative THD was employed to evaluate the delamination severity and the nonlinear effects. Results show that the relative THD, which is based on the nonlinear characteristics of the output signals, are correlated to the damage extent and reveals high sensitivity to the nonlinearity induced by the delamination damage.

Next, the finite element model is established for the damage and the composite plate specimens employed in the experiments. Several physical models are proposed and implemented in the finite element modeling. A beam model – with the same length, thickness and material properties, but only one element in the width direction – is employed to investigate the model parameters. The parameters are investigated for each proposed delamination model in the beam model and the sensitivity zone of each parameter is obtained. Then the sensitive parameters are applied to the original plate model and output signals are obtained. The proposed DIs are employed for evaluating the delamination severity and the nonlinear effects. The nonlinear model investigations show that the proposed models are able to reproduce the mechanical behavior of the delamination damage. Particularly, the contact/friction model induces the largest nonlinear effects in terms of DI. All the proposed models have similar behavior on the proposed DIs. Among all the indicators, the relative THD values show the highest sensitivity to the delamination damage.

5.2 Future works

In future studies, the following aspects are to be focused:

- Obtained results address mechanical interaction at delamination, mainly via analyses of electrical signals on PZT elements. More direct mechanical measurements would allow for closer understanding of the response at damage and further validate modeling.
- Combinations of DI can be tested for better model identification.
- Further investigations should include wider parametric exploration of frequency and amplitude range, as well as other signal types.
- Obtained results and mechanisms will be applied to the SHM process and the presented finite element models can be used for the application of damage detection and quantification, especially for barely invisible damages.

Appendix A

Résumé de la thèse

A.1 Introduction

A.1.1 Context

L'un des problèmes les plus importants en ingénierie est la surveillance et la détection précoce des dommages structurels pour prévenir les défaillances catastrophiques[1, 2, 3]. Ce processus est appelé Structural Health Monitoring (SHM) et sa mise en œuvre devrait apporter des améliorations considérables en termes de sécurité et de coûts de maintenance [1]. Le SHM est une technologie révolutionnaire et innovante pour déterminer l'intégrité structurale des structures et est principalement utilisée dans l'ingénierie aéronautique, le génie civil, etc. Elle est développée à partir d'essais non destructifs traditionnels. Cette technologie utilise un réseau de transducteurs intégré à la structure pour effectuer une détection en ligne en temps réel et obtenir des informations en temps réel sur l'état de la structure, les conditions de fonctionnement et l'environnement de service. Sur la base des données du capteur, des résultats de diagnostic en temps réel sont obtenus, l'état de santé de la structure est prédit et la décision de contrôle correspondante est assistée. Dans l'industrie aéronautique, la mise en œuvre de la technologie SHM des aéronefs peut améliorer efficacement la sécurité de la structure des aéronefs, augmenter considérablement la sécurité des vols, réduire les coûts de maintenance des aéronefs et prolonger les cycles de service.

Ces dernières années, les matériaux composites sont de plus en plus utilisés dans divers domaines industriels et notamment dans l'aéronautique en raison de leur faible densité, de leur résistance et de leur rigidité spécifiques élevées. Pour les avions commerciaux, le pourcentage de matériaux composites renforcés de fibres peut atteindre 50% de la masse. Malgré de grands avantages, les matériaux composites ne sont pas exempts d'inconvénients. En particulier, les composites peuvent être soumis à divers types de dommages. Étant donné que la dégradation des composites se produit généralement à l'intérieur des composites, les dommages sont généralement invisibles et difficiles à observer. Par conséquent, l'application de SHM aux composites pour la détection des dommages est cruciale.

Le délaminage est l'un des types de dommages les plus courants dans les matériaux composites. Elle peut être définie comme la séparation des plis composites adjacents. Les dommages de type délaminage peuvent gravement dégrader les performances des

composites et doivent être identifiés à temps. Dans cette thèse, nous nous concentrons sur la détection et la quantification des dommages de type délaminage dans les stratifiés composites.

A.1.2 Objectif de la thèse

L'objectif de cette thèse est de mieux comprendre physiquement l'interaction des ondes de Lamb avec un délaminage réaliste, qui, en tant qu'interface de contact, peut présenter un comportement non linéaire. Plus précisément, son objectif est d'étudier le mécanisme physique de la génération des phénomènes non linéaires, c'est-à-dire les super-harmoniques dues à la présence du dommage de délaminage dans une plaque composite, et d'évaluer quantitativement les influences de l'existence du délaminage sur les propriétés acoustiques non linéaires. des plaques composites. Pour y parvenir, des expérimentations et des simulations par éléments finis sont menées. Plusieurs modèles représentant le comportement mécanique des dommages de délaminage sont présentés pour étudier l'interaction entre l'onde de Lamb et un dommage de délaminage réel bien contrôlé. Quatre plaques composites contenant différentes tailles de délaminage sont utilisées pour étudier l'influence de la taille des dommages sur la non-linéarité acoustique, dont une plaque composite ne contenant aucun dommage comme référence. Plusieurs indices d'endommagement (ID) sont analysés, en particulier ceux sensibles aux réponses non linéaires, comme le THD relatif, afin d'évaluer la sensibilité des ID aux non-linéarités induites par l'endommagement.

A.2 Expériences sur la détection des dommages dans les plaques composites

A.2.1 Spécimens composites

Les échantillons utilisés dans les expériences sont fabriqués à partir de composites de polymère renforcé de fibres de carbone (CFRP). L'épaisseur de chaque pli est 0.14 mm. Chaque plaque contient 16 plis à la séquence d'empilement de $[0°/90°]_8$ avec les dimensions de $315 \times 100 \times 2.24$ mm^3. Les propriétés matérielles des spécimens sont répertoriées dans Table A.1

Table A.1: Propriétés du matériau de l'éprouvette composite [60].

Poisson's ratio ν	E_{11}(per ply)	E_{22}(per ply)	G_{12}(per ply)	Mass density ρ
0.3	140 GPa	9 GPa	4.5 GPa	1594 kg/m^3

Dans nos expériences, quatre plaques composites sont considérées ici : une plaque intacte ne contenant aucun dommage, une plaque contient un impact laser représentant le dommage de type délaminage au diamètre de 7 mm, une plaque contenant deux impacts laser représentant le dommage de type délaminage au diamètre de 14 mm et

une plaque contenant trois impacts laser représentant le dommage de type délaminage au diamètre de 21 mm.

Le schéma est comme indiqué dans Figure A.1. Les dommages de délaminage ont été introduits dans des échantillons de manière calibrée en utilisant la technique des ondes de choc laser (Laser shock wave technique, LSWT).

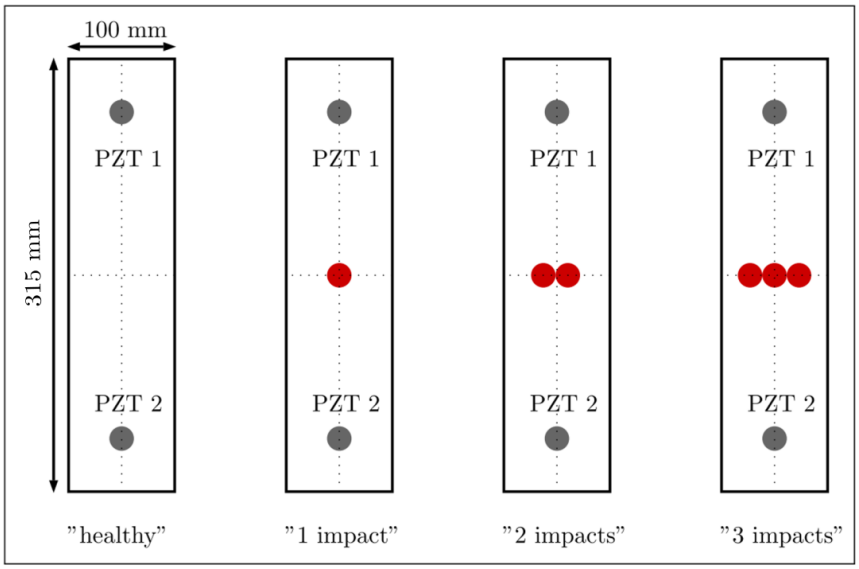

FIGURE A.1: Schéma des quatre éprouvettes et des positions des délaminations [51].

Figure A.2 montre un exemple d'image C-scan des dommages de délaminage calibrés par choc laser. Dans cet exemple, la taille et la position en profondeur de ce délaminage est précisément déterminée en contrôlant l'énergie et le retard temporel des faisceaux laser [51, 59].

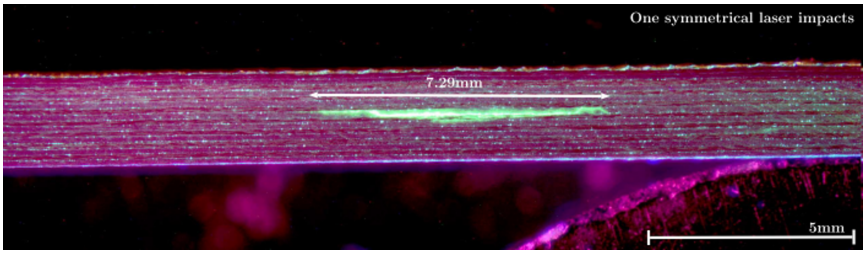

FIGURE A.2: Vue latérale du délaminage à l'intérieur de l'éprouvette composite [51].

Chaque plaque composite est équipée de deux éléments piézoélectriques (PZT NCE51, fabriqué par Noliac), comme le montre la Figure A.3. Ces éléments piézoélectriques, qui peuvent fonctionner à la fois en modes d'actionnement et de détection, sont collés en permanence à la surface de la plaque composite pour garantir qu'ils ont les mêmes effets de couplage. Lors de la réalisation d'expériences SHM, un PZT est utilisé comme émetteur (PZT1) et l'autre est utilisé comme récepteur de signal (PZT2). Les propriétés des éléments piézoélectriques sont répertoriées dans le tableau A.2

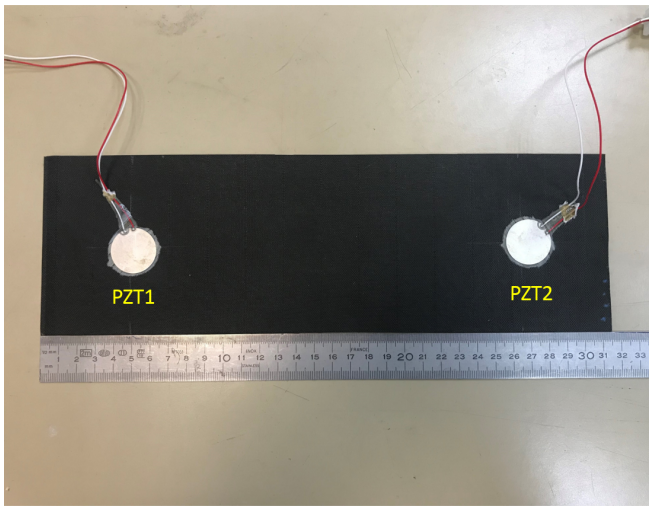

FIGURE A.3: Une éprouvette composite équipée de deux PZTs.

TABLE A.2: Mass and size of NCE51 from Noliac.

Diameter	Thickness	Weight	Mass density
25 mm	0.5 mm	1.86 g	7600 kg/m^3

A.2.2 Description du système SHM

Les expériences sont menées à l'aide d'un système SHM développé par le laboratoire de l'auteur. Ce système est composé de l'échantillon, des transducteurs piézoélectriques, du générateur de signal, de l'amplificateur et du système d'acquisition de données. Une image du système expérimental SHM est montrée dans la Figure A.4a. L'éprouvette est suspendue à une poutre de manière à ce que les bords de la structure soient libres de toute contrainte extérieure pour éviter que l'éprouvette n'interagisse avec d'autres supports (ex: banc d'essai).

La méthode pitch-catch est utilisée pour la détection des dommages de délaminage. La figure A.4b montre un schéma illustrant la procédure pour les expériences SHM. Lors de la réalisation d'expériences, un signal d'excitation électrique est généré et amplifié. Ensuite, ce signal est transmis au PZT1 (utilisé comme actionneur), qui transforme le signal électrique en une vibration mécanique (effet piézoélectrique), générant ainsi des ondes élastiques à l'intérieur de la structure d'essai. Les ondes élastiques se propagent à travers la région endommagée à l'intérieur de l'échantillon et arrivent à PZT2. Puis PZT2 (utilisé comme capteur) mesure la déformation mécanique de la structure, qui est ensuite convertie en signaux électriques.

Un système d'acquisition Nicolet Genesis LDS enregistre les signaux mesurés. Un multiplexeur permet également d'automatiser la procédure d'excitation-acquisition, évitant ainsi de connecter et de déconnecter les câbles des PZT lorsqu'ils agissent en mode « actionneur » ou en mode « capteur ». En effet, cette automatisation est indispensable lorsqu'un grand nombre d'acquisitions de données doivent être réalisées sur plusieurs structures de test. Enfin, toutes les données collectées sont post-traitées

à l'aide du logiciel MATLAB.

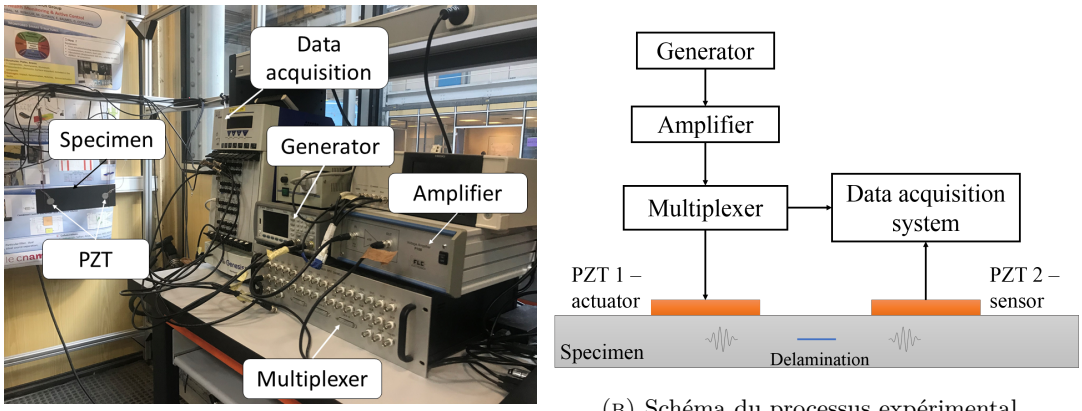

(A) Le montage expérimental.

(B) Schéma du processus expérimental.

FIGURE A.4: Système expérimental.

A.2.3 Sélection des signaux d'entrée

Pour la sélection de la forme d'onde, des formes sinusoïdales pures et un signal sinusoïdal fenêtré sont souvent utilisés comme signaux d'entrée dans SHM. En particulier, ce dernier est largement utilisé pour sa bande passante étroite, son énergie centralisée et sa caractéristique de non-dispersion [62]. Dans cette étude, les excitations sinusoïdales continues et les excitations sinusoïdales modulées sont utilisées comme formes de signal d'entrée.

De plus, il est également important de déterminer la fréquence d'entrée puisque les ondes fondamentales et les harmoniques supérieures dépendent toutes de la fréquence d'entrée. Dans cette section, les fréquences de résonance PZT sont calculées analytiquement et numériquement pour l'analyse de la fréquence d'excitation.

La fréquence de résonance PZT dans la direction circulaire peut être calculée comme suit [1]:

$$f_r = \frac{N_p}{2r} \tag{A.1}$$

où f_r indique la fréquence de résonance du PZT, N_p représente la constante de fréquence du disque PZT et r est le rayon. Dans cette étude, le N_p des disques PZT est de 1300 fourni par le fabricant du PZT. Par conséquent, la fréquence de résonance du disque PZT dans la direction radiale est de 52 kHz. Par ailleurs, une simulation par éléments finis est menée dans ABAQUS pour identifier le mode dans le plan du disque PZT en complément du calcul analytique. La fréquence de résonance du premier mode dans la direction radiale se produit à 51,6 kHz, environ à 52 kHz. La distribution de l'amplitude du déplacement PZT est illustrée sur la figure A.5. Par conséquent, à partir des investigations ci-dessus, la fréquence d'entrée peut être de 52 kHz.

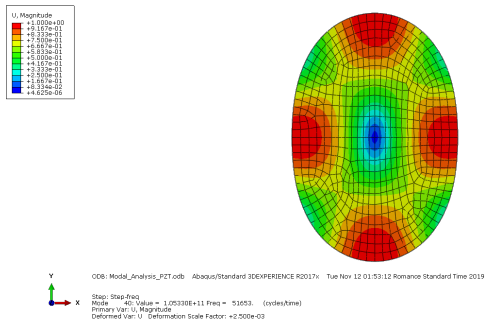

FIGURE A.5: Résultats de simulation de l'analyse de fréquence naturelle du disque PZT.

A.2.4 Indice de dégâts

Afin d'évaluer la sévérité du délaminage, des indices de dommages (DI) sont utilisés dans cette étude. En particulier dans cette étude, les effets acoustiques non linéaires dans la propagation des ondes de Lamb dans les plaques composites sont focalisés et utilisés pour la détection du délaminage. La distorsion harmonique totale (THD) est une valeur courante utilisée pour mesurer la distorsion harmonique présente dans un signal dans un système audio. Elle est définie comme le rapport de la somme des puissances de toutes les composantes harmoniques à la puissance de la fréquence fondamentale :

$$THD_n = \frac{\sqrt{\sum_{j=2}^{n} A_j^2}}{A_1} \tag{A.2}$$

où n est l'ordre maximal calculé des harmoniques supérieures, A_1 indique l'amplitude de la fréquence fondamentale et A_j représente l'amplitude de la super-harmonique $j$ième ordre.

Ici, dans notre étude, en raison de la limitation des équipements de test (les spectres de fréquence au-delà des troisièmes harmoniques sont tous des bruits de fond), nous avons défini n comme $n = 3$, ce qui implique que seules les deuxième et troisième harmoniques sont concernées, et ce THD devient

$$THD_3 = \frac{\sqrt{A_2^2 + A_3^2}}{A_1} \tag{A.3}$$

où A_2 et A_3 sont respectivement les amplitudes des deuxième et troisième harmoniques. Ainsi, la valeur THD dans cette étude peut être utilisée pour évaluer l'énergie totale des deuxième et troisième harmoniques par rapport à l'énergie de la fréquence fondamentale des signaux de sortie.

Pour évaluer quantitativement comment les dommages de délaminage dans les spécimens affectent les effets acoustiques non linéaires, un indice d'endommagement (DI) est proposé sur la base de la valeur THD relative des signaux de sortie du boîtier

endommagé par rapport aux signaux de sortie du boîtier sain, qui est défini comme

$$\widehat{THD} = \frac{THD_3^{damage} - THD_3^{healthy}}{THD_3^{healthy}} \tag{A.4}$$

où THD_3^{damage} et $THD_3^{healthy}$ sont respectivement la valeur THD ($n = 3$) du boîtier endommagé et du boîtier non endommagé. Cette DI évalue la différence entre l'énergie des harmoniques de second et troisième ordre du cas endommagé et celle du cas sain.

De plus, d'autres ID sont employés [63], qui sont définis sur la base des caractéristiques linéaires extraites des signaux de sortie dans le domaine temporel. Un DI basé sur le coefficient de corrélation de Pearson entre les signaux du boîtier endommagé et du boîtier intact est défini comme [63]:

$$CRC = 1 - r[x(t), y(t)] \tag{A.5}$$

où $x(t)$ est le signal de sortie de la plaque saine, $y(t)$ est le signal de sortie de la plaque endommagée et $r(x, y)$ est le coefficient de corrélation de Pearson entre les signaux x et y. Si un signal a des observations scalaires N, alors le coefficient de corrélation entre le signal de référence x et le signal courant y est défini comme [63]:

$$r(x, y) = \frac{1}{N-1} \sum_{i=1}^{N} \left(\frac{x_i - \mu_x}{\sigma_x} \right) \left(\frac{y_i - \mu_y}{\sigma_y} \right) \tag{A.6}$$

où μ_x et σ_x sont la moyenne et l'écart type du signal x, et μ_y et σ_y sont respectivement la moyenne et l'écart type du signal y.

Une autre DI est définie en fonction de l'énergie résiduelle normalisée entre le signal courant et le signal de référence :

$$NRE = \frac{\int_0^T (x(t) - y(t))^2 \, dt}{2 \times \left(\int_0^T x(t)^2 \, dt + \int_0^T y(t)^2 \, dt \right)} \tag{A.7}$$

A.2.5 Résultats expérimentaux

A.2.5.1 Excitation sinusoïdale

Les résultats de l'entrée d'onde sinusoïdale sont illustrés dans cette section. La fréquence d'excitation est choisie à 52 kHz et l'amplitude est de 10 V du pic à zéro.

La figure A.6 montre la réponse typique de la structure non endommagée et endommagée soumise à une excitation sinusoïdale respectivement. Dans les deux diagrammes, on peut observer que les signaux de réponse temporelle ont tendance à se stabiliser après une courte période de zone transitoire.

Figure A.7a montre une comparaison des réponses dans le domaine fréquentiel pour la plaque intacte et la plaque endommagée contenant deux impacts. Les courbes des spectres de fréquence sont obtenues en appliquant une transformée de Fourier rapide (FFT) aux signaux bruts reçus par le PZT et sont normalisées par rapport à

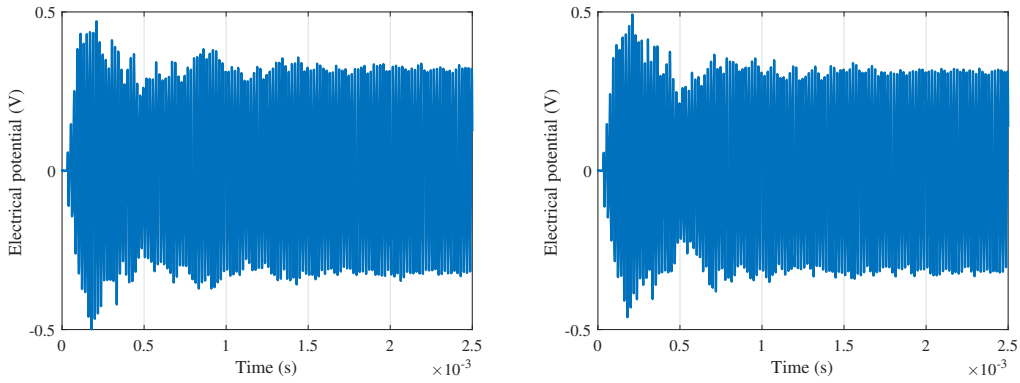

FIGURE A.6: Signaux de sortie typiques des excitations sinusoïdales du boîtier non endommagé (à gauche) et du boîtier endommagé avec deux impacts (à droite).

leurs valeurs maximales respectivement. Les magnitudes sont indiquées en échelle de dB. A partir de cette figure, à l'exception du pic principal à la fréquence fondamentale, plusieurs autres pics à des multiples de la fréquence fondamentale peuvent être clairement observés. Dans l'encart de la figure A.7a, deux super-harmoniques sont données à titre de comparaison : les harmoniques de deuxième et troisième ordre ; les amplitudes des deuxième et troisième harmoniques du spectre de la plaque à deux impacts sont plus grandes que celles de la plaque non endommagée. On peut conclure que la présence de l'impact de délaminage amplifie les effets non linéaires.

La figure A.7b montre le spectre de fréquence du signal résiduel entre la plaque à deux impacts et la plaque intacte, qui est obtenu en soustrayant le signal de réponse de la plaque intacte de la réponse de la plaque à deux impacts et en transformant au domaine fréquentiel. Notez que le spectre est normalisé à la valeur maximale. Dans cette figure, les harmoniques les plus hautes peuvent évidemment être observées. Cela indique que de fortes non-linéarités existent dans le signal de différence de la plaque endommagée par rapport au cas de référence.

Ensuite, les signaux de sortie sont étudiés en termes de DI basé sur le THD relatif et les résultats sont présentés dans la Figure A.8. Afin d'étudier les effets de la taille de la délamination sur la non-linéarité, les mêmes signaux d'entrée sont testés sur les quatre échantillons. La figure A.8a montre la variation de DI basée sur le THD relatif par rapport au nombre d'impacts contenus dans les échantillons composites avec des amplitudes d'excitation de 10V et 50V respectivement. Pour les deux amplitudes d'excitation, ce DI augmente de manière monotone avec l'augmentation du nombre d'impacts.

Ensuite, les effets de l'amplitude d'excitation sur la non-linéarité sont étudiés. Pour mettre cela en œuvre, cinq amplitudes d'excitation différentes, 10V, 20V, 30V, 40V et 50V sont excitées sur les quatre spécimens. Les DI basés sur le THD relatif sont tracés pour chaque spécimen par rapport aux amplitudes d'excitation, et les résultats sont présentés sur la figure A.8b. À partir de cette figure, on peut observer qu'avec l'augmentation de l'amplitude d'excitation, les variations des spécimens à un

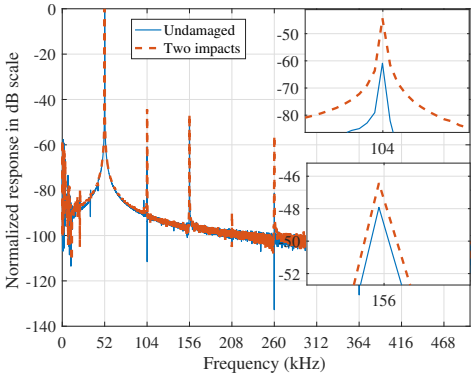

(A) Comparaison entre plaque intacte et plaque à double impact.

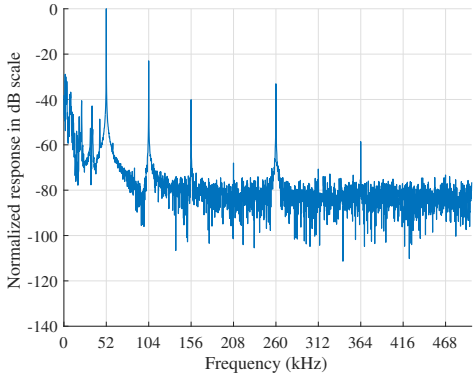

(B) Signal de différence entre la plaque endommagée à deux impacts et la plaque intacte.

FIGURE A.7: Spectre de fréquence des signaux de sortie à partir de signaux d'entrée sinusoïdaux continus. Chaque courbe est dérivée du signal correspondant dans le domaine temporel à l'aide d'une transformée de Fourier rapide et est normalisée à son amplitude maximale.

impact et à deux impacts augmentent d'abord puis diminuent légèrement, tandis que la variation de la plaque à trois impacts montre une tendance légèrement décroissante. avec de petites fluctuations. C'est parce qu'il existe d'autres caractéristiques non linéaires dans ce système, et la non-linéarité acoustique en fait partie. Pour toutes les amplitudes d'excitation, les valeurs relatives de THD augmentent avec le nombre croissant d'impacts de dommages, indiquant que le THD relatif est sensible à la sévérité des dommages de délaminage.

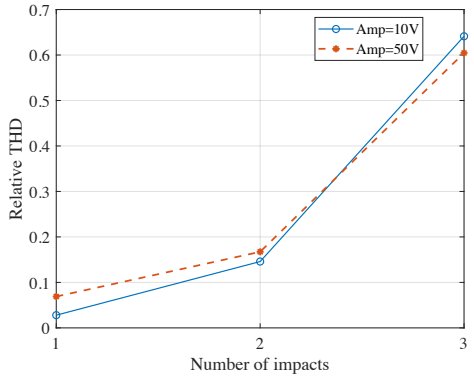

(A) Relative THD against number of impactsv.

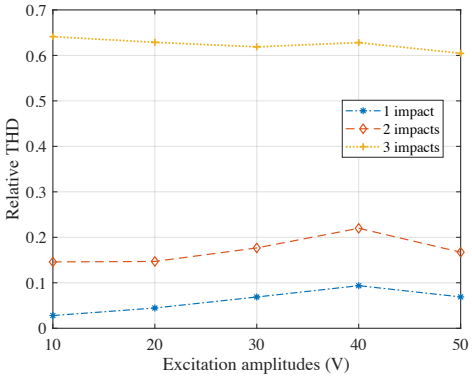

(B) THD relatif par rapport à l'amplitude d'excitation.

FIGURE A.8: Etude du THD relatif sur les amplitudes d'excitation et différents spécimens.

A.2.5.2 Excitation sinusoïdale modulée

Dans cette section, une onde sinusoïdale à cinq cycles modulée par une fenêtre sinusoïdale a été utilisée comme signal d'excitation. Les signaux de sortie de la plaque

intacte et de la plaque à deux impacts dans le domaine fréquentiel sont illustrés à la figure A.9.

La figure A.9a montre la comparaison des réponses dans le domaine fréquentiel pour la plaque non endommagée et la plaque endommagée contenant deux impacts soumis à l'excitation d'onde modulée. A partir de cette figure, à l'exception du pic à la fréquence fondamentale, on distingue deux pics perceptibles correspondant respectivement aux deuxième et troisième harmoniques (104kHz et 156kHz). Dans l'encart de la Figure A.9a, les harmoniques sont données à titre de comparaison ; les amplitudes des deuxième et troisième harmoniques du spectre de la plaque à deux impacts sont plus grandes que celles de la plaque non endommagée. On peut conclure que les non-linéarités sont amplifiées par la présence des impacts de délaminage. Cela peut également être prouvé par le spectre de fréquence du signal résiduel entre la plaque endommagée par deux impacts et la plaque non endommagée illustrée sur la figure A.9b. Notez que la réponse en fréquence est normalisée à la valeur maximale. Par conséquent, les super-harmoniques, en particulier les deuxième et troisième harmoniques, fournissent un outil sensible pour la détection du délaminage par impact laser dans les plaques composites.

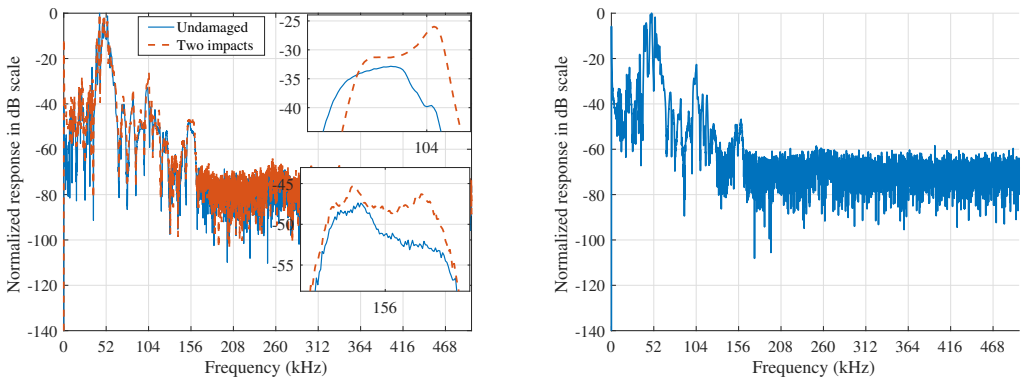

(A) Comparaison entre plaque intacte et plaque à double impact.

(B) Signal de différence entre la plaque à double impact et la plaque intacte.

FIGURE A.9: Spectre de fréquence des signaux de sortie à partir des signaux d'entrée modulés. Chaque courbe est normalisée à son amplitude maximale.

Ensuite, les effets de la taille de la délamination et de l'amplitude d'excitation sur la non-linéarité acoustique sont étudiés et les résultats sont présentés sur la figure A.10.

La figure A.10a affiche la variation du DI proposé en fonction du nombre d'impacts de délamination avec l'amplitude d'excitation de 10V et 50V. A partir de cette figure, on peut observer que le DI augmente de manière monotone avec le nombre d'impacts de délaminage quelle que soit l'amplitude d'excitation. Cela indique que le DI proposé est remarquablement sensible à la taille du délaminage.

La figure A.10b présente la variation de DI en fonction de l'amplitude d'excitation sur différents spécimens. L'amplitude d'excitation varie de 10V à 50V au pas de 10V.

A partir de cette figure, on peut observer que le DI affiche des tendances plutôt plates avec quelques petites variations. Pour le spécimen à impact unique, la courbe de DI montre une tendance légèrement croissante avec l'augmentation de l'amplitude d'excitation. Pour les spécimens à deux et trois impacts, les courbes DI sont presque plates. Cette tendance à la variation pourrait être due aux non-linéarités du système.

En conclusion, par rapport à l'influence de la taille des dommages, l'amplitude d'excitation a des effets mineurs sur le DI proposé.

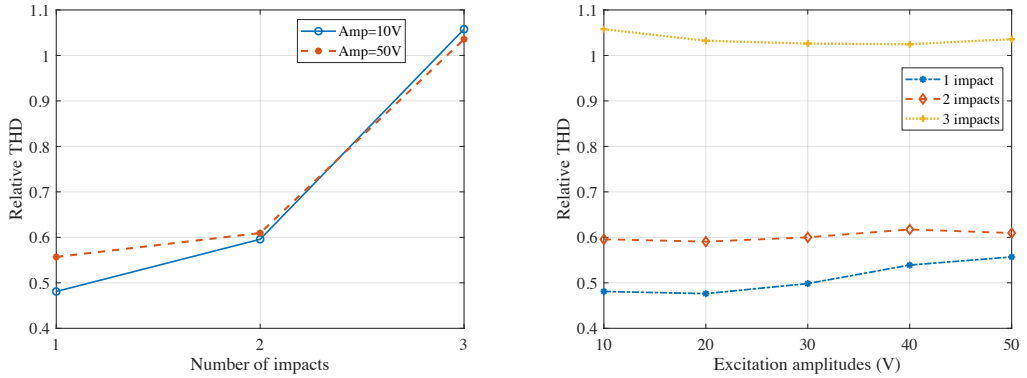

(A) THD relatif par rapport au nombre d'impacts.

(B) THD relatif par rapport à l'amplitude d'excitation.

FIGURE A.10: Etude du THD relatif sur différentes amplitudes d'excitation et différents spécimens.

A.3 Simulations par éléments finis

A.3.1 Modèles éléments finis pour plaques composites et délaminage

La méthode des éléments finis (EF) est utilisée pour simuler la propagation des ondes de Lamb dans la plaque composite laminée à plis croisés qui est disponible expérimentalement. La figure A.11 montre le modèle EF de la plaque composite construite dans MATLAB à l'aide de Structural Dynamics Toolbox (SDT). La plaque composite contenant 16 plis est modélisée en collant deux couches de coque ensemble à l'aide de liaisons rigides à l'exception de la région de délaminage. Chaque couche contient 8 plis, assurant que la délamination se situe au niveau du plan médian de la plaque composite. Le délaminage est situé au centre dans la direction dans le plan. Puisque le modèle est symétrique par rapport à l'axe x, seule la moitié de la plaque est modélisée et une condition aux limites symétrique est appliquée à l'axe longitudinal. Les propriétés des matériaux sont répertoriées dans le tableau A.3.

Deux patchs piézoélectriques (PZT) sont collés à la surface de la plaque pour la génération et la détection des ondes de Lamb. Le diamètre des PZT est de 25 mm. Le potentiel électrique des surfaces inférieures des éléments PZT est fixé à zéro. Le signal d'entrée est appliqué sur la surface supérieure du PZT d'actionnement et le potentiel électrique sur la surface supérieure du PZT de détection est mesuré. Une

onde sinusoïdale à 5 cycles modulée par une fenêtre sinusoïdale à 52 kHz est utilisée comme signal d'entrée.

Une plaque intacte est modélisée comme une référence avec toutes les régions de la plaque liées ensemble à l'aide de connexions rigides. La taille globale du maillage est définie sur 1 mm et un maillage plus fin (0.5 mm) est utilisé localement au niveau de la région de délaminage. Le pas de temps est de 2×10^{-7} s. Des éléments quadratiques sont utilisés pour assurer l'exactitude des résultats. L'amortissement de Rayleigh est utilisé dans cette étude, les coefficients d'amortissement sont

$$\alpha = 0, \quad \beta = 4.3 \times 10^{-8} \tag{A.8}$$

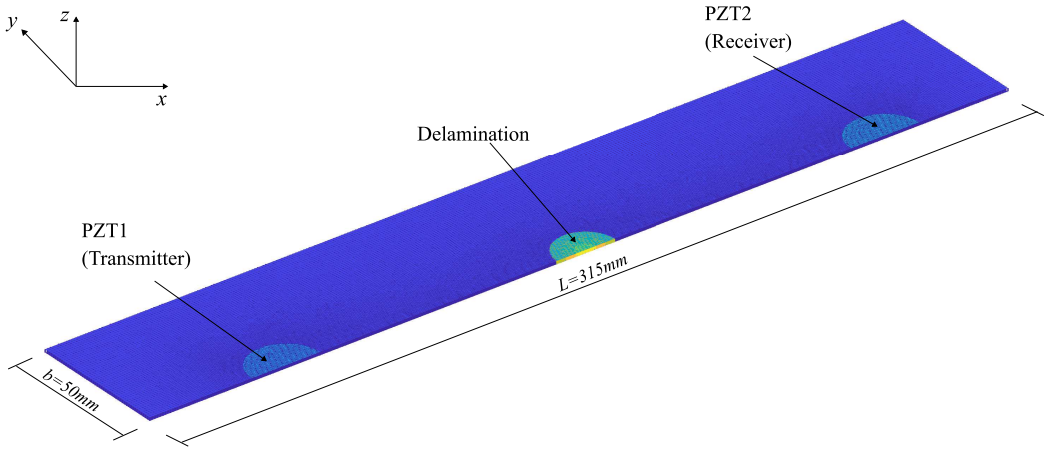

FIGURE A.11: Schéma du modèle éléments finis en trois dimensions.

TABLE A.3: Propriétés matérielles des plaques composites.

Poisson's ratio ν	0.3
E_{11}(per ply)	149 GPa
E_{22}(per ply)	9 GPa
E_{12}(per ply)	4.9 GPa

A.3.2 Modèle de dommages pour les dommages de type délaminage dans les composites

Dans cette section, nous étudierons plusieurs modèles physiques pour le délaminage et identifierons le paramètre du modèle. Plusieurs modèles de délaminage sont proposés et introduits.

A.3.2.1 Modèle de réduction de rigidité

Dans ce modèle, la rigidité locale au niveau de la région endommagée est réduite, simulant ainsi les effets de l'endommagement par délaminage sur l'ensemble de la

rigidité de la structure. Nous avons défini un coefficient de réduction $Ecoef$ et appliqué ce coefficient aux modules d'Young et de cisaillement au niveau de la région de délaminage. De cette manière, la rigidité au niveau de la région de délaminage est réduite. Notez que les surfaces supérieure et inférieure de la région de délaminage dans ce modèle sont désossées ensemble à l'aide de connexions rigides, comme le montre Figure A.12.

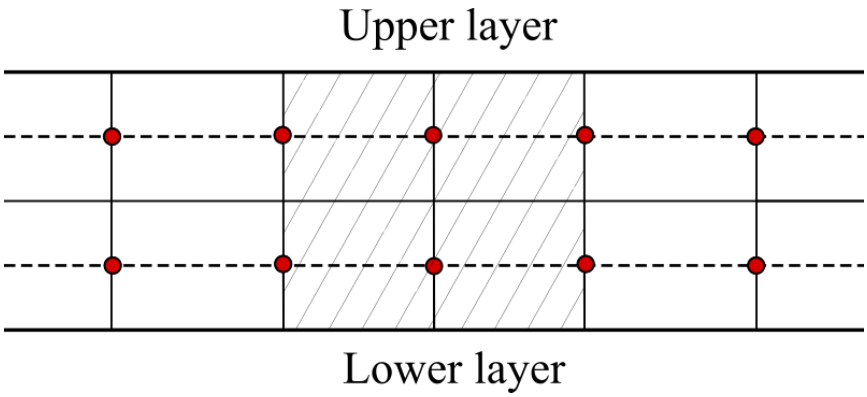

FIGURE A.12: Schéma du modèle de réduction de rigidité.

A.3.3 Modèles à ressort

Ce modèle est mis en œuvre en appliquant un ensemble d'éléments ressort reliant les nœuds des couches supérieure et inférieure répartis au niveau de la région de délaminage, pour modéliser les interactions mécaniques entre les interfaces de délaminage.

La figure A.13 montre le schéma du modèle de ressort non linéaire. Dans cette figure, les lignes pointillées indiquent respectivement le plan médian des couches supérieure et inférieure du modèle de plaque. Les points rouges indiquent les nœuds sur les couches supérieure et inférieure. Les nœuds de la couche supérieure sont connectés aux nœuds correspondants de la couche inférieure à la même position dans le plan. En dehors de la région de délaminage, les couches supérieure et inférieure sont liées par une liaison rigide, tandis qu'à l'intérieur de la région de délaminage, les couches sont reliées par des éléments ressorts. k^{spr} indique la raideur du ressort.

A.3.3.1 Modèle à ressort linéaire

Dans ce modèle, une relation linéaire entre la force du ressort et le déplacement relatif entre les couches supérieure et inférieure dans la direction hors du plan est définie. Le rapport entre la force et le déplacement relatif est défini comme la raideur du ressort.

A.3.3.2 Modèle de ressort non linéaire

(a) Interaction hors du plan

Dans la direction hors du plan, l'interaction entre deux surfaces de délaminage est souvent modélisée comme un contact "dur", c'est-à-dire que lorsque deux surfaces sont en contact, la force normale tend à les séparer pour éviter la pénétration entre

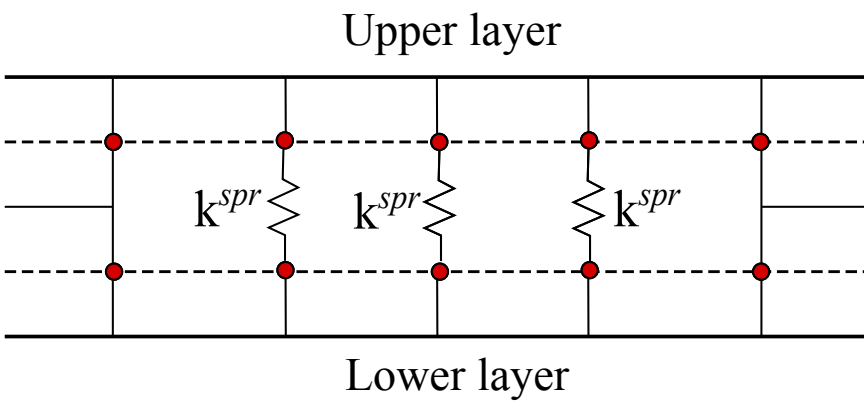

FIGURE A.13: Schéma de la modélisation de l'interaction de surface dans la région de délaminage en appliquant des ressorts non linéaires.

deux surfaces, et lorsque les deux les surfaces sont séparées, aucune force n'est exercée sur elles. Ainsi, des ressorts non linéaires sont utilisés dans ce modèle, et une relation bilinéaire simplifiée entre la déformation et la force est attribuée aux ressorts.

Figure A.14 montre la relation entre la force du ressort et les déplacements relatifs entre les surfaces supérieure et inférieure du délaminage dans la direction hors du plan. F_z est la force du ressort dans la direction normale, u_z est les déplacements relatifs dans la direction hors du plan entre les deux interfaces de délaminage, et k^{spr} indique la rigidité du ressort dans la zone linéaire. Lorsque u_z est positif, indiquant que les surfaces de contact sont séparées et qu'aucune pénétration ne se produit, la raideur du ressort est de 0, formant une condition aux limites libre. Lorsque u_z est négatif, ce qui signifie qu'une pénétration se produit, une rigidité élevée est attribuée aux ressorts pour maintenir la pénétration aussi petite que possible.

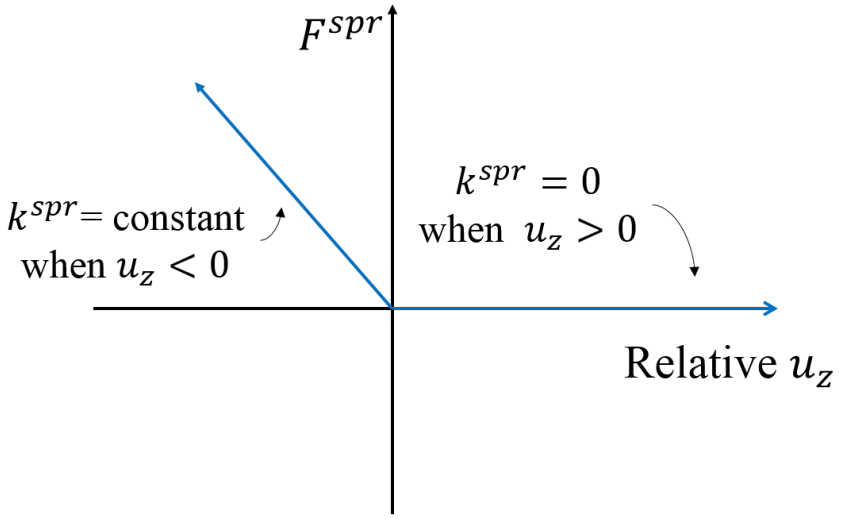

FIGURE A.14: Relation entre la force et le déplacement relatif des ressorts non linéaires dans la région de délaminage.

(b) Interaction dans le plan

Dans la direction dans le plan, le frottement est l'interaction dominante des interfaces de délaminage. Ainsi, le frottement est défini sur les interfaces du délaminage.

Pour ce faire, un modèle de frottement visqueux modifié est mis en œuvre pour simuler le comportement mécanique dans le plan du délaminage.

La figure A.15 montre un schéma du modèle dans le plan illustrant la relation non linéaire entre la force d'interaction et la vitesse relative. La relation force-vitesse dans la plage $(-v_f, v_f)$ est linéaire, tandis que la force reste constante dans les autres parties. Dans ce modèle défini par quatre points, v_f et F_0 sont des paramètres définissant ce modèle non linéaire. Ils sont dérivés de cette manière : d'abord, un modèle de plaque sans aucune interaction dans le plan ou hors du plan dans la région de délaminage est utilisé et la réponse de ce modèle est calculée. Ensuite, la vitesse du nœud central du délaminage le long de la direction de propagation des ondes est dérivée, et la valeur maximale de la réponse en vitesse est extraite. Cette valeur maximale est une référence pour définir la valeur v_f. Puisque nous espérons que la réponse en vitesse des nœuds au niveau de la région de délaminage couvre à la fois la zone linéaire et non linéaire dans le modèle mécanique dans le plan, le v_f appliqué ne peut être ni trop grand ni trop petit. Si ce paramètre v_f est trop grand, les paires $(v_x,\ F_x)$ pourraient être toutes dans la zone de plateau et seuls quelques points se situent dans la zone linéaire. Si ce paramètre v_f est trop petit, les paires $(v_x,\ F_x)$ seront toutes dans la zone linéaire, et nous ne pourrons pas obtenir une relation force-vitesse non linéaire. Par conséquent, ce paramètre v_f doit être un peu plus petit que la vitesse maximale dans le plan extraite à l'étape précédente.

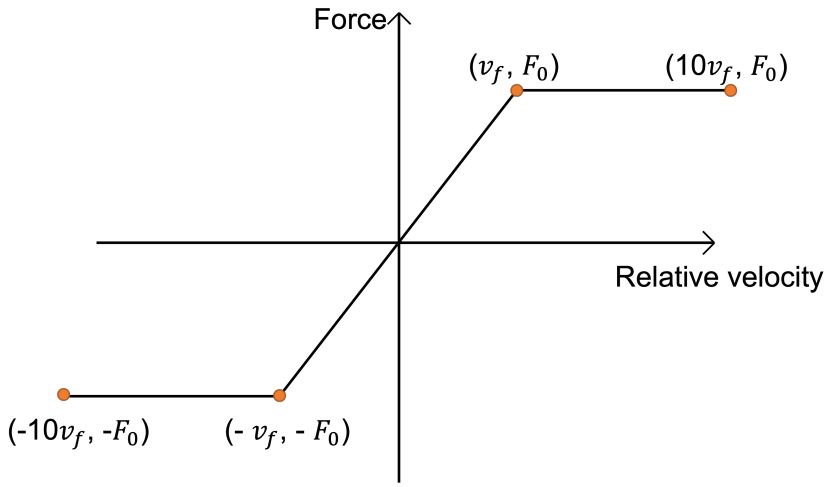

FIGURE A.15: Schéma du modèle d'interaction non linéaire dans le plan.

A.3.3.3 Modèle contact/frottement

Dans la plupart des études sur la non-linéarité acoustique de contact, le frottement est négligé, en particulier dans les simulations par éléments finis. Cependant, en réalité, les surfaces de contact de la zone de délaminage sont généralement des surfaces rugueuses. Lorsque le délaminage interagit avec les ondes de Lamb, les ondes de mode S_0 peuvent provoquer un mouvement relatif dans le plan des interfaces de délaminage,

le frottement doit donc être pris en compte dans les simulations. Dans le modèle mentionné précédemment, les interactions normales et tangentielles sont calculées séparément et n'affectent pas l'une l'autre. Cependant, dans le processus d'interaction vague/dommage, la répartition des contraintes sur les surfaces de contact n'est pas uniforme, de sorte que la pression de contact normale dans certaines parties est plus grande, et dans certaines parties très faible [**Li2019**]. Comme nous le savons, la pression normale affectera la force de frottement, conduisant ainsi à une situation particulière où les zones faiblement comprimées dans la région de contact et les zones non en contact glissent, tandis que les zones fortement comprimées peuvent coller. Par conséquent, un modèle combiné contact/frottement est proposé dans cette section pour mieux simuler le comportement mécanique des interfaces de délaminage.

Dans ce modèle, les ressorts non linéaires sont toujours utilisés dans la direction hors du plan pour formuler l'interaction de contact normale entre les interfaces de délaminage : lorsque les interfaces sont séparées dans la direction normale, la force du ressort est nulle, et lorsque les interfaces sont pénétrées, le ressort présentera une grande raideur pour résister à cette pénétration. Cela peut être exprimé comme

$$F_N = \begin{cases} k^{spr} u_z, & u_z < 0 \\ 0, & u_z > 0 \end{cases} \tag{A.9}$$

où k_z est la raideur du ressort dans la direction normale.

Dans la direction tangentielle (dans le plan), le modèle de frottement de Coulomb est utilisé. Selon la loi de frottement, lorsque le glissement relatif se produit entre les deux surfaces de contact, la force de frottement est proportionnelle à la force normale exercée par chaque surface sur l'autre. Lorsqu'il n'y a pas de déplacement relatif entre deux surfaces en contact, la force de frottement est en fait incertaine [67]. Pour la simplification du calcul, le modèle suivant est utilisé représentant l'interaction dans le plan :

$$F_T = \begin{cases} -\mu F_N, & F_N > 0 \ \& \ b \neq 0 \\ 0, & \text{others} \end{cases} \tag{A.10}$$

où F_T est la force tangentielle, F_N est la force normale exercée par chaque surface sur l'autre perpendiculaire (normale) à la surface, μ est le coefficient de frottement, et b est le glissement relatif . Lorsqu'il y a glissement relatif ($b \neq 0$) et compression ($F_N > 0$) entre les surfaces de contact, la force de frottement existe et est égale au produit du coefficient de frottement par la force normale, dans une direction opposée au glissement relatif.

A.4 Résultats et discussion

Dans cette section, les résultats de simulation sont présentés et comparés aux résultats expérimentaux, afin de vérifier le modèle de simulation.

A.4.1 Plaque intacte

La plaque non endommagée est utilisée pour la vérification du modèle en comparant la sortie électrique et son spectre de fréquence avec les résultats expérimentaux, comme illustré à la figure A.16. La figure de gauche montre les signaux du domaine temporel et la figure de droite montre les caractéristiques du domaine fréquentiel des deux signaux. Dans la figure de gauche, on peut observer que les premiers paquets d'ondes des signaux bruts du domaine temporel provenant à la fois de la simulation et des expériences sont en bon accord. Dans la figure de droite, on peut voir qu'à l'exception de la fréquence fondamentale, les deuxième et troisième harmoniques des résultats de simulation et d'expérience peuvent être clairement observées. Les amplitudes des deuxième et troisième harmoniques des expériences sont plus élevées que celles de la simulation. Cet écart pourrait être dû à la fréquence d'échantillonnage différente de la simulation et des expériences. De plus, en raison de l'influence du bruit environnemental et du système expérimental, le niveau de bruit de l'expérience est supérieur à celui de la simulation.

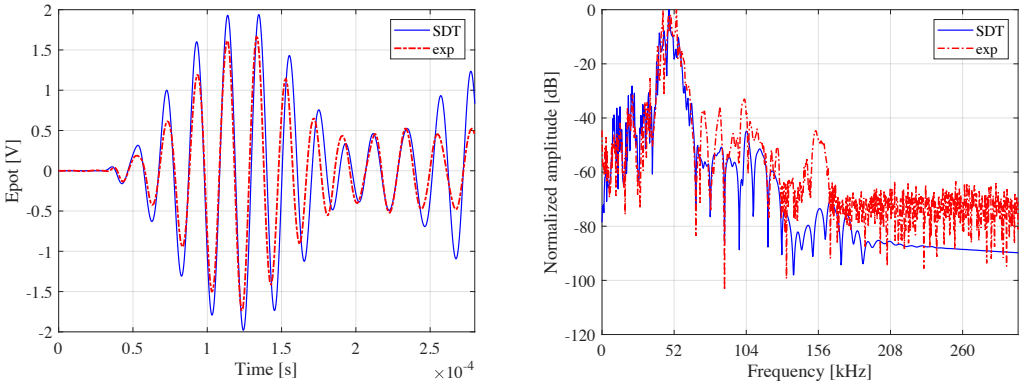

(A) Signal de domaine temporel. (B) Spectres de fréquence.

FIGURE A.16: Comparaison de la sortie électrique dans les domaines temporel et fréquentiel entre les résultats de la simulation et de l'expérience pour la plaque non endommagée. Les signaux de fréquence sont normalisés à la valeur maximale de chaque spectre respectivement.

A.4.2 Plaques endommagées

A.4.2.1 Signaux dans le domaine temporel

Figure A.17 montre la comparaison des signaux de sortie électriques dans le domaine temporel entre les résultats de l'expérience et de la simulation. Ces tracés représentent les amplitudes des ondes sur la région de délaminage prédites par différents modèles de simulation et résultats expérimentaux. On peut constater que les modèles de printemps ont prédit des vagues assez similaires à celles de l'expérience.

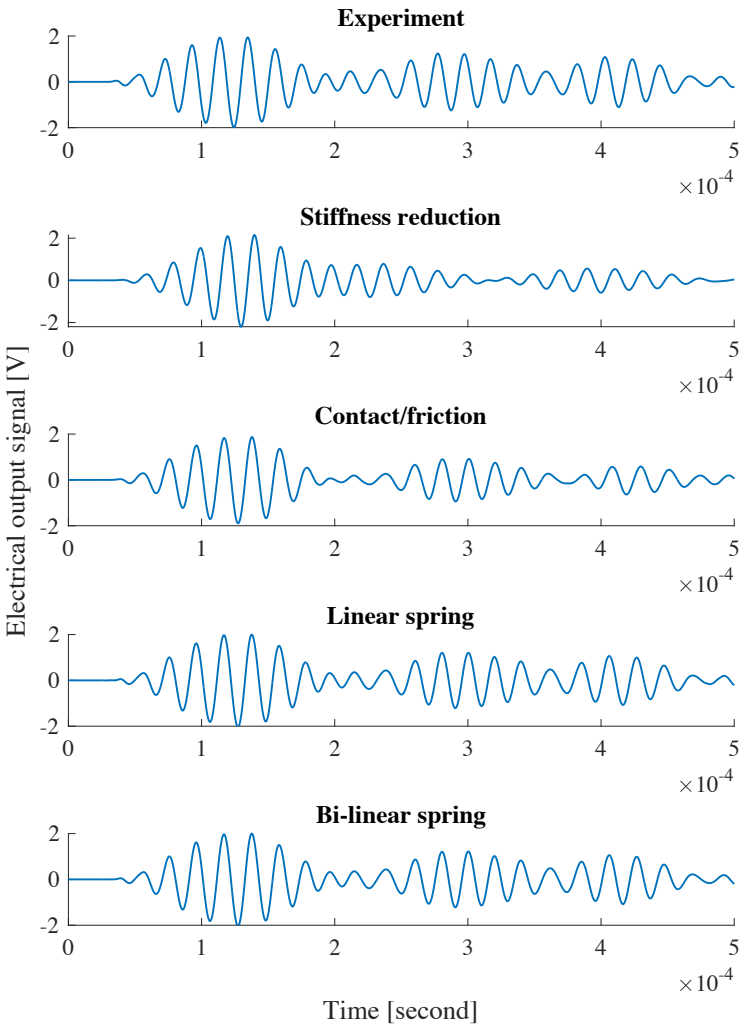

FIGURE A.17: Comparaison des signaux de sortie électriques dans le domaine temporel entre les résultats de l'expérience et de la simulation.

A.4.2.2 Signaux dans le domaine fréquentiel

Dans la figure A.18, une série de comparaisons entre des plaques endommagées (trois impacts) et saines (intactes) a été réalisée par le biais d'expériences et de modèles de simulation. Dans tous les tracés de la figure A.18, la composante de fréquence fondamentale peut être clairement observée à 52 kHz où l'amplitude maximale apparaît. Les résultats de l'expérience dans la figure A.18a impliquent que les amplitudes des deuxième et troisième harmoniques pour les plaques endommagées sont beaucoup plus élevées que celles de la plaque saine. Dans les simulations, l'amplitude de la deuxième harmonique pour les plaques endommagées est supérieure à celle de la plaque saine pour tous les modèles de simulation. Pour la troisième harmonique, les amplitudes du modèle de contact/frottement et du modèle de rigidité bilinéaire sont plus évidentes que les deux autres modèles. Cela indique que les réponses en fréquence du modèle

de rigidité bilinéaire et du modèle de contact/frottement montrent un meilleur accord avec les résultats expérimentaux.

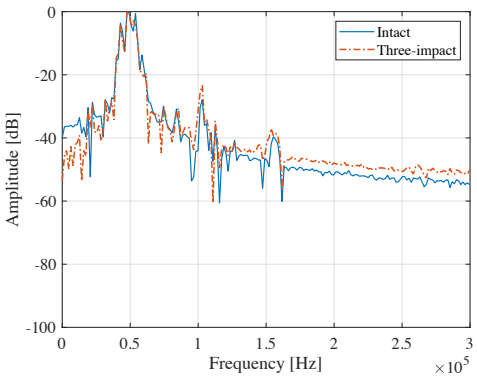

(A) Expérience.

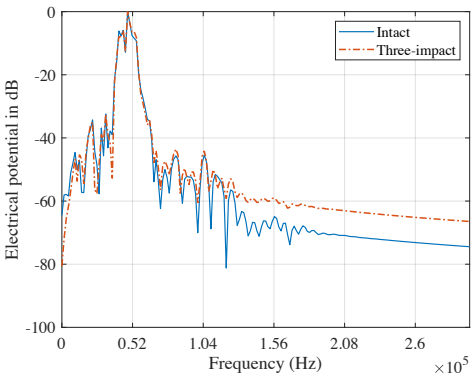

(B) Modèle de réduction de rigidité.

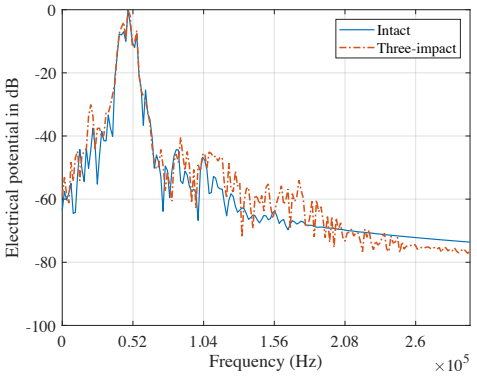

(C) Modèle contact/frottement.

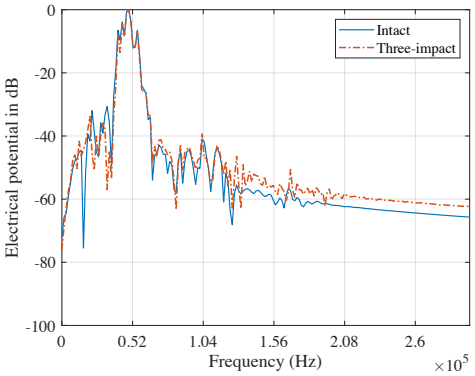

(D) Modèle de ressort bilinéaire.

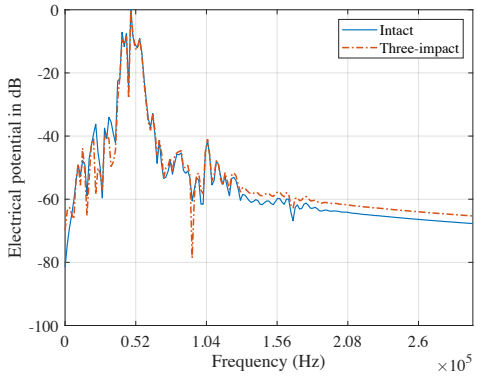

(E) Modèle à ressort linéaire.

FIGURE A.18: FFT normalisée des signaux de sortie de la plaque saine et de la plaque à trois impacts provenant respectivement de l'expérience et des simulations.

A.4.2.3 Indice de dommage

Plusieurs ID sont utilisés pour évaluer la gravité des dommages.

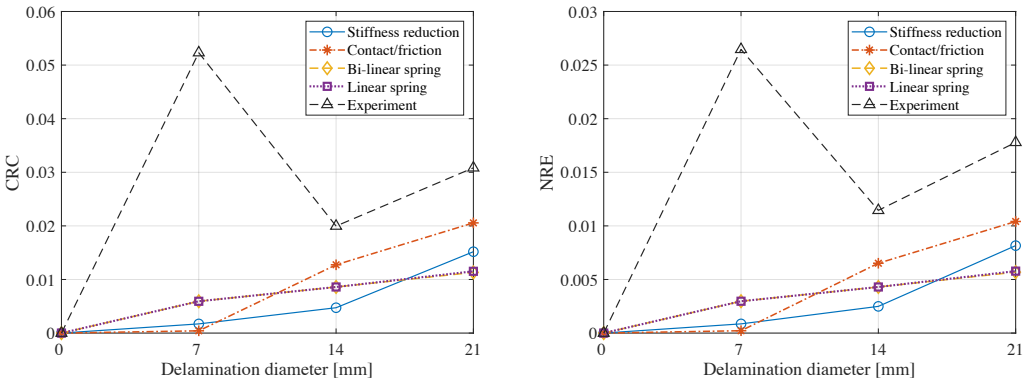

(A) Comparaison du CRC entre les simulations et l'expérience. (B) Comparaison des NRE entre simulations et expérimentation.

Figure A.19a présente la comparaison du CRC entre des résultats expérimentaux et plusieurs prédictions numériques (modèle de réduction de rigidité, modèle de contact/frottement, modèle bilinéaire et modèle de ressort). La réponse expérimentale manifeste un comportement d'oscillation avec l'augmentation du diamètre de délaminage. Les résultats prédits par ces modèles numériques présentent une tendance à l'augmentation continue avec l'augmentation du diamètre de délaminage.

La variation de NRE avec l'augmentation du diamètre de délaminage pour les résultats expérimentaux et les prédictions numériques (comme le montre la figure A.19b) a une tendance similaire à celle du CRC dans la figure A.19a. Dans le cas des mêmes diamètres de délaminage, NRE indique des valeurs d'endommagement plus faibles par rapport à la mesure CRC en termes de résultats expérimentaux et de simulations numériques.

Afin d'enrichir les considérations et d'évaluer plus précisément les résultats, d'autres ID sont employés. Un indicateur de mesure de la gravité des dommages basé sur l'énergie résiduelle normalisée (notée NRE2 pour se distinguer de NRE) est défini comme [63]:

$$NRE2 = \frac{\int_0^T x(t)^2\,dt - \int_0^T y(t)^2\,dt}{max\left(\int_0^T x(t)^2\,dt, \int_0^T y(t)^2\right)} \tag{A.11}$$

où $x(t)$ est la réponse de la plaque endommagée et $y(t)$ est la réponse de la plaque saine.

En utilisant cet indicateur, les comparaisons entre les résultats expérimentaux et les simulations sont illustrées dans la figure A.20. Contrairement aux résultats expérimentaux adoptant les manières CRC et NRE, l'indicateur NRE2 donne une courbe plus lisse. En ce qui concerne les prédictions numériques, des valeurs plus petites ont été générées par rapport aux résultats expérimentaux.

Une autre différence maximale en pourcentage de corrélation croisée (CCMPD) basée sur DI est définie comme [63]:

$$CCMPD = 1 - \frac{\left|\max\left(\hat{R}\{x(t), y(t)\}\right) - \max\left(\hat{R}\{x(t), x(t)\}\right)\right|}{\max\left(\hat{R}\{x(t), x(t)\}\right)} \tag{A.12}$$

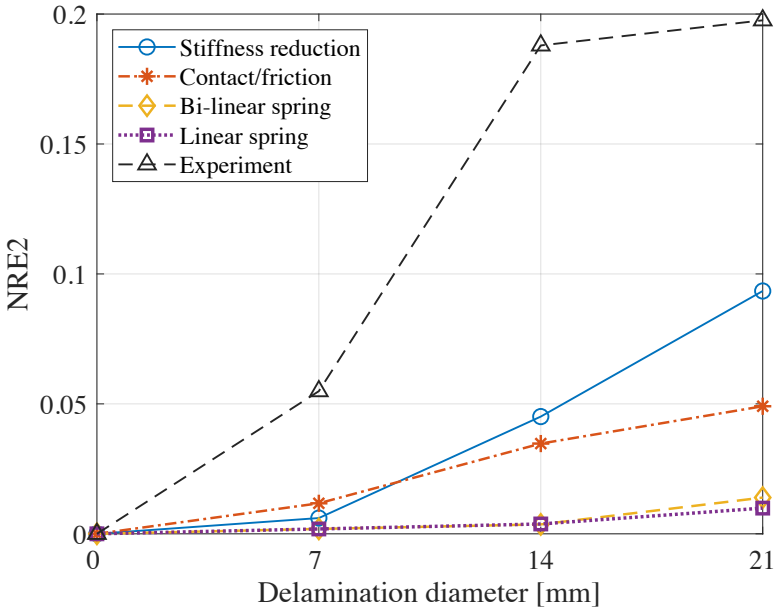

FIGURE A.20: Comparaison de NRE2 entre simulations et expérience.

où $\hat{R}\{x(t), y(t)\}$ indique la corrélation croisée des signaux $x(t)$ et $y(t)$. Figure A.21 présente une comparaison du CCMPD entre les résultats expérimentaux et les prédictions numériques. On peut constater que pour un petit diamètre de délaminage (par exemple, 7 mm), les résultats expérimentaux sont assez similaires aux résultats de simulation prédits par ces modèles numériques. Il convient de noter que le modèle de contact/frottement a prédit une tendance à la baisse à un diamètre de délaminage plus grand.

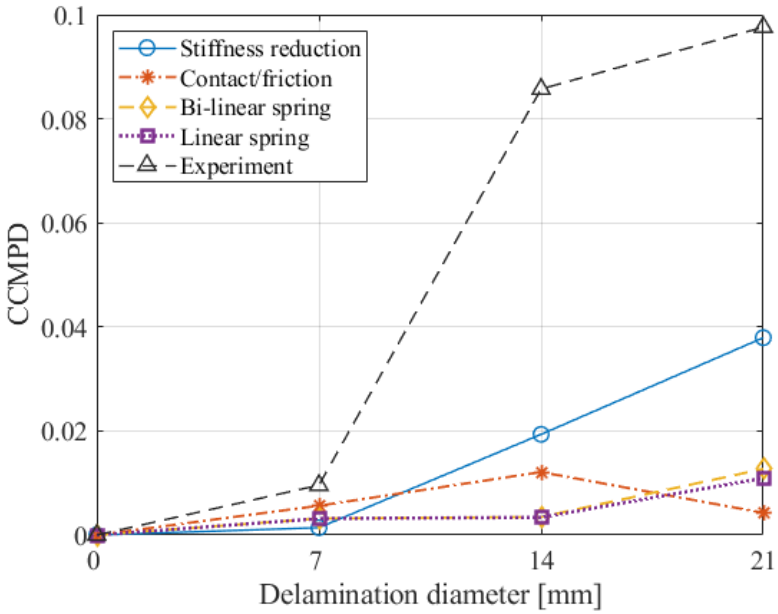

FIGURE A.21: Comparaison du CCMPD entre simulations et expérience.

Dans la figure A.22, les résultats de simulation expérimentale et numérique sont comparés par la mesure du THD relatif. En se concentrant sur la courbe expérimentale de la figure A.22, elle montre une amplitude beaucoup plus grande contrairement à plusieurs comparaisons mentionnées ci-dessus (CRC, NRE, NRE2 et CCMPD). En ce qui concerne les prédictions numériques, le modèle contact/frottement prédit des dommages plus sévères (pour un diamètre de délaminage supérieur à 7 mm) par rapport aux trois autres modèles qui présentent des prédictions presque similaires.

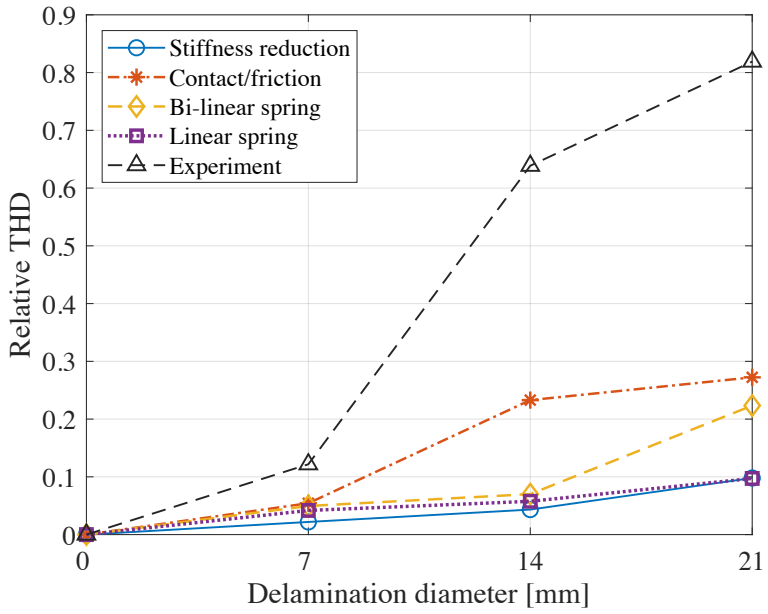

FIGURE A.22: Comparaison du THD relatif entre les simulations et l'expérience.

A.5 Conclusion

Dans cette thèse, les non-linéarités acoustiques dues à la présence de dommages ont été étudiées, et les indices de dommages sont utilisés pour l'évaluation des dommages de délaminage. En particulier, un DI basé sur la distorsion harmonique totale relative a été calculé et validé expérimentalement et numériquement.

Les expériences et les simulations ont été menées sous les excitations d'une variété de fréquences. En particulier, une excitation sinusoïdale à cinq cycles modulée par une fenêtre sinusoïdale à 52 kHz est utilisée pour les études de non-linéarité. La technique des ondes de choc laser a été utilisée pour générer des dommages réalistes de type délaminage dans les échantillons composites et contrôler leurs sévérités et leurs positions. D'après les résultats expérimentaux, on peut conclure que la présence de dommages de délaminage ajoute aux non-linéarités présentées dans les signaux de sortie. Le DI basé sur le THD relatif a été utilisé pour évaluer la sévérité de la délamination et les effets non linéaires. Les résultats montrent que le THD relatif, qui est basé sur les caractéristiques non linéaires des signaux de sortie, est corrélé à

l'étendue des dommages et révèle une sensibilité élevée à la non-linéarité induite par les dommages de délaminage.

Ensuite, le modèle d'éléments finis est établi pour les dommages et les spécimens de plaques composites utilisés dans les expériences. Plusieurs modèles physiques sont proposés et implémentés dans la modélisation par éléments finis. Les études de modèles non linéaires montrent que les modèles proposés sont capables de reproduire le comportement mécanique des dommages de délaminage. En particulier, le modèle contact/frottement induit les effets non linéaires les plus importants en termes de DI. Tous les modèles proposés ont un comportement similaire sur les ID proposés. Parmi tous les indicateurs, les valeurs THD relatives montrent la sensibilité la plus élevée aux dommages de délaminage.

Bibliography

[1] Victor Giurgiutiu. *Structural health monitoring of aerospace composites*. 2015, pp. 1–457. ISBN: 9780124104419. DOI: 10.1016/C2012-0-07213-4.

[2] Lammering Rolf et al. *Lamb-Wave Based Structural Health Monitoring in Polymer Composites*. 2018, p. 479. ISBN: 978-3-319-49714-3. URL: http://link.springer.com/10.1007/978-3-319-49715-0.

[3] Fuh Gwo Yuan. *Structural Health Monitoring (SHM) in Aerospace Structures*. 2016, pp. 285–306. ISBN: 9780081001486. DOI: 10.1016/B978-0-08-100148-6.00010-X. arXiv: arXiv:1011.1669v3. URL: http://www.sciencedirect.com/science/article/pii/B978008100148600010X.

[4] Rytter. "Aalborg Universitet Vibrational Based Inspection of Civil Engineering Structures Rytter , Anders". In: (1993).

[5] J Cai et al. "Structural health monitoring for composite materials". In: *Composites and their applications, chapter structura*. 2012, pp. 37–60.

[6] Robert M. Jones. *Mechanics of Composite Materials*. CRC Press, 1999, pp. 307–319. ISBN: 9781315272986. DOI: 10.1201/9781498711067. URL: https://www.taylorfrancis.com/books/9781498711067.

[7] Meriem Ghrib et al. "Generation of controlled delaminations in composites using symmetrical laser shock configuration". In: *Composite Structures* 171 (2017), pp. 286–297. ISSN: 02638223. DOI: 10.1016/j.compstruct.2017.03.039. URL: http://dx.doi.org/10.1016/j.compstruct.2017.03.039.

[8] george H. Staab. *Laminar Composites*. 1999. ISBN: 9788578110796. DOI: 10.1017/CBO9781107415324.004. arXiv: arXiv:1011.1669v3.

[9] M. M. Shokrieh, Z. Daneshjoo, and M. Fakoor. "A modified model for simulation of mode I delamination growth in laminated composite materials". In: *Theoretical and Applied Fracture Mechanics* 82 (2016), pp. 107–116. ISSN: 01678442. DOI: 10.1016/j.tafmec.2015.12.012. URL: http://dx.doi.org/10.1016/j.tafmec.2015.12.012.

[10] S. L. Ogin, P. Brøndsted, and J. Zangenberg. *Composite materials: Constituents, architecture, and generic damage*. Elsevier, 2016, pp. 3–23. ISBN: 9781782422860. DOI: 10.1016/B978-1-78242-286-0.00001-7. URL: http://dx.doi.org/10.1016/B978-1-78242-286-0.00001-7.

[11] F. Gao et al. “Damage accumulation in woven-fabric CFRP laminates under tensile loading: Part 1. Observations of damage accumulation”. In: *Composites Science and Technology* 59.1 (1999), pp. 123–136. ISSN: 02663538. DOI: 10.1016/S0266-3538(97)00231-5.

[12] D. Broda et al. “Modelling of nonlinear crack-wave interactions for damage detection based on ultrasound - A review”. In: *Journal of Sound and Vibration* 333.4 (2014), pp. 1097–1118. ISSN: 0022460X. DOI: 10.1016/j.jsv.2013.09.033. URL: http://dx.doi.org/10.1016/j.jsv.2013.09.033.

[13] Vitalyi Gusev, Vincent Tournat, and Bernard Castagnde. “Nonlinear Acoustic Phenomena in Micro-inhomogenous Media”. In: *Materials and Acoustics Handbook*. London, UK: ISTE, 2010, pp. 431–471. DOI: 10.1002/9780470611609.ch17. URL: http://doi.wiley.com/10.1002/9780470611609.ch17.

[14] L A Ostrovsky and P A Johnson. “Dynamic nonlinear elasticity in geomaterials”. In: *Rivista del Nuovo Cimento* 24.7 (2001), pp. 1–46. URL: https://www.scopus.com/inward/record.uri?eid=2-s2.0-0039192883&partnerID=40&md5=ca5a282ddeb3de83bdb021baa2e24645.

[15] Hyunjo Jeong et al. “A nondestructive method for estimation of the fracture toughness of CrMoV rotor steels based on ultrasonic nonlinearity”. In: *Ultrasonics* 41.7 (2003), pp. 543–549. ISSN: 0041624X. DOI: 10.1016/S0041-624X(03)00154-9.

[16] Siming Liu et al. “Measuring bulk material nonlinearity using harmonic generation”. In: *NDT and E International* 48 (2012), pp. 46–53. ISSN: 09638695. DOI: 10.1016/j.ndteint.2012.02.009. URL: http://dx.doi.org/10.1016/j.ndteint.2012.02.009.

[17] P. Gudmundson. “The dynamic behaviour of slender structures with cross-sectional cracks”. In: *Journal of the Mechanics and Physics of Solids* 31.4 (1983), pp. 329–345. ISSN: 00225096. DOI: 10.1016/0022-5096(83)90003-0.

[18] M. I. Friswell and J. E. T. Penny. “Crack Modeling for Structural Health Monitoring”. In: *Structural Health Monitoring: An International Journal* 1.2 (2002), pp. 139–148. ISSN: 1475-9217. DOI: 10.1177/147592170200100202. URL: http://journals.sagepub.com/doi/10.1177/147592170200100202.

[19] Yanfeng Shen. “Structural health monitoring using linear and nonlinear ultrasonic guided waves”. In: *PhD Dissertation* (2014), p. 224.

[20] Victor Giurgiutiu, Andrei Zagrai, and Jing Jing Bao. “Piezoelectric wafer embedded active sensors for aging aircraft structural health monitoring”. In: *Structural Health Monitoring* 1.1 (2002), pp. 41–61. ISSN: 14759217. DOI: 10.1177/147592170200100104.

[21] Robert A. Guyer and Paul A. Johnson. "Nonlinear mesoscopic elasticity: Evidence for a new class of materials". In: *Physics Today* 52.4 (1999), pp. 30–36. ISSN: 00319228. DOI: 10.1063/1.882648. URL: http://physicstoday.scitation.org/doi/10.1063/1.882648.

[22] John Conrad Jaeger, Neville G W Cook, and Robert Zimmerman. *Fundamentals of rock mechanics*. John Wiley & Sons, 2009.

[23] Srinivasan Gopalakrishnan, Massimo Ruzzene, and Sathyanaraya Hanagud. *Computational Techniques for Structural Health Monitoring*. Springer Series in Reliability Engineering. London: Springer London, 2011, p. 352. ISBN: 978-0-85729-283-4. DOI: 10.1007/978-0-85729-284-1. URL: http://link.springer.com/10.1007/978-0-85729-284-1.

[24] D. A. Saravanos and D. A. Hopkins. "Effects of delaminations on the damped dynamic characteristics of composite laminates: Analysis and experiments". In: *Journal of Sound and Vibration* 192.5 (1996), pp. 977–993. ISSN: 0022460X. DOI: 10.1006/jsvi.1996.0229.

[25] Siavash Shoja, Viktor Berbyuk, and Anders Boström. "Delamination detection in composite laminates using low frequency guided waves: Numerical simulations". In: *Composite Structures* 203.October 2017 (2018), pp. 826–834. ISSN: 02638223. DOI: 10.1016/j.compstruct.2018.07.025.

[26] Reza Soleimanpour, Ching-Tai Ng, and Chun H. Wang. "Higher harmonic generation of guided waves at delaminations in laminated composite beams". In: *Structural Health Monitoring: An International Journal* 16.4 (2017), pp. 400–417. ISSN: 1475-9217. DOI: 10.1177/1475921716673021. URL: http://journals.sagepub.com/doi/10.1177/1475921716673021.

[27] Joost Segers et al. "Backside delamination detection in composites through local defect resonance induced nonlinear source behavior". In: *Journal of Sound and Vibration* 479 (2020), p. 115360. ISSN: 10958568. DOI: 10.1016/j.jsv.2020.115360.

[28] Yi Yang et al. "Second harmonic generation at fatigue cracks by low-frequency Lamb waves: Experimental and numerical studies". In: *Mechanical Systems and Signal Processing* 99 (2018), pp. 760–773. ISSN: 10961216. DOI: 10.1016/j.ymssp.2017.07.011. URL: http://dx.doi.org/10.1016/j.ymssp.2017.07.011.

[29] Alfredo Lamberti and Fabio Semperlotti. "Detecting closing delaminations in laminated composite plates using nonlinear structural intensity and time reversal mirrors". In: *Smart Materials and Structures* 22.12 (2013). ISSN: 09641726. DOI: 10.1088/0964-1726/22/12/125006.

[30] Ming Hong et al. "Modeling nonlinearities of ultrasonic waves for fatigue damage characterization: Theory, simulation, and experimental validation". In: *Ultrasonics* 54.3 (2014), pp. 770–778. ISSN: 0041624X. DOI: 10.1016/j.ultras.2013.09.023. URL: http://dx.doi.org/10.1016/j.ultras.2013.09.023.

[31] Michael Smith. *ABAQUS Documentation user's guide for v6.14-5*. United States: Dassault Systèmes Simulia Corp, 2014.

[32] B. W. Drinkwater, R. S. Dwyer-Joyce, and P. Cawley. "A study of the interaction between ultrasound and a partially contacting solid-solid interface". In: *Proceedings of the Royal Society A: Mathematical, Physical and Engineering Sciences* 452.1955 (1996), pp. 2613–2628. ISSN: 13645021. DOI: 10.1098/rspa.1996.0139. URL: https://royalsocietypublishing.org/doi/abs/10.1098/rspa.1996.0139.

[33] D. Liaptsis, B. W. Drinkwater, and R. Thomas. "The interaction of oblique incidence ultrasound with rough, partially contacting interfaces". In: *Nondestructive Testing and Evaluation* 21.3-4 (2006), pp. 109–121. ISSN: 1058-9759. DOI: 10.1080/10589750601056920. URL: https://www.tandfonline.com/doi/abs/10.1080/10589750601056920http://www.tandfonline.com/doi/abs/10.1080/10589750601056920.

[34] Shiro Biwa. "Second-harmonic generation at contacting interfaces". In: *Nonlinear Ultrasonic and Vibro-Acoustical Techniques for Nondestructive Evaluation*. 2018, pp. 263–299. ISBN: 9783319944760. DOI: 10.1007/978-3-319-94476-0_7.

[35] Shiro Biwa, Shunsuke Hiraiwa, and Eiji Matsumoto. "Stiffness evaluation of contacting surfaces by bulk and interface waves". In: *Ultrasonics* 47.1-4 (2007), pp. 123–129. ISSN: 0041624X. DOI: 10.1016/j.ultras.2007.08.005.

[36] Naoki Mori and Shiro Biwa. "Transmission characteristics of the S0 and A0 Lamb waves at contacting edges of plates". In: *Ultrasonics* 81 (2017), pp. 93–99. ISSN: 0041624X. DOI: 10.1016/j.ultras.2017.06.009. URL: http://dx.doi.org/10.1016/j.ultras.2017.06.009.

[37] Tianming Ye, Shiro Biwa, and Naoki Mori. "Second-harmonic generation of the lowest-order antisymmetric Lamb wave at a closed parallel crack". In: *The Journal of the Acoustical Society of America* 148.4 (2020), pp. 2073–2085. ISSN: 0001-4966. DOI: 10.1121/10.0002171.

[38] Steven Delrue and Koen Van Den Abeele. "Three-dimensional finite element simulation of closed delaminations in composite materials". In: *Ultrasonics* 52.2 (2012), pp. 315–324. ISSN: 0041624X. DOI: 10.1016/j.ultras.2011.09.001. URL: http://dx.doi.org/10.1016/j.ultras.2011.09.001.

[39] Bibi I. S. Murat, Pouyan Khalili, and Paul Fromme. "Scattering of guided waves at delaminations in composite plates". In: *The Journal of the Acoustical Society of America* 139.6 (2016), pp. 3044–3052. ISSN: 0001-4966. DOI: 10.1121/1.4953016.

[40] Cara A.C. Leckey et al. “Simulation of guided-wave ultrasound propagation in composite laminates: Benchmark comparisons of numerical codes and experiment”. In: *Ultrasonics* 84 (2018), pp. 187–200. ISSN: 0041-624X. DOI: 10.1016/J.ULTRAS.2017.11.002. URL: https://www.sciencedirect.com/science/article/pii/S0041624X17305462?via%3Dihub.

[41] W. K. Chiu, L. R.F. Rose, and N. Nadarajah. “Scattering of the Fundamental Anti-symmetric Lamb Wave by a Mid-plane Edge Delamination in a Fiber-composite Laminate”. In: *Procedia Engineering* 188 (2017), pp. 317–324. ISSN: 18777058. DOI: 10.1016/j.proeng.2017.04.490. URL: http://dx.doi.org/10.1016/j.proeng.2017.04.490.

[42] Angelo De Fenza et al. “Post-impact damage detection on a winglet structure realized in composite material”. In: *Composite Structures* 169 (2017), pp. 129–137. ISSN: 02638223. DOI: 10.1016/j.compstruct.2016.10.004.

[43] Ming Hong et al. “Locating fatigue damage using temporal signal features of nonlinear Lamb waves”. In: *Mechanical Systems and Signal Processing* 60 (2015), pp. 182–197. ISSN: 10961216. DOI: 10.1016/j.ymssp.2015.01.020.

[44] Hoon Sohn and Seuno Bum Kim. “Development of dual PZT transducers for reference-free crack detection in thin plate structures”. In: *IEEE Transactions on Ultrasonics, Ferroelectrics, and Frequency Control*. Vol. 57. 1. 2010, pp. 229–240. DOI: 10.1109/TUFFC.2010.1401.

[45] Jian Chen et al. “On-line prognosis of fatigue crack propagation based on Gaussian weight-mixture proposal particle filter”. In: *Ultrasonics* 82 (2018), pp. 134–144. ISSN: 0041624X. DOI: 10.1016/j.ultras.2017.07.016. URL: https://doi.org/10.1016/j.ultras.2017.07.016https://linkinghub.elsevier.com/retrieve/pii/S0041624X17304407.

[46] Jeong Beom Ihn and Fu Kuo Chang. “Detection and monitoring of hidden fatigue crack growth using a built-in piezoelectric sensor/actuator network: I. Diagnostics”. In: *Smart Materials and Structures* 13.3 (2004), pp. 609–620. ISSN: 09641726. DOI: 10.1088/0964-1726/13/3/020. URL: https://iopscience.iop.org/article/10.1088/0964-1726/13/3/020https://iopscience.iop.org/article/10.1088/0964-1726/13/3/020/meta.

[47] J Prawin and A Rama Mohan Rao. “Vibration-based breathing crack identification using non-linear intermodulation components under noisy environment”. In: *Structural Health Monitoring* (2019), p. 147592171983695. ISSN: 1475-9217. DOI: 10.1177/1475921719836953. URL: http://journals.sagepub.com/doi/10.1177/1475921719836953.

[48] Jun Chen et al. “Experimental characterization of granite damage using nonlinear ultrasonic techniques”. In: *NDT and E International* 67 (2014), pp. 10–16. ISSN: 09638695. DOI: 10.1016/j.ndteint.2014.06.005.

[49] Deba Datta Mandal and Sauvik Banerjee. "Identification of breathing type disbonds in stiffened panels using non-linear lamb waves and built-in circular PWT array". In: *Mechanical Systems and Signal Processing* 117 (2019), pp. 33–51. ISSN: 10961216. DOI: 10.1016/j.ymssp.2018.07.040. URL: https://doi.org/10.1016/j.ymssp.2018.07.040.

[50] Nitesh P. Yelve, Mira Mitra, and Prasanna M. Mujumdar. "Spectral damage index for estimation of breathing crack depth in an aluminum plate using nonlinear Lamb wave". In: *Structural Control and Health Monitoring* 21.5 (2014), pp. 833–846. ISSN: 15452263. DOI: 10.1002/stc.1604. URL: http://doi.wiley.com/10.1002/stc.1604.

[51] Meriem Ghrib. "Structural Health Monitoring of composite structures: LASER shock delamination generation and machine learning-based quantification". PhD thesis. L'École Nationale Supérieure d'Arts et Métiers, 2017.

[52] R. Ecault et al. "Development of the laser shock wave adhesion test on bonded CFRP composite". In: *International Journal of Structural Integrity* 5.4 (2014), pp. 253–261. ISSN: 17579872. DOI: 10.1108/IJSI-10-2013-0032/FULL/HTML.

[53] J. W Trainor, R. J; Graboske, H. C ; Long, K. S; Shaner. "Application of High-Power Lasers To Equation-of-State Research At Ultrahigh Pressures". In: (1978).

[54] Michel Arrigoni et al. "An Industrial Challenge Based on the Wave Propagation : the Shock Adhesion Test". In: *Wave Propagation* January (2012), pp. 605–633.

[55] L. Berthe et al. "Shock waves from a water-confined laser-generated plasma". In: *Journal of Applied Physics* 82.6 (1997), pp. 2826–2832. ISSN: 00218979. DOI: 10.1063/1.366113.

[56] R. Fabbro et al. "Physical study of laser-produced plasma in confined geometry". In: *Journal of Applied Physics* 68.2 (1990), pp. 775–784. ISSN: 00218979. DOI: 10.1063/1.346783.

[57] Romain Ecault et al. "Laser shock adhesion test numerical optimization for composite bonding assessment". In: *Composite Structures* 247 (2020). ISSN: 02638223. DOI: 10.1016/j.compstruct.2020.112441.

[58] R. Ecault et al. "Laser shock waves: A way to test and damage composite materials for aeronautic applications". In: *AIP Conference Proceedings* 1464 (2012), pp. 126–137. ISSN: 0094243X. DOI: 10.1063/1.4739867.

[59] M Ghrib et al. "LASER shock delamination generation and machine learning-based damage quantification in CFRP composites plates". In: (2018).

[60] Meriem Ghrib et al. "Automatic damage type classification and severity quantification using signal based and nonlinear model based damage sensitive features". In: *Journal of Process Control* 83 (2019), pp. 136–146. ISSN: 09591524. DOI: 10.1016/j.jprocont.2018.08.002. URL: https://linkinghub.elsevier.com/retrieve/pii/S0959152418301975.

[61] O. Giannini, P. Casini, and F. Vestroni. "Nonlinear harmonic identification of breathing cracks in beams". In: *Computers and Structures* 129 (2013), pp. 166–177. ISSN: 00457949. DOI: 10.1016/j.compstruc.2013.05.002. URL: http://dx.doi.org/10.1016/j.compstruc.2013.05.002.

[62] Zhongqing Su, Lin Ye, and Ye Lu. "Guided Lamb waves for identification of damage in composite structures: A review". In: *Journal of Sound and Vibration* 295.3-5 (2006), pp. 753–780. ISSN: 10958568. DOI: 10.1016/j.jsv.2006.01.020.

[63] Emmanuel Lize. "Détection d'endommagement sans état de référence et estimation de la température pour le contrôle santé intégré de structures composites par ondes guidées." PhD thesis. L'École Nationale Supérieure d'Arts et Métiers, 2018. URL: http://www.theses.fr/2018ENAM0058.

[64] Joseph Lee Rodgers and W Alan Nicewander. "Thirteen Ways to Look at the Correlation Coefficient". In: *The American Statistician* 42.1 (1988), pp. 59–66. ISSN: 0003-1305. DOI: 10.1080/00031305.1988.10475524. URL: https://doi.org/10.1080/00031305.1988.10475524.

[65] Friedrich Moser, Laurence J. Jacobs, and Jianmin Qu. "Modeling elastic wave propagation in waveguides with the finite element method". In: *NDT E International* 32.4 (1999), pp. 225–234. ISSN: 0963-8695. DOI: 10.1016/S0963-8695(98)00045-0. URL: https://www.sciencedirect.com/science/article/pii/S0963869598000450.

[66] Christophe Geuzaine and Jean François Remacle. "Gmsh: A 3-D finite element mesh generator with built-in pre- and post-processing facilities". In: *International Journal for Numerical Methods in Engineering* 79.11 (2009), pp. 1309–1331. ISSN: 00295981. DOI: 10.1002/nme.2579.

[67] Vladislav Aleshin et al. "Two dimensional modeling of elastic wave propagation in solids containing cracks with rough surfaces and friction – Part I: Theoretical background". In: *Ultrasonics* 82 (2018), pp. 11–18. ISSN: 0041624X. DOI: 10.1016/j.ultras.2017.07.002. URL: https://doi.org/10.1016/j.ultras.2017.07.002.

Xixi LI

Lamb waves propagation in composite structures in presence of LASER induced delamination: simulation and experiments

Résumé : Cette thèse aborde la problématique de la surveillance de la santé structurelle (SHM), liée à l'utilisation d'une technique ultrasonique basée sur les ondes de Lamb pour les structures à parois minces, en se concentrant particulièrement sur les dommages de type délaminage dans les composants de structures composites. Le comportement mécanique du délaminage, ainsi que l'interaction entre les ondes Lamb et le délaminage sont abordés. Une étude expérimentale est menée à l'aide d'un système SHM, composé d'un générateur de signaux, d'un amplificateur, d'un multiplexeur, de spécimens, d'un système d'acquisition de données et d'un ordinateur. Les spécimens sont des plaques stratifiées en polymère renforcé par fibres de carbone, équipées de transducteurs piézoélectriques (PZT). Des échantillons intacts et endommagés avec des délaminages d'étendue différente sont utilisés pour les expériences. Les délaminages sont générés à l'aide d'une technique de choc laser, permettant de contrôler l'emplacement et la taille spécifiques du délaminage. Des éléments PZT collés à la surface de la structure sont utilisés comme actionneurs et capteurs des ondes de Lamb dans les interrogations de type "pitch-and-catch". Plusieurs indicateurs de dommages (DI) sont mis en œuvre et utilisés pour évaluer la gravité du délaminage, sur la base des caractéristiques dans les domaines temporel et fréquentiel. Les DI proposés sont utilisés pour évaluer la sévérité du délaminage et les effets non linéaires. Les résultats montrent que la sensibilité du système à diverses tailles de dommages induit des réponses différentes selon le DI considéré. La modélisation par éléments finis des structures endommagées comprend une construction en couches des plaques composites, séparées dans la zone de délaminage. L'utilisation d'éléments de plaques piézoélectriques pour les capteurs-actionneurs permet une simulation directe d'une interrogation SHM en termes de signaux électriques d'entrée et de sortie. Au stade de l'analyse des paramètres du modèle d'interface de délaminage, des investigations préliminaires sont menées sur des modèles 2D. Ainsi, des plages de paramètres pertinentes ont été examinées, en termes de comportement physique, mais aussi en termes de DI. Enfin, une fois ces observations transposées sur un modèle 3D, un modèle de structure complet est construit, conduisant à une comparaison avec l'observation expérimentale, directement en termes de signaux et en termes de divers DI.

Mots clés : Contrôle santé intégré, Ondes de Lamb, Dynamique non linéaire, structures composites.

Abstract : This dissertation addresses structural health monitoring (SHM) problematic, related to the use a Lamb wave-based ultrasonic technique for thin-walled structures, particularly focusing on delamination-type damage in composite structure components. The mechanical behavior of the delamination, as well as the interaction between Lamb waves and delamination are addressed. An experimental investigation is conducted employing an SHM system, which is composed of a signal generator, an amplifier, a multiplexer, specimens, a data acquisition system and a computer. The specimens are carbon fiber reinforced polymer laminate plates equipped with piezoelectric transducers (PZT). Sample set including intact and damaged with delaminations of different extent are employed for the experiments. The delaminations are generated using a Laser Shock technique, which can provide specific location and size of the delamination. PZT elements bonded to the structure surface are used as actuator and sensor of the Lamb waves in pitch-and-catch interrogations. Several damage indicators (DI) are implemented and employed to evaluate the severity of the delamination, based on time and frequency domain features. The proposed DIs are employed to evaluate the delamination severity and the nonlinear effects. Results show that the system's sensitivity to various damage sizes induces different responses depending on DI considered. Finite element modeling of damaged structures includes a layered construction of the composite plates, split in the delamination area. The use of piezoelectric plate elements for the sensors-actuators enables a direct simulation of an SHM interrogation in terms of electric input and output signals. At the stage of delamination interface model parameters analysis, preliminary investigations are conducted on 2D models. Thus, relevant parameter ranges were examined, in terms of physical behavior, but also in terms of DI. Finally, once those observations transposed to a 3D model, full structure model is built, leading to a comparison to the experimental observation, directly in signals and in terms of various DIs.

Keywords : Structural health monitoring, Lamb waves, Nonlinear dynamics, composite structures.